

Application of SeaWinds Scatterometer Data to the Study of Antarctic Icebergs

Keith M. Stuart

A dissertation submitted to the faculty of
Brigham Young University
in partial fulfillment of the requirements for the degree of

Doctor of Philosophy

David G. Long, Chair
Richard W. Christiansen
David J. Comer
Dah Jye Lee
Julie C. Vanderhoff

Department of Electrical and Computer Engineering

Brigham Young University

December 2012

Copyright © 2012 Keith M. Stuart

All Rights Reserved

ABSTRACT

Application of SeaWinds Scatterometer Data to the Study of Antarctic Icebergs

Keith M. Stuart

Department of Electrical and Computer Engineering

Doctor of Philosophy

Knowledge of iceberg location and size is important for safety reasons as well as for understanding many geophysical and biological processes. This dissertation analyzes large tabular icebergs in the Southern Ocean using the SeaWinds scatterometer. SeaWinds is a spaceborne radar designed to measure the microwave backscatter from the Earth's surface. Using resolution-enhancement techniques, backscatter measurements are processed into backscatter images in which icebergs can be observed.

An iceberg detection methodology is formalized using daily scatterometer images. Radar profiles from common Antarctic scatterers are quantified and an iceberg detection methodology is formalized using daily scatterometer images. Iceberg positions are determined in real-time and a time-series of iceberg positions is maintained in an Antarctic iceberg database. Using the Antarctic iceberg database, characteristic iceberg motion trends are identified. Iceberg detection and tracking is demonstrated through real-time operational support of the 2005, 2008, and 2009 National Science Foundation Antarctic cruises.

To supplement iceberg position reports, I develop multiple algorithms to estimate iceberg size and rotational orientation from backscatter images and from raw backscatter measurements. Estimates derived from SeaWinds images are found to be more accurate. Using iceberg size parameters in conjunction with Newton's equations of motion and forcing profiles (e.g., ocean and air currents), I also develop an iceberg motion model to predict the translational and rotational motion of large tabular icebergs. To improve model results, a Kalman filter is used to incorporate actual iceberg measurements into the motion model, and statistics from the Kalman filter are used to evaluate model performance. Simulated iceberg motion is found to best coincide with observed iceberg motion in regions where slower iceberg drift speeds are observed. The model is less accurate at high speeds.

The iceberg motion model is inverted to produce estimates of ocean currents given observations of iceberg size and motion. Multiple ocean current estimates are combined using reconstruction techniques and compared with numerically-derived ocean currents from the Ocean Circulation and Climate Advanced Modeling (OCCAM) project. It is found that reconstructed ocean currents coincide with OCCAM currents in regions where observed iceberg motion is not extreme. Also, reconstructed ocean currents coincide more with OCCAM currents that have been averaged over multiple years than with monthly-reported values.

Keywords: SeaWinds, scatterometer, iceberg, Southern Ocean

ACKNOWLEDGMENTS

I would like to thank the many teachers and mentors who have inspired, guided, and shown me that there are always wonderful things to explore. I acknowledge the guidance of Dr. David Long, my academic adviser who introduced me to the field of remote sensing.

I would also like to thank the National Science Foundation for their support of the 2005, 2008, and 2009 Antarctic cruises as well as the officers, crew, and scientists aboard the first cruise ARSV L.M. Gould cruise LMG05-014A and the second and third cruises RVIB N.B. Palmer, NBP08-06 and NBP09-02, for their hard work at sea.

Most of all, I acknowledge my wife, Jessica Stuart, whose support and encouragement has made this work possible.

Table of Contents

List of Tables	ix
List of Figures	x
1 Introduction	1
1.1 Motivation	1
1.2 Previous Work	1
1.2.1 Safety	1
1.2.2 Science	3
1.2.3 Radar	5
1.3 Approach	7
1.4 Research Contributions	8
1.5 Outline	9
2 Background	10
2.1 Introduction	10
2.2 SeaWinds	10
2.3 Resolution Enhancement	13
3 Detecting Icebergs	17
3.1 Introduction	17

3.2	SeaWinds Backscatter Images	17
3.3	Scattering Theory	18
3.4	Antarctic Backscatter Profiles	21
3.5	Iceberg Detection	25
3.5.1	Detection Methodology	26
3.5.2	NRT Iceberg Detection	28
3.6	Conclusion	28
4	Tracking Icebergs	29
4.1	Introduction	29
4.2	Iceberg Database	29
4.3	Iceberg Counts	30
4.4	Iceberg Movement Profiles	30
4.5	Case Study of Iceberg C19a	33
4.6	NSF Cruise Case Studies	33
4.6.1	The 2005 Cruise	35
4.6.2	The 2008 Cruise	37
4.6.3	The 2009 Cruise	38
4.6.4	Sample Data	41
4.7	Discussion	43
4.8	Conclusion	45
5	Estimating Iceberg Size and Orientation	47
5.1	Introduction	47
5.2	Background	47
5.3	Iceberg Model	49

5.4	Estimation Algorithm	51
5.4.1	Image-based Estimation	51
5.4.2	Measurement-based Estimation	53
5.4.3	Algorithm Comparison	54
5.5	Performance	55
5.5.1	Simulation	55
5.5.2	Case Study	59
5.5.3	Time-series	64
5.6	Discussion	72
5.7	Conclusion	74
6	Estimating Iceberg Motion	76
6.1	Introduction	76
6.2	Background	78
6.2.1	Climatological Datasets	78
6.2.2	Iceberg Datasets	79
6.3	Iceberg Model	80
6.4	Estimation Algorithm	82
6.4.1	Equations of Motion	82
6.4.2	Numerical Integration	87
6.4.3	Data Assimilation	89
6.5	Performance	91
6.5.1	Simulation	91
6.5.2	Case Study	100
6.5.3	Data Assimilation	105

6.6	Discussion	114
6.7	Conclusion	119
7	Estimating Ocean Currents	121
7.1	Introduction	121
7.2	Models	122
7.2.1	Iceberg Motion Model	122
7.2.2	Physical Iceberg Model	124
7.2.3	Ocean Model	124
7.3	Estimation Algorithms	125
7.3.1	Iceberg Tracks Simulation	125
7.3.2	Ocean Currents	126
7.4	Performance	129
7.4.1	Iceberg Tracks	129
7.4.2	Ocean Currents	132
7.5	Conclusion	139
8	Conclusion	140
8.1	Summary of Contributions	140
8.2	Future Work	142
	Bibliography	144
A	Map of the Southern Ocean	152
B	A Review of Microwave Scattering from Antarctic Targets	154
B.1	Surface and Volume Scattering	154

B.2	Antarctic Scatterers	155
B.2.1	Sea Water	155
B.2.2	Sea Ice	156
B.2.3	Glacial Ice	157
C	Drag on an Iceberg due to Internal Ocean Waves	158

List of Tables

3.1	Expected backscatter from sea water, sea ice, and glacial ice	23
4.1	Iceberg counts reported to the NSF Antarctic cruises	34
4.2	Icebergs detected during the 2005 NSF Antarctic cruise	36
4.3	Icebergs detected during the 2008 NSF Antarctic cruise	39
4.4	Icebergs detected during the 2009 NSF Antarctic cruise	42
5.1	Iceberg size estimation simulation results	56
5.2	Comparison of size estimates with variable regularization	58
5.3	Results of size estimation algorithms	62
5.4	Differences between iceberg size estimates and high-res. imagery estimates	65
5.5	Count of accurate size estimates of iceberg A22a	70
7.1	RMS differences between averaged iceberg-derived ocean currents and averaged OCCAM currents	132
7.2	Average iceberg-based and OCCAM surface current velocities	133
7.3	RMS differences between daily iceberg-derived ocean currents and daily OCCAM currents	136
7.4	RMS differences between daily iceberg-derived ocean currents and averaged OCCAM currents	138

List of Figures

2.1	SeaWinds scanning geometry	11
2.2	SeaWinds footprint geometry	12
2.3	Sample backscatter image of Antarctica	15
2.4	Sample backscatter image of the Weddell Sea	16
3.1	Backscatter images of South Georgia Island	19
3.2	Backscatter image of the Ross Sea	22
3.3	Backscatter histograms of sea water, sea ice, and glacial ice	23
3.4	Multi-day backscatter histograms of sea water, sea ice, and glacial ice	24
3.5	Expected backscatter from sea water, sea ice, and glacial ice	25
3.6	Average annual sea ice extent in the Southern Ocean	26
4.1	Iceberg count using SeaWinds	31
4.2	Iceberg tracks detected using SeaWinds	32
4.3	Time-series of backscatter images of iceberg C19a	34
4.4	Icebergs detected during the 2005 NSF Antarctic cruise	37
4.5	Icebergs detected during the 2008 NSF Antarctic cruise	40
4.6	Icebergs detected during the 2009 NSF Antarctic cruise	41
4.7	Sample NRT iceberg update images	44
4.8	Validation images of iceberg C19a	45
4.9	Validation images of iceberg A22a	46

5.1	Top-down physical iceberg model	50
5.2	Iceberg size estimation simulation	57
5.3	Monte Carlo results of image-based size estimation algorithm	60
5.4	Monte Carlo results of measurement-based size estimation algorithm	61
5.5	Validation of iceberg size estimation using DMSP	63
5.6	Validation of iceberg size estimation using MODIS	63
5.7	Validation of iceberg size estimation using AVHRR	64
5.8	Time-series of major-axis length estimates of iceberg A22a	66
5.9	Time-series of NIC reports and composite estimates of major-axis length	67
5.10	Time-series of minor-axis length estimates of iceberg A22a	68
5.11	Time-series of NIC reports and composite estimates of minor-axis length	69
5.12	Time-series of angle of rotational orientation of iceberg A22a	71
5.13	Time-series of composite estimates of angle of rotational orientation	72
6.1	Three-dimensional physical iceberg model	81
6.2	Iceberg motion simulation with variable regularization	92
6.3	Force orders in the iceberg motion model	94
6.4	Comparison of simulated iceberg velocity with average ocean current velocity	95
6.5	Water and air profiles over an iceberg	97
6.6	Average water velocity around an iceberg	98
6.7	Average air velocity over an iceberg	99
6.8	Positions of iceberg B09a	101
6.9	Time-series of size estimates for iceberg B09a	102
6.10	Time-series of angle of rotation estimates for iceberg B09a	103
6.11	Performance of the iceberg motion model of iceberg B09a	104

6.12	Histograms of the average velocity of iceberg B09a	106
6.13	Positions of iceberg B09a with highlighted velocity segments	107
6.14	Segmented velocity profiles of iceberg B09a	108
6.15	Trace of the Kalman filter covariance matrix given random updates	111
6.16	Norm of the Kalman filter covariance matrix given random updates	112
6.17	Norm of the Kalman filter covariance sub-matrix given random updates	113
6.18	Trace of the Kalman filter covariance matrix given deterministic updates	115
6.19	Norm of the Kalman filter covariance matrix given deterministic updates	116
6.20	Norm of the Kalman filter covariance sub-matrix given deterministic updates	117
7.1	Regions of characteristic iceberg motion	126
7.2	Physical iceberg shape model superimposed over ocean current grid	128
7.3	Tracks of 80 icebergs observed using SeaWinds, 2000-2004	130
7.4	Tracks of 80 simulated icebergs from 2000-2004	131
7.5	Eastward iceberg-derived ocean currents, 1999-2009	133
7.6	Northward iceberg-derived ocean currents, 1999-2009	134
7.7	Eastward difference between iceberg-derived ocean currents and OCCAM currents, 2000-2004	135
7.8	Northward difference between iceberg-derived ocean currents and OCCAM currents, 2000-2004	136
7.9	Eastward RMS differences between daily iceberg-derived ocean currents and daily OCCAM currents	137
7.10	Northward RMS differences between daily iceberg-derived ocean currents and daily OCCAM currents	138
A.1	Map of Antarctica and the Southern Ocean	153

Chapter 1

Introduction

1.1 Motivation

An iceberg is a floating mass of freshwater ice that has calved (broken off) from a glacier or an ice shelf. Tracking iceberg positions is important for navigation and safety reasons as well as for understanding many geophysical, chemical and biological processes. For example, icebergs affect shipping lanes, outline ocean currents, and influence biological productivity. Observed physical and electromagnetic properties of icebergs are also useful in estimating local weather conditions and for analyzing the induction of fresh water into the ocean, a dominant driving force in Earth's thermohaline circulatory system [1–3].

The impact of an iceberg on its environment is related to iceberg properties such as physical size, spatial orientation, relative velocity, and composition. Because of the importance and scope of these parameters, an understanding of iceberg processes is necessary. To better understand the contributions of this dissertation, a brief overview of the history of iceberg detection and tracking is provided.

1.2 Previous Work

Historical studies involving icebergs can be categorized by the initial purpose of the study: safety reasons (e.g., collision avoidance) and scientific research. A historical review of iceberg tracking is presented with respect to maritime safety, scientific interests, and technological advances for iceberg detection (e.g., radar).

1.2.1 Safety

Before April 1912 there was no system to track icebergs in order to guard ships against potential collisions. The sinking of the RMS Titanic sparked the demand for a system to regu-

larly observe and track icebergs. For the remainder of the ice season in 1912, the United States Navy patrolled the trade and transit corridors in the Atlantic ocean and monitored ice flow. In November 1913, the International Conference on the Safety of Life at Sea met in London to devise a more permanent cooperative system of observing icebergs. Within three months, participating maritime nations jointly formed the International Ice Patrol (IIP) to collect meteorological and oceanographic data in the Atlantic and Arctic Oceans.

For the last 100 years, the IIP has been the principal agency monitoring and reporting iceberg movements for safety purposes in the Northern Hemisphere. To accomplish this goal, the IIP tracks icebergs using three primary methods listed in their historical order of appearance: surface ships, airborne platforms, and space sensors.

Icebergs were first tracked using visual surveillance aboard surface ships sailing between North America and Europe. Sailors found that standing at the highest point of their vessel and surveying with binoculars was one of the most effective ways of detecting icebergs. Icebergs were detected from ships traveling in the Atlantic and Arctic Oceans. The ships were referred to as “the thousand eyes of the Ice Patrol”. While ship reports mitigated potential collisions, sailors found that the visual discovery of icebergs depends largely on the alertness of the ship’s watchkeepers.

In addition to visual surveillance, ships experimented using indirect methods of detecting icebergs but met with mixed success. For example, the crews of several IIP vessels found that some icebergs could be detected using echoes from the ship’s steam whistle. They concluded that the existence of an echo means an obstruction, but its absence proved nothing. Consequently, visual iceberg detection from ships remained the primary method of locating icebergs until the advent of shipboard radars during World War II [4].

Immediately following World War II, the IIP began using aircraft for iceberg reconnaissance since aircraft can cover a larger area in a fraction of the time compared to surface ships. The patrol aircraft were equipped with both visual observers and radars. However, the reliability of radar measurements was frequently inconclusive due to target identification challenges. For instance, icebergs and wooden ships commonly used for fishing presented similar radar echoes. Consequently, visual detection remained the primary method of locating icebergs until 1983 with the development of more sophisticated radars and signal processing techniques.

The third method to track icebergs is by using spaceborne remote sensors. Since the first weather satellite was put into orbit in 1960, the IIP has been eager to use space-based systems for iceberg reconnaissance. However, the sensors on the early satellites were visual and infrared, neither of which could reliably detect objects through clouds. Furthermore, the sensors were designed to monitor large scale weather systems and thus were incapable of detecting anything but the very largest icebergs. By the mid-1990s, microwave radars were placed into orbit, providing the ability to detect targets regardless of cloud cover and solar illumination. As discussed below, microwave radars have proven to be very effective instruments in detecting icebergs.

Using these three methods, the IIP has safeguarded shipping routes from icebergs between North America and Europe; however, the largest icebergs originate in the Southern Hemisphere. The threat of icebergs interfering with transportation routes in the Southern Ocean is increasing because large container ships are unable or unwilling to use routes such as the Panama Canal. Consequently, the United States Navy and the National Ocean and Atmospheric Administration (NOAA) created a joint venture named the Navy/NOAA Joint Ice Center in 1976 to carry out the role of the IIP (i.e., safeguard shipping lanes) in the Southern Hemisphere. This agency was renamed the National Ice Center (NIC) in 1995 when the United States Coast Guard became a partner. The goal of the National Ice Center produces global sea ice charts and various cryosphere data products.

The NIC plays a major role in tracking the location of Antarctic icebergs larger than 10 nautical miles across. Current NIC methods for tracking icebergs primarily involve using optical satellite imagery, augmented by radar images. Optical sensors produce high-resolution images but are unable to penetrate cloud cover and are dependent on solar illumination.

1.2.2 Science

In addition to the organization of the IIP and the NIC to regularly survey Earth's oceans to promote maritime safety, international cooperations have also been organized to study icebergs for scientific purposes. The International Polar Year (IPY) is perhaps the most famous example. Inspired by Austro-Hungarian naval officer Karl Weyprecht and proposed by Georg Neumayer, the International Polar Year is a joint international event organized around every 50 years where

multiple countries share costs and maximize coverage in coordinated scientific research of the polar regions.

Starting with 11 countries, including the United States, the first IPY occurred in 1882-1883 with 25 coordinated missions to the Arctic and Antarctic. More than 14 meteorological observatories were established around the world to study oceanographic and atmospheric phenomena. The initial studies of sea ice and glacial ice produced from this event were some of the first extensive studies of iceberg phenomenology and helped pave the way for future iceberg-related projects.

The second IPY took place from 1932-1933 with over forty participating countries who collaborated from over 40 remote meteorological observatories. Studies that contributed to the understanding of iceberg processes include developments in the fields of ocean currents, tides, and the structure and motion of ice. Research that contributed to developments in radar used to track icebergs include meteorology, atmospheric science, and the mapping of ionospheric phenomena.

Due to developments in the fields of rocketry and seismography, a third IPY was proposed in the 1950's. Because of the technology developments, the International Council of Scientific Unions broadened the research focus of the third IPY to include polar studies as well as geophysical research. (Consequently, the third IPY is also known as the International Geophysical Year.) The third IPY took place from 1957-1958 with the cooperation of more than 70 national scientific organizations. During this event, special emphasis was placed on studying oceanography and glaciology. To accomplish these goals, several Russian expeditions surveyed the Southern Ocean and cataloged iceberg sizes and maximum distances between observed icebergs and the Antarctic glacial continent. This database remained one of the primary means of comparing iceberg motion trends until the advent of spaceborne microwave remote sensing, discussed below.

The fourth IPY took place from 2007-2009 with more than 225 participants from both scientific communities and educational outreach programs from over 60 countries. Research during the fourth IPY focused on multiple atmospheric, oceanographic, and cryospheric studies. Resources were compiled using on-site resources, remote meteorological stations, and satellite remote sensors of which some of the work in this dissertation is a part (see Chapter 4). A list of completed and ongoing research emphases and contributions can be found at [5].

1.2.3 Radar

As previously mentioned, the IIP and NIC use radar as the primary instrument to track icebergs. Radars are devices that transmit electromagnetic energy in the form of radio waves or microwaves which potentially reflect off objects in their path. The reflected wave returns a fraction of the initial transmitted energy to a receiver. Two general types of satellite radar have been used to detect the presence of large distributed targets (e.g., icebergs): scatterometers and synthetic aperture radars (SAR). Scatterometers are imaging radars that detect the power in reflected radar waves. Using various processing techniques, multiple scatterometer power measurements are combined to produce radar images.

In addition to measuring the power, a SAR also detects the phase of the radar echo. Using the phase in conjunction with signal processing techniques enables formation of radar images that have a higher spatial resolution than scatterometers. Compared to optical sensors, some of the advantages of using radar to detect icebergs are that radars operate independent of solar illumination and can penetrate cloud cover.

To track icebergs, radars were first incorporated onto ground-based platforms such as coastlines and surface ships. To expand operational coverage, scatterometers and SARs were placed onboard aerial platforms and eventually on orbital satellites. This study emphasizes the latter and briefly highlights significant scatterometers, SARs, and signal processing developments used for tracking icebergs.

Launched in 1978, the Seasat-A scatterometer (SASS) was the first spaceborne scatterometer. Using a fixed antenna that operated at Ku-band (14 GHz), SASS recorded radar echoes from multiple incidence angles that were used for detecting near-surface wind speeds over the ocean. Due to the spatial size of radar measurements on the Earth's surface, only very large (≥ 50 km) icebergs could be detected. While SASS lasted only about 100 days due to a power supply failure, its mission demonstrated the utility of using scatterometers for polar ice studies.

After SASS, the European Space Agency (ESA) launched the Advanced Microwave Instrument (AMI) scatterometer onboard the ERS-1 spacecraft in 1991, followed by the ERS-2 AMI scatterometer in 1995. Both AMI instruments operated at C-band (5 GHz). The resolution of AMI limited the detection of icebergs to those larger than 50 km.

In 1996, NASA launched the NASA Scatterometer (NSCAT). NSCAT was an advanced version of SASS, designed to increase ground coverage by using multiple fixed antennas that operated at Ku-band. Using this configuration, NSCAT was able to detect icebergs larger than 25 km. Due to solar panel failure, the NSCAT mission lasted only 10 months.

As a result of the premature end of the NSCAT mission, the SeaWinds scatterometer onboard the QuikSCAT spacecraft was launched in 1999 as a “quick recovery” mission to fill the gap in Ku-band scatterometry surveillance. SeaWinds was the first scatterometer to implement a rotating antenna, allowing for greater coverage of Earth’s surface during each orbital pass. With its orbit and wide swath, SeaWinds covered more than 90% of Earth’s surface every 24 hours. For over a decade, icebergs larger than 25 km were detected using SeaWinds measurements.

The first SAR instrument, Radarsat-1, was placed into orbit by the Canadian Space Agency in 1995. Radarsat-1 was the first SAR to be used to regularly track icebergs. Using onboard signal processing techniques, measurements from Radarsat-1 were combined to produce images with variable spatial resolutions. For iceberg tracking, images with 100 m resolution were used, thus Radarsat-1 could detect iceberg fragments larger than 100 m. With the increased spatial resolution of SARs over scatterometers, Radarsat became the primary source of surveillance data utilized by the IIP and NIC for detecting icebergs.

While Radarsat was noted for its increased spatial resolution over scatterometers, one trade-off was that it required more power due to demanding hardware and increased onboard computation. As a result, Radarsat was only active up to 10% of each orbit period and recharged the remainder of each orbit cycle. Another key limitation of Radarsat was its temporal resolution. Due to orbit geometry and power requirements, Radarsat completely surveyed the Earth’s surface every 24 days. There were always multiple requests for Radarsat resources, thus Radarsat was frequently tasked to non-polar studies and was not always available to track icebergs.

The ESA launched the Environmental Satellite (ENVISAT) in 2002. Advances in SAR technology were incorporated into ENVISAT which was capable of detecting changes in surface heights with sub-millimeter precision. ENVISAT also operated at C-band and onboard settings were regularly set to detect icebergs larger than 150 m in the polar oceans.

A follow-on to Radarsat-1, the Canadian Space Agency launched Radarsat-2 in 2007. The spatial resolution of Radarsat-2 images were comparable to its predecessors and were used to detect

icebergs larger than 100 m. However, unlike Radarsat-1, antenna location and orbit geometry of Radarsat-2 emphasized more extensive coverage of icebergs around Antarctica. Consequently, Radarsat-2 is one of the preferred instruments utilized by the NIC to track icebergs in the Southern Ocean.

Further developments in signal processing techniques enabled scatterometers to again be used as a primary source for tracking icebergs. In 1999, the scatterometer image reconstruction (SIR) algorithm was developed to create enhanced-resolution scatterometer images, similar to SAR radar images. Applied in post-processing, the SIR algorithm combines individual power measurements using knowledge of the radar and orbital parameters into a composite radar image. SIR images have a spatial resolution finer than the resolution of the individual measurements and can be used to detect phenomena that are difficult to detect using only raw scatterometer measurements.

Recent studies have used SIR images to evaluate the NIC's iceberg database. For example, scatterometer measurements from SASS, NSCAT, and SeaWinds were processed using the SIR algorithm, resulting in high-resolution radar images [6]. These SIR images have been used to catalog the positions of icebergs larger than 15-20 km, 10 km, and 5 km, respectively, into an Antarctic iceberg database as part of the Scatterometer Record Pathfinder (SCP) Project by Brigham Young University's Microwave Earth Remote Sensing (MERS) Laboratory [7, 8]. This database is used throughout this dissertation and is referred to as the MERS Antarctic iceberg database. Iceberg parameters (e.g., position, count, etc.) from the MERS Antarctic iceberg database have been compared with iceberg parameters reported by the NIC over the past 35 years [8, 9].

1.3 Approach

In this dissertation, I present research on how to exploit microwave scatterometry to track icebergs. Research focuses on five key areas: 1) detecting icebergs, 2) tracking icebergs, 3) estimating iceberg size, 4) estimating iceberg motion, and 5) estimating ocean currents that drive iceberg motion.

This dissertation emphasizes the use of scatterometer data, specifically the SeaWinds scatterometer onboard the QuikSCAT spacecraft due to the availability of radar measurements from 1999-2009. During this period, tabular icebergs larger than 5-6 km were detected using SeaWinds SIR images. Tabular icebergs are characterized as a rough ice plateau above the surrounding sea

water or sea ice. Because icebergs of this size primarily originate from Antarctica, this study emphasizes large ($\geq 5\text{-}6$ km) tabular icebergs in the Southern Ocean. A more detailed overview of the SeaWinds scatterometer is included in Chapter 2

1.4 Research Contributions

Valuable contributions are made by this research in understanding iceberg processes. This section briefly highlights research contributions of the studies included in this dissertation. Contributions are both theoretical as well as operational. Multiple publications are associated with these contributions which include two peer-reviewed journal publications [8, 10], one journal article currently in review [11], one journal article submitted for review [12], one magazine article [13], and multiple conference papers [14–16].

The first contribution is formalizing the methodology for detecting icebergs in microwave scatterometer images [8]. Using this methodology, iceberg positions are detected on a daily basis and a time-series of iceberg positions is maintained in the MERS Antarctic iceberg database [7, 15]. With this tool, I extend the iceberg tracking abilities to operate in real-time and provide real-time support for the 2008 and 2009 Antarctic cruises funded by the United States National Science Foundation as part of research conducted during the fourth International Polar Year [8]. Using the MERS Antarctic iceberg database, iceberg tracks are compiled to identify characteristic iceberg motion trends and dominant movement profiles to aid in collision avoidance and to assist in on-site research endeavors [8, 12, 13].

Using signal processing techniques, I develop and compare multiple algorithms to estimate iceberg size using SeaWinds radar measurements. Benefits and trade-offs of each algorithm are reviewed. Estimates of iceberg size may now be included with iceberg position reports in the MERS Antarctic iceberg database [10, 16].

Using iceberg size estimates and external forcing fields, I develop an iceberg motion model to predict iceberg motion. As part of the model, I analytically calculate the non-homogeneous drag profiles along the iceberg's exterior. To take advantage of iceberg observations, data assimilation techniques are used to incorporate observed iceberg parameters into the motion model, improving model performance [11].

Last, the iceberg motion model is inverted and augmented with observed iceberg motion to produce estimates of ocean current velocities driving iceberg motion. Multiple empirically-derived ocean current velocities are combined using reconstruction techniques, resulting in empirically-derived climatological averages of ocean current profiles in the Southern Ocean. These iceberg-based current profiles are compared with conventional numerical-generated ocean currents produced as part of the Ocean Circulation and Climate Advanced Modeling (OCCAM) Project [12].

1.5 Outline

The dissertation is organized by research topic in the following manner: Chapter 2 briefly reviews the SeaWinds scatterometer and the scatterometer image reconstruction algorithm. Chapter 3 investigates radar backscatter from icebergs and formalizes the theory required for using SeaWinds to detect icebergs. Chapter 4 analyzes characteristic iceberg motion trends and dominant movement profiles. Chapter 5 develops multiple algorithms to estimate iceberg size and spatial orientation using scatterometer measurements. Chapter 6 develops a motion model to describe the movement of large tabular icebergs. Chapter 7 derives climatological ocean currents in the Southern Ocean. Finally, Chapter 8 summarizes results and contributions presented in this dissertation and proposes topics of future research.

Chapter 2

Background

2.1 Introduction

To provide a framework for the iceberg detection process, the SeaWinds radar and corresponding measurements are briefly introduced. Radar measurements from SeaWinds are collected and processed using resolution enhancement techniques to produce daily radar images with a sufficient resolution to track tabular icebergs larger than 5 km.

2.2 SeaWinds

QuikSCAT was launched in 1999 to observe oceanic winds. Its orbit and wide swath enable near-complete coverage of the Earth's surface every 24 hours. Daily coverage of the polar regions make it an ideal platform for high-latitude studies.

The primary instrument onboard QuikSCAT is the SeaWinds radar, a Ku-band scanning pencil-beam scatterometer. Scatterometers operate by transmitting a pulse of microwave energy towards the Earth's surface and measuring the reflected energy. In order to account for noise in each radar measurement, a separate measurement of the noise-only power is made and subtracted from the signal-and-noise measurement to determine the signal power. Given the signal-only power, the radar equation is used to calculate the normalized radar cross-section, σ° , of the surface [17].

To collect backscatter measurements, the SeaWinds antenna rotates at 18 rpm and has two scanning conical beams, as illustrated in Fig. 2.0. The inner beam is horizontally polarized (h-pol) at a nominal incidence of 46° , and the outer beam is vertically polarized (v-pol) at a nominal incidence angle of 54° [18]. This design provides for four independent looks of the region lying within the inner swath and two independent looks of targets contained within the outer swath [19,20].

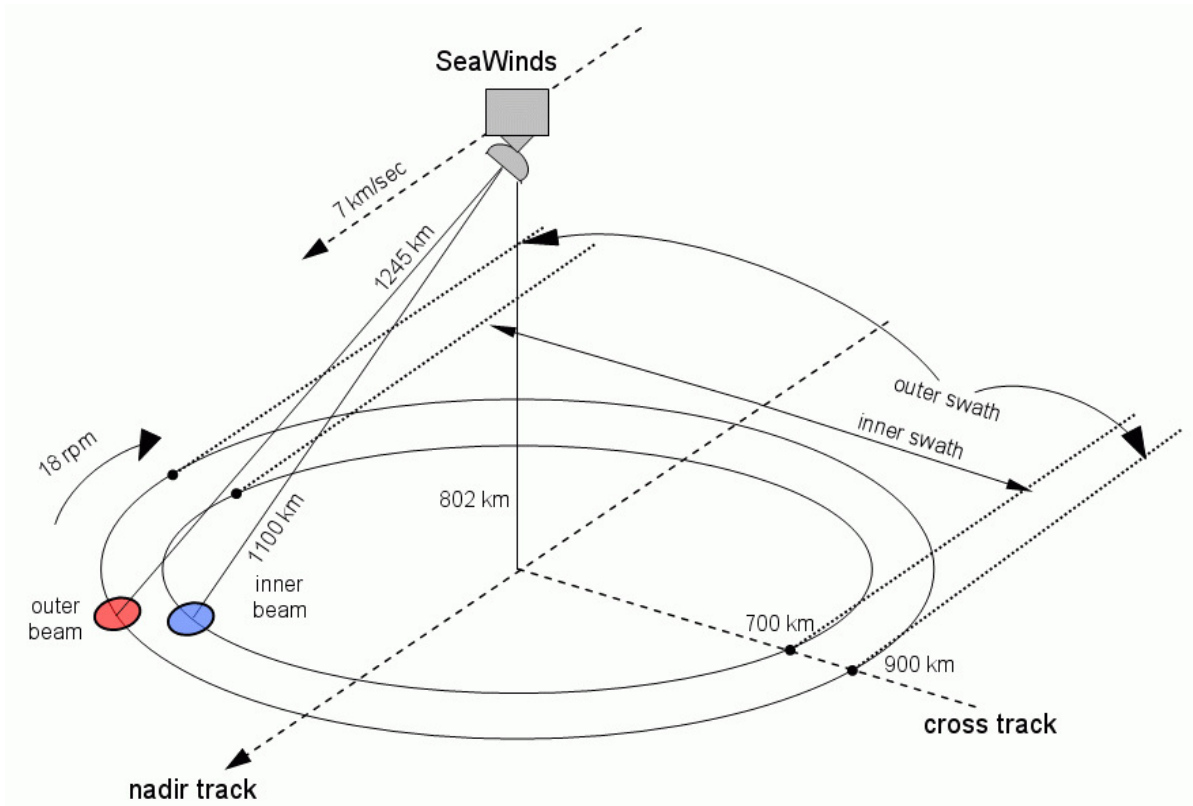


Figure 2.1: An illustration of the SeaWinds observation geometry. SeaWinds has two scanning conical beams. The inner beam is horizontally polarized (h-pol) at a nominal incidence of 46° , and the outer beam is vertically polarized (v-pol) at a nominal incidence angle of 54° . This design provides for four different azimuth looks of the region lying within the inner swath and two azimuth looks of targets contained within the outer swath.

Each backscatter measurement represents the microwave return corresponding to an oval patch on the Earth’s surface. Because of this shape, the backscatter values corresponding to these measurements are called “egg” backscatter values. SeaWinds uses onboard range-Doppler processing to separate each egg measurement into 12 subregions termed “slices” where each has a separate backscatter measurement [20, 21]. However, due to high error and noise levels in the outer-most slice measurements, usually only the inner 8 slice measurements are used in processing [19, 20]. Because of the rapid roll-off of the aperture response function corresponding to each slice, individual response patterns are frequently represented as a binary mask corresponding to the 6 dB contour of each slice footprint, measuring approximately 6 x 25 km [22]. Diagrams corresponding to the 6 dB contour of a single egg and associated 8 slice antenna patterns are displayed in Fig. 2.1.

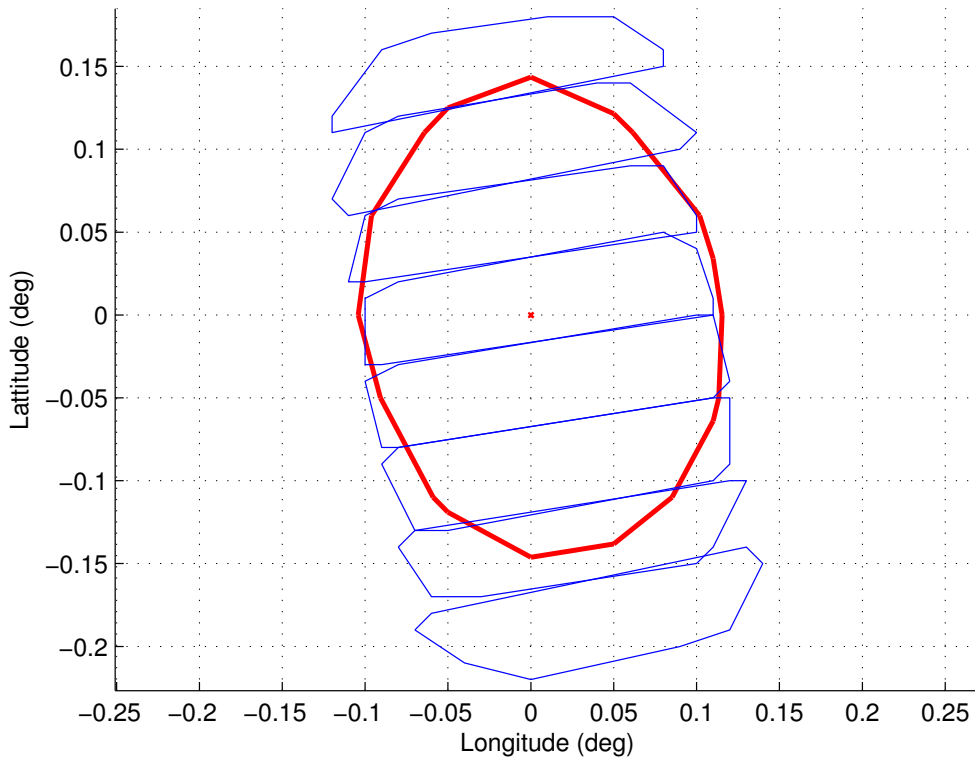


Figure 2.2: An illustration of the 6 dB “egg” and “slice” antenna footprint on the Earth for a single SeaWinds backscatter egg measurement and associated slice measurements. The dark (red) oval corresponds to the egg measurement and measures approximately 35 x 25 km. The light (blue) contours represent slice measurement contours and measure approximately 25 x 6 km.

Slice backscatter measurements can be modeled as a combination of the true signal power σ_i° and multiplicative noise, specifically

$$\sigma^\circ = \sigma_i^\circ (1 + K_p v) \quad (2.1)$$

where σ_i° is the true backscatter, K_p is a dimensionless coefficient embodying the geophysical and instrumentation noise, and v is a Gaussian random variable with zero mean and unit variance [21]. Because each range-Doppler-filtered slice has a large spatial footprint compared to the operating wavelength, each σ_i° may be modeled as a linear combination of spatial backscatter distributions,

$$\sigma_i^\circ = \frac{\int A(\tau) \sigma_{pt}^\circ(\tau) d\tau}{\int A(\tau) d\tau} \quad (2.2)$$

where $A(\tau)$ is the antenna gain of the two-dimensional ground illumination footprint and $\sigma_{pt}^\circ(\tau)$ is the spatial distribution of σ_i° at the Earth's surface. The integrals are over the antenna footprint with respect to the two-dimensional spatial index τ [18]. Note that in many applications, as well as in this dissertation, $A(\tau)$ is simplified and represented as a binary mask that corresponds to the 6 dB antenna footprint [22, 23].

Equation 2.1 can be written as

$$\sigma^\circ = \sigma_i^\circ + v' \quad (2.3)$$

where $v' \sim N(0, K_p^2 \sigma_i^{\circ 2})$. For SeaWinds $K_p = \sqrt{\alpha + \beta/\sigma_i^\circ + \gamma/\sigma_i^{\circ 2}}$ where α , β , and γ are related to the signal-to-noise ratio and the parameters of the radar equation. These values are computed for each spatial response function [21]. The corresponding Gaussian probability distribution function of a single σ° measurement can explicitly be modeled as

$$P(\sigma^\circ | \sigma_i^\circ) = \frac{1}{\sqrt{2\pi}\xi} \exp \left\{ -\frac{(\sigma^\circ - \sigma_i^\circ)^2}{2\xi^2} \right\} \quad (2.4)$$

where

$$\xi^2 = \alpha \sigma_i^{\circ 2} + \beta \sigma_i^\circ + \gamma. \quad (2.5)$$

2.3 Resolution Enhancement

While individual σ° measurements are useful in point-target analysis, it is desirable to generate backscatter images for macro-scale studies. A simple way to perform this task is a drop-in-the-bucket approach where measurements are binned by spatial location. This technique is termed “gridding” and produces gridded (GRD) images. Measurements from multiple passes are combined in image formation to provide sufficient coverage. The effective resolution of the resulting image is similar to the largest dimension of the spatial footprint (25 km), resulting in a coarse-resolution image [20]. Alternately, σ° measurements can be combined on a higher-resolution grid where values from each radar pulse are binned by spatial location and averaged by a weighting function where the weighting corresponds to the scatterometer spatial response function. This image technique is termed “AVE” [24]. While GRD and AVE images are effective in some large-scale

studies, the dense sampling of SeaWinds measurements in the polar regions facilitates use of image reconstruction techniques to produce higher-resolution images [20].

The scatterometer image reconstruction (SIR) algorithm combines multiple backscatter measurements into a composite image with higher-spatial resolution than the associated aperture response via reconstruction techniques [19]. SIR is an iterative multiplicative algebraic reconstruction technique that combines overlapping measurements to produce a resolution-enhanced backscatter image. The SIR algorithm depends on dense, overlapping measurements which are assured by using radar measurements from multiple satellite passes. This results in a trade-off between spatial and temporal resolution. Daily SIR images produced from the egg dataset have a resolution of 8-10 km and are reported on a 4.45 km grid. Images reconstructed from slice measurements have a higher effective resolution of 4-5 km and are reported on a 2.225 km grid [19]. Separate h-pol and v-pol images are created for each input type. For each case, the optimal number of iterations that minimizes the root-mean-squared error in simulation has been determined and is used to produce the SIR images. The GRD, AVE, and SIR images are produced as standard SeaWinds image data products [7].

An example of a resolution-enhanced backscatter image of Antarctica and the Southern Ocean is shown in Fig. 2.2. Antarctica is in the center and appears the brightest at microwave frequencies. Antarctica is surrounded by sea ice with a medium backscatter value, and the outermost dark region corresponds to sea water. Due to the orbit geometry of QuikSCAT, no measurements are recorded over the South Pole which is represented by a dark circle in the middle of Antarctica.

A second example of the Weddell Sea is shown in Fig. 2.3. Similarly, the brightest radar returns correspond to the Antarctic glacial continent, medium returns correspond to sea ice, and the darkest regions correspond to sea water. The characteristic backscatter profiles of sea water, sea ice, and glacial ice are further explored in Chapter 3. Geographic regions in Figs. 2.2 and 2.3 are labeled in Appendix A.

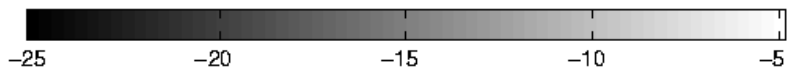
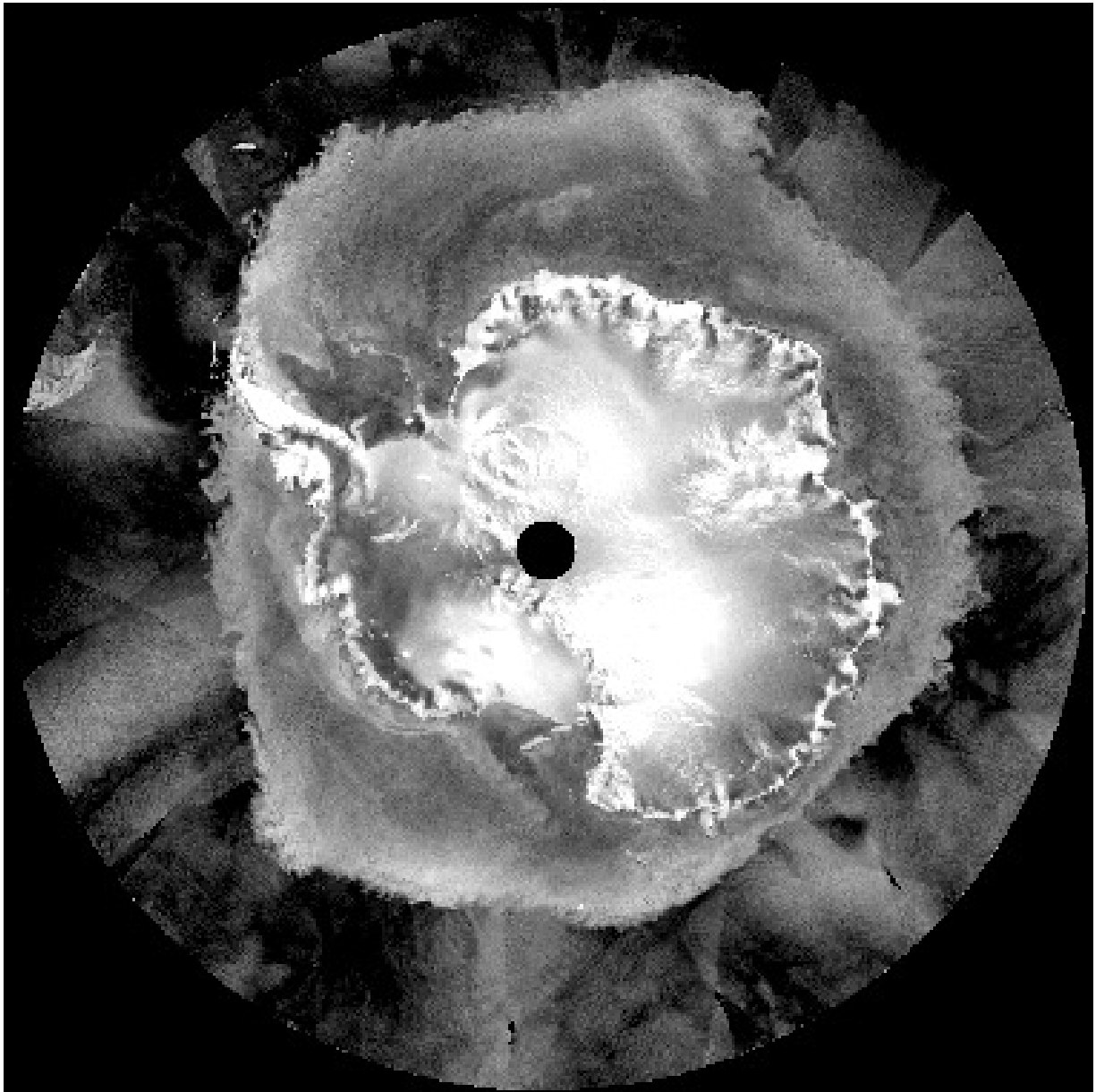


Figure 2.3: Standard SeaWinds h-pol backscatter image of Antarctica and the Southern Ocean for Julian day 300 of year 2000. The image is centered on the Antarctic glacial continent that has a bright backscatter return, surrounded by sea ice with a medium backscatter profile. The outermost region corresponds to sea water that has a low backscatter profile. Backscatter is in dB.

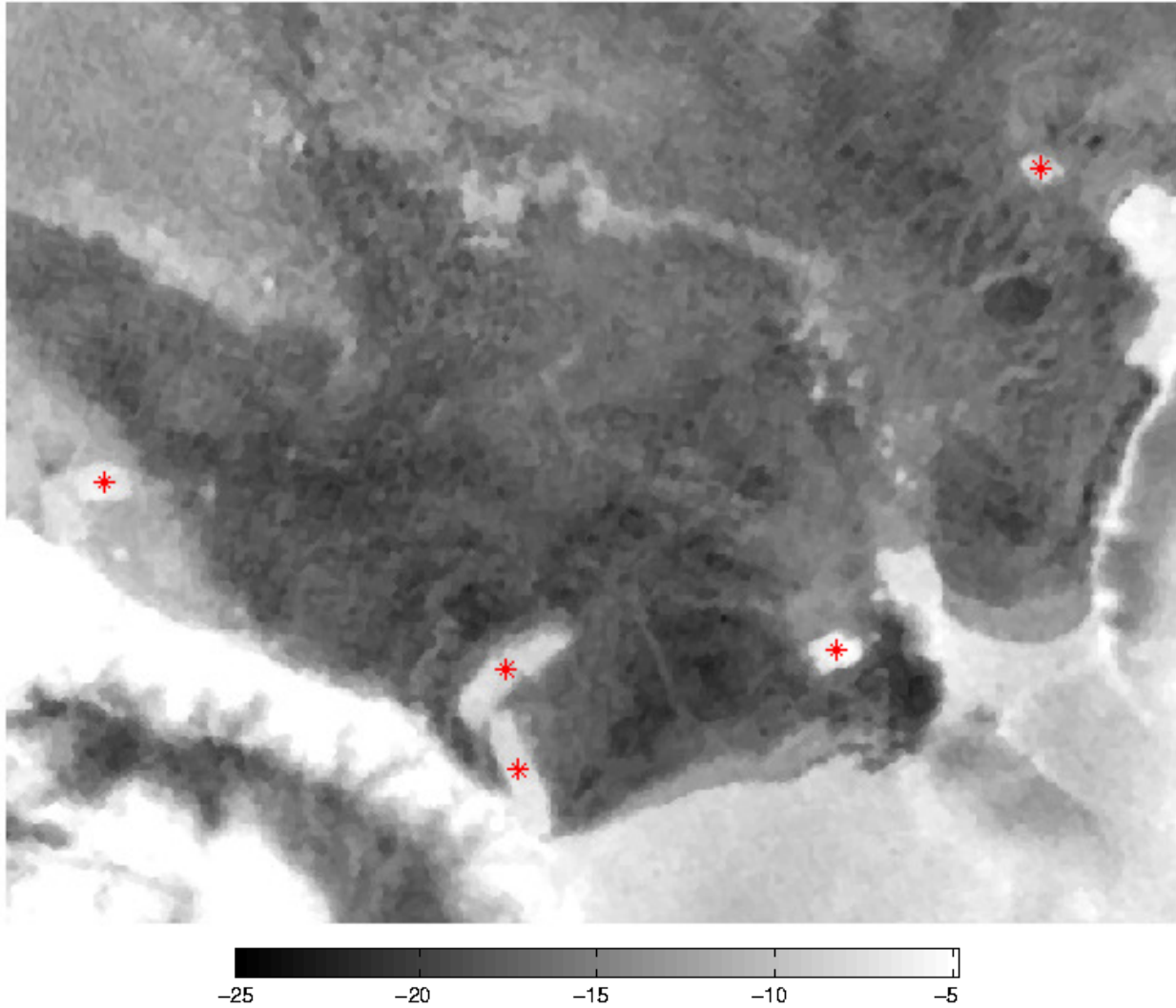


Figure 2.4: Standard SeaWinds h-pol backscatter image of the Weddell Sea for Julian day 300 of year 2000. Bright backscatter regions at bottom and at right correspond to the Antarctic glacial continent. Bright targets that appear separate from the glacial continent correspond to large tabular icebergs. The approximate centroid of some icebergs have been labeled with a “*”. Backscatter is in dB.

Chapter 3

Detecting Icebergs

3.1 Introduction

This chapter documents the detection methodology for large tabular icebergs using the SeaWinds scatterometer. The icebergs of interest are generally larger than 5 km and can be characterized as a rough ice plateau above the surrounding sea water or sea ice. Because SeaWinds operates at microwave frequencies, its radar measurements penetrate cloud cover and are independent of external illumination. QuikSCAT's sun-synchronous orbit allows SeaWinds to completely observe the polar regions daily. Backscatter measurements over a 24-hour period are collected and image reconstruction techniques are used to produce daily backscatter images that are used in the iceberg detection process. In these images icebergs are detected as high-backscatter targets surrounded by lower-backscatter sea water or sea ice.

Originally applied in post-processing, the iceberg detection methodology is also used in near-real-time (NRT). In this chapter, the methodology is described, unique concerns associated with detecting icebergs in NRT are highlighted, and respective solutions and trade-offs are outlined. The utility of the iceberg detection methodology in delayed post-processing as well as in NRT is explored in Chapter 4.

3.2 SeaWinds Backscatter Images

The standard SeaWinds images used for the iceberg detection process are 24-hour slice-based h-pol SIR backscatter images. The temporal resolution of the images is set at 24 hours to minimize noise in the reconstruction process yet provide for a short enough time segment to account for daily iceberg movement. In using 24-hour images, I assume there is generally negligible intra-day iceberg movement. SIR images are used to maximize the reconstructed spatial resolution, slice-based images are used because of their higher inherent spatial resolution, and h-pol backscat-

ter images are used to maximize the backscatter contrast between common Antarctic scatterers, see Sec. 3.3. The differences between using h-pol and v-pol images are explored in Sec. 3.4.

Examples of standard SeaWinds h-pol backscatter images are displayed in Fig. 3.0, centered on South Georgia Island on Julian day (JD) 4, 2009. Egg-based and slice-based GRD, AVE, and SIR images are displayed for comparison in Fig. 3.0. In the center of each image is the high-backscatter signature of South Georgia Island, surrounded by low-backscatter sea water. Notice the greater spatial resolution inherent in the images derived from slice measurements. Also note the sharper contrast in backscatter around the perimeter of the island in the SIR images compared to AVE. For a more comprehensive outline and detailed explanation of the standard SeaWinds products see [7]. Trade-offs between using each image type in the iceberg detection process are discussed in Sec. 3.5.1.

3.3 Scattering Theory

To interpret backscatter images, a brief explanation and comparison of the scattering properties of common Antarctic scatterers (sea water, sea ice, and glacial ice) is provided. Backscatter measurements collected by SeaWinds are the result of a combination of surface scatter and volume scatter. Surface scatter is the portion of energy reflected at the air-surface boundary. Volume scatter is the portion of energy transmitted into the snow and ice that reflect off internal particles. Both scattering components depend on the physical geometry and the dielectric of the material where the physical geometry characterizes both surface and internal parameters of the structure [25]. The dielectric constant of sea ice and glacial ice is approximately unity except when moisture is present [26].

Because sea water is a good conductor, all incident energy is reflected at the air-surface boundary, resulting in a dominant surface scattering component. The directivity of the reflected wave at the surface is governed by antenna geometry and sea surface roughness [25]. Because SeaWinds transmits at an oblique angle with respect to the ocean's surface, the reflected pulse is generally directed away from the scatterometer, resulting in low σ° measurements. The dominant surface feature affecting backscatter from sea water is the presence of wind-generated waves [27, 28]. Near-surface winds induce capillary waves on the ocean's surface which roughen the ocean's surface, resulting in higher backscatter. The backscatter intensity is a function of wind speed, wind

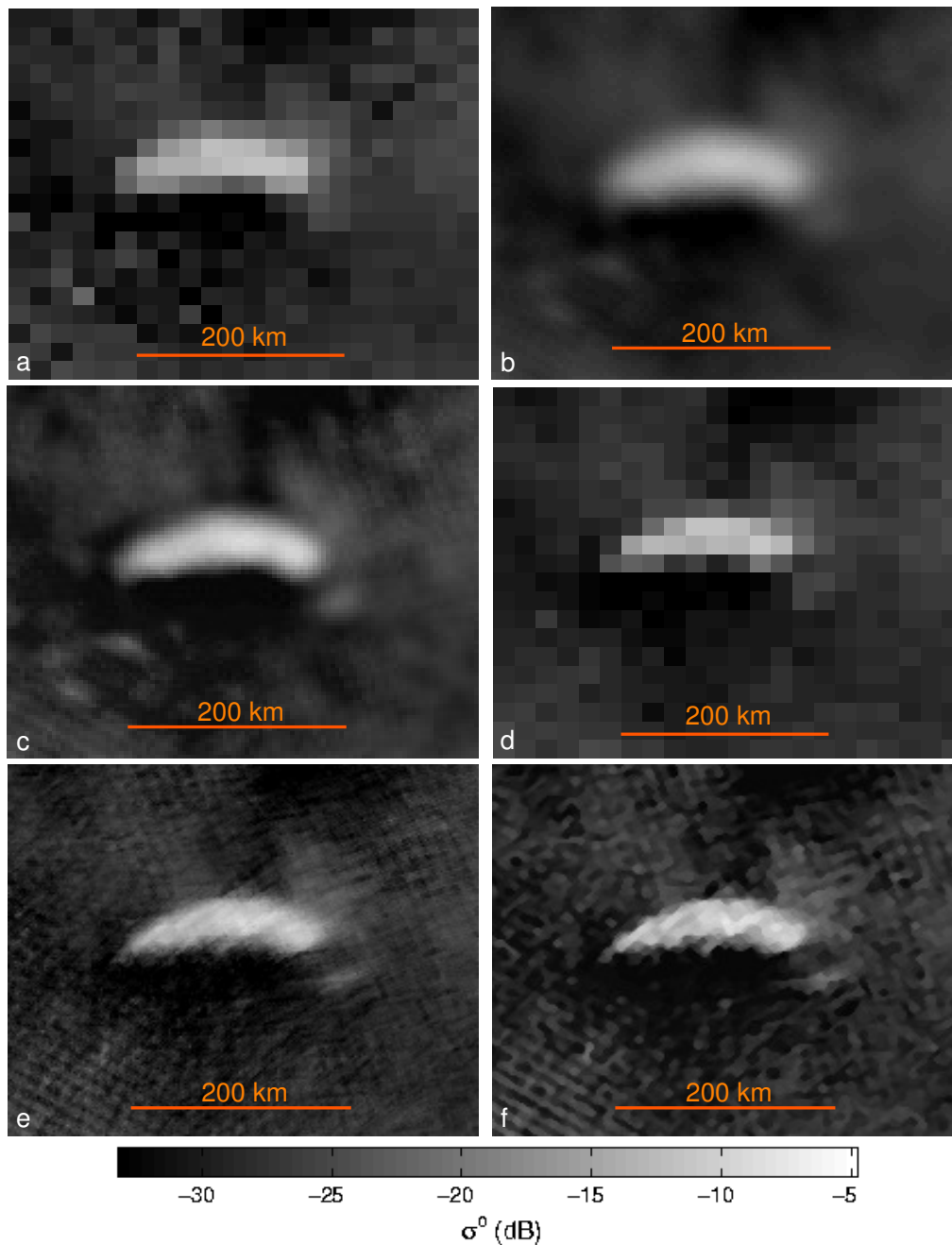


Figure 3.1: Standard SeaWinds h-pol backscatter images of South Georgia Island for Julian day 4, 2009. Images differ by input data type (egg or slice) and processing method (GRD, AVE, or SIR). a) Egg-based GRD image. b) Egg-based AVE image. c) Egg-based SIR image. d) Slice-based GRD image. e) Slice-based AVE image. f) Slice-based SIR image. Pixel sizes correspond to 22.25 km, 4.45 km, and 2.225 km in the GRD, AVE, and SIR images, respectively. In the center of each image is the high-backscatter South Georgia Island, surrounded by low-backscatter sea water. Speckle in the low-backscatter regions is due to the temporal change and direction dependence in the wind-induced backscatter of the ocean, amplified by the reconstruction process.

direction, and radar polarization. Sea water σ° varies from -32 dB to -15 dB in daily SeaWinds images (see Sec. 3.4), depending on wind speed, with higher winds resulting in higher σ° [27–29].

Backscatter from sea ice is dependent on surface and volume scattering and the sea ice concentration. Surface roughness is the dominant factor influencing surface scatter and is dependent on sea ice history. Sea ice history also defines the amount of volume scatter, e.g., multi-year sea ice is thicker and more compact, resulting in more internal particles reflecting incident radar energy and thus has a higher associated σ° than thinner first-year sea ice [30, 31]. Sea ice concentration is the percentage of the surface covered in sea ice, with higher sea ice concentrations resulting in generally higher σ° . Sea ice has rough surface features and generally scatters more energy back to the radar than open water [32]. Sea-ice backscatter varies from -32 dB to -5 dB in daily SeaWinds images and is dependent on ice characteristics and water content [33].

Glacial ice is made of accumulated layers of snow which have a large particle size, dense crystalline structure, and a large penetration depth at microwave frequencies. The internal particles act as multiple reflectors, resulting in a dominant volume scattering component. Thus glacial ice tends to have a bright microwave return compared to both sea water and sea ice [32]. Glacial ice exhibits a σ° of -25 dB to -2 dB in SeaWinds images.

It is important to note that the backscatter signatures from ice are dependent on weather. Liquid water due to melting drastically affects the dielectric constant of snow and ice, resulting in reduced σ° during melting [33–35]. During the austral ablation, surface snow and ice on large tabular icebergs often melt, creating pools of freshwater. These pools are often extensive and are sometimes better characterized as lakes [33, 35, 36]. At microwave frequencies, these lakes lower the overall backscatter of the glacial ice, camouflaging it as open ocean. While generally undesirable, extreme melting conditions occasionally allow for a method of secondary iceberg detection. For example, if such an iceberg is surrounded by (i.e., encapsulated in) sea ice, there is frequently enough contrast between the low-backscatter surface water on the top of the iceberg and the medium-backscatter sea ice to identify the iceberg location. However, icebergs in open sea water that have significant surface water can be difficult to detect.

A sample backscatter image illustrating the σ° returns from sea water, sea ice, and glacial ice is provided in Fig. 3.1. Land is characterized by high backscatter because of glacial ice covering the surface, sea ice has medium-backscatter values, and the lowest-backscatter regions correspond

to sea water. The high-backscatter spots away from the continent correspond to icebergs and islands. Islands, being stationary at known locations, are readily distinguishable from icebergs. However, icebergs grounded on the ocean floor may appear as islands; this case is further explored in Sec. 3.5.1.

A more detailed discussion of the surface and volume scattering from sea water, sea ice, and glacial ice at microwave frequencies is included in Appendix B.

3.4 Antarctic Backscatter Profiles

To characterize the radar backscatter from common Antarctic scatterers, Ku-band backscatter measurements of sea water, sea ice, and glacial ice below 55°S have been compiled from 1999-2009. To emphasize annual trends, backscatter values of all pixels of a given type are averaged by Julian day and compiled into histograms of daily backscatter values. In order to represent the overall backscatter probability distribution functions (PDFs), the histograms are normalized such that the area under the curve is equal to unity. Figure 3.2 illustrates the normalized average h-pol backscatter corresponding to sea water, sea ice, and glacial ice for Julian day 1, years 1999-2009. This is near the peak of the melting season. Notice how the peaks of each medium are separately defined. Accurate classification of sea water, sea ice, and glacial ice depends on sufficient contrast (i.e., separation between peaks in Fig. 3.2) between these PDFs.

As the daily backscatter PDFs in Fig. 3.2 are compiled for the entire Julian calendar, seasonal backscatter trends are observable. The h-pol and v-pol backscatter time-series for sea water, sea ice, and glacial ice for Julian days 1-365 are illustrated in Fig. 3.3. The statistical expectation of the PDFs in Fig. 3.3 are displayed in Fig. 3.4, with the geometric mean and variance of the expected values presented in Table 3.0. Standard daily slice-based SIR images are used in this analysis.

Seasonal trends in the backscatter PDFs are caused by variations in the electromagnetic and physical roughness of each medium [25, 26]. Note that sea water backscatter is generally higher during the austral winter, peaking around Julian day 225. This trend is due to increased winds during the austral winter. We note that the average σ° value of sea water is 0.6 dB higher at v-pol compared to h-pol.

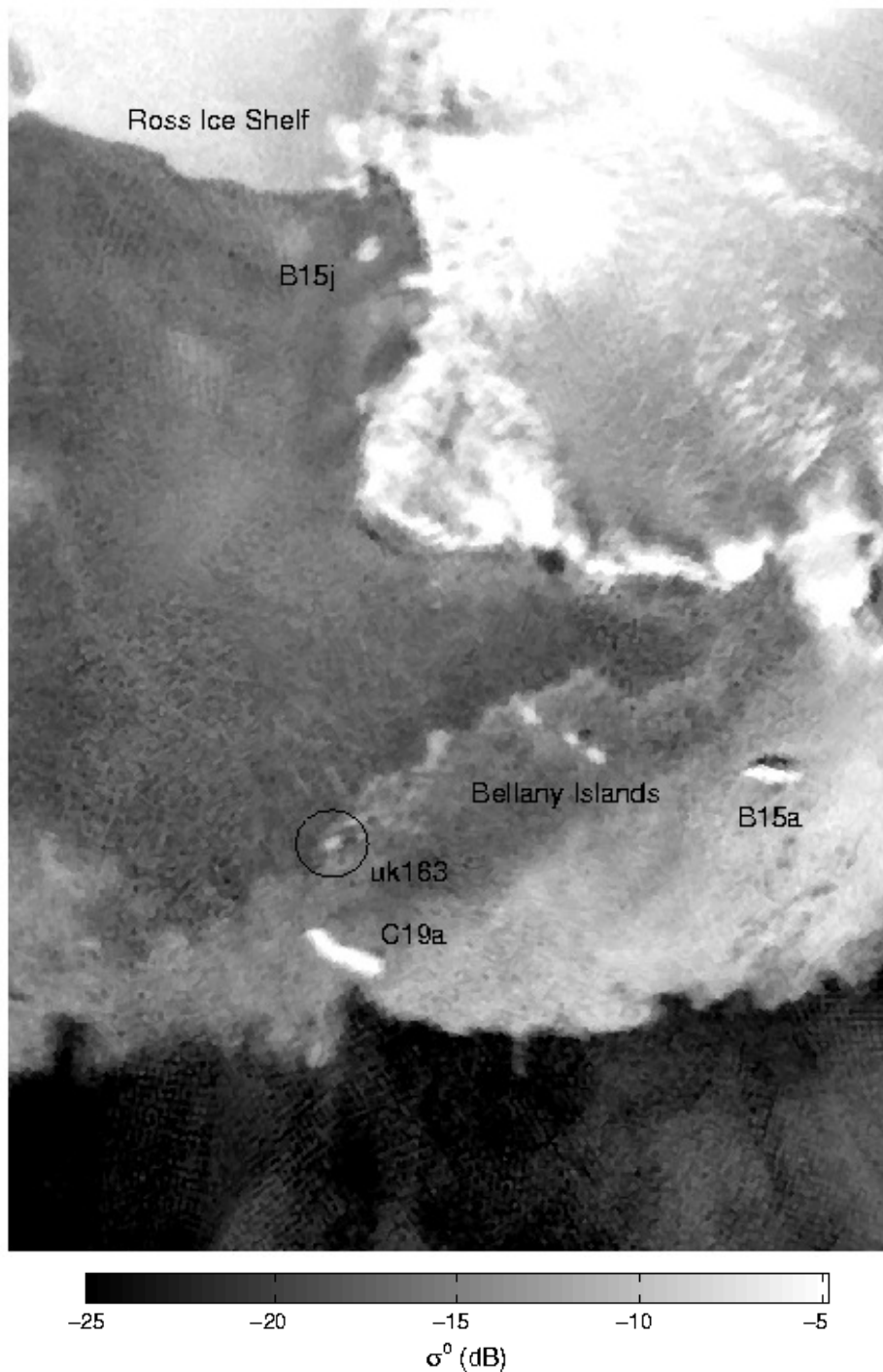


Figure 3.2: H-pol backscatter image of the Ross Sea on 2007 Julian day 200. The highest-backscatter region corresponds to the Antarctic glacial continent which is surrounded by medium-backscatter sea ice. The lowest-backscatter regions correspond to sea water. The high-backscatter spots away from the glacial continent correspond to icebergs and islands.

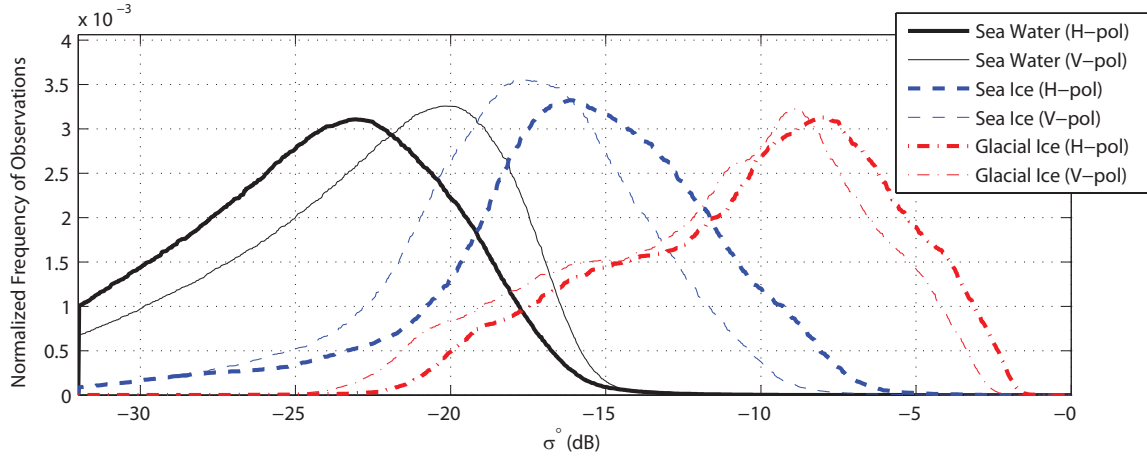


Figure 3.3: Normalized backscatter histograms of sea water, sea ice, and glacial ice below 55°S on Julian day 1 from 1999-2009. Backscatter values from Julian day 1 of each year are averaged and subsequent values are normalized in order to estimate the backscatter probability distribution. Measurements are derived from standard daily slice-based SIR images.

Table 3.1: Geometric mean and variance of the expected backscatter return from sea water, sea ice, and glacial ice below 55° as measured by the SeaWinds scatterometer from 1999-2009.

Medium	Polarization	Mean (dB)	Variance (dB)
Sea Water	H	-22.42	0.66
	V	-21.12	0.56
Sea Ice	H	-14.58	1.86
	V	-16.53	2.08
Glacial Ice	H	-9.71	0.04
	V	-10.93	0.05

Backscatter from sea ice is highest around Julian day 50, at the end of the austral summer. This is related to differences in overall sea ice area in the Southern Ocean, see Fig. 3.5. Most of the 19 million km² of sea ice around Antarctica during the austral winter is first-year sea ice, while the majority of the 3 million km² of sea ice that survives the austral ablation is multi-year sea ice. The relatively-high backscatter detected during the austral summer, Julian day 1-100, corresponds to multi-year sea ice. The low-backscatter profile of the period from Julian day 100-150 is from both multi-year sea ice and newly-grown first-year sea ice that has a lower σ° . Backscatter from Julian day 150-300 thus predominantly characterizes the 19 million km² of first-year sea ice. The period Julian day 300-350 characterizes the onset of the austral ablation and corresponds to first-

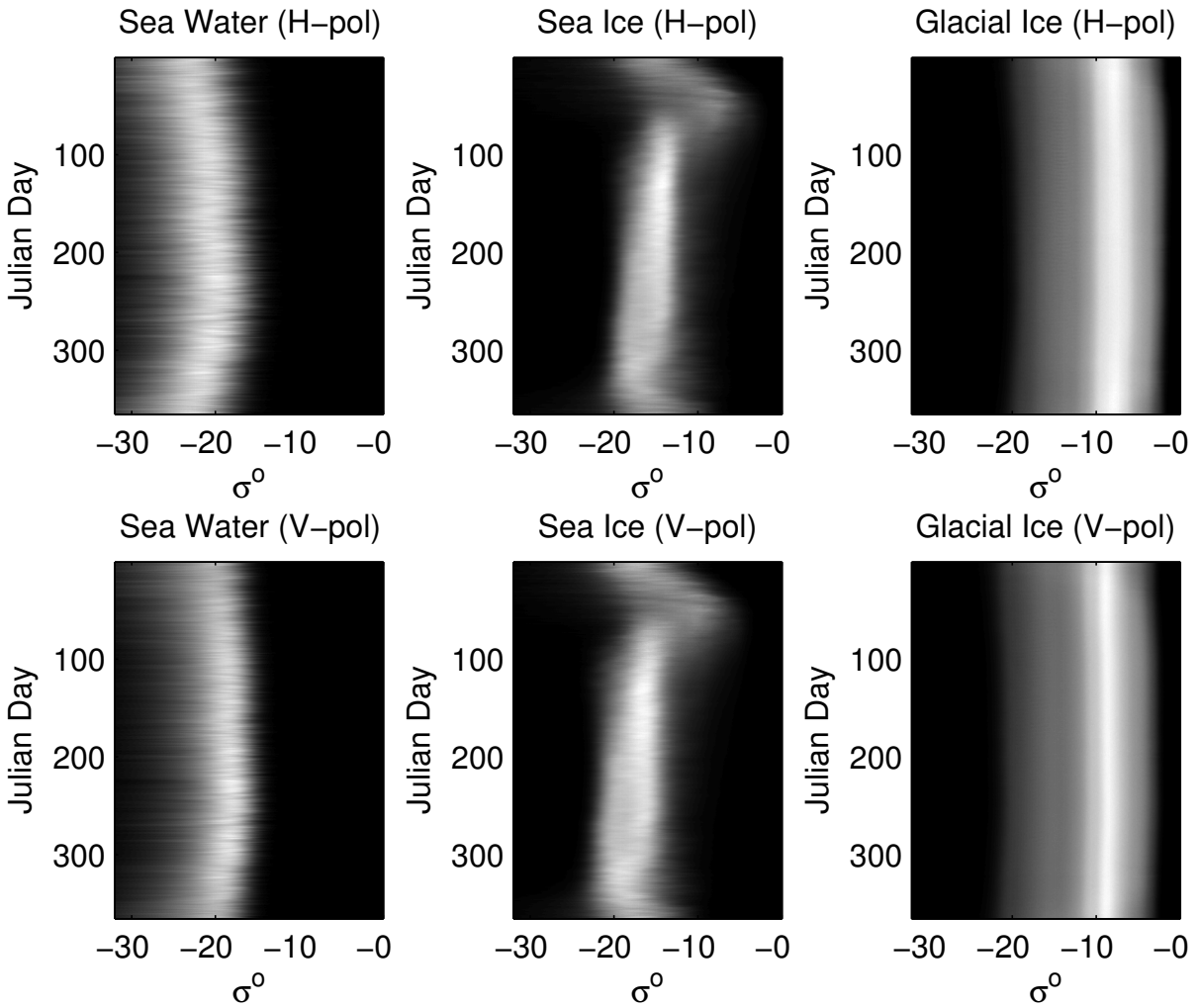


Figure 3.4: Normalized histograms of SeaWinds h- and v-pol backscatter associated with sea water, sea ice, and glacial ice below 55°S from 1999-2009. Backscatter distributions for each Julian day are averaged and normalized in order to represent the time-varying backscatter PDFs of sea water, sea ice, and glacial ice. Backscatter values are derived from standard daily slice-based SIR images. Because each histogram is normalized, the intensity scale is arbitrary.

year sea-ice recession. Average sea-ice returns are on average 2 dB higher at h-pol compared to v-pol. The average backscatter from glacial ice remains relatively constant throughout the year, with average h-pol measurements 1.2 dB higher than v-pol.

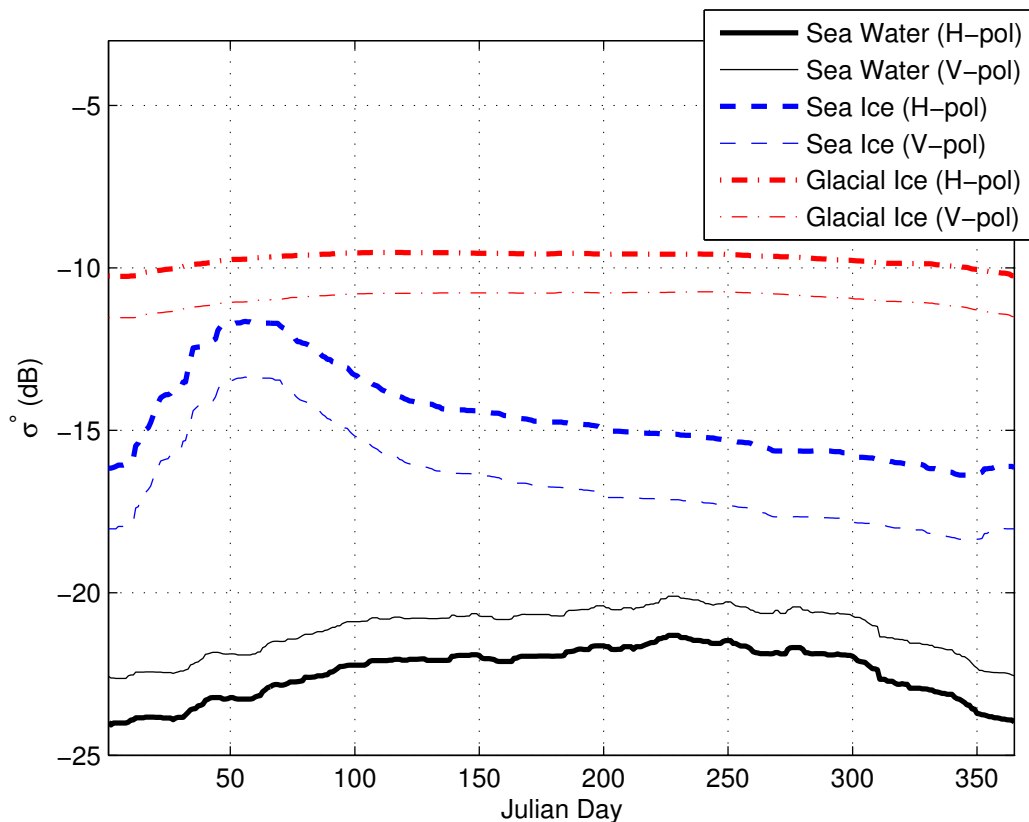


Figure 3.5: The statistical expectation of the backscatter PDFs in Fig 3.3 showing a time-series of the mean h- and v-pol σ° for sea water, sea ice, and glacial ice below 55°S from 1999-2009. Corresponding mean and variance parameters are contained in Table 3.0.

3.5 Iceberg Detection

Scatterometer iceberg tracking exploits the backscatter differences between sea water, sea ice, and glacial ice to detect floating glacial ice fragments, i.e., icebergs. SeaWinds backscatter measurements are post-processed using the SIR algorithm and iceberg positions are manually determined from the daily images. In the following subsections, the methodology for detecting icebergs from daily SIR images is outlined and alternative methods for tracking icebergs are also discussed. Concerns with tracking icebergs in near-real-time (NRT) are addressed, and respective solutions and trade-offs are presented.

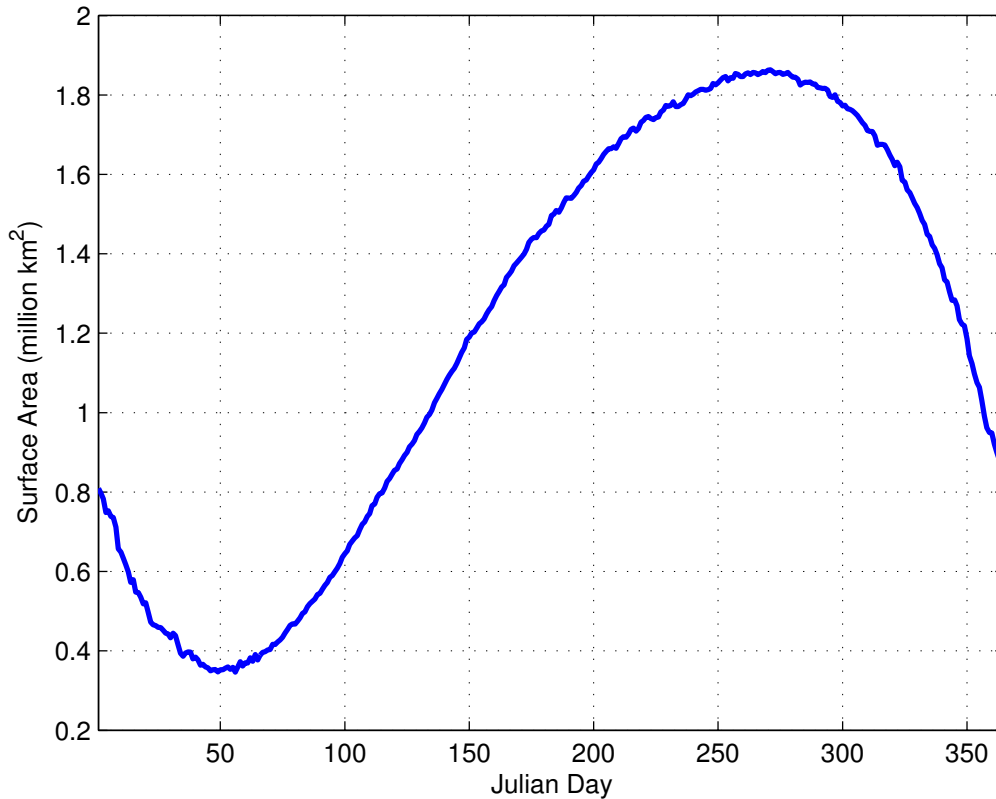


Figure 3.6: Average sea ice extent in the Southern Ocean from 1999-2009 as measured by the SeaWinds scatterometer.

3.5.1 Detection Methodology

Icebergs are detected in daily SIR images as high-backscatter targets surrounded by lower-scattering sea water and sea ice, such as in Fig. 3.1. The estimated centroid of the high-backscatter targets are manually cataloged as the center of icebergs. Daily tracking takes advantage of previously observed iceberg positions. The detection process is aided with knowledge of the common locations where icebergs are found and an understanding of iceberg movement patterns. The former is explored here and the latter is highlighted in Section 4.4.

Icebergs in the Antarctic calve from the terminus of glaciers or from ice sheets, potentially forming very large tabular icebergs [37, 38]. The largest observed iceberg was B15 at approximately 11000 km² [39, 40]. Once broken away from a stationary glacier, icebergs fall under four basic categories: 1) free-floating icebergs free of sea ice, 2) grounded icebergs free from sea ice,

3) free-floating icebergs encapsulated in sea ice, and 4) grounded icebergs encapsulated in sea ice. Generally high contrast between icebergs and sea water make identification of icebergs an easy process. When icebergs are near the glacial continent in cases two and four, an established mask of the Antarctic glacial continent is helpful in differentiating between grounded icebergs and islands.

However, correctly detecting iceberg positions is difficult if the backscatter contrast between the iceberg and the background is insufficient. Backscatter contrast is reduced 1) when an iceberg is located in open water and high surface winds are present, 2) when an iceberg's surface experiences significant melting, 3) when an iceberg becomes too small (on the order of the image resolution), or 4) when an iceberg is in close proximity to land, ice, or other icebergs. The first two cases are discussed in Section 3.3. The third case is dependent on the resolution of SeaWinds images. The effective spatial resolution of the standard slice-based 24-hour SIR products is 5-6 km. For an iceberg this size or smaller, the iceberg is frequently no longer discernible from its surroundings. Limited spatial resolution can also prevent accurate iceberg detection when icebergs are in close proximity to other glacial ice fragments. One location where this is common is "Iceberg Alley" in the Weddell Sea where icebergs occasionally collide or pass closely to other icebergs due to complex ocean currents [39,41–43].

To ameliorate the difficulties of detecting icebergs in low-contrast environments and when icebergs pass closely, I use time-series animations of the daily backscatter images. These animations provide for a smooth framework to observe iceberg movement patterns, resulting in more complete iceberg tracks and reduced ambiguity. As a result, icebergs larger than 5 km can generally be tracked year-round on a daily basis [7].

While daily slice-based SIR images optimize spatial and temporal resolution in the iceberg detection process from SeaWinds data, it is appropriate to consider other image types: in particular, multi-day images. Multi-day SIR images are helpful when increased spatial resolution is desired at the expense of temporal resolution. With the inclusion of more measurements, noise is reduced and the resolution improved in the reconstruction process. As a result, stationary targets appear sharper in definition, while targets in motion may appear blurred.

AVE images [24] may also be used to detect icebergs. As seen in Fig. 3.0e, the backscatter contrast in AVE images is more smoothed and is not as defined as in SIR images. However, AVE images are less computationally expensive than SIR images and have sufficient resolution to detect

and track most large tabular icebergs [19]. As a result, AVE images are frequently used in real-time tracking.

3.5.2 NRT Iceberg Detection

The methodology for tracking icebergs previously outlined extends to tracking icebergs in NRT. However, there are three main concerns when tracking icebergs in a NRT environment. They are: 1) accounting for the time difference between when backscatter measurements are recorded and when iceberg updates are received, 2) updating the positions of existing icebergs, and 3) accurately detecting and differentiating new icebergs from short-lived high-backscatter targets in the daily SIR images.

There is a variable delay between when SeaWinds radar measurements are collected and when iceberg positions are analyzed and then reported via email. Factors contributing to the time lag include the time required by SeaWinds to accumulate and down-link backscatter measurements, processing of radar measurements into SIR images, iceberg identification, and position up-link to the surface ship. While these functions may be streamlined to some extent, a minimum delay time exists. During periods of rapid iceberg movement, this delay time may result in some discrepancy between reported and actual iceberg positions after the delay.

To improve accuracy in the NRT iceberg detection process, it may be necessary to compensate for iceberg movement by 1) observing the behavior of nearby icebergs and sea ice and 2) predicting iceberg positions from past measurements. The first is demonstrated in Chapter 4. The second requires the development of an iceberg motion model, a topic explored in Chapter 6.

3.6 Conclusion

Even though SeaWinds was never designed to track icebergs, this chapter outlines a methodology to detect large tabular icebergs in enhanced-resolution scatterometer images. In addition to detecting icebergs, the methodology developed here extends to detecting any geophysical phenomena that 1) has a unique microwave backscatter signature and 2) is larger than the effective resolution of standard SIR images.

Chapter 4

Tracking Icebergs

4.1 Introduction

Using the iceberg detection techniques developed in Chapter 3, icebergs are tracked on a daily basis and cataloged in an Antarctic iceberg database. With this database of iceberg positions, studies of iceberg characteristics are possible. For instance iceberg counts may be calculated and movement patterns may be examined. In the following sections, the Antarctic iceberg database is introduced, and the count of icebergs tracked in SeaWinds backscatter images from 1999-2009 is presented. Long-term movement patterns are identified and short-term movement patterns are highlighted via case study of iceberg C19a. Finally, the ability and accuracy of using SeaWinds to track icebergs in near-real-time (NRT) is demonstrated via operational support of the 2005, 2008, and 2009 NSF Antarctic cruises [1, 8].

4.2 Iceberg Database

Using the iceberg detection techniques developed in Chapter 3, icebergs were tracked using the SeaWinds scatterometer (and are currently being tracked using additional microwave scatterometers) on a daily basis and cataloged as part of the Scatterometer Climate Record Pathfinder (SCP) project at Brigham Young University's (BYU) Microwave Earth Remote Sensing (MERS) Laboratory [7]. From 1999-2009, the MERS Antarctic iceberg database contains daily positions and microwave backscatter values of nearly all of the icebergs reported by the NIC in addition to over 350 additional icebergs. The iceberg database was updated periodically throughout the SeaWinds mission with icebergs added via delayed post-processing and in NRT [7]. Where possible, iceberg names in the MERS database correspond to names issued by the NIC. The standard NIC naming convention consists of naming an iceberg with a letter corresponding to the quadrant where it was first detected, followed by an incremental number. As icebergs fragment, each frag-

ment name is appended with a letter [44]. Quadrant designations are listed in Appendix A. Icebergs in the MERS database not reported in the NIC iceberg database are labeled as “UK” (unknown) with an incremental number.

In a NRT environment, previously-detected icebergs are not always distinguishable in current images from high-backscatter anomalies that may correspond to glacial ice fragments, multi-year sea-ice fragments, or other short-lived high-backscatter targets. Because accurate identification of new or resynchronization of lost icebergs may take several days, newly-detected high-backscatter signatures are designated “TK” (temporary known) contacts. If these contacts survive and are confirmed in post-processing to be new icebergs, they are relabeled “UK” contacts. We note that while “UK” contacts are included in the final MERS Antarctic iceberg database, “TK” contacts are not. To service special requests (e.g., the 2005, 2008, and 2009 NSF Antarctic cruises), additional iceberg datasets have been created which do include “TK” contacts.

4.3 Iceberg Counts

Figure 4.0 presents the number of icebergs detected in SeaWinds backscatter images from 1999 to 2009 and the number of icebergs reported by the NIC during the same period. The NIC tracks icebergs larger than 10 nautical miles (nm) using optical sensors. The SeaWinds-derived iceberg database includes all of the NIC icebergs, plus additional icebergs visible in the SeaWinds images.

The annual fluctuations in the iceberg count at the peak of the austral ablation is due to melt conditions at the peak of the austral ablation. As noted previously, austral melting conditions decrease backscatter contrast between glacial ice, sea ice, and sea water, making iceberg detection more difficult and reducing the reported count. The iceberg count recovers after each ablation cycle for icebergs that survive the summer melt cycle. The count is also increased by fragmentation of existing icebergs.

4.4 Iceberg Movement Profiles

Because tabular icebergs have a deep draft and thus are deeply embedded in the ocean current, iceberg movement is typically dominated by oceanic currents [45]. Near the coast of

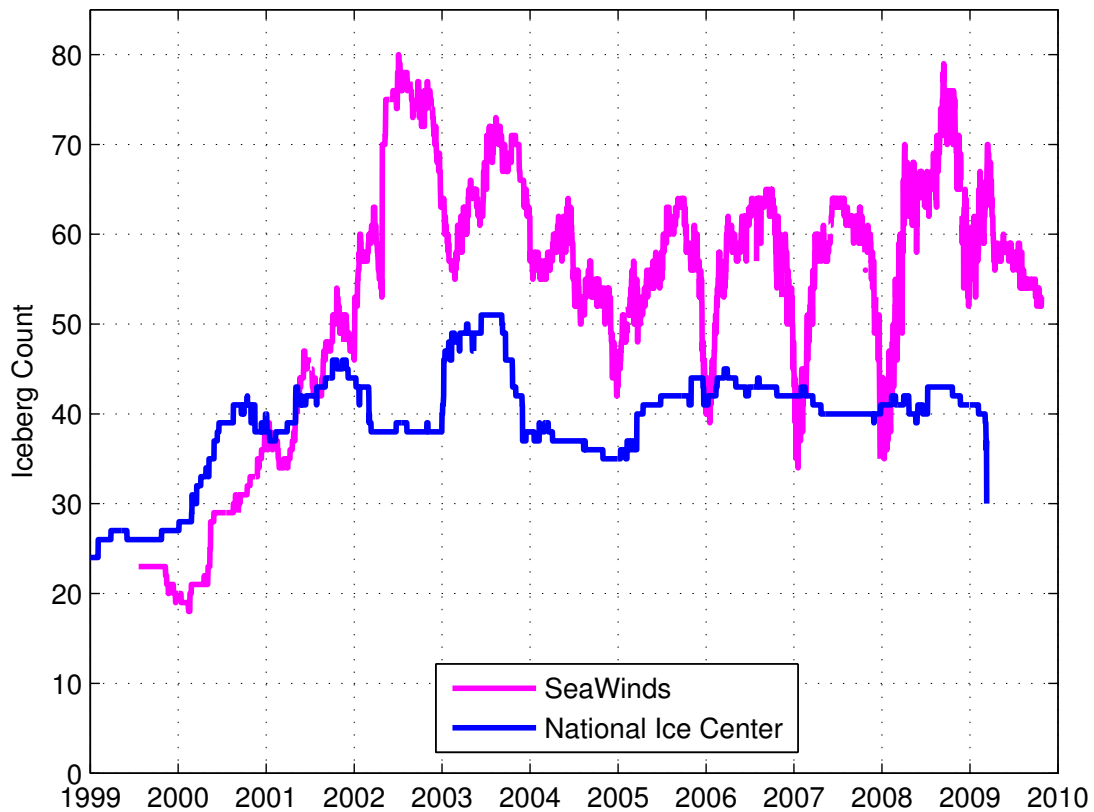


Figure 4.1: Count of the number of Antarctic icebergs detected in daily SeaWinds backscatter images and reported by the NIC from 1999-2009. SeaWinds reports are daily; however, because the NIC reports iceberg positions periodically, the NIC iceberg count is an interpolated estimate, e.g., if the NIC reports positions for an iceberg on Julian days 10 and 250, this graph counts the iceberg over the entire interval.

Antarctica, these currents sweep most icebergs in a counter-clockwise motion until they accumulate in the Weddell Sea, see Fig. 4.1. Icebergs are then propelled northward into the Scotia Sea along the “Iceberg Alley” corridor at approximately 50°W. Around 60°S, icebergs start moving in an eastward direction as they are swept into the Antarctic Circumpolar Current (ACC). By the time most icebergs reach the ACC, they have broken up; some however survive for longer periods. As the size of fragments shrink, they become less detectable in the backscatter images [7, 36, 46]. The icebergs that do not follow this general pattern are pushed away from the glacial continent by katabatic winds while encapsulated in sea ice, and enter the ACC at other longitudes.

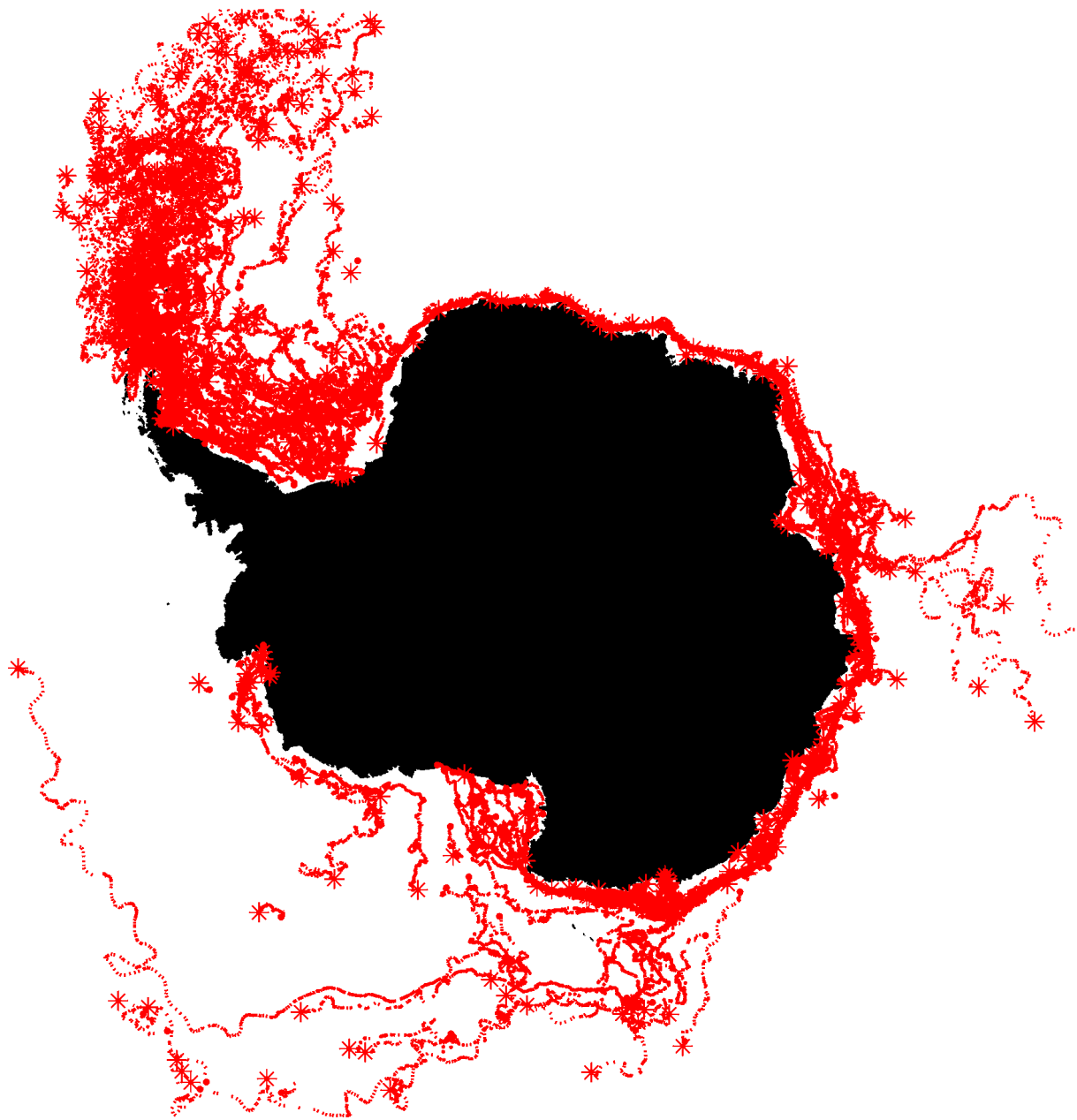


Figure 4.2: A depiction of Antarctic icebergs detected by SeaWinds from 1999 to 2009. The majority of icebergs travel counter-clockwise around the perimeter of Antarctica and accumulate in the Weddell Sea. They are then propelled into the Scotia Sea along a northward corridor, frequently called “Iceberg Alley.” Upon reaching 60°S, icebergs are swept into the Antarctic Circumpolar Current (ACC). Icebergs that do not follow this general pattern are pushed away from the glacial continent by katabatic winds while encapsulated in sea ice, causing these icebergs to enter the ACC at other longitudes. Initial and final iceberg positions are marked with a dot and star, respectively, and are connected with dotted lines. For convenience, geographic regions are labeled in Fig. A.0.

From 1999-2009, 90% of the icebergs contained in the MERS Antarctic iceberg database follow the general pattern described above. 8% of icebergs are pushed away from the Antarctic continent by katabatic winds in the Ross Sea and drift into the southern Pacific Ocean. Approximately 2% of icebergs are pushed away from the glacial continent near the Davis Sea and float into the southern Indian Ocean. These patterns coincide with research performed in [42].

4.5 Case Study of Iceberg C19a

Sample iceberg tracking results are demonstrated in Fig. 4.2 for iceberg C19a for Julian days 283-298 in 2008 when C19a was in open water. This time-series illustrates changes in daily backscatter during the summer melt. Notice the gradual counter-clockwise rotation of iceberg C19a over the time interval. Figure 4.2f illustrates a negative consequence of using multiple passes to create SIR images. Since multiple satellite passes over a 24-hour period are used to create SIR images, very rapid changes in the iceberg orientation from pass to pass may cause an echo effect in the daily SIR images; however, this is rare. Figure 4.2k depicts a melt event on 2008 Julian day 291. Spanning over 100 km, one end of iceberg C19a remains frozen and retains its high backscatter profile while the opposite end is likely undergoing surface melt. The increase in surface moisture results in decreased microwave penetration and thus a decrease in volume scatter. As a result, the backscatter from the left end of iceberg C19a in Fig. 4.2k is diminished, resulting in reduced contrast compared to the surrounding sea water.

4.6 NSF Cruise Case Studies

In 2005, 2008, and 2009, the NSF funded three cruises to travel to the Scotia and Weddell Seas to observe and record data related to iceberg characteristics and the impact of icebergs on nearby pelagic communities [1]. To help direct ships to the dynamic positions of icebergs, the MERS Laboratory at BYU provided daily iceberg position updates to these cruises. Daily updates were begun pre-mission to allow for efficient path planning, during the cruise to coordinate scientific efforts to locate moving icebergs, and post-mission for several weeks to allow for continued short-term scientific analysis. The number of updates provided during each cruise is detailed in Table 4.0. The variability in the number of updates provided per mission is addressed in each case study.

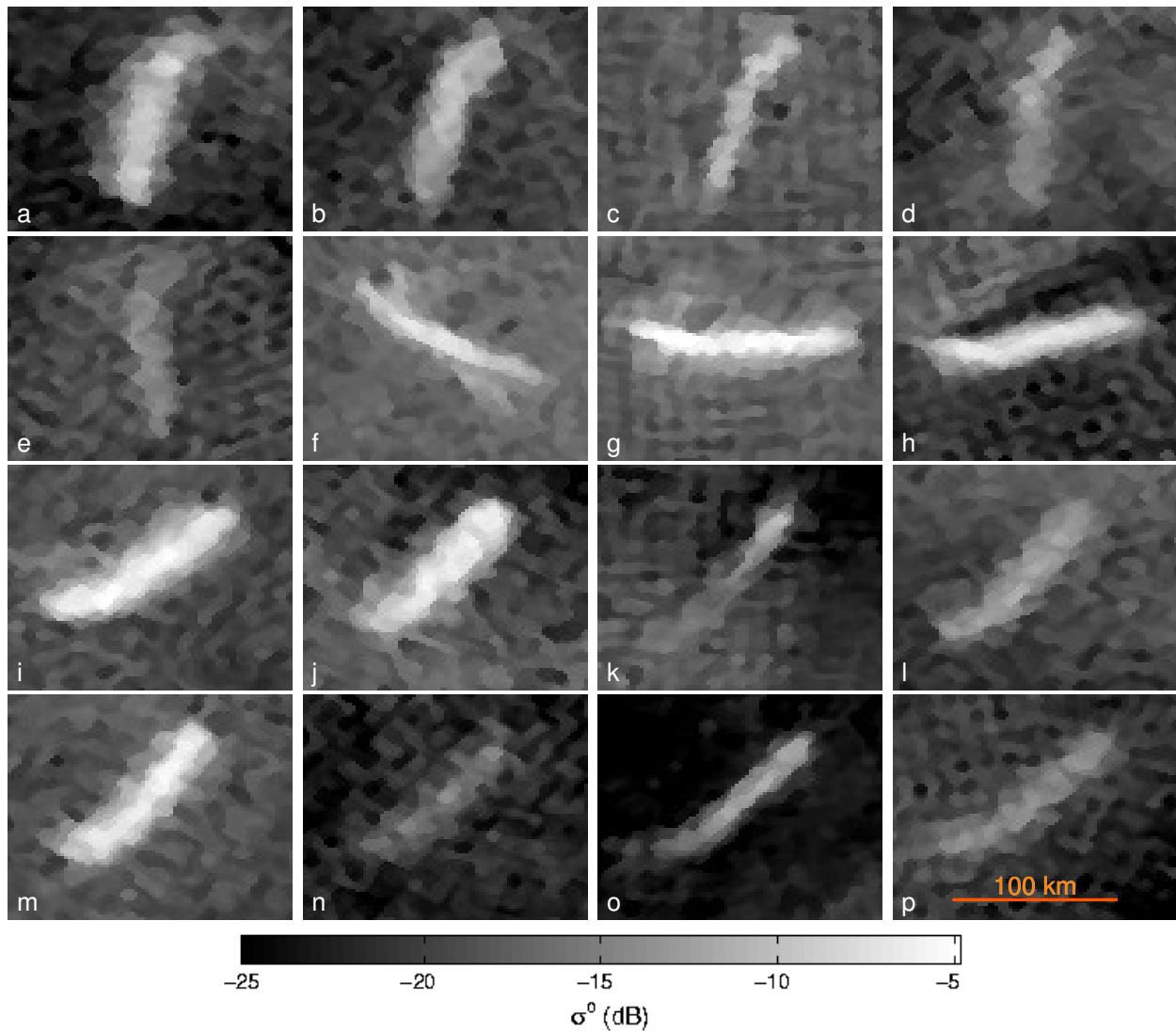


Figure 4.3: Daily SeaWinds h-pol backscatter time-series of iceberg C19a for 2008, Julian days 283-298. Higher-backscatter values correspond to iceberg C19a and lower-backscatter values correspond to sea water.

Table 4.1: Number of iceberg position reports provided for each NSF Antarctic cruise. Counts are divided into preliminary, interim, and post-mission updates. For an explanation of the temporal spacing of the iceberg reports, see the text.

Cruise	Pre-Mission	Interim	Post-Mission	Total
2005	14	31	7	52
2008	26	44	11	81
2009	15	40	2	57

To facilitate close-proximity research of icebergs during the NSF cruises, scatterometer images were also used to map the sea-ice edge. Note that even though cruise logistics and sea-ice proximity limited the close-proximity research to only a select few icebergs, tracking all nearby contacts, including “TK” contacts, proved to be helpful in subjectively determining ocean current speed and direction for estimating future iceberg positions. All backscatter measurements have since been post-processed and iceberg positions have been updated from standard SIR images. These are available at <<http://www.scp.byu.edu>>. In the following, each cruise is considered and operations unique to each mission are reviewed.

4.6.1 The 2005 Cruise

The first NSF Antarctic cruise took place in 2005 from Julian day 331 to 361. This first cruise required the initial setup of NRT processing of SIR images for the region of intent. Once this process was developed, daily iceberg positions were extracted from the most recent SIR images and subsequently included in the daily reports. Corresponding SIR images with iceberg annotations were also included in the daily updates; however, due to up-link size constraints, smaller custom SIR images were created. These custom backscatter images were bounded by 65°S, 55°S, 60°W, and 40°W. Images were manually annotated to indicate iceberg positions and sea-ice extent. General wind conditions were estimated based on sea-surface roughness observed in the backscatter images.

Throughout the cruise, a total of 15 icebergs were tracked in the Scotia and Weddell Seas. A summary of some of the lifetime and mission-specific statistics of icebergs and high-backscatter contacts during this time is included in Table 4.2, detailing detection dates, initial and final tracking positions, initial and final positions with respect to the cruise, average daily movement during the cruise, a flag indicating sea ice encapsulation during the cruise, and iceberg dimensions as reported by the NIC during the cruise. Iceberg tracks during the time of the cruise are illustrated in Fig. 4.3. Even though this cruise took place during the austral ablation, the outlying sea ice had yet to melt away from the south Scotia Sea; therefore, the majority of icebergs in the Weddell Sea were encapsulated in first-year sea ice during the cruise period. As a result, only iceberg A52 was visited (twice) of the 15 icebergs tracked.

Table 4.2: Compilation of icebergs and high-backscatter targets detected by the SeaWinds scatterometer in the Weddell and Scotia Seas during the 2005 NSF Antarctic cruise. Lifetime and mission-specific statistics are illustrated for each contact including detection dates, position, average daily movement during the cruise, a flag indicating sea ice encapsulation during the cruise, and iceberg dimensions reported by the NIC. See Fig. 4.3 for corresponding track illustration. Icebergs visited during the cruise are indicated with “*”.

Name	Lifetime Information			Cruise-Specific Information (2005 JD 331-361)				
	Track Dates	Initial Pos. (° N, ° E)	Final Pos. (° N, ° E)	Initial Pos. (° N, ° E)	Final Pos. (° N, ° E)	Avg. Daily Movement	Sea Ice	NIC Size (nm)
A27	99JD200-09JD244	-76.23, -43.33	-74.84, -39.88	-76.26, -43.60	-76.26, -43.60	0.0 km	Y	10 x 8
A22a	99JD202-07JD296	-76.36, -46.07	-48.63, -16.27	-65.40, -53.86	-64.23, -54.04	6.7 km	Y	36 x 27
A23a	99JD202-09JD244	-76.27, -41.81	-76.05, -41.35	-76.15, -41.66	-76.15, -41.66	0.0 km	Y	46 x 43
A43d	01JD123-09JD244	-71.20, -58.70	-70.52, -58.08	-71.30, -58.56	-71.30, -58.56	0.0 km	Y	27 x 18
A43f	01JD157-09JD021	-71.63, -59.40	-50.77, -25.27	-66.59, -59.44	-66.52, -60.02	5.1 km	Y	29 x 17
A52*	03JD063-06JD124	-65.69, -60.95	-54.70, -37.29	-61.13, -51.64	-60.69, -53.26	10.8 km	N	21 x 10
A53a	05JD120-08JD116	-67.11, -60.24	-51.44, -33.25	-67.22, -60.25	-67.03, -60.04	0.8 km	Y	29 x 14
UK138	05JD110-06JD261	-69.91, 6.40	-65.22, -54.16	-73.47, -38.48	-74.13, -44.70	4.4 km	Y	—
UK139	05JD202-05JD365	-72.29, -23.35	-71.71, -43.44	-71.43, -36.53	-71.83, -43.54	9.8 km	Y	—
UK140	05JD202-05JD355	-70.43, -20.50	-70.70, -30.64	-69.78, -28.11	-70.70, -30.64	8.1 km	Y	—
UK206	04JD315-05JD348	-75.47, -35.61	-64.96, -40.54	-64.65, -40.22	-64.96, -40.54	9.9 km	Y	—
UK207	04JD318-06JD275	-76.21, -40.03	-56.85, -36.38	-67.37, -47.73	-66.70, -49.52	5.3 km	Y	—
UK210	04JD358-05JD359	-78.08, -43.90	-65.96, -52.93	-67.86, -51.02	-65.96, -52.93	12.4 km	Y	—
UK215	05JD018-06JD306	-67.83, 33.64	-62.87, -41.40	-73.28, -27.87	-74.35, -33.49	7.6 km	Y	—
UK221	05JD124-06JD022	-66.17, -59.57	-66.27, -60.78	-65.78, -58.86	-66.07, -59.85	1.6 km	Y	—

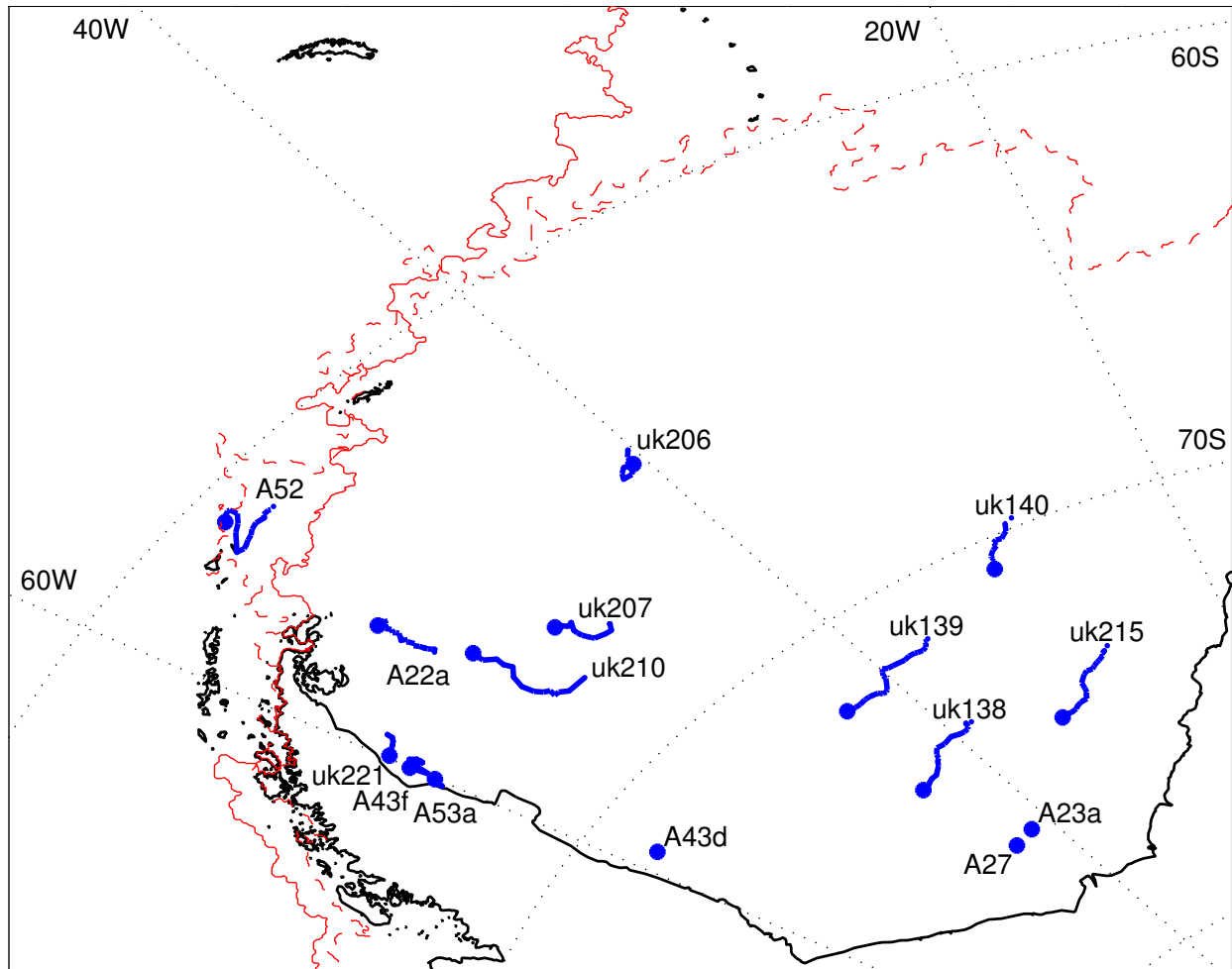


Figure 4.4: Tracks of Antarctic icebergs and high-backscatter contacts detected using SeaWinds in the Weddell and Scotia Seas during the 2005 NSF Antarctica cruise, Julian days 331-361. Final iceberg tracking positions are indicated with “*”. The Antarctic peninsula and the Filchner-Ronne Ice Shelf are outlined at the bottom of the image. The sea-ice edge at the beginning and ending of the cruise is indicated by solid and dashed lines. See Table 4.2 for corresponding iceberg statistics.

4.6.2 The 2008 Cruise

The second NSF Antarctic cruise took place in 2008 from Julian day 153 to 177. During this cruise, multiple icebergs were detected and tracked in the Scotia and northern Weddell Seas. Corresponding iceberg and “TK” contact information and statistics are presented in Table 4.3. Corresponding iceberg track illustrations are in Fig. 4.4. Many icebergs were located near the sea-ice edge. As a result of a late austral fall, exploration in the Weddell Sea was prevented because of advancing sea ice. Consequently, only iceberg A43k and contacts UK238 and UK250 were visited.

One iceberg (UK238) was encapsulated in sea ice part of the time during the cruise. As a result, the sea-ice encapsulation flag for this iceberg is indicated as “M” (“Mixed”) in Table 4.3.

Similar to the 2005 cruise, daily updates included iceberg positions and custom SIR images. However, due to an increase in the number of accessible icebergs, there was a need for greater temporal resolution. To meet this need, a specialized SIR product was implemented for NRT operation to enable iceberg position updates twice per day. The morning update was derived from multiple SIR images produced using the backscatter measurements collected from the previous 12 and 24 hours. Compared to the 24-hour SIR images, the 12-hour SIR images have greater temporal resolution at the expense of reduced spatial resolution and reduced backscatter contrasts between sea water, sea ice, and glacial ice. If sufficient contrast existed in the 12-hour SIR images, iceberg positions were extracted. If not, 24-hour SIR images were used. This process was repeated in the evening.

Upon post-mission review, it was found that while 12-hour SIR images provided greater temporal resolution, spatial resolution and image contrast were frequently too degraded to support reliable iceberg tracking. As a result, the majority of updates provided during the 2008 cruise were based on 24-hour SIR images.

In addition to tracking iceberg positions in real-time, the sea-ice edge was annotated in the daily iceberg reports during the 2008 and 2009 NSF cruises. While auto-tracking the sea-ice edge from daily SeaWinds images is possible [47–49], I manually tracked the edge in the NRT reports. As previously discussed, the sea-ice edge is visible in backscatter images as a region whose associated backscatter typically lies between low-backscatter sea water and high-backscatter icebergs, such as in Fig. 3.1. In the event of iceberg surface melting, the sea-ice edge can be differentiated between iceberg signatures with an iceberg tracking time-series, such as in Fig. 4.8b.

4.6.3 The 2009 Cruise

The third NSF Antarctic cruise took place in 2009, Julian days 68 to 101. During this time, most of the icebergs detected were in the Weddell Sea. Extensive sea ice recession, characteristic of the height of the austral ablation, allowed for close observation of these icebergs. Icebergs tracked during this mission are included in Table 4.4 with corresponding tracks in Fig. 4.5.

Table 4.3: Compilation of icebergs and high-backscatter targets detected by the SeaWinds scatterometer in the Weddell and Scotia Seas during the 2008 NSF Antarctic cruise. Lifetime and mission-specific statistics are illustrated for each contact including detection dates, position, average daily movement during the cruise, a flag indicating sea ice encapsulation during the cruise, and iceberg dimensions reported by the NIC. See Fig. 4.4 for corresponding track illustration. Icebergs visited during the cruise are indicated with “*”.

Name	Lifetime Information			Cruise-Specific Information (2008 JD 153-177)				
	Track Dates	Initial Pos. (° N, ° E)	Final Pos. (° N, ° E)	Initial Pos. (° N, ° E)	Final Pos. (° N, ° E)	Avg. Daily Movement	Sea Ice	NIC Size (nm)
A23a	99JD202-09JD244	-76.27, -41.81	-76.05, -41.35	-76.14, -41.59	-76.14, -41.59	0.0 km	Y	40 x 32
A27	99JD200-09JD244	-76.23, -43.33	-74.84, -39.88	-75.15, -41.56	-75.15, -41.56	0.0 km	Y	10 x 8
A43d	01JD123-09JD244	-71.20, -58.70	-70.52, -58.08	-71.29, -58.47	-71.29, -58.47	0.0 km	Y	21 x 15
A43f	01JD157-09JD021	-71.63, -59.40	-50.77, -25.27	-56.44, -34.35	-52.89, -36.75	22.3 km	N	27 x 9
A43k*	08JD003-09JD095	-62.37, -53.59	-51.55, -11.10	-57.77, -43.54	-58.01, -42.52	5.4 km	N	25 x 8
A56	08JD148-09JD244	-77.12, -50.12	-77.15, -49.94	-77.14, -50.04	-77.15, -50.01	2.5 km	Y	14 x 7
A57	08JD151-09JD145	-77.40, -48.24	-77.60, -47.59	-77.40, -48.05	-77.50, -47.90	4.0 km	Y	19 x 5
B15d	00JD231-08JD330	-76.38, -179.02	-49.06, -37.51	-55.83, -43.67	-55.13, -42.81	11.2 km	N	25 x 5
B15l	07JD054-09JD244	-66.48, 46.60	-62.06, -37.97	-71.47, -37.68	-70.58, -38.40	5.9 km	Y	16 x 7
C8	99JD202-09JD244	-67.30, 147.08	-60.87, -43.21	-65.93, -55.67	-65.92, -55.42	0.6 km	Y	15 x 8
C18a	05JD152-09JD244	-65.20, 115.25	-59.92, -45.05	-73.50, -47.17	-72.34, -47.63	6.3 km	Y	17 x 3
C19d	03JD173-09JD244	-69.53, 163.30	-57.08, -49.17	-74.68, -35.88	-74.26, -38.63	6.0 km	Y	17 x 8
C21a	05JD079-08JD208	-66.09, 90.27	-54.62, -40.61	-56.80, -46.83	-56.02, -45.01	11.1 km	N	10 x 8
D18	06JD053-09JD028	-69.96, 8.92	-56.79, -17.88	-60.21, -39.18	-59.00, -39.88	7.0 km	Y	11 x 4
UK148	06JD085-08JD288	-67.52, 44.39	-68.05, -36.69	-73.32, -40.19	-72.44, -41.27	5.7 km	Y	—
UK157	07JD032-09JD244	-76.51, -46.70	-73.97, -42.52	-76.27, -46.58	-76.25, -46.74	0.7 km	Y	—
UK177	07JD030-08JD330	-74.21, -32.59	-50.88, -32.97	-59.72, -44.15	-56.99, -39.00	14.9 km	N	—
UK235	08JD019-08JD237	-63.63, -51.91	-55.57, -40.58	-57.59, -46.50	-59.47, -46.05	18.1 km	N	—
UK238*	08JD090-08JD165	-60.74, -52.53	-60.40, -48.85	-60.63, -51.82	-60.40, -48.85	14.2 km	M	—
UK246	08JD090-08JD200	-74.25, -27.93	-71.50, -39.32	-72.49, -38.03	-71.92, -38.55	6.2 km	Y	—
UK247	08JD074-09JD103	-59.86, -47.90	-55.46, -35.52	-59.51, -46.72	-58.56, -43.97	16.6 km	N	—
UK248	08JD102-08JD344	-58.61, -44.39	-51.93, -37.58	-56.87, -43.74	-55.27, -41.06	23.3 km	N	—
UK250*	08JD131-08JD216	-61.97, -56.83	-59.80, -46.86	-60.51, -55.88	-59.43, -52.72	16.6 km	N	—

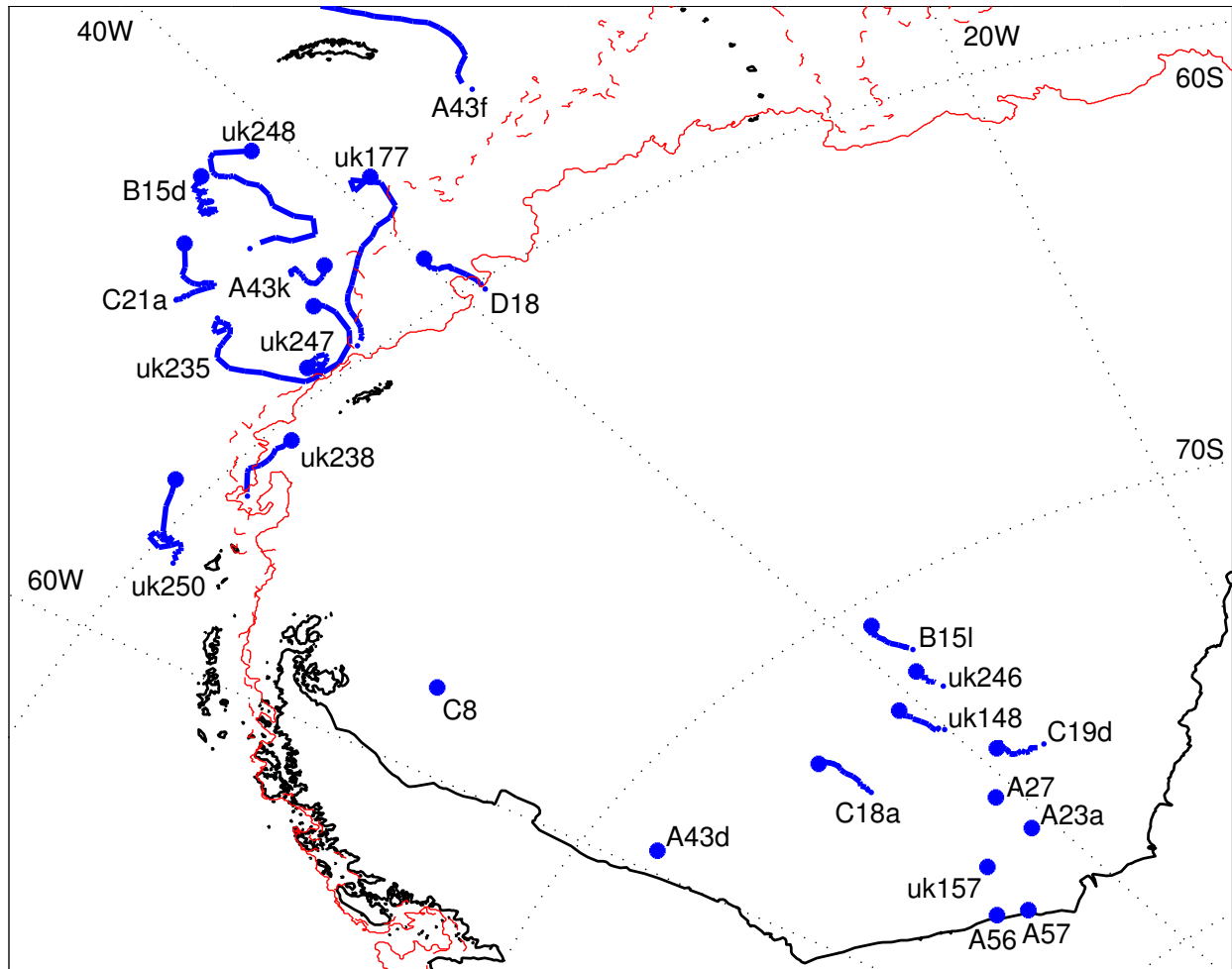


Figure 4.5: Tracks of Antarctic icebergs and high-backscatter contacts detected using SeaWinds in the Weddell and Scotia Seas during the 2008 NSF Antarctica cruise, Julian days 153-177. Final iceberg tracking positions are indicated with “*”. The Antarctic peninsula and the Filchner-Ronne Ice Shelf are outlined at the bottom of the image. The sea-ice edge at the beginning and ending of the cruise is indicated by solid and dashed lines. See Table 4.3 for corresponding iceberg statistics.

For the 2009 cruise, there were two iceberg position reporting methodologies. Initially, iceberg reports were relayed twice per day based upon the 24-hour SIR images developed for the 2008 cruise. However, in order to expand the search to icebergs in the Weddell Sea and gain an understanding of sea-ice extent and momentum, the boundaries of the 24-hour SIR images were expanded from 55-65°S and 60-40°W to 55-67°S and 60-25°W during the initial week of the cruise. Due to file size constraints, reports were reduced in frequency to once per day. This is the primary reason behind the lower number of iceberg updates reported in 2009 compared to 2005 and

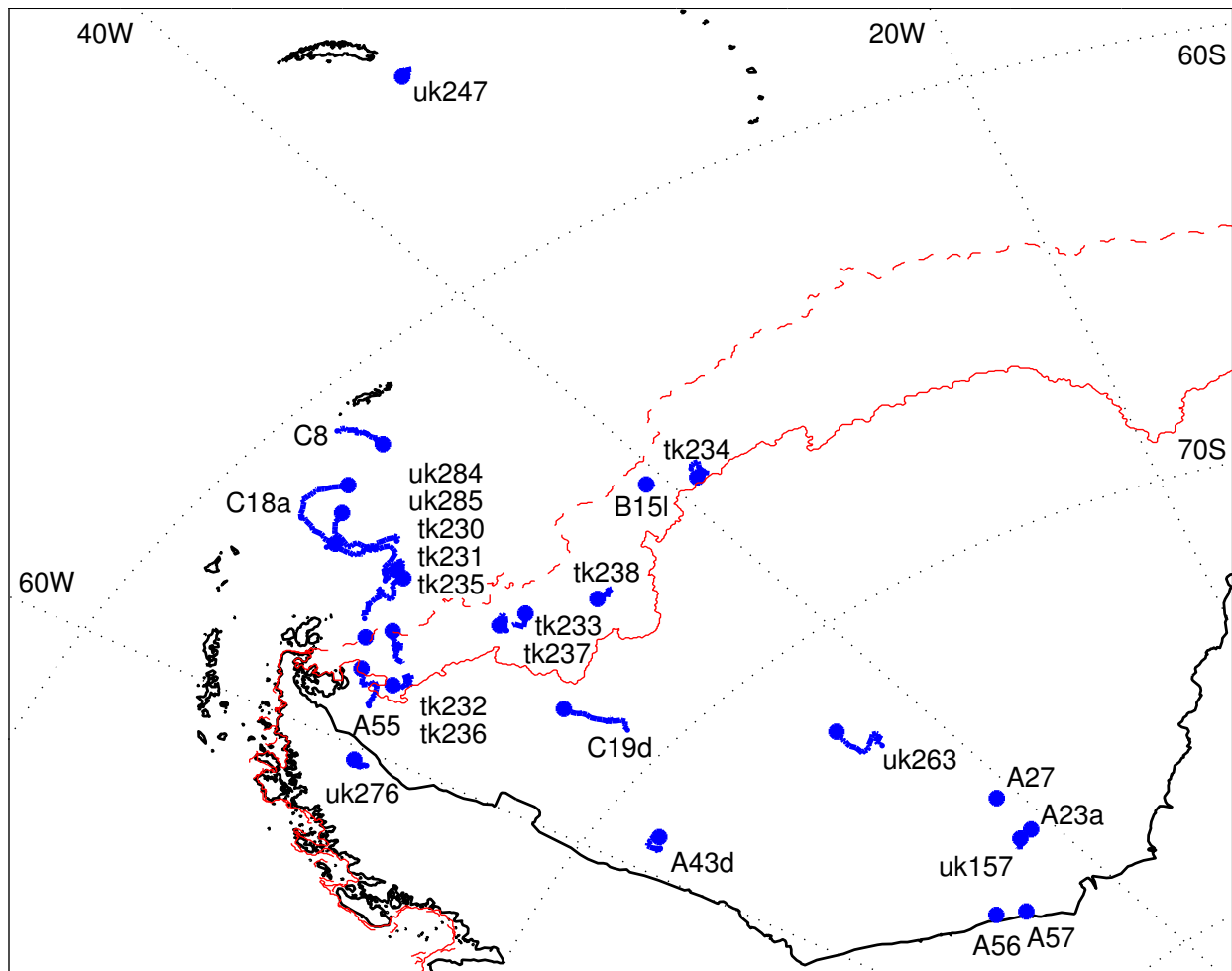


Figure 4.6: Tracks of Antarctic icebergs and high-backscatter contacts detected using SeaWinds in the Weddell and Scotia Seas during the 2009 NSF Antarctica cruise, Julian days 68-101. Final iceberg tracking positions are indicated with “*”. The Antarctic peninsula and the Filchner-Ronne Ice Shelf are outlined at the bottom of the image. The sea-ice edge at the beginning and ending of the cruise is indicated by solid and dashed lines. See Table 4.4 for corresponding iceberg statistics.

2008 in Table 4.0. Using this methodology, the 2009 cruise ship successfully intercepted icebergs C18a (twice) and B15l.

4.6.4 Sample Data

To facilitate close-proximity iceberg studies, backscatter images from SeaWinds and subsequently derived iceberg positions were transmitted to a surface ship in the Weddell and Scotia Seas during the 2005, 2008, and 2009 NSF Antarctic cruises. Examples of these periodic updates are included in Fig. 4.6. Figure 4.6a emphasizes the Scotia Sea and was primarily used for the 2005

Table 4.4: Compilation of icebergs and high-backscatter targets detected by the SeaWinds scatterometer in the Weddell and Scotia Seas during the 2009 NSF Antarctic cruise. Lifetime and mission-specific statistics are illustrated for each contact including detection dates, position, average daily movement during the cruise, a flag indicating sea ice encapsulation during the cruise, and iceberg dimensions reported by the NIC. See Fig. 4.5 for corresponding track illustration. Icebergs visited during the cruise are indicated with “*”.

Name	Lifetime Information			Cruise-Specific Information (2009 JD 068-101)				
	Track Dates	Initial Pos. (° N, ° E)	Final Pos. (° N, ° E)	Initial Pos. (° N, ° E)	Final Pos. (° N, ° E)	Avg. Daily Movement	Sea Ice	NIC Size (nm)
A23a	99JD202-09JD244	-76.27, -41.81	-76.05, -41.35	-76.11, -41.58	-76.11, -41.58	0.0 km	Y	40 x 32
A27	99JD200-09JD244	-76.23, -43.33	-74.84, -39.88	-75.14, -41.63	-75.14, -41.44	1.4 km	Y	10 x 8
A43d	01JD123-09JD244	-71.20, -58.70	-70.52, -58.08	-71.25, -58.26	-71.12, -57.45	3.4 km	Y	21 x 16
A55	08JD258-09JD216	-65.73, -60.81	-63.60, -56.48	-65.13, -57.78	-64.55, -56.23	5.4 km	Y	14 x 4
A56	08JD148-09JD244	-77.12, -50.12	-77.15, -49.94	-77.08, -49.89	-77.11, -49.87	2.5 km	Y	14 x 7
A57	08JD151-09JD145	-77.40, -48.24	-77.60, -47.59	-77.54, -48.04	-77.46, -47.96	1.6 km	Y	19 x 5
B151*	07JD054-09JD244	-66.48, 46.60	-62.06, -37.97	-65.44, -40.72	-65.43, -40.79	2.5 km	M	16 x 7
C8	99JD202-09JD244	-67.30, 147.08	-60.87, 43.21	-60.80, -47.40	-61.59, -46.74	4.0 km	N	15 x 8
C18a*	05JD152-09JD244	-65.20, 115.25	-59.92, -45.05	-62.40, -51.92	-61.78, -49.06	7.8 km	N	17 x 3
C19d	03JD173-09JD244	-69.53, 163.30	-57.08, -49.17	-69.19, -52.29	-67.99, -53.06	6.7 km	Y	17 x 8
UK157	07JD032-09JD244	-76.51, -46.70	-73.97, -42.52	-76.26, -43.13	-76.15, -42.80	3.4 km	Y	—
UK247	08JD074-09JD103	-59.86, -47.90	-55.46, -35.52	-55.45, -35.54	-55.49, -35.72	4.2 km	N	—
UK263	08JD228-09JD206	-74.46, -30.64	-68.48, -50.13	-72.82, -43.83	-72.01, -44.98	6.9 km	Y	—
UK276	08JD334-09JD244	-65.92, -60.95	-65.42, -60.73	-65.81, -60.73	-65.55, -60.70	3.2 km	Y	—
UK284	09JD046-09JD244	-63.50, -51.44	-60.95, -43.70	-63.26, -50.01	-62.11, -50.24	7.4 km	N	—
UK285	09JD027-09JD138	-64.09, -53.70	-61.70, -49.52	-63.67, -51.70	-62.47, -51.59	7.8 km	N	—
TK230	09JD064-09JD099	-64.05, -54.93	-64.19, -54.76	-64.15, -54.74	-64.19, -54.76	3.9 km	N	—
TK231	09JD070-09JD116	-63.92, -53.98	-63.54, -51.21	-63.92, -53.98	-63.89, -51.34	8.0 km	N	—
TK232	09JD060-09JD099	-64.79, -55.51	-64.49, -53.86	-64.99, -55.01	-64.49, -53.86	7.0 km	M	—
TK233	09JD070-09JD075	-66.07, -50.93	-66.06, -49.65	-66.07, -50.93	-66.06, -49.65	15.5 km	N	—
TK234	09JD071-09JD090	-65.65, -38.77	-65.87, -38.88	-65.65, -38.77	-65.87, -38.88	6.0 km	N	—
TK235	09JD073-09JD096	-63.68, -51.90	-63.67, -51.14	-63.68, -51.90	-63.67, -51.14	8.0 km	N	—
TK236	09JD073-09JD084	-65.36, -55.79	-65.21, -56.28	-65.36, -55.79	-65.21, -56.28	10.1 km	N	—
TK237	09JD073-09JD082	-66.05, -50.97	-65.89, -50.89	-66.05, -50.97	-65.89, -50.89	10.2 km	N	—
TK238	09JD076-09JD089	-66.80, -46.21	-66.78, -46.91	-66.80, -46.21	-66.78, -46.91	6.8 km	N	—

and 2008 cruise. Figure 4.6b portrays the Scotia Sea and Weddell Sea during the 2009 cruise. The Antarctic peninsula land mass is outlined at the bottom-left of both images. The sea ice extent has been marked with hand-drawn lines. Notice how the glacial continent and icebergs have the greatest backscatter signatures, sea ice has a moderate radar return, and sea water is characterized by varying low σ° values.

4.7 Discussion

Validating iceberg positions in the MERS Antarctic iceberg database is accomplished by correlating iceberg positions using high-resolution imagery from the NIC and other sources. An example of a SeaWinds backscatter image and collocated MODIS optical image reported by the NIC of iceberg C19a is displayed in Fig. 4.7. Similarly, high-resolution images of iceberg A22a are displayed in Fig. 4.8. Figures 4.8a-d correspond to SeaWinds h-pol backscatter images on 2006 Julian day 110, 2006 Julian day 303, 2007 Julian day 064, and 2007 Julian day 152. Figures 4.8e-h correspond to an infra-red image from the Defense Meteorological Satellite Program (DMSP), an optical photograph from the Moderate-Resolution Imaging Spectroradiometer (MODIS), a near-infra-red image from the Advanced Very High Resolution Radiometer (AVHRR), and an optical photography from astronauts on the International Space Station (ISS) on the same days. Because the ISS photograph was shot with a hand-held camera at a highly oblique angle, iceberg dimensions in the photograph may be slightly exaggerated but I note the similarities in overall shape between the photograph and the corresponding SeaWinds image.

Iceberg A22a is observed in Fig. 4.8a as the high-backscatter target in the center. A likely melt event between 2006 Julian day 110 and 303 likely changed the dielectric of the iceberg's surface, reducing backscatter and causing iceberg A22a to appear as bright as nearby sea ice in Fig. 4.8b. Fig. 4.8f gives a higher-resolution look of the nearby sea ice. Similarly, the backscatter reduction in Fig. 4.8c is likely caused by surface melt. In Fig. 4.8d, melt conditions have abated and the high-backscatter profile of iceberg A22a is observed once more.

As mentioned in Section 3.5.2, during periods of rapid iceberg movement, a time delay between when SeaWinds radar measurements are collected and when iceberg positions are analyzed and reported may result in discrepancies between the reported and the actual iceberg positions. During the NSF cruises, this delay ranged between 12-30 hours, resulting in iceberg position dis-

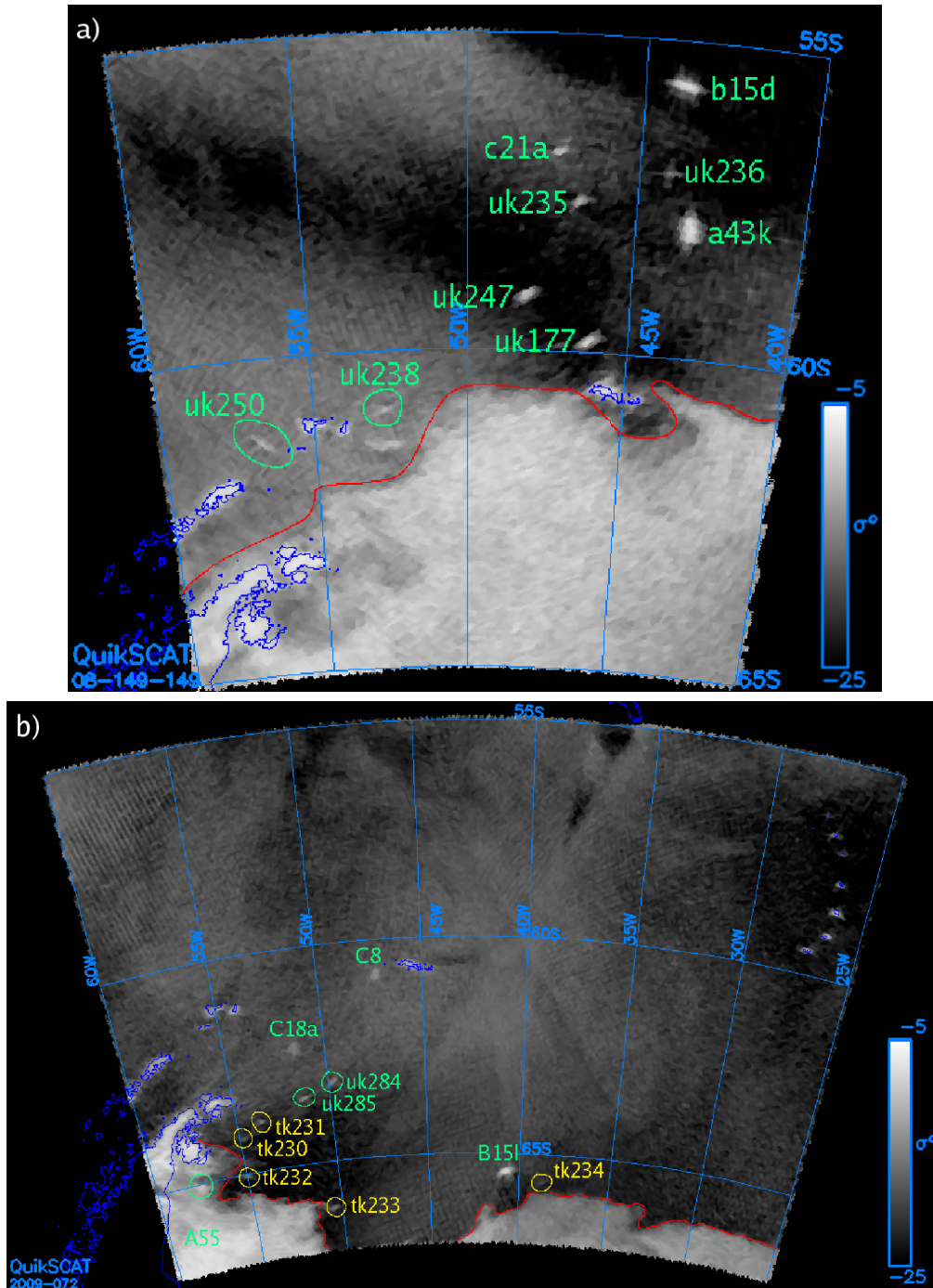


Figure 4.7: Custom 24-hour SIR images created from SeaWinds h-pol backscatter measurements for the NSF Antarctic cruises. These images were included in iceberg position reports during the NSF Antarctic cruises on (a) 2008 Julian day 149 and (b) 2009 Julian day 72. High, medium, and low-backscatter regions are characteristic of glacial ice, sea ice, and sea water, respectively. The positions of Antarctic icebergs and temporary contacts are labeled. The Antarctic peninsula land mass is outlined at the bottom-left of both images. Sea ice extent is also indicated with hand-drawn lines.

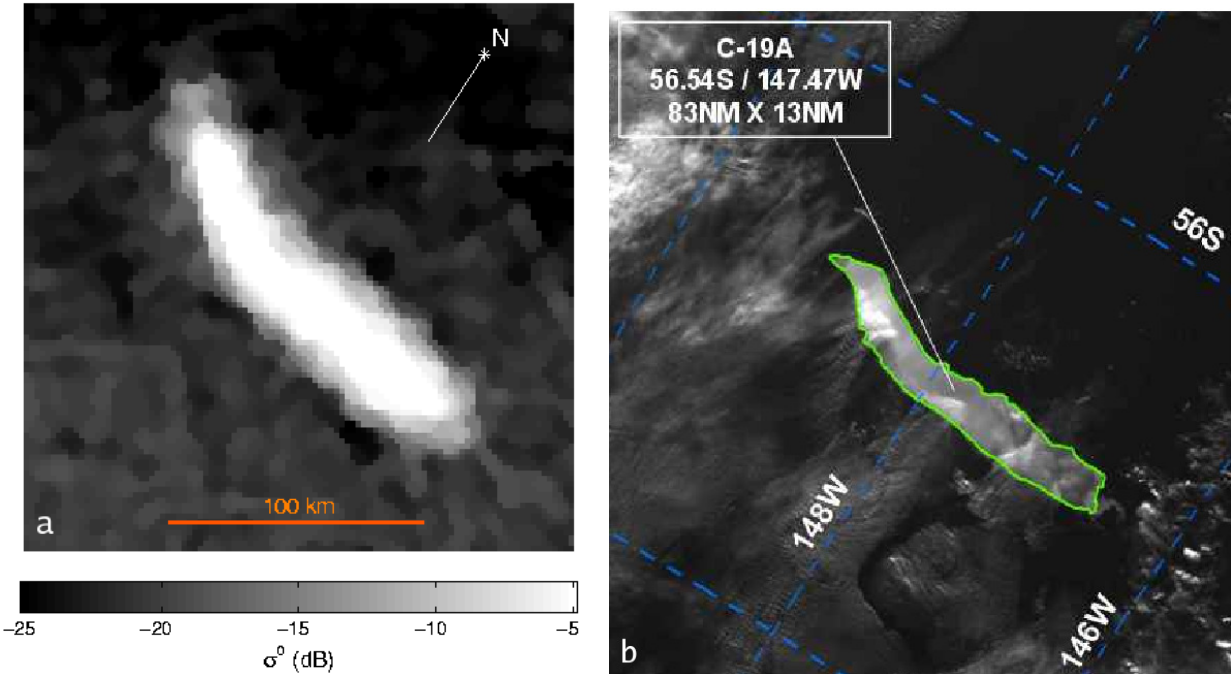


Figure 4.8: Images of iceberg C19a on 2008 Julian day 170 from a) the SeaWinds scatterometer and b) MODIS (an optical imager). Annotation in (b) performed by the NIC.

crepancies up to 25 km. Because ocean currents are the dominant factor influencing free-floating iceberg movement [43,45], NRT iceberg movement was compensated for by analyzing nearby and recent iceberg movement patterns. Iceberg locations were estimated given the last known iceberg position and velocity to enable ship interception and navigation.

4.8 Conclusion

Even though SeaWinds was never designed to track icebergs, our results demonstrate the utility of using SeaWinds measurements in developing an iceberg position database and in tracking icebergs in real-time. Iceberg positions have been validated by using collocated high-resolution satellite imagery and by navigating cruise ships to physically intercept several large tabular icebergs in the Weddell and Scotia Seas during three NSF Antarctic cruises [1, 8]. While QuikSCAT is no longer operational, other scatterometers can also be used to reliably track icebergs in the future.

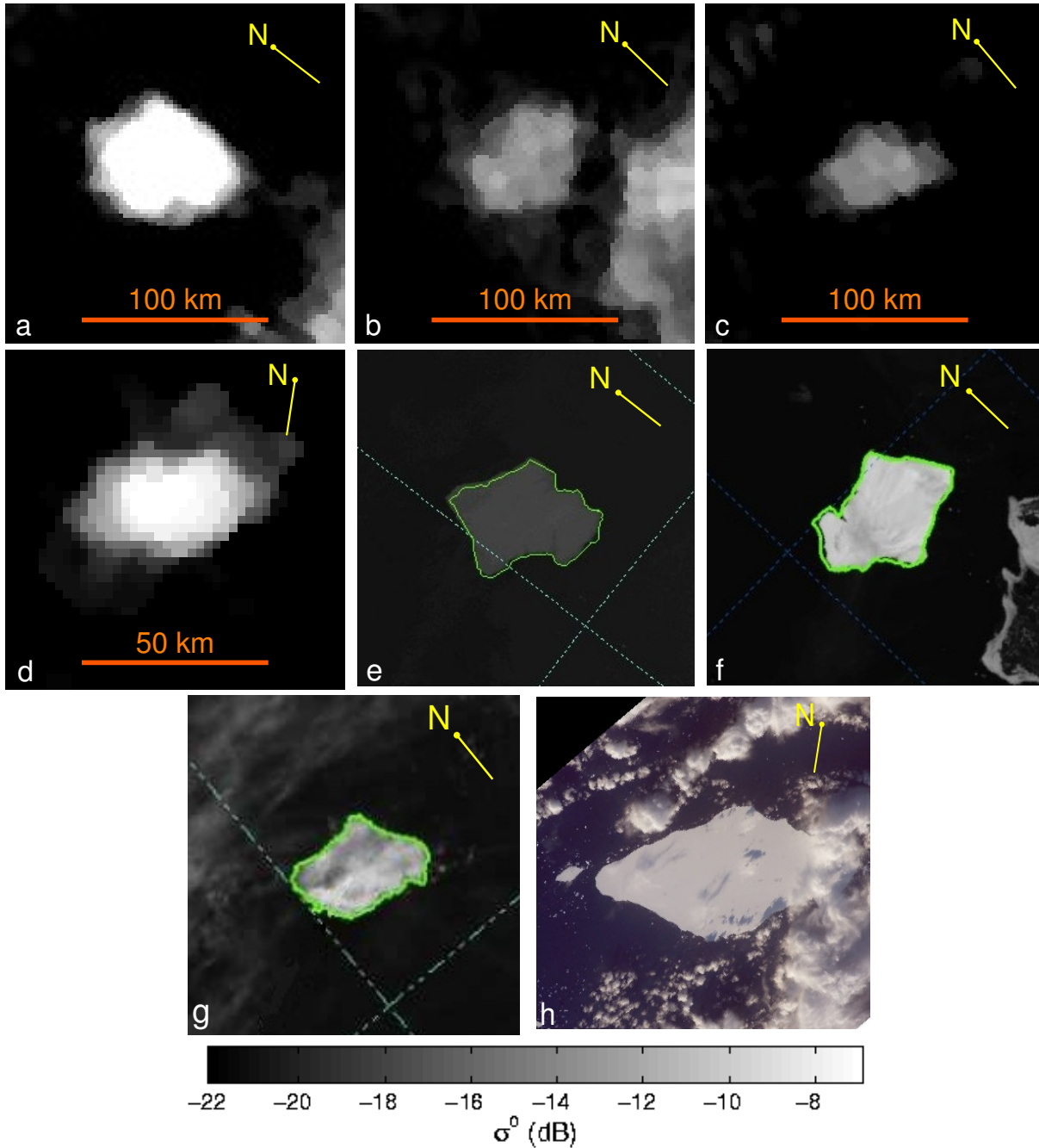


Figure 4.9: Images of iceberg A22a from the SeaWinds scatterometer and other high-resolution sensors. Figures 4.8a-d correspond to SeaWinds h-pol backscatter SIR images on 2006 Julian day 110, 2006 Julian day 303, 2007 Julian day 64, and 2007 Julian day 152. Figures 4.8e-h correspond to a DMSP IR image on 2006 Julian day 110, a MODIS image on 2006 Julian day 303, an AVHRR image on 2007 Julian day 64, and an optical photograph taken by astronauts on the ISS on 2007 Julian day 152 (compliments of NASA). The bright area at the right of (b) is due to the sea-ice edge. (b) and (c) appear darker than (a) and (d) due to surface melt conditions on these days. The colorbar at the bottom corresponds to (a-d). Annotation in (e-g) performed by the NIC. (e-g) were obtained from the NIC. (h) was obtained from NASA.

Chapter 5

Estimating Iceberg Size and Orientation

5.1 Introduction

This chapter extends the analysis of SeaWinds iceberg observations to include iceberg major-axis length, minor-axis length, and rotational orientation via automated maximum-likelihood (ML) estimation techniques. This study presents an iceberg model to characterize iceberg dimensions and develops both an image-based and a measurement-based approach to estimate the parameters of the iceberg model from SeaWinds backscatter data. Objective functions for each case are developed. Simulation is employed to explore and compare the effectiveness of each algorithm. Finally, the algorithms are explored via a case study of iceberg A22a. Subsequent image-based and measurement-based estimates are compared with estimates extracted from high-resolution imagery and reports collected by the United States National Ice Center (NIC).

This chapter is organized as follows: Section 5.2 reviews pertinent information about the SeaWinds instrument and corresponding high-resolution image products used to track icebergs. Section 5.3 presents the model used to characterize size and shape of icebergs. Section 5.4 outlines the objective functions for both the image-based and measurement-based estimates. Section 5.5 describes the implementation for both algorithms in both a simulation and in a case study. Section 5.6 discusses trade-offs in both estimation approaches, and Section 5.7 concludes.

5.2 Background

Previously, various studies have been performed using SeaWinds SIR images to estimate iceberg parameters. One approach estimates iceberg position using a subjective, manual process along with previous location information to track daily iceberg position in SIR images [50]. Because it requires human input, this methodology is time-intensive and contains errors related to the competency level and experience of the analyst. In a second historical approach, iceberg position

is extracted from daily SIR imagery using known iceberg statistics via a correlation method [46]. Previously, information regarding iceberg size has primarily only been obtainable from high-resolution optical imagery which has limited spatial and temporal coverage, suffers from cloud interference, and depends on external illumination. In this study I am interested in the inverse of the problem presented in [46], i.e. I estimate fundamental iceberg characteristics such as position, shape, and size given estimates of the previous position.

A particular methodology is based on using daily SeaWinds SIR images. Consider a backscatter image that contains an iceberg such that only the iceberg and the immediately surrounding background is visible. I am interested in classifying each pixel in the image as either corresponding to an iceberg or a non-iceberg medium. Backscatter images of the Southern Ocean primarily consist of open water, sea ice, and glacial ice. If the backscatter values corresponding to the iceberg and the background are relatively homogeneous, then a classification scheme such as a simple Neyman-Pearson hypothesis test can be used to classify each resolution cell. The resulting binary image can then be analyzed to determine overall iceberg shape and size. Troglia [51], in mapping craters in images, fit a model to a binary image. The estimates of the model were the estimates of the crater size. The same approach can be used for icebergs. While this thresholding approach is numerically efficient, its effectiveness varies with the noise level in backscatter images. Furthermore it is limited to homogeneous scenes and does not work well when the iceberg is near the sea-ice edge. Consequently, a more robust estimation methodology is needed to estimate iceberg size and shape using SeaWinds SIR images.

An elliptical model to describe the size and shape of an iceberg is proposed because it has a simple construction with few parameters and, to first order, it conforms to the general shape of large tabular icebergs [52–54]. Furthermore I propose using SeaWinds data to estimate the parameters of this model, specifically major-axis length, minor-axis length, and angle of orientation. There are two potential levels of SeaWinds data that can be used in the estimation process, the previously-mentioned SIR backscatter images and the raw SeaWinds measurements. Consequently, two model-based estimation approaches are proposed: one based on images and the other based on the raw data. The elliptical model used to describe iceberg size and shape is developed in Section 5.3. The approaches used to estimate model parameters are derived in Section 5.4.

5.3 Iceberg Model

This section develops the model used to characterize the top-down shape of large tabular icebergs. As previously mentioned, a generalized elliptical model is chosen because it is a simple construction with few parameters and, to first order, it reflects the general top-down shape of large tabular icebergs [52–54]. The iceberg backscatter is modeled as nearly constant over an elliptical shape with the edges of the shape smoothed via a simple spatial window. This results in an elliptically-shaped bump with slightly rounded edges. Formally, a simple analytic form for spatially modeling the backscatter profile of a large tabular iceberg is

$$\sigma^\circ(x, y, \vec{\alpha}) = (C - B) \cdot \exp\left\{-\left(|a|^p + |b|^p\right)^{\frac{n}{p}}\right\} + B \quad (5.1)$$

where

$$a = \frac{(x - \mu_x) \cos(\theta) + (y - \mu_y) \sin(\theta)}{\rho_{ma}}$$

and

$$b = \frac{(x - \mu_x) \sin(\theta) - (y - \mu_y) \cos(\theta)}{\rho_{mi}}$$

where x and y are the free-space indices of the 2-dimensional grid on the Earth's surface. In Eq. 5.1, the variable C defines the center backscatter value corresponding to glacial ice, and B is the background backscatter value. The parameter n controls the sharpness of the transition between C and B where a larger n results in a smaller transition band. Variables μ_x and μ_y define the center with respect to the local frame. Parameters ρ_{ma} and ρ_{mi} correspond to the length of the major and minor axes, respectively. The variable θ is the angle of orientation of the major axis with respect to the local frame where 0° corresponds to horizontal position and a positive increasing angle corresponds to clockwise motion. The super-ellipse parameter p controls the squareness of the ellipse. Note that functionally, p is only required to be positive, however for purposes of shape estimation, there is a potential shape ambiguity between models when p is unity and when p is large. Therefore, to prevent geometric ambiguity and for computational efficiency, p is limited to the range $p \in [1, 2]$. The model parameters in Eq. 5.1 constitute $\vec{\alpha}$, the model parameter vector where $\vec{\alpha} = [C, B, n, p, \mu_x, \mu_y, \rho_{ma}, \rho_{mi}, \theta]$.

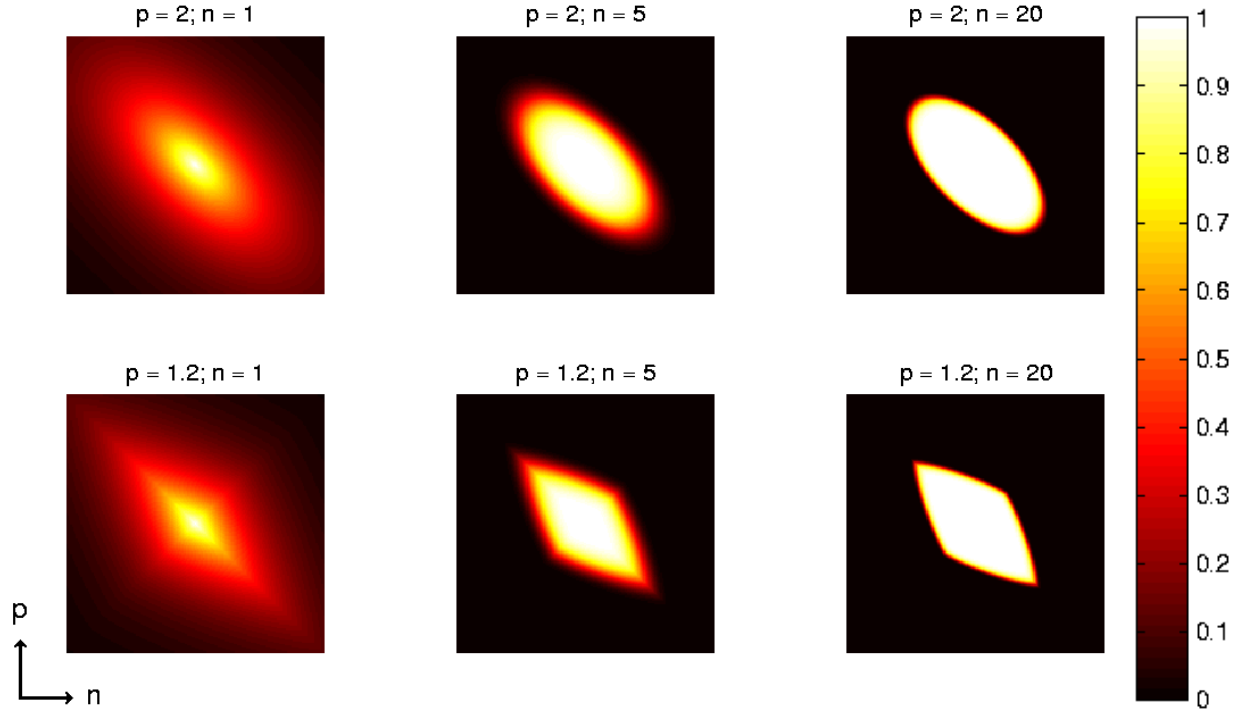


Figure 5.1: Iceberg model (Eq. 5.1) plotted for various realizations of $\vec{\alpha} = [1, 0, n, p, \mu_x, \mu_y, 2 \cdot \rho_{mi}, \rho_{mi}, 45^\circ]$ where n and p are varied with μ_x and μ_y chosen to correspond to the center of the region. The horizontal scale is arbitrary.

Example instances of Eq. 5.1 are displayed in Fig. 5.0 for $C = 1$, $B = 0$, variable n and p , arbitrary μ_x and μ_y , $\rho_{ma} = 2 \cdot \rho_{mi}$, and $\theta = 45^\circ$. I note that increasing n results in a more plateau-like model and decreasing p results in the elliptical model becoming more squared.

I find that icebergs of adequate size and sufficient backscatter contrast result in accurate model parameter estimates. However, if the size or contrast is insufficient, the solution space becomes ill-conditioned, potentially resulting in degenerate estimates. For instance, if an iceberg is rounded in shape, the major-axis length and minor-axis length are similar in value and the angle estimate may be ill-conditioned. Also, if an iceberg's size reduces to the order of the size of the ground illumination footprint, image contrast decreases. The backscatter contrast necessary for successful parameter estimation is discussed in Section 5.5.1. Degenerate estimation cases and ways to test for degenerate cases *a priori* are discussed in Section 5.6.

5.4 Estimation Algorithm

To estimate the position, shape, and rotational orientation of tabular icebergs using the model, two estimation methodologies are presented in this section. In the first, iceberg model parameters are derived from SeaWinds SIR images. In the second, the parameters are estimated directly from raw SeaWinds measurements without forming an image. These two approaches are referred to as the image-based (IB) and measurement-based (MB) estimation approaches, respectively. Both approaches have advantages and limitations. First, image-based estimation is explored. Next, measurement-based estimation is developed, then the two algorithms are compared. Last, assumptions and implications inherent from using the iceberg model in the estimation process are discussed.

5.4.1 Image-based Estimation

To estimate iceberg size and rotational orientation from the SeaWinds backscatter images, I use the standard enhanced-resolution SeaWinds h-pol SIR backscatter images as input. Because a SIR image consists of a combination of measurements, each pixel backscatter value σ_{pix}° is a function of the raw measurements described in Eq. 2.3. The backscatter at each pixel may be expressed as a combination of a true pixel-wise signal power and additive noise, i.e. $\sigma_{pix}^{\circ} = \sigma_{pix,t}^{\circ} + v$ where v is the effective noise. Although iceberg parameters are estimated over a temporal window of 24 hours, $\sigma_{pix,t}^{\circ}$ is considered a constant in the estimation process. The corresponding probability distribution function of σ_{pix}° can be modeled as

$$P(\sigma_{pix}^{\circ} | \sigma_{pix,t}^{\circ}) = \frac{1}{\sqrt{2\pi}\xi_{pix}} \exp \left\{ -\frac{(\sigma_{pix}^{\circ} - \sigma_{pix,t}^{\circ})^2}{2\xi_{pix}^2} \right\} \quad (5.2)$$

where ξ_{pix}^2 is the variance of σ_{pix}° and is computed in the SIR reconstruction process [20]. I estimate $\sigma_{pix,t}^{\circ}$ using the iceberg model developed in Eq. 5.1 to select the model parameters $\vec{\alpha}$ that maximize the probability of σ_{pix}° given $\sigma_c^{\circ}(x, y, \vec{\alpha})$.

The estimation process minimizes the difference between the measured backscatter and the model-based construction by adjusting model parameters. For a single pixel (x_o, y_o) , this probability distribution is

$$P(\sigma_{pix}^\circ(x_o, y_o) | \sigma_c^\circ(x_o, y_o, \vec{\alpha})) = \frac{1}{\sqrt{2\pi}\xi_{pix}(x_o, y_o)} \exp \left\{ -\frac{[\sigma_{pix}^\circ(x_o, y_o) - \sigma_c^\circ(x_o, y_o, \vec{\alpha})]^2}{2\xi_{pix}^2(x_o, y_o)} \right\}. \quad (5.3)$$

For multiple pixels and assuming each pixel is mutually independent of adjacent pixels, the joint distribution of $\sigma_{pix}^\circ(x, y)$ given $\sigma_c^\circ(x, y, \vec{\alpha})$ is a joint distribution of independent Gaussian random variables and has the form

$$P(\vec{\sigma}_{pix}^\circ(x, y) | \vec{\sigma}_c^\circ(x, y, \vec{\alpha})) = \prod_{x, y \in X, Y} P(\sigma_{pix}^\circ(x, y) | \sigma_c^\circ(x, y, \vec{\alpha})) \quad (5.4)$$

where $\vec{\sigma}_{pix}^\circ(x, y)$ and $\vec{\sigma}_c^\circ(x, y, \vec{\alpha})$ represent vectorized forms of $\sigma_{pix}^\circ(x, y)$ and $\sigma_c^\circ(x, y, \vec{\alpha})$ and where (X, Y) spans the image of estimation.

Maximizing Eq. 5.4 yields a maximum-likelihood estimate. However, for practical purposes, I maximize the log of Eq. 5.4. The image-based ML estimate of $\vec{\alpha}$ may be expressed as

$$\vec{\alpha}_{IB}^* = \arg \max_{\vec{\alpha}} \{ \log P(\vec{\sigma}_{pix}^\circ(x, y) | \vec{\sigma}_c^\circ(x, y, \vec{\alpha})) \} \quad (5.5)$$

where $\vec{\alpha}_{IB}^*$ is the parameter vector that maximizes Eq. 5.4. Explicitly solving Eq. 5.5 and simplifying by removing constant terms yields

$$\vec{\alpha}_{IB}^* = \arg \min_{\vec{\alpha}} \sum_{x, y \in X, Y} \left[\frac{[\sigma_{pix}^\circ(x, y) - \sigma_c^\circ(x, y, \vec{\alpha})]^2}{\xi_{pix}^2(x, y)} + \ln(\xi_{pix}^2(x, y)) \right]. \quad (5.6)$$

However, low variances in our data cause the left term in brackets in Eq. 5.6 to occasionally become ill-conditioned. As a result, a variance-regularization term, λ_{IB} , is introduced so that Eq. 5.6 becomes

$$\vec{\alpha}_{IB}^* = \arg \min_{\vec{\alpha}} \sum_{x, y \in X, Y} \left[\frac{(\sigma_{pix}^\circ(x, y) - \sigma_c^\circ(x, y, \vec{\alpha}))^2}{\chi_{pix}^2(x, y)} + \ln(\chi_{pix}^2(x, y)) \right] \quad (5.7)$$

where $\chi_{pix}^2(x,y) = (1 - \lambda_{IB}) + \lambda_{IB} \cdot \xi_{pix}^2(x,y)$ where $\lambda_{IB} \in [0, 1]$. The $\lambda_{IB} = 0$ case corresponds to a least-squares objective function while $\lambda_{IB} = 1$ corresponds to the image-based maximum-likelihood case. I can vary λ_{IB} to allow us to select an estimation approach that lies between these two cases which can be useful to mitigate the adverse effects of low image contrast or image contamination. This is discussed further in Section 5.6.

Choosing $\vec{\alpha}$ to maximize the objective function provides the best fit in a maximum-likelihood sense for the parameters of the model, thereby yielding estimates of the size and orientation of the iceberg. By repeating this to produce a time-series of estimates, I obtain the evolution of the size and rotation of the iceberg.

5.4.2 Measurement-based Estimation

The measurement-based estimation approach uses the individual slice measurements and their associated spatial response functions directly without first forming an image. The measurement-based approach can be derived similarly to the image-based case (Eq. 5.2-5.7) if the pixel backscatter, $\sigma_{pix}^\circ(x,y)$, is replaced with the SeaWinds backscatter measurements, $\sigma^\circ(j)$, where j indexes the set of raw SeaWinds measurements; the modeled backscatter, $\sigma_c^\circ(x,y,\vec{\alpha})$, is replaced with a measurement-referenced model backscatter term, $\sigma_c^\circ(j,\vec{\alpha})$; and the pixel-based variance, $\xi_{pix}^2(x,y)$, is replaced with $\xi^2(j)$, the variance of $\sigma^\circ(j)$. The functional form for $\xi^2(j)$ is given in Eq. 2.5. Note that in the measurement-based approach, $\xi^2(j)$ can be chosen to be a function of either $\sigma^\circ(j)$ or $\sigma_c^\circ(j,\vec{\alpha})$. Due to computational complexity, I choose to use the former.

As previously mentioned, the variables $\sigma_{pix}^\circ(x,y)$ and $\sigma^\circ(j)$ are related through the SeaWinds antenna point-spread function introduced in Eq. 2.2. The point-spread function acts as a mathematical operator that samples the two-dimensional space spanned by $\sigma_{pix}^\circ(x,y)$ and produces backscatter values that lie in the backscatter space observed by SeaWinds. Using Eq. 2.2, variables $\sigma_c^\circ(x,y,\vec{\alpha})$ and $\sigma_c^\circ(j,\vec{\alpha})$ also share this relationship. Consequently, $\sigma_c^\circ(j,\vec{\alpha})$ can be interpreted as the backscatter value that results from projecting the j th SeaWinds antenna aperture onto the space spanned by the iceberg model.

Explicitly solving for the measurement-based ML model estimates, including regularization terms to mitigate the adverse effects of extreme values of $\xi^2(j)$, yields

$$\vec{\alpha}_{MB}^* = \arg \min_{\vec{\alpha}} \sum_j \left[\frac{(\sigma^\circ(j) - \sigma_c^\circ(j, \vec{\alpha}))^2}{\chi^2(j)} + \ln(\chi^2(j)) \right] \quad (5.8)$$

where $\vec{\alpha}_{MB}^*$ is the parameter vector that minimizes the measurement-wise ML objective function and $\chi^2(j) = (1 - \lambda_{MB}) + \lambda_{MB} \cdot \xi^2(j)$ where $\lambda_{MB} \in [0, 1]$. Similar to the image-based approach, the case where $\lambda_{MB} = 0$ corresponds to a least-squares objective function and the case where $\lambda_{MB} = 1$ corresponds to the unaltered measurement-based maximum-likelihood case. I can vary λ_{MB} to allow us to select an estimation approach that lies between these two cases which is helpful in mitigating the adverse effects of low variances. This is discussed further in Section 5.6.

Choosing $\vec{\alpha}$ to maximize the objective function yields the best fit in the maximum-likelihood sense for the parameters of the model from the raw backscatter measurements. Repeating this for a time-series of raw measurement sets, I obtain the measurement-derived temporal evolution of the size and rotation of the iceberg. Note that in the noise-free case, both Eq. 5.7 and 5.8 have a single maxima. However, in a noisy environment, neither Eq. 5.7 nor 5.8 is guaranteed to have a unique solution, therefore a search of the solution space is necessary.

5.4.3 Algorithm Comparison

Theoretical differences between the image-based and the measurement-based estimation methodologies are illustrated by expressing both approaches as optimization problems. The image-based estimation approach may be expressed as: minimize $\sum_{x,y \in X,Y} \frac{(\sigma_{pix}^\circ(x,y) - \sigma_c^\circ(x,y, \vec{\alpha}))^2}{\chi_{pix}^2(x,y)} + \ln(\chi_{pix}^2(x,y))$ [or equivalently maximize $P(\vec{\sigma}_{pix}^\circ | \vec{\sigma}_c^\circ(x,y, \vec{\alpha}))$] with respect to $\vec{\alpha}$ where $\chi_{pix}^2(x,y) = (1 - \lambda_{IB}) + \lambda_{IB} \cdot \xi_{pix}^2(x,y)$ and $\lambda_{IB} \in [0, 1]$.

The measurement-based estimation approach may be expressed as: minimize $\sum_j \frac{(\sigma^\circ(j) - \sigma_c^\circ(j, \vec{\alpha}))^2}{\chi^2(j)} + \ln(\chi^2(j))$ [or equivalently maximize $P(\vec{\sigma}^\circ | \vec{\sigma}_c^\circ(j, \vec{\alpha}))$] with respect to $\vec{\alpha}$ subject to $\vec{\sigma}_c^\circ(j, \vec{\alpha}) = A(\vec{\sigma}_c^\circ(x,y, \vec{\alpha}))$ where $A(\cdot)$ is the linear sampling operator that maps the solution space spanned by the model to the observation space sampled by SeaWinds via the antenna impulse-response function (Eq. 2.2) and $\chi^2(j) = (1 - \lambda_{MB}) + \lambda_{MB} \cdot \xi^2(j)$ where $\lambda_{MB} \in [0, 1]$.

The introduction of regularization terms enable us to trade off between information usage and problem conditioning. It changes the underlying problem so that the estimates are the projection of an underlying solution onto the spaces spanned by $\vec{\sigma}_c^\circ(x, y, \vec{\alpha})$ and $A(\vec{\sigma}_c^\circ(x, y, \vec{\alpha}))$, respectively. Maximizing λ_{IB} and λ_{MB} ensures minimal projection error. Choosing λ_{IB} and λ_{MB} small mitigates the adverse effects of small variance terms, resulting in better-conditioned solution spaces. To illustrate the dependence of regularization on each estimation approach, multiple values of λ_{IB} and λ_{MB} are selected and compared in Section 5.5.

Both estimation approaches are constrained by the model. Since in practice, large tabular icebergs tend to have elliptical-like shapes, I generally obtain good results. The fact that the model does not precisely describe the actual iceberg shape is not critical for determining the relative orientation and rotation angle which are of interest to scientists studying ocean currents that affect iceberg motion.

5.5 Performance

To explore the performance of both the image-based and model-based iceberg estimates, simulation is first employed. The utility of both approaches is then analyzed in a case study of iceberg A22a using actual data. Iceberg nomenclature is standardized by the United States National Ice Center (NIC) where the name begins with a letter corresponding to the quadrant where it was first detected, followed by an incremental number. As icebergs fragment, each fragment name is appended with a letter [55]. Iceberg size and orientation estimates are analyzed using collocated high-resolution imagery and reports collected by the NIC. A time-series of extracted iceberg parameter estimates is also presented.

5.5.1 Simulation

Simulation is employed to analyze the effectiveness of both the image-wise and measurement-wise estimates. First, a synthetic truth image is generated using the iceberg model with $\vec{\alpha}$ parameters: $C = -9$ dB, $B = -21$ dB, $n = 20$, $p = 1.8$, $\rho_{ma} = 35$ km, $\rho_{mi} = 21$ km, and $\theta = 45^\circ$. Actual SeaWinds antenna responses are used in simulation. The μ_x and μ_y location parameters correspond to a latitude and longitude of 60.1888° S and 51.3135° W on Julian day (JD) 100 of 2006.

Table 5.1: Simulation results of the image-based and measurement-based ML estimates of the major axis, minor axis, and angle of orientation from Fig. 5.1. Both sets of estimates were calculated using the same noise realization.

	True Value	Image-base Estimates	Measurement-based Estimates
ρ_{ma} (km)	70.0	69.96	71.48
ρ_{mi} (km)	42.0	41.98	43.22
θ ($^{\circ}$)	45.0	45.0	47.6

The truth image is sampled by projecting the SeaWinds antenna response patterns from two passes of the SeaWinds sensor onto the truth image, generating simulated truth backscatter values σ_i° . Observational boundaries are chosen to include two SeaWinds passes where each pass contains one forward look and one aft look, resulting in four total looks. Each look corresponds to approximately 300 slice measurements, resulting in a total of approximately 1200 backscatter measurements. To generate noisy σ° measurements, Monte Carlo noise is added to the σ_i° measurements using Eq. 2.3 where the α , β , and γ parameters correspond to the expected values for each observation.

For the image-based estimation approach, the noisy σ° values are processed into a corresponding SIR image and this backscatter image is used as the input into the image-based estimation process. For the measurement-based simulation, the noisy σ° values are used directly in the estimation process.

Figure 5.1a illustrates a simulated truth image where the iceberg is centered in the image. The 6 dB-contour of the forward and aft-looking slice aperture responses over the iceberg for a single pass are displayed in Figs. 5.1b and c. The SIR image created from the truth dataset is displayed in Fig. 5.1d. The SIR image created from $\vec{\sigma}^{\circ}$ is displayed in Figs. 5.1e, f, and g. Elliptical shapes based on iceberg size and orientation estimates are superimposed on Figs. 5.1f and g where the former corresponds to the image-based estimates and the latter to the measurement-based estimates. Values for both estimates are presented in Table 5.0. Note that both approaches perform relatively well, with the image-based estimates marginally closer to the true parameters.

To better analyze the utility of both estimation approaches, it is helpful to study the behavior of both methodologies given multiple noise realizations. The sensitivity of each approach is

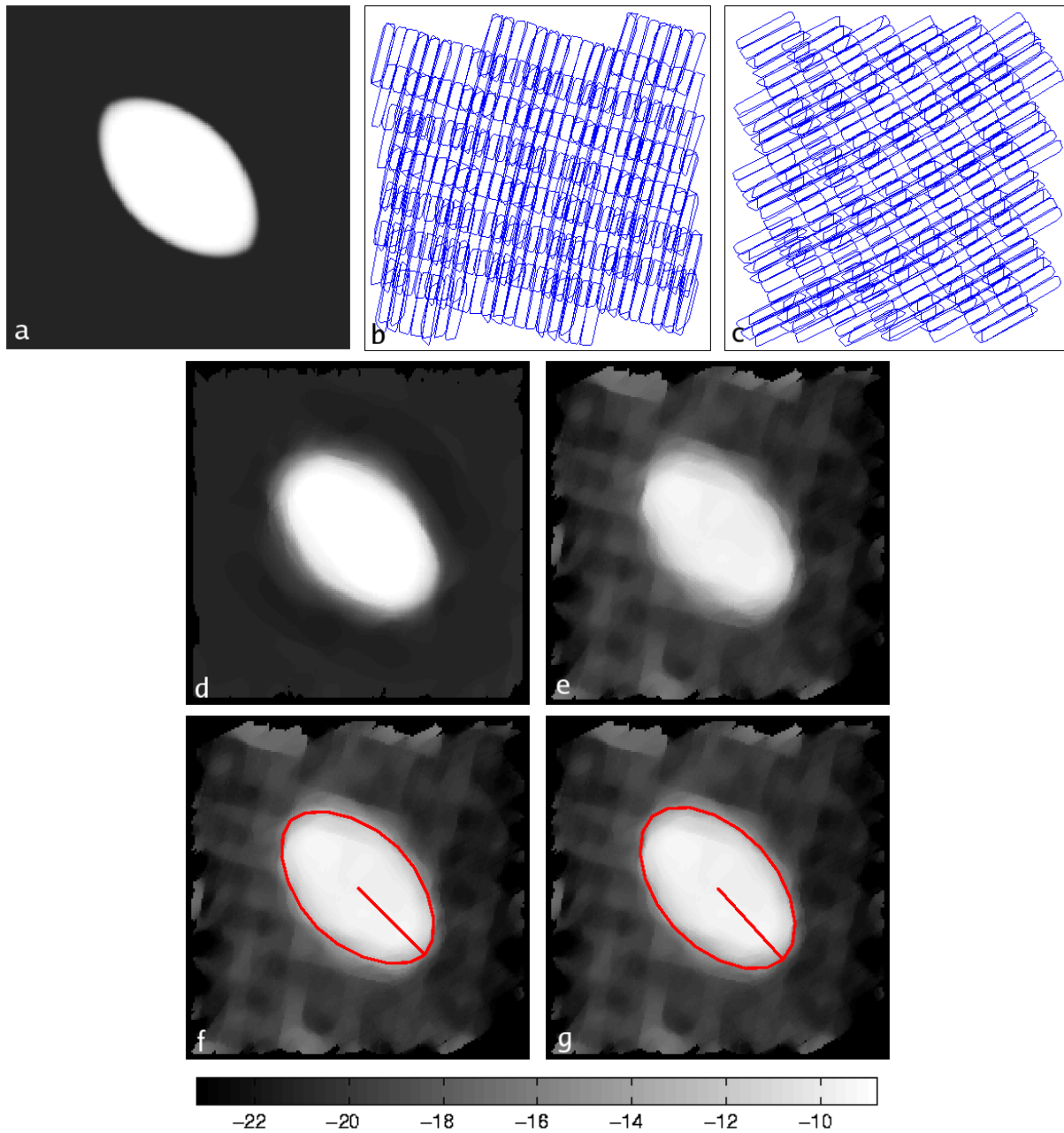


Figure 5.2: Simulation results of estimating the size and orientation of an elliptical iceberg. a) The true iceberg model. b) A 6 dB-contour plot of the forward-looking SeaWinds slice measurements for a single pass. There are approximately 300 slices, each approximately 25 x 6 km in dimension. c) Aft-looking slice measurements for the same pass. d) SIR image created from noise-free backscatter values generated by projecting the antenna response functions from (b) and (c) onto the truth image (a). e) SIR image created from the noisy backscatter values. f) SIR image from (e) with an elliptical shape superimposed based upon image-based iceberg estimates. g) SIR image from (e) with an elliptical shape superimposed based upon measurement-based estimates. The colorbar is backscatter in dB. Images are approximately 125 x 125 km.

Table 5.2: Statistics comparing the image-based and measurement-based ML estimation approaches in simulation with corresponding truth data. Statistics were created using 100 independent noise realizations.

Estimate Type	λ	ρ_{ma} (km)		ρ_{mi} (km)		θ ($^\circ$)	
		Mean	STD	Mean	STD	Mean	STD
True	—	70.00	—	42.00	—	45.00	—
IB	0.00	69.96	0.029	41.98	0.021	45.00	0.011
IB	0.50	69.98	0.022	42.00	0.015	45.00	0.011
IB	0.75	70.00	0.025	42.00	0.017	45.00	0.016
IB	0.90	69.98	0.027	42.00	0.019	45.00	0.013
IB	0.99	70.00	0.022	42.00	0.013	45.00	0.013
IB	1.00	70.00	0.036	42.00	0.025	44.99	0.017
MB	0.00	70.12	0.40	42.16	0.35	45.11	1.05
MB	0.50	69.92	0.26	42.12	0.23	44.98	0.41
MB	0.75	70.02	0.27	42.24	0.26	45.07	0.55
MB	0.90	70.00	0.26	42.04	0.22	45.03	0.51
MB	0.99	69.92	0.26	42.10	0.40	45.11	0.49
MB	1.00	71.28	0.88	44.76	1.8	46.19	2.93

analyzed by sweeping λ_{IB} and λ_{MB} . One hundred simulations are performed for each estimation approach where $\lambda_{IB} = \lambda_{MB} = [0, 0.5, 0.75, 0.9, 0.99, 1.00]$ and each has an independent noise realization. Noise realizations were generated using Eq. 2.1. The resulting statistics are presented in Table 5.1. Note that the mean of both estimation approaches are close to the true values of ρ_{ma} , ρ_{mi} , and θ . While the mean of both algorithms are comparable, the standard deviation of the IB and MB estimates differ by an order of magnitude with the IB approach out-performing the MB algorithm.

From Table 5.1, the statistics for the simulated IB estimates show minimal variation with λ_{IB} ; however, choosing $\lambda_{IB} = 0.99$ maximizes information usage with minimal associated projection error. Similarly, choosing $\lambda_{MB} = 0.90$ provides an appropriate trade-off by ensuring small overall variance while preserving maximum information usage.

In addition to observation noise, estimate accuracy is a function of backscatter contrast between the iceberg and surrounding medium. Simulation is used to quantify this relationship using the simulation parameters mentioned earlier. To gain insight into the accuracy of the iceberg size model with respect to multiple model shape parameters, estimation accuracy is quantified using a weighted error metric derived from the major-axis length, minor-axis length, and angle of

rotational orientation parameters such that

$$\% \text{ Error} = \frac{1}{3} \left(\left| \frac{\rho'_{ma} - 35 \text{ km}}{35 \text{ km}} \right| + \left| \frac{\rho'_{mi} - 21 \text{ km}}{21 \text{ km}} \right| + \left| \frac{\theta' - 45^\circ}{180^\circ} \right| \right) \cdot 100 \quad (5.9)$$

where ρ'_{ma} , ρ'_{mi} , and θ' are the model parameter estimates. To deal with the 180° model direction ambiguity, Eq. 5.9 is calculated using the unwrapped θ' about 180° to minimize the difference in the third term. The results are displayed in Figs. 5.2 and 5.3 for the IB and MB cases, respectively. The estimation error is inversely related to backscatter contrast. Note that the average error in both the IB and MB cases is smaller when λ_{IB} and λ_{MB} are less than unity, supporting the earlier observation that both estimation approaches benefit from regularization.

5.5.2 Case Study

Both estimation techniques are applied to SeaWinds backscatter measurements of iceberg A22a. Iceberg A22a is selected because it is non-circular, it is visible for an extended period of time away from sea ice, and because collocated high-resolution optical imagery is available.

Three days are highlighted in this study: 2006 Julian days 110 and 303 and 2007 Julian day 64. For these days, annotated high-resolution images of iceberg A22a are available from DMSP, MODIS, and AVHRR. For the first day, the high-res. image is displayed in Fig. 5.4a. Corresponding SeaWinds backscatter images for the first day are displayed in Figs. 5.4b and c. Elliptical shapes based on iceberg size and orientation estimates are superimposed on the backscatter images where the image-based estimate ($\lambda_{IB} = 0.99$) corresponds to the former and the measurement-based estimate ($\lambda_{MB} = 0.90$) to the latter. Similarly, high-res. images for the second and third days as well as corresponding SIR images with elliptical shapes are displayed in Figs. 5.5 and 5.6, respectively. Associated quantitative measurements are compared with NIC reports in Table 5.3.

In Table 5.3, note that two values are extracted for the minor axis from the high-resolution images. The first minor axis estimate intersects the midpoint of the major axis at a 90° angle. The second is the largest possible value of the minor axis, without constraints. The SeaWinds image-based and measurement-based estimates fall between these two minor-axis lengths. Also, note the consistency of iceberg orientation between the high-resolution images and the SeaWinds estimates.

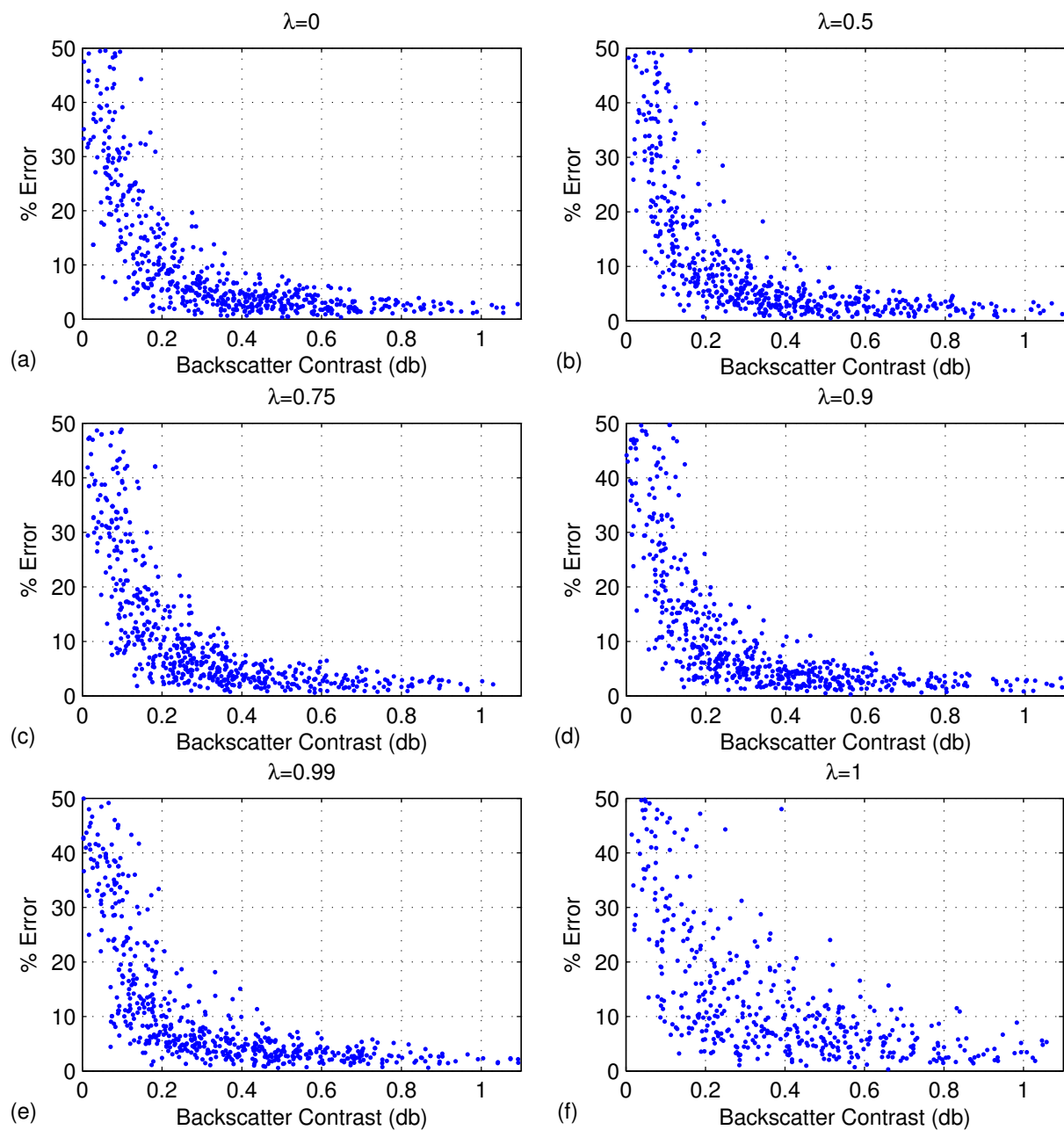


Figure 5.3: Monte Carlo simulation results of the accuracy of IB iceberg parameter estimates with respect to the backscatter contrast between the iceberg and the surrounding medium for varying λ_{IB} . a-f) corresponds to $\lambda_{IB} = [0 \ 0.5 \ 0.75 \ 0.9 \ 0.99 \ 1]$, respectively. The percent error metric is computed using the estimated major-axis length, minor-axis length, and angle of rotational orientation parameters according to Eq. 5.9.

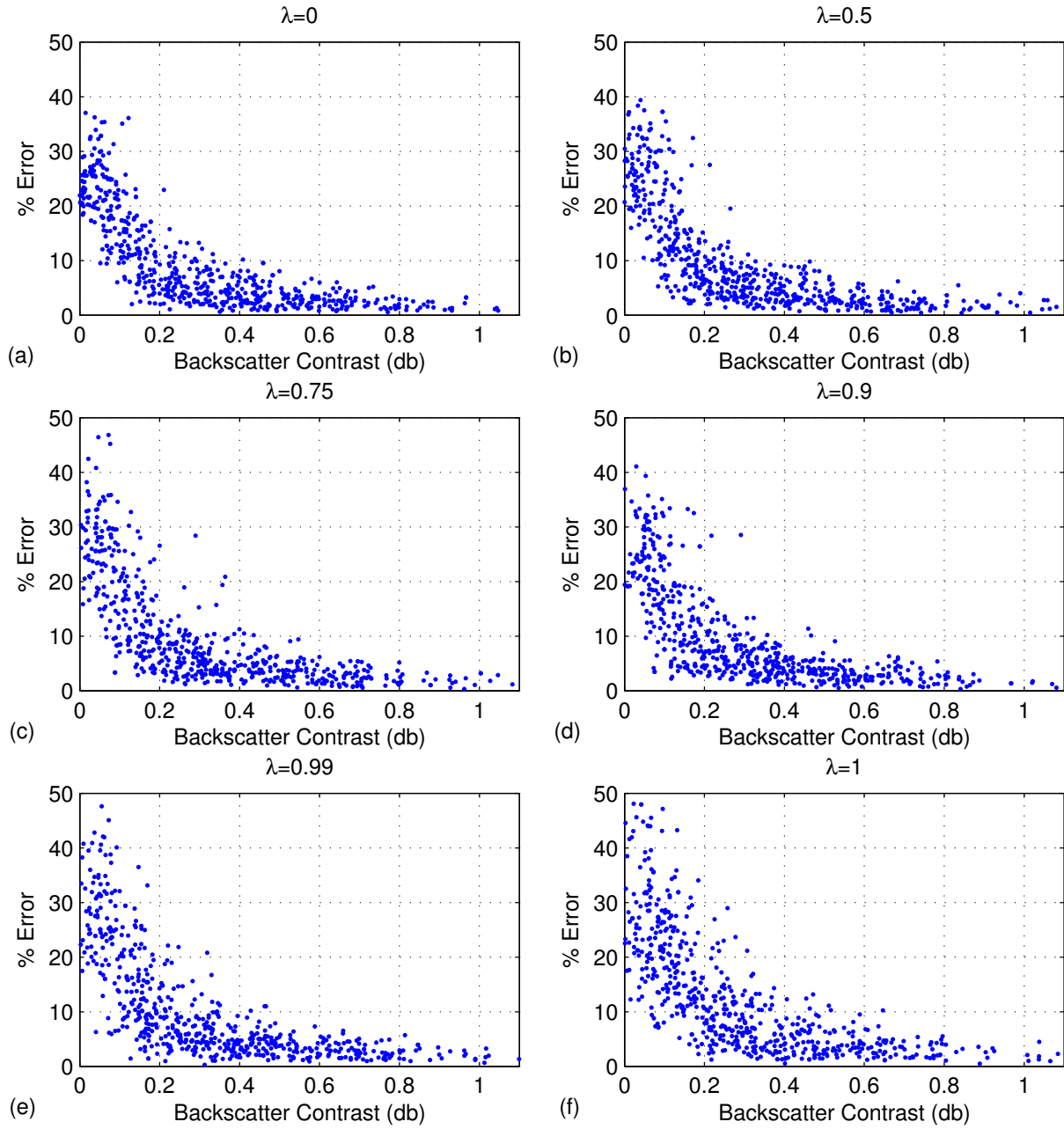


Figure 5.4: Monte Carlo simulation results of the accuracy of MB iceberg parameter estimates with respect to the backscatter contrast between the iceberg and the surrounding medium for varying λ_{MB} . a-f) corresponds to $\lambda_{MB} = [0 \ 0.5 \ 0.75 \ 0.9 \ 0.99 \ 1]$, respectively. The percent error metric is computed using the estimated major-axis length, minor-axis length, and angle of rotational orientation parameters according to Eq. 5.9.

Table 5.3: Major axis, minor axis, and angle of orientation estimates of iceberg A22a using high-resolution (HR) imagery, estimates from SeaWinds data, and NIC reports. Angle of orientation is with respect to the image frame where horizontal is 0° and positive increasing is in the clockwise direction. For average error statistics with respect to values extracted from the high-res. images, see Table 5.3.

Estimates Type	λ	2006 Julian day 110			2006 Julian day 303			2007 Julian day 64		
		ρ_{ma} (km)	ρ_{mi} (km)	θ ($^\circ$)	ρ_{ma} (km)	ρ_{mi} (km)	θ ($^\circ$)	ρ_{ma} (km)	ρ_{mi} (km)	θ ($^\circ$)
HR	—	61.7	45.2-53.7	14	62.4	39.9-47.3	142	51.3	29.7-34.9	167
NIC	—	67.7	50.0	—	67.7	50.0	—	44.5	37.0	—
IB	0.00	65.4	50.4	11	63.8	47.6	137	56.2	35.6	171
IB	0.50	64.5	49.9	13	62.0	43.7	139	55.2	35.1	172
IB	0.75	64.8	50.0	14	62.0	43.7	139	55.2	35.0	172
IB	0.90	63.7	49.8	13	62.0	43.7	139	55.2	35.0	172
IB	0.99	64.0	49.9	14	62.0	43.7	139	55.1	34.9	172
IB	1.00	63.9	49.8	13	62.0	43.7	139	55.2	35.0	172
MB	0.00	65.8	48.6	7	73.1	47.5	149	61.7	35.7	171
MB	0.50	66.8	48.5	8	70.7	47.6	143	61.3	35.4	171
MB	0.75	69.6	50.7	12	70.6	47.7	143	61.4	35.4	171
MB	0.90	72.2	52.2	13	70.4	47.8	143	61.4	35.3	171
MB	0.99	72.3	44.7	8	70.7	48.6	143	61.3	35.4	171
MB	1.00	50.6	22.3	11	79.3	62.3	136	72.4	36.1	172

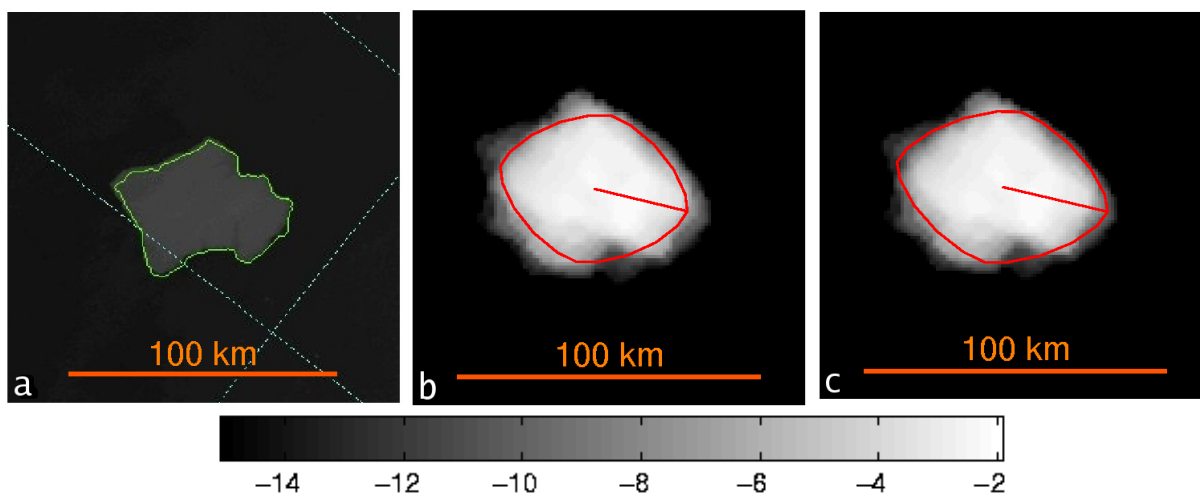


Figure 5.5: Images and parameter estimates of iceberg A22a on Julian day 110, 2006. a) DMSP IR image. b) Elliptical shape based on image-based estimates superimposed on the SeaWinds backscatter image. c) Elliptical shape based on measurement-based estimates superimposed on the SeaWinds backscatter image. Image is approximately 125×125 km. Colorbar is backscatter in dB. Iceberg perimeter marking in the high-res. image was performed by the NIC. For estimate comparison, see Table 5.3.

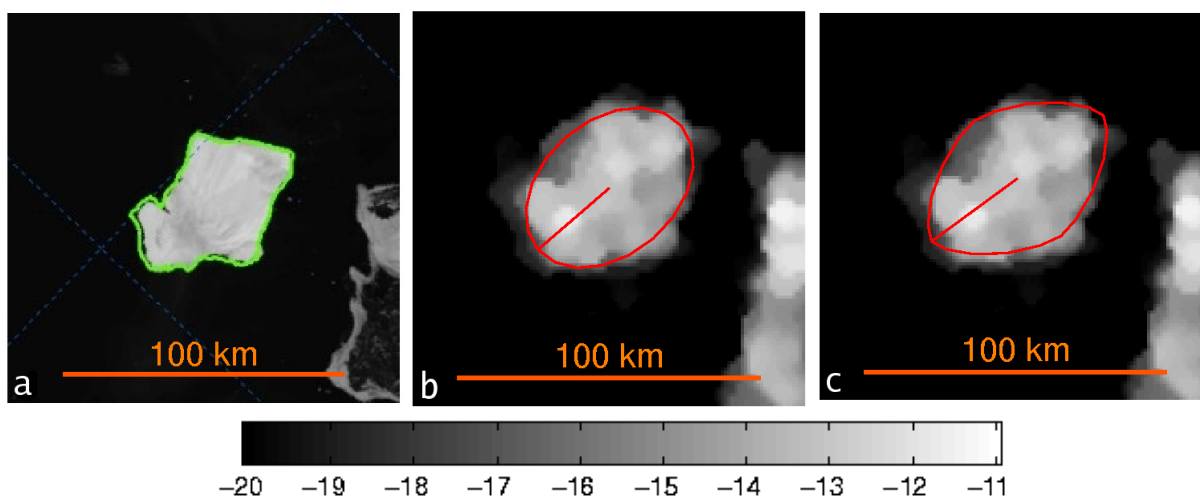


Figure 5.6: Images and parameter estimates of iceberg A22a on Julian day 303, 2006. a) MODIS image. b) Elliptical shape based on image-based estimates superimposed on the SeaWinds backscatter image. c) Elliptical shape based on measurement-based estimates superimposed on the SeaWinds backscatter image. Image is approximately 125×125 km. Colorbar is backscatter in dB. Iceberg perimeter marking in the high-res. image was performed by the NIC. For estimate comparison, see Table 5.3.

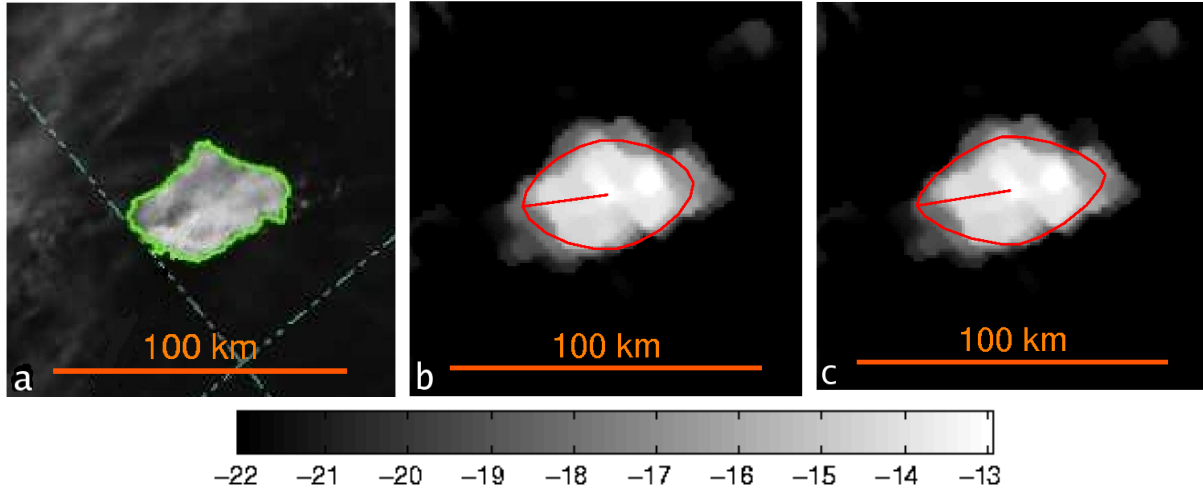


Figure 5.7: Images and parameter estimates of iceberg A22a on Julian day 64, 2007. a) AVHRR image. b) Elliptical shape based on image-based estimates superimposed on the SeaWinds backscatter image.. c) Elliptical shape based on measurement-based estimates superimposed on the SeaWinds backscatter image. Image is approximately 125×125 km. Colorbar is backscatter in dB. Iceberg perimeter marking in the high-res. image was performed by the NIC. For estimate comparison, see Table 5.3.

The average errors between the actual SeaWinds estimates and the values extracted from the high-resolution imagery are presented in Table 5.3. The average errors between parameters reported by the NIC and high-resolution data are also included in Table 5.3. Note that SeaWinds IB estimation errors show minimal variation with λ_{IB} , an observation consistent with simulation results. This behavior supports the selection of $\lambda_{IB} = 0.99$ in order to maximize information usage. Also note that the average error over all SeaWinds MB estimation error metrics is similar for $\lambda_{MB} \leq 0.9$ and increases for $\lambda_{MB} > 0.9$, demonstrating the need for regularization in the MB estimation approach.

5.5.3 Time-series

Applying this estimation approach to a time-series of SeaWinds measurements, I obtain the temporal evolution of the iceberg's axis and rotation. Both the image-based and the measurement-based estimation algorithms are applied to SeaWinds measurements of iceberg A22a from 2006 Julian day 50 to 2007 Julian day 276. During this period, iceberg A22a is detected in 553 of the 593 daily SIR images [7].

Table 5.4: Average errors of SeaWinds IB estimates, SeaWinds MB estimates, and NIC reports of the major-axis length, minor-axis length, and angle of rotational orientation with respect to high-resolution imagery of iceberg A22a on 2006 JD 110, 2006 JD 303, and 2007 JD 64. For underlying values, see Table 5.3.

Type	λ	ρ_{ma} (%) Avg Error	ρ_{mi} (%) Avg Error	θ (°) Avg Difference
NIC	—	10	4	—
IB	0.00	6	1	4
IB	0.50	4	0	3
IB	0.75	4	0	3
IB	0.90	4	0	3
IB	0.99	4	0	3
IB	1.00	4	0	3
MB	0.00	15	1	6
MB	0.50	14	1	4
MB	0.75	15	1	2
MB	0.90	17	1	2
MB	0.99	17	7	4
MB	1.00	29	31	5

I can directly use the daily iceberg estimates computed using the IB and MB approaches, however to mitigate noise and measurement uncertainty, time-averaging estimates is helpful. A weighted time-average of the daily estimates over a short temporal window (e.g., an Epanechnikov filter) reduces the estimate variance and provides a more accurate estimate of iceberg parameters.

SeaWinds IB and MB estimates of the major axis of iceberg A22a are displayed in Fig. 5.7. NIC estimates over the same interval are displayed in Fig. 5.8. To highlight general trends, each dataset is filtered using a 71-pt Epanechnikov filter, overlaid on each respective image. For comparison purposes, trend lines are displayed on Figs. 5.7 and 5.8 along with estimates derived from the high-resolution images from Section 5.5.2. Estimates of the minor axis are similarly displayed in Figs. 5.9 and 5.10. Note how the trends for both SeaWinds-based estimates reflect a gradual reduction in size as iceberg A22a moves away from the Antarctic continent, towards the warmer waters of the Antarctic Circumpolar Current. Dominant factors that contributed to the ablation of iceberg A22a are discussed in Section 5.6. For comparison, NIC axis trends have extended flat regions because the irregular reports are rounded to the nearest nautical mile. I note that NIC measurements vary in consistency because of changes in analysts [55].

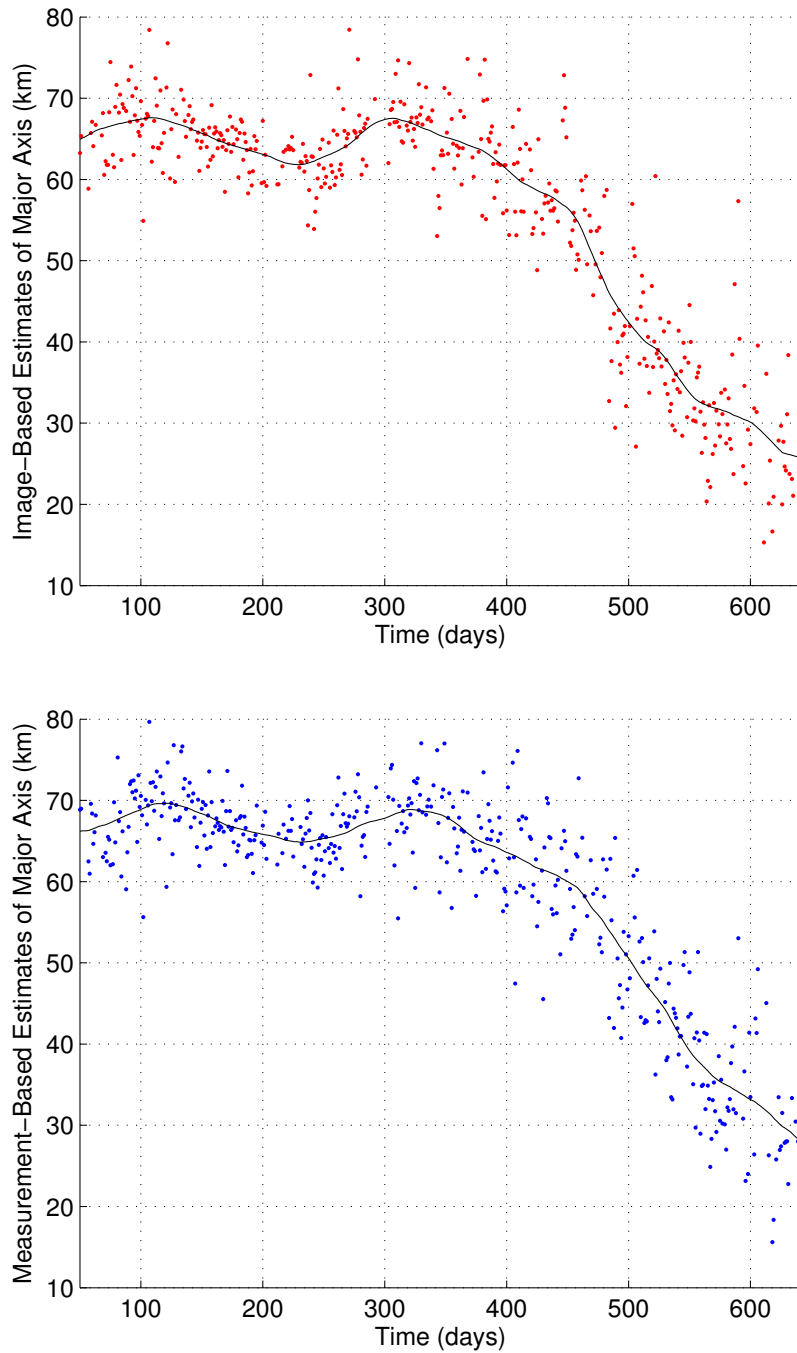


Figure 5.8: Major axis comparisons of iceberg A22a from 2006 JD 50 to 2007 JD 276. JD 1 on the horizontal axis corresponds to 2006 JD 1. To highlight macro-scale trends, image-based estimates, measurement-based estimates, and NIC datasets were filtered using a 71-pt Epanechnikov filter and superimposed over the respective measurements. Top) Image-based estimates of the major axis. Bottom) Measurement-based estimates of the major axis.

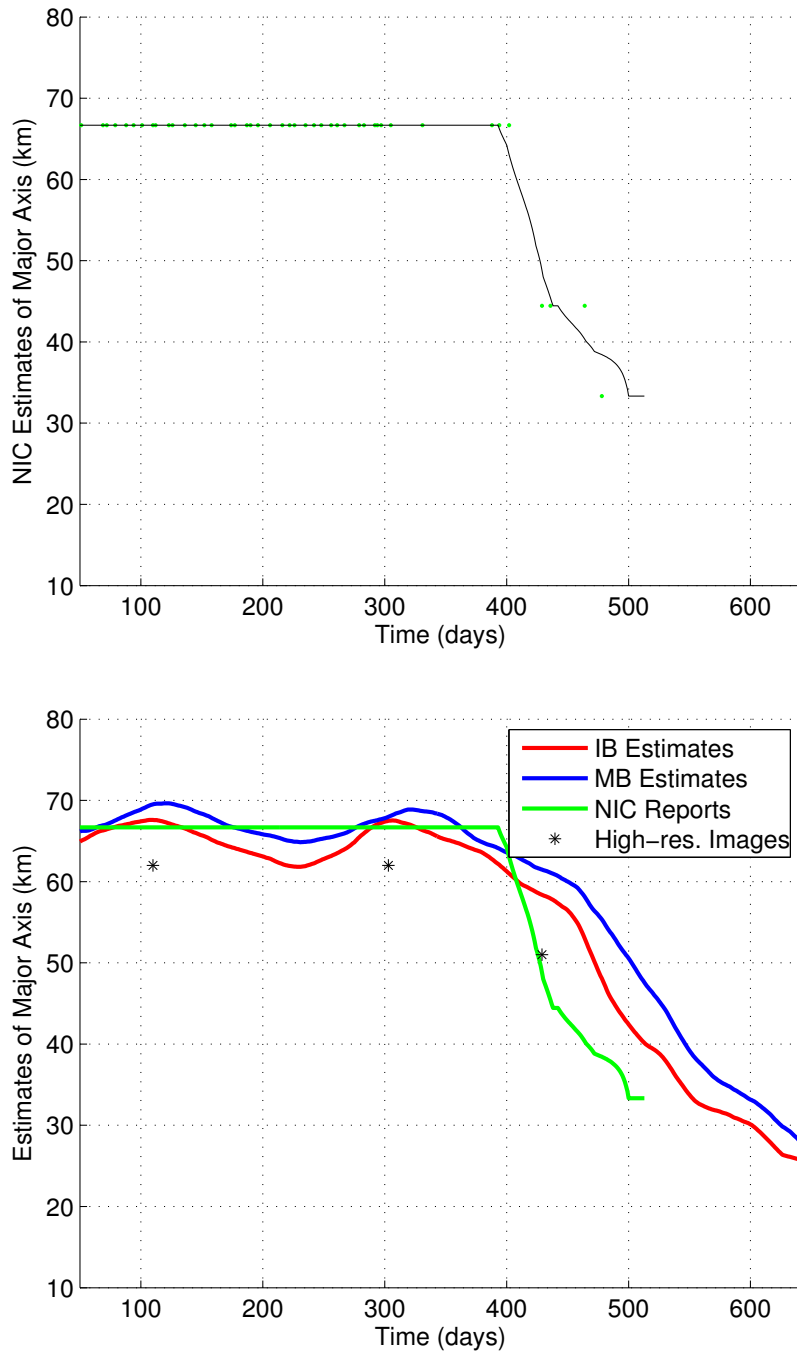


Figure 5.9: Major axis comparisons of iceberg A22a from 2006 JD 50 to 2007 JD 276. JD 1 on the horizontal axis corresponds to 2006 JD 1. To highlight macro-scale trends, image-based estimates, measurement-based estimates, and NIC datasets were filtered using a 71-pt Epanechnikov filter and superimposed over the respective measurements. Top) NIC estimates of the major axis. Bottom) Composite trends of the major axis.

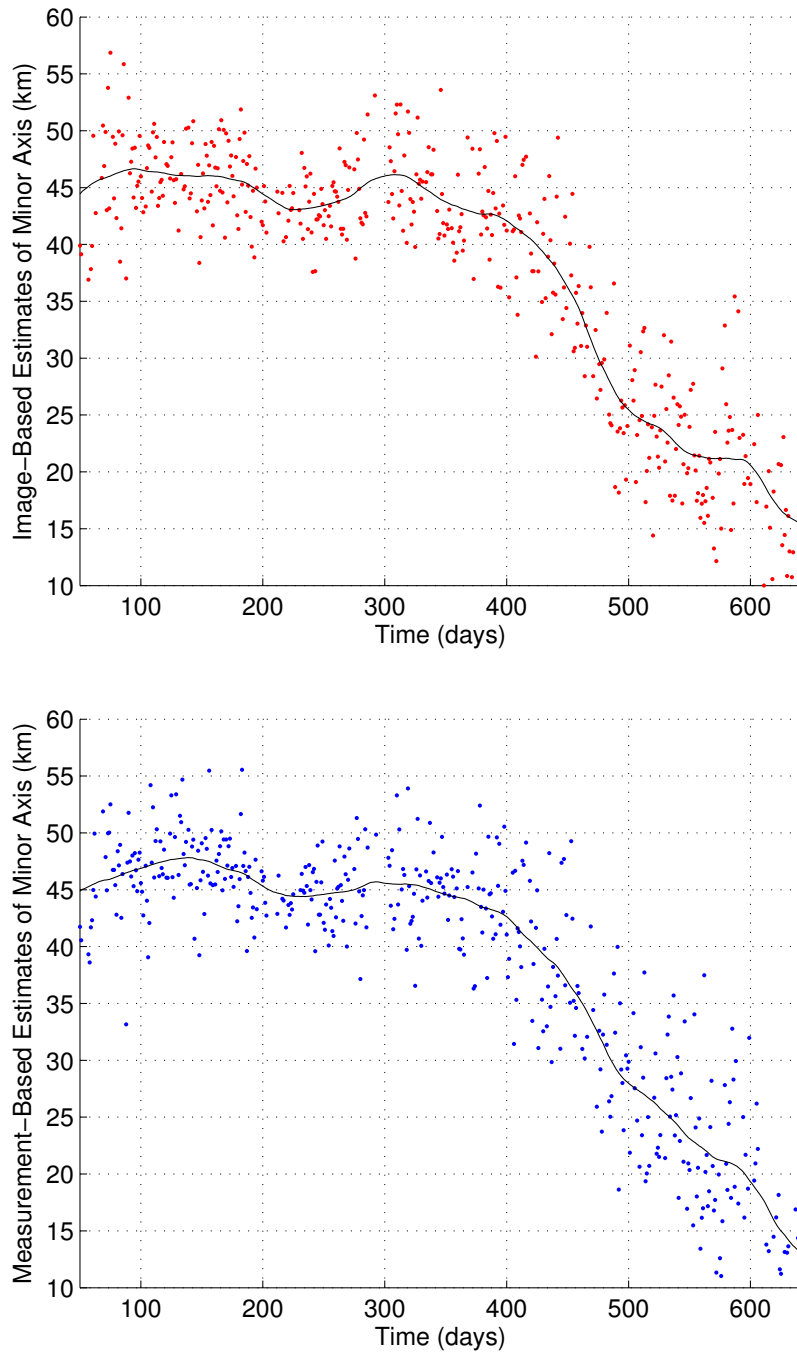


Figure 5.10: Minor axis comparisons of iceberg A22a from 2006 JD 50 to 2007 JD 276. JD 1 on the horizontal axis corresponds to 2006 JD 1. To highlight macro-scale trends, image-based estimates, measurement-based estimates, and NIC datasets were filtered using a 71-pt Epanechnikov filter and superimposed over the respective measurements. Top) Image-based estimates of the minor axis. Bottom) Measurement-based estimates of the minor axis.

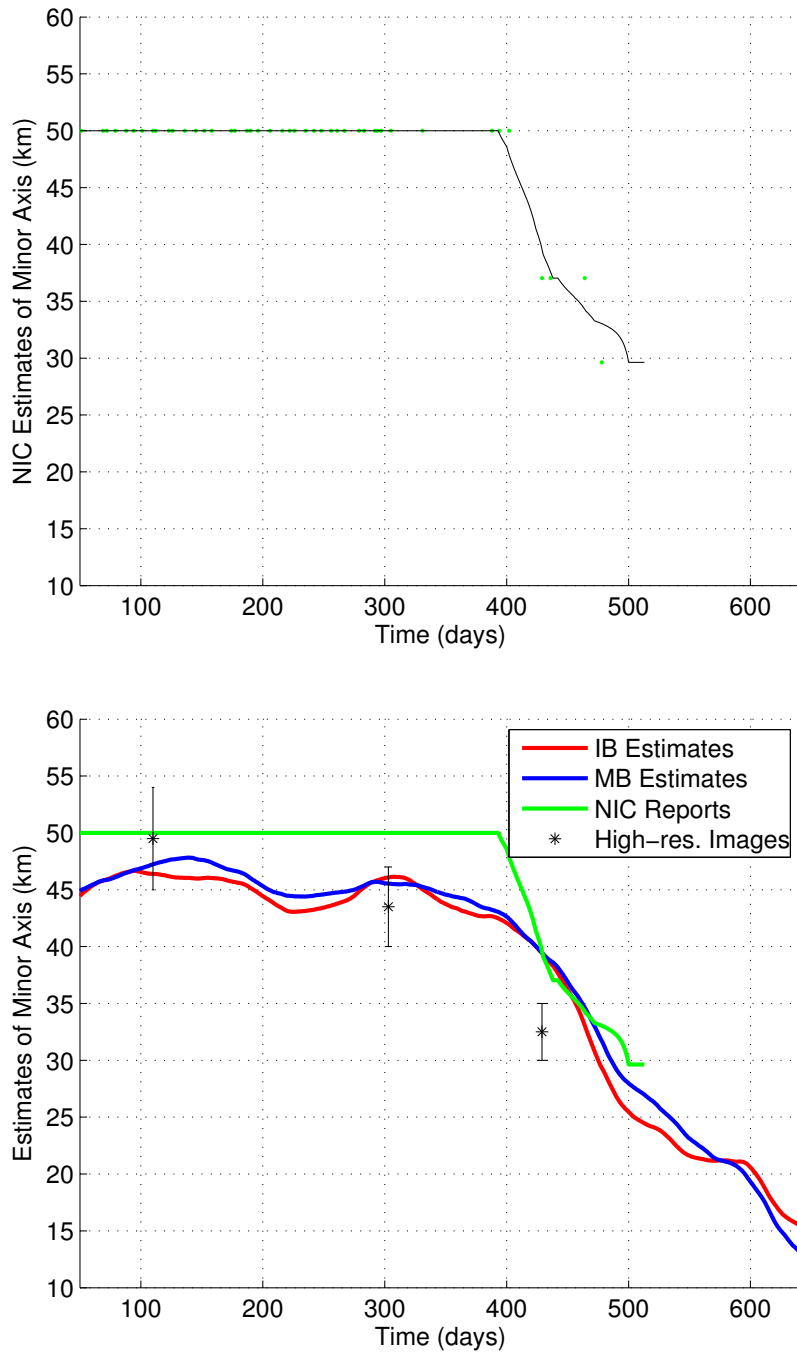


Figure 5.11: Minor axis comparisons of iceberg A22a from 2006 JD 50 to 2007 JD 276. JD 1 on the horizontal axis corresponds to 2006 JD 1. To highlight macro-scale trends, image-based estimates, measurement-based estimates, and NIC datasets were filtered using a 71-pt Epanechnikov filter and superimposed over the respective measurements. Top) NIC estimates of the minor axis. Bottom) Composite trends of the minor axis.

Table 5.5: Count and statistics of accurate daily SeaWinds IB and MB estimates of iceberg A22a from 2006 JD 50 to 2007 JD 276, a span of 593 days.

Type	λ	Estimate Count	ρ_{ma} (km) STD	ρ_{mi} (km) STD	θ ($^{\circ}$) STD
NIC	—	44	1.7	0.7	—
IB	0.00	407	4.8	3.7	25.7
IB	0.50	437	5.0	3.7	25.4
IB	0.75	439	5.0	3.8	24.9
IB	0.90	437	5.0	3.9	24.7
IB	0.99	437	5.0	3.9	24.7
IB	1.00	421	5.1	3.9	25.3
MB	0.00	396	5.3	4.6	25.4
MB	0.50	426	5.1	4.3	25.2
MB	0.75	426	5.1	4.3	25.2
MB	0.90	426	5.1	4.3	25.0
MB	0.99	424	5.2	4.4	26.1
MB	1.00	84	4.8	2.9	30.0

Estimates of the local angle of rotation of iceberg A22a are displayed in Figs. 5.11 for image-based and measurement-based estimates, respectively. An 11-pt Epanechnikov filter is fitted to each set of θ estimates to highlight net movement. Both trends are presented in Fig. 5.12 for comparison. Note that both sets of estimates are consistent in overall net movement.

Note that angle estimates are similar in shape from day 1 until around day 450. Day 450 and after corresponds to when iceberg A22a was moving rapidly from the Weddell Sea to the Scotia Sea along the iceberg corridor commonly called “Iceberg Alley”. Because icebergs are assumed to be spatially stationary during the estimation window (24 hours), rapid movement during this period causes the iceberg profile to become smeared in daily SIR images, distorting iceberg estimates. One potential remedy for this situation is to shorten the estimation window, however the trade-off is a decrease in the number of measurements used in the minimization process and thus a reduced SNR in the estimation problem.

Statistics describing how many of the days have sufficient backscatter contrast to allow for accurate estimates are presented in Table 5.4. Conditions that result in inaccurate estimates during this period are discussed in the following section.

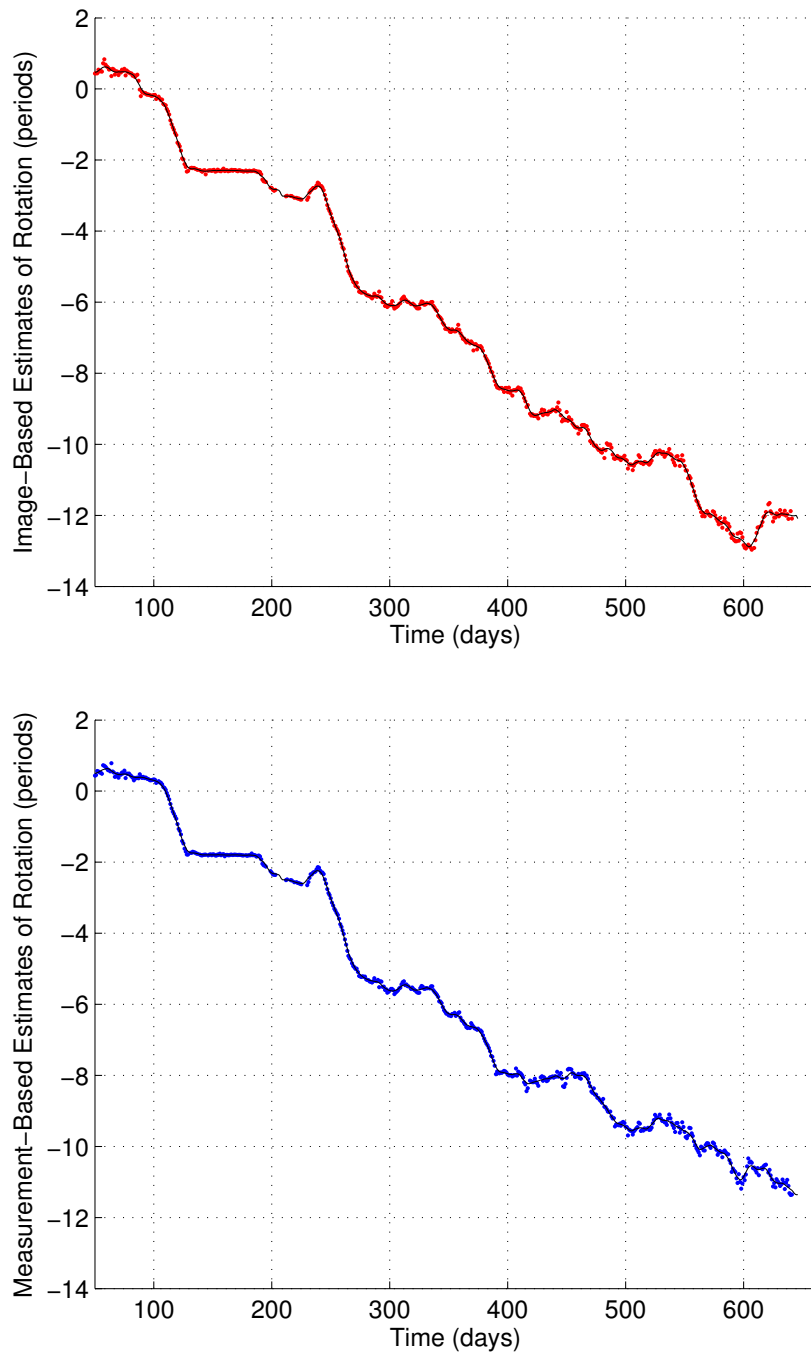


Figure 5.12: Angle of rotational orientation estimates for iceberg A22a from 2006 JD 50 to 2007 JD 276. JD 1 on the horizontal axis corresponds to 2006 JD 1. A trend curve for each dataset is created using an 11-pt Epanechnikov filter to highlight net movement. Top) Image-base estimates of θ . Bottom) Measurement-based estimates of θ . Vertical axes have been scaled such that 360° corresponds to one iceberg rotation, and estimates have been unwrapped with respect to the initial day of study to show rotational evolution. An increasingly positive rotation corresponds to clockwise motion while a decreasing trend corresponds to counter-clockwise motion.

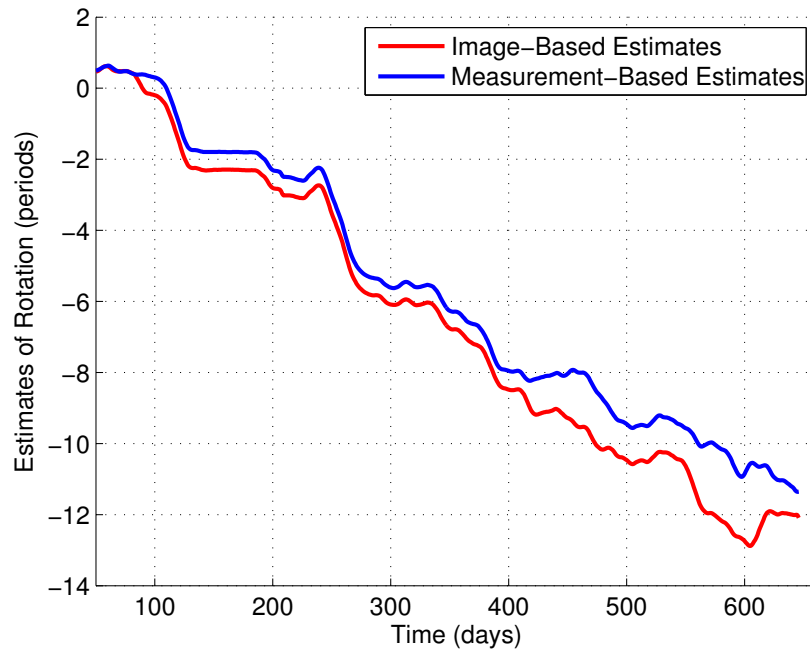


Figure 5.13: Composite trend estimates of θ from Fig. 5.11. Vertical axes have been scaled such that 360° corresponds to one iceberg rotation, and estimates have been unwrapped with respect to the initial day of study to show rotational evolution. An increasingly positive angle corresponds to clockwise motion while a decreasing trend corresponds to counter-clockwise motion.

5.6 Discussion

As previously mentioned, the image-based and measurement-based estimation algorithms successfully provide accurate estimates of iceberg A22a’s major-axis length, minor-axis length, and angle of rotational orientation for 421 (with $\lambda_{IB} = 0.99$) and 424 (with $\lambda_{MB} = 0.90$) days out of a total of 593 days, respectively. A discussion of why either or both of the estimation algorithms failed to produce valid estimates of iceberg parameters for the remaining days highlights the limitations of both estimation techniques.

Conditions that contribute to estimation inaccuracies may be divided into three categories: 1) geophysical contamination, 2) insufficient backscatter contrast, and 3) measurement sampling inconsistencies. Geophysical contamination can be further divided into a) cases where external high-backscatter targets are included in the frame of estimation, b) periods of iceberg fragmentation, and c) conditions where significant intra-day iceberg movement is present.

Inaccurate estimates resulting from having multiple high-scattering targets in the frame of estimation are expected and are stated in Section 5.2 as an assumption for the iceberg parameters estimation process. The probability of such an event occurring depends primarily upon external parameters, such as the presence of nearby glacial ice or sea ice. For example, an ambiguity may arise when sea ice has an associated backscatter as high as the backscatter from glacial ice [50], such as the radar return from multi-year sea ice. The presence of sea ice may cause an ambiguity in the estimation process where the image-based or measurement-based models are inappropriately fitted to a combination of glacial ice and sea ice. Mitigation of this case of contamination is possible using the MERS Antarctic iceberg database to flag the proximity of nearby icebergs and using SeaWinds sea ice products to flag the presence of surrounding sea ice [7].

Contamination from multiple high scattering targets is also caused by iceberg fragmentation. Upon calving from the terminus of glaciers or ice sheets, large tabular icebergs experience varying degrees of ablative forces. These forces result in general perimeter melting and in some cases, large-scale iceberg fragmentation. After fragmentation, iceberg fragments commonly drift in close proximity, showing up as a single target in low resolution radar images, however, eventually the paths of the iceberg fragments diverge. For the case study of iceberg A22a, this is observed in only a few cases of the daily SeaWinds backscatter images. Note that while the reduction in size of iceberg A22a is caused by both perimeter melting and iceberg fragmentation, the low-resolution scatterometer data precludes us from being able to uniquely identify which method dominates in the ablative process [36, 38, 56]. As a result, an automated estimation algorithm must be applied with care.

The third cause of contamination is the violation of the assumption in Section 5.5.3 of negligible intra-day iceberg movement. For instance, if the SeaWinds measurements used to create the daily SIR backscatter image are recorded over an iceberg at the beginning and end of a day where significant iceberg movement is present, the reconstruction process may reconstruct a backscatter image where the single iceberg appears as two icebergs that are spatially separated, resulting in an echo-like effect. This case of contamination is detectable using *a priori* knowledge of iceberg position, available in the MERS Antarctic iceberg database, in conjunction with temporal characteristics of SeaWinds measurements [7].

Factors that influence backscatter contrast and subsequent iceberg estimation include local environmental conditions and iceberg geometry. At Ku-band, environmental conditions that primarily affect scattering properties over the ocean include ablation, rain, and wind. Both ablation and rain influence surface moisture. The presence of surface moisture on an iceberg dampens the associated volume scatter, reducing the backscatter contrast between the iceberg and background. Similarly, rain roughens the ocean surface and high winds induce capillary waves on the ocean's surface which raise the overall backscatter from the ocean, lowering the image contrast ratio. Note that for both the image-based and measurement-based algorithms, these factors are observed as the dominant cause of inaccurate estimates produced in the iceberg A22a case study.

It is also important to note that as an iceberg is reduced in size due to ablation its associated backscatter signature decreases. Once an iceberg is reduced in size to the order of 5-6 km, the iceberg's backscatter intensity blends into ocean noise and remaining fragments are no longer detectable using SeaWinds measurements [50].

The third effect, which primarily affects MB estimates, is measurement sampling inconsistencies, specifically when a SeaWinds sampling swath passes over the iceberg location and only partially covers the frame of observation. This partial swath may bias the iceberg estimation, and while an estimate is produced, iceberg estimates are exaggerated with respect to the orientation of the antenna footprints. In the case study of iceberg A22a, inaccurate estimates are observed when a partial sampling swath is included with less than three full sampling swaths. The automatic detection of partial swaths in the observation frame is possible using the SIR image dataset [7].

5.7 Conclusion

In summary, I have developed and evaluated two algorithms to estimate an iceberg's major-axis length, minor-axis length, and angle of rotational orientation from scatterometer data. The first algorithm is an image-based approach and the second is a measurement-based approach that uses raw SeaWinds measurements. Maximum-likelihood objective functions that relate backscatter to model-based simulated backscatter for each case are developed. Furthermore, each estimation approach is supplemented with regularization terms to mitigate the effects of small measurement variances.

The utility of both estimation approaches is analyzed in simulation where both approaches performed well on average. The performance of the image-based approach is found to be consistent regardless of regularization; however, the performance of the measurement-based approach is found to improve with the inclusion of a minimal regularization term. On average, both estimation methodologies converge to true values; however, the standard deviation of the image-based estimates are reduced by an order of magnitude over the measurement-based approach.

The utility of both estimation approaches is also analyzed in a case study of iceberg A22a where image-based estimates of the major and minor axes differ from true estimates extracted from high-resolution imagery to within an average of 2.3%. Measurement-based estimates differ by 12.2%, and NIC estimates differ by 7.2%. On average, SeaWinds image-based and measurement-based estimates of the angle of orientation differ from high-res. estimates by 3.2° and 3.8° , respectively. Coinciding with simulation results, image-based and measurement-based estimation error is reduced and information usage is maximized for $\lambda_{IB} = 0.99$ and $\lambda_{MB} = 0.90$, respectively.

Next, a long-term analysis is performed using both approaches to estimate parameters of iceberg A22a from 2006 Julian day 50 to 2007 Julian day 276. During this span, 71% of the daily image-based estimates (for $\lambda_{IB} = 0.99$) and 72% of the measurement-based estimates (for $\lambda_{MB} = 0.90$) result in non-degenerate cases, compared with only 7% reported by the NIC over the same period. While both approaches are viable, the image-based iceberg size and orientation estimates out-perform measurement-based techniques and provide more accurate daily estimates of iceberg parameters from resolution-enhanced scatterometer images.

Even though SeaWinds was never designed to track icebergs, previous work has demonstrated the utility of using SeaWinds backscatter images to detect icebergs on a daily basis [50], and this study demonstrates the utility of using SeaWinds data to supplement iceberg position reports with estimates of size and orientation. These estimates may be used to supplement other modeling processes related to iceberg and ocean current studies. Because the non-uniform shape of icebergs is important in iceberg dynamics models, the estimates proposed in this chapter provide the necessary data to test model adequacy and potentially improve model predictions.

Chapter 6

Estimating Iceberg Motion

6.1 Introduction

Because of the importance of tracking icebergs (e.g., Chapter 1.1), forecasting the future positions of icebergs is advantageous, especially for large tabular icebergs. In order to understand how icebergs move, observed external driving forces can be used to model iceberg motion.

Historically, two types of approaches have been explored to estimate dynamic iceberg motion: probabilistic and deterministic. When insufficient external forcing information is available, the former approach is advantageous. While this approach is sufficient for select icebergs over a sufficiently short temporal window, accurate motion models must be tailored to each case [57]. The deterministic motion model is generally favored when sufficient external forcing datasets (or estimates of these parameters) exist, resulting in the development of characteristic force-budget equations to model iceberg motion—a potentially complex and exotic task which is further complicated by low-quality data. While both techniques have merit and inherent trade-offs, advances in satellite remote sensing have allowed for the accurate measurement of iceberg parameters and surrounding climatological parameters; therefore, I choose to explore the latter.

To explicitly model iceberg motion, previous studies have developed characteristic force-budget equations based upon Newton's Second Law of Motion [58]. To increase accuracy, several studies have supplemented the force-budget equations with additional forces and more accurate model parameters. For example, Gladstone and Bigg [59] includes horizontal atmospheric and water drag components, a periodic wind forcing term, and a weighting to dampen surface waves with respect to sea ice. Similarly, Lichey and Hellmer [60] supplement the characteristic sea ice forces with a scaling term to better describe the coupling between sea ice concentration and iceberg motion, and Kubat and Sayed [61] use a stratified ocean current profiles to scale the air and water drag force coefficients.

While these studies have produced valuable results, their models are limited by the assumptions imposed on 1) the iceberg, 2) the forcing fields, and 3) the interactions between the iceberg and the forcing fields. For example, the force-budget equations in the studies above are applied to icebergs whose spatial support (i.e., displaced volume) is described using single mass-point geometry. While potentially appropriate for small icebergs, this spatial approximation is not capable of accurately modeling the interactions of non-homogeneous forcing fields upon an iceberg with large physical size [62]. To compensate, icebergs are assumed to travel with their long axis parallel to the surrounding water flow; however, since many icebergs undergo an inertial rotation, this approach is only approximate and cannot be expected to work well for all icebergs [63]. Additionally, several previous studies assume constant forcing fields in space, in time, or in both space and time [59]. Again, these approximation are only expected to produce accurate results over a sufficiently short window. Third, in quantifying environment-iceberg interactions, most models calculate external forces using static drag coefficients [58–60, 63, 64]. Dynamic in nature, fluidic coefficients of drag are a function of iceberg size, geometry, and relative velocities between the iceberg and climatological fields. Consequently, static drag coefficients only represent the iceberg state at the moment of observation. In order to improve the spatial and temporal accuracy of iceberg motion estimation, it is advantageous to augment current iceberg models to eliminate these assumptions.

In this study, I use the systems of equations as presented by Bigg et al, Gladstone and Bigg, and Lichey et al [58–60] and augment them with 1) updated external forcing fields, 2) a spatial iceberg model, 3) analytical solutions of the iceberg motion equations, and 4) data assimilation techniques to incorporate iceberg observations into the motion model. This study focuses only on the dynamic motion of icebergs; this study does not consider iceberg breakup. Because long-term iceberg motion depends on iceberg size and thus a characteristic thermodynamic profile, a time-dependent iceberg size profile is empirically derived using remote sensing by Stuart and Long [10].

The study described in this chapter is organized as follows. The multiple datasets used in this chapter are introduced and briefly reviewed in Section 6.2. The physical iceberg model is developed in Section 6.3. The iceberg motion model and data assimilation methodology is presented in Section 6.4. Model performance is analyzed in simulation and case studies in Section 6.5. Dis-

cussion of results is in Section 6.6, and Section 6.7 concludes. A large-scale analysis of the iceberg model is performed in a companion study by Stuart and Long [12].

6.2 Background

Two types of datasets are included in this section: 1) estimates of external forcing profiles and 2) observations of physical iceberg parameters. This section briefly explains each dataset. Explicit mathematical representation is set forth in Section 6.4.

6.2.1 Climatological Datasets

It has been found in previous studies by Bigg et al and Eik [58, 64] that multiple external forcing factors contribute to the motion of icebergs. In order to model iceberg motion, knowledge of the external forcing fields is necessary. Since specific measurements are limited, I use climatological datasets. The datasets used in this study include datasets to model atmospheric wind speed, ocean current velocity, sea-ice concentration, and sea-ice velocity.

The atmospheric wind speeds used in this study are taken from the European Center for Medium-Range Weather Forecasts (ECMWF). The near-surface wind speeds 10 m from the ocean's surface (U-10) are used and are assumed constant over the freeboard vertical profile of the tabular iceberg. The incorporated dataset has a spatial resolution dependent on the availability of external sensors and a temporal resolution of 6 hours from 2000-2008.

To calculate the water forcing fields, I use the ocean current velocities and depth profiles from the Ocean Circulation and Climate Advanced Modeling (OCCAM) project. The dataset used in this study has a top-down spatial resolution of $1/12^\circ$ in latitude and longitude, resulting in a more finely sampled dataset at extreme latitudes. The ocean current model is non-linearly stratified with depth resolution inversely related to ocean depth. The first 30 layers of the ocean model are used which correspond to the range of ocean currents at the surface down to 575 m below the ocean's surface. Temporal resolution is monthly from 1994-2004 [65].

To reduce the order of OCCAM's complexity, small oceanic islands were excluded from the modeling space, resulting in averaged ocean currents in a given area without considering land proximity effects. Consequently, the performance of iceberg modeling is expected to degrade when an iceberg is in close proximity to oceanic islands. This is discussed in Section 6.6.

Sea-ice concentrations are gathered from the Nimbus-7 SMMR and DMSP SSM/I-SSMIS satellites as reported by the NSIDC. Spatial resolution is 25×25 km, and temporal resolution is daily from 1996-2007 [66]. Sea-ice velocities are gathered from the AVHRR, SSM/I, and SSMIS satellite programs via the United States National Snow and Ice Data Center (NSIDC). Spatial resolution is 25×25 km. Data ranges from 1978-2006 are included for this study [67].

Because the datasets used as input are not always overlapping, I limit the study period to between 2000-2004. This data range is expanded in Chapter 7.

6.2.2 Iceberg Datasets

Iceberg parameters used in this study include a catalog of iceberg positions and a physical description of each iceberg. For large tabular icebergs, the physical description is frequently subdivided into independent estimates of a top-down shape profile and a vertical height profile.

To judge model performance, iceberg positions are imported from Brigham Young University's Microwave Earth Remote Sensing (MERS) Antarctic iceberg database [7]. This database spans over the lifecycle of several satellite remote sensing instruments from 1978 to the present. In this study, I focus on the portion of the dataset that corresponds to the SeaWinds scatterometer onboard the QuikSCAT spacecraft, 1999-2009. Temporal frequency of reported iceberg positions is 24 hours on a spatial grid of 2.5×2.5 km. Note that only large (> 5 km) tabular icebergs are tracked by SeaWinds and thus our study focuses only on such large tabular icebergs [8]. The utility of using the iceberg model presented in this chapter for other iceberg sizes is discussed in Section 6.3.

Recent developments in remote sensing research has enabled the ability to estimate the top-down size and shape profile of large tabular icebergs using SeaWinds image products [10]. The iceberg size estimation methodology outlined in [10] is used to estimate the time-evolving size and angular orientation of the icebergs used in this study.

The vertical profiles of the icebergs used in this study are determined from the average iceberg profile that corresponds to the parent glacial ice sheet as provided by [68]. Of this vertical profile, the density of pure ice would suggest that 13% of the iceberg should be out of the seawater. However, in the Southern Ocean icebergs have been observed to have up to 18% of their vertical height above water due to wave terracing [69]. I adopt the argument provided in [58] which

averages the expected height-to-keel ratio with observed cases and assumes a ratio of draught to freeboard of 5:1 (16.7%).

6.3 Iceberg Model

Most previous iceberg motion models assume the entire iceberg mass to be located at a single point in space. For an iceberg with large spatial support (e.g., a large tabular iceberg), the point-source mass assumption is poor because external spatially-varying forcing fields vary over the iceberg’s physical size, resulting in degraded motion estimates. To sufficiently model interactions between spatially-varying forcing fields and large icebergs, I have chosen to implement a three-dimensional iceberg model.

Using an ellipse as a general approximation to the top-down shape of a large iceberg [10, 70], an elliptical cylinder construction is chosen to represent the three-dimensional structure of a large tabular iceberg. To model the iceberg’s mass, I choose a discrete rigid-body model where the spacing of each mass point corresponds to the spacing of available external forcing data. The volume of the elliptical cylinder is discretized about each mass point, partitioning the iceberg shape into multiple voxels. Mass points are assumed to be located at the center of each voxel and are weighted according to the volume of each associated voxel.

Horizontal discretization is defined on a Cartesian grid with spacing of 1×1 km. Vertical discretization corresponds to the waterline and the ocean current stratification as defined in the OCCAM dataset [65]. This parameterization results in the iceberg’s volume being divided into voxels of $1 \times 1 \times d_i$ km where d_i is the depth of the i th stratified ocean current layer. See Fig. 6.0 for a top-down and side-view example of the iceberg model. Lines show the discretization of the iceberg’s volume into voxels. A piece-wise ellipse of 20 segments is used (only 12 segments are shown in Fig. 6.0 for ease of visualization). Note that the grid size is targeted to model large (≥ 5 km) tabular icebergs. For smaller tabular icebergs, the grid size could be reduced to minimize quantization error.

Each voxel (and corresponding mass point) along the iceberg’s exterior also has an associated surface area which is used to calculate drag profiles. For voxels along the top and bottom of the iceberg model, the outward-facing surface area of each voxel is used. However, to more

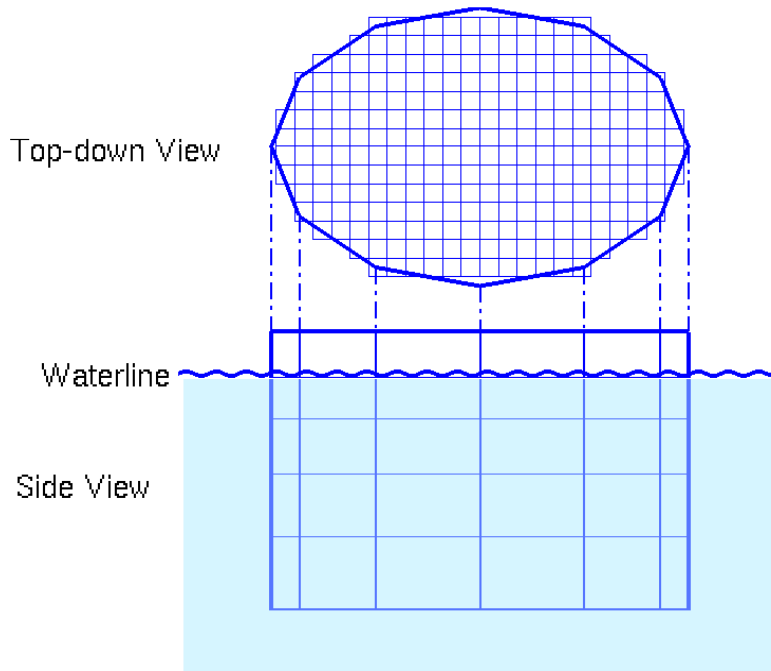


Figure 6.1: Discrete model of an elliptical cylinder used to model tabular icebergs in the iceberg motion estimation process. At top is the top-down representation of the iceberg model where a piece-wise ellipse is divided into pixels of horizontal scale 1×1 km. At bottom is the side view of the iceberg model where the vertical discretization corresponds to the waterline and the stratified ocean current depths defined in the OCCAM dataset.

accurately model a smooth surface along an iceberg’s perimeter, I use the surface areas defined by the top-down ellipse (not the individual voxels) and the stratified ocean current layers.

Because the iceberg motion model is built upon datasets reported on a polar-stereographic map projection plane, spatial coordinates of the driving forces are not uniformly spaced. As a result, a linear trilateration scheme is used to spatially interpolate the forcing fields. Linear interpolation in time produces cusps which potentially exacerbate numerical instabilities while solving the equations of motion; therefore, cubic interpolation is used due to its ability to produce datasets that are differentiable. In addition to the interpolation scheme being more conducive to numerical computation, the use of a cubic interpolation scheme is more consistent with naturally occurring geophysical phenomena which can frequently be described as differentiable forcing fields.

I recognize that previous models such as Jongma et al [63] include iceberg rolling parameters; however, the icebergs considered in this dissertation are too large to roll.

6.4 Estimation Algorithm

To characterize the kinematic motion of large tabular icebergs, a force-budget based on Newton's second law of motion is presented in this section. First, the translational and rotational force-budget model is developed. Next, mathematical integration of the force-budget is reviewed and a regularization technique is presented to mitigate potential numerical instabilities. Last, data assimilation techniques are introduced to augment iceberg model estimates with actual data, resulting in more accurate iceberg parameter estimates.

6.4.1 Equations of Motion

The iceberg motion model used in this chapter is based upon the force-budget drift model presented by [58]. Additional papers with varying degrees of modification have also appeared, see Section 6.1. To minimize confusion, the equations and assumptions adopted in this study are explicitly stated. Our force-budget equation describes the translational motion of an iceberg with mass m and velocity \vec{V}_i as

$$m \frac{d\vec{V}_i}{dt} = \vec{F}_w + \vec{F}_a + \vec{F}_s + \vec{F}_r + \vec{F}_c + \vec{F}_h \quad (6.1)$$

where \vec{F}_w is the force due to the surrounding water, \vec{F}_a is the force due to the atmosphere (i.e. near-surface winds), \vec{F}_s is the sea-ice drag, and \vec{F}_r is the wave radiation force. Forces induced as a result of an accelerating reference frame (i.e. the Earth's rotation) are the Coriolis force, \vec{F}_c , and the horizontal-pressure gradient force, \vec{F}_h . Furthermore, I am interested only in the components of the force and velocity vectors that lie in the two-dimensional plane that contains an iceberg's northing and easting translational motion.

The general drag equation used to quantify the drag forces at each mass point along the exterior of the iceberg is

$$\vec{F}_* = \frac{1}{2} \rho_* A_* C_* \left| \vec{V}_* - \vec{V}_i \right| \left(\vec{V}_* - \vec{V}_i \right) \quad (6.2)$$

where the subscript $*$ refers to atmosphere (a), water (w), or sea ice (s), respectively. ρ_* is the respective density of the forcing medium, A_* is the appropriate area of the affected iceberg surface to which the stressing force is applied, and C_* is the associated drag coefficient. Drag coefficients

are a function of the climatological Reynold's number, R , which can be calculated as

$$R = \frac{\vec{V}_* \cdot D}{\nu_*} \quad (6.3)$$

where D is the associated fetch distance and ν is the kinematic viscosity of the forcing medium.

The force due to the atmospheric wind has two components: a pressure drag component along the perimeter, $\vec{F}_{a,perim}$, and a friction drag component along the top surface, $\vec{F}_{a,top}$, where $\vec{F}_a = \vec{F}_{a,perim} + \vec{F}_{a,top}$. The pressure drag component due to the atmosphere may be found using Eq. 6.2 where A_a is the orthographic projection of the iceberg perimeter onto the plane perpendicular to the vector defined by the difference between the oncoming air velocity and the iceberg's velocity. For this study, ρ_a is chosen to be 1.225 kg/m^3 [64]. To calculate $C_{a,perim}$, I must first quantify the type of flow around the iceberg (e.g., laminar, intermediate, or turbulent) [71]. For this analysis, I assume an austral wind velocity of $> 1 \text{ m/s}$ and a fetch distance of 5 km . For air, $\nu = 1.46\text{e-}5 \text{ m}^2/\text{s}$. These values produce Reynold's numbers in excess of 10^8 which correspond to a completely turbulent drag profile [71]. Little research has been performed to analytically describe the coefficients of drag in the extremely turbulent case; however, drag coefficients are available from empirical studies. In this study, coefficients of drag are interpolated from data presented by Akiba et al, Wang and Catalano, and Khan et al [72–74].

The friction drag component due to the atmosphere is calculated using Eq. 6.2 where A_a is the iceberg's top-down surface area defined in Section 6.3 (1 km^2). I assume that the spatial distribution of the wind over an iceberg's surface is homogeneous (see Section 6.5.1); therefore, a flat-plate body-drag approximation is used. Under extremely turbulent conditions, the friction drag coefficient is independent of the Reynold's number and the drag is modeled by

$$C_{a,top} = [1.89 - 1.62 \log(\epsilon_{top}/D)]^{-2.5} \quad (6.4)$$

where ϵ_{top} is the average top-side surface roughness of the iceberg (in m). Based on empirical observations presented by Scambos [75], ϵ_{top} is set to 1 m in this study. Due to assuming a homogeneous wind field, D is assumed to be a flat plate and is set to the length of the iceberg projected onto a line parallel to the vector defined by the difference between the oncoming wind

velocity and the iceberg’s velocity, making the drag force a function of both relative iceberg speed as well as iceberg orientation angle.

Similar to the air drag case, the drag force upon an iceberg due to oceanic currents has a pressure drag component along the iceberg’s perimeter and a friction drag component along the iceberg’s bottom where $\vec{F}_w = \vec{F}_{w,perim} + \vec{F}_{w,bottom}$. The pressure drag component is calculated using Eq. 6.2 where A_w is as defined for the air case, and $\rho_w = 1027 \text{ kg/m}^3$ [64]. To calculate $C_{w,perim}$, I must first determine the region of dynamic flow by calculating the associated Reynold’s number. Using Eq. 6.3, I assume an iceberg-water differential velocity $> 0.001 \text{ m/s}$ (see Section 6.5.1) and a fetch distance of 5 km. For water, $\nu = 1.12\text{e-}6 \text{ m}^2/\text{s}$ which results in Reynold’s numbers in excess of 10^6 . This value corresponds to a completely turbulent drag profile [71], and water pressure drag coefficients are calculated identically as in the air profile case.

The friction drag component due to the water is calculated using Eq. 6.2 where A_w is the same as for the air friction case. Due to lack of information regarding sub-surface iceberg profiles, ϵ_{bottom} is set to 1 m. In contrast to the air case, the water profile over the spatial extent of a large iceberg is not homogeneous (see Section 6.5.1); therefore, I have chosen to utilize a piece-wise drag profile to characterize the water drag coefficient along the iceberg’s bottom layer. Using Eq. 6.4, a drag coefficient is calculated for each surface area where the fetch distance is calculated as the distance the residual water vector has traveled over the iceberg profile, permitting relative deviations in heading $\leq |30^\circ|$. I believe that permitting this range of heading deviations allows for an accurate representation of the fetch distance incident upon an affected surface area. Note that by analytically computing the water drag coefficients based upon iceberg geometry and fluid dynamics, there is no need to include an additional “effective mass” term to account for entrained ocean water such as those included in previous studies [57, 58, 61].

The force induced by sea ice is calculated by using the construction presented by Gladstone and Bigg [59], i.e., the sea ice is treated as a distributed fluid suspension. Using Eq. 6.2, A_s is defined as the orthographic projection of the horizontal line distance of the iceberg affected by the stressing medium multiplied by the sea ice thickness. For the Southern Ocean, the majority of sea ice is first-year sea ice with sea ice thickness $\leq 2 \text{ m}$. While models that describe the strict entrainment of icebergs in surrounding sea ice have been developed [60, 76], characteristic model constants vary and are not clearly defined as a function of iceberg size or physical location, making

adoption of these models problematic. Because icebergs are known to facilitate the formation of sea ice [63], an average sea-ice thickness of 2 m is assumed in this analysis. I realize that our sea ice calculations may underestimate the forcing effects of sea ice in cases where sea ice concentration is extreme (e.g., > 90% in [60]). Further research is needed in this area.

The force induced by the wave radiation force is

$$\vec{F}_r = \frac{1}{4} \rho_w g a^2 L \frac{\vec{V}_a}{|\vec{V}_a|} \quad (6.5)$$

where L is the length of the iceberg normal to the incident waves of amplitude a which are assumed to have the same direction as \vec{V}_a , and g is the gravitational acceleration constant. Using the mapping

$$a = \frac{1}{2} 0.02025 |\vec{V}_a|^2, \quad (6.6)$$

surface capillary wave amplitude a may be calculated directly from the near-surface wind profile. To account for the dampening effects of sea ice on capillary wave amplitude, the final wave amplitude is weighted by $\frac{1}{2} \cdot [1 + \cos(c^3 \pi)]$ where c is sea ice concentration [59].

The Coriolis force is

$$\vec{F}_c = -m \cdot f (\vec{k} \times \vec{V}_i) \quad (6.7)$$

where \vec{k} is a unit vector perpendicular to the ocean's surface, pointing away from the Earth's center, and f is the Coriolis frequency parameter

$$f = 2 \cdot 7.2921 \times 10^{-5} \cdot \sin(\phi) \quad (6.8)$$

and ϕ is the latitude of interest. The horizontal-pressure gradient (HPG) force is

$$\vec{F}_h = m \cdot f (\vec{k} \times \vec{V}_w) + m \frac{d\vec{V}_w}{dt}. \quad (6.9)$$

To account for the spatial support of the icebergs in this study, the mean water velocity over the iceberg's displaced volume is used. Because ocean currents are spatially interpolated over the iceberg's volume, we observe that the horizontal-pressure-gradient force is driven by only the first term in Eq. 6.9; however, for completeness, both terms are maintained.

To model the rotational profile of an iceberg, the angular acceleration about the centroid must be quantified. Using standard rigid-body mechanics, the acceleration about the iceberg's axis of rotation (i.e., the top-down center of the elliptical cylinder) is

$$\sum_{j \in S} \vec{M}_j = I \cdot \ddot{\theta} \quad (6.10)$$

where I is the moment of inertia, $\ddot{\theta}$ is the angular acceleration about the axis of rotation, and \vec{M}_j is the spatial acceleration of the j th mass point in relation to the axis of rotation, and S represents the set of all iceberg mass points. As mentioned in Section 6.3, I constrain iceberg rotation such that the iceberg is only allowed to rotate in the plane containing the iceberg's translational motion. For an elliptical cylinder with this constraint, $I = \frac{1}{4}m(a^2 + b^2)$ where a and b are the major and minor axis lengths of the iceberg, respectively. The summation is over each spatial acceleration component where $\vec{M}_j = \vec{r}_j \times \vec{F}_j$ for each force \vec{F}_j used in computing the iceberg's translational motion where \vec{r} is defined as the vector perpendicular to the axis of rotation that extends from the axis of rotation to each exterior mass point. Rotation of the iceberg is a function of the instantaneous rotational acceleration as calculated using Eq. 6.10 as well as the evolving rotational momentum from previous time-steps. Both are accounted for in the iceberg model. These rotation rates are used in calculating the relative speed of each mass point (and associated surface area) along the iceberg's perimeter, an important variable for calculating the spatially-varying drag coefficients and translational forces over an iceberg's exterior.

In addition to the forces included in Eq 6.1, two other forces affecting translational motion are considered and are briefly analyzed here. The first arises from the coupled effects of iceberg motion and ocean circulation around the iceberg (i.e., the Magnus effect), resulting in a side "lift" force upon a rotating iceberg in steady translational motion [77]. The magnitude of the lift force can be represented as

$$F = \pi \rho_w |V_i - V_w| L^2 H |\dot{\theta}| \quad (6.11)$$

where L is the average top-down radius of the iceberg, H is the keel depth of the iceberg, and $\dot{\theta}$ is the angular velocity about the axis of rotation [70, 77].

The second extra force considered in this chapter is caused when tabular icebergs interrupt ocean isopycnals, resulting in the generation of internal ocean waves. Icebergs generate internal waves as ocean currents flow over the lower portion of an iceberg in the same manner as the flow of water over stationary ocean bottom topography and ridges generates internal waves [78–83]. When internal ocean waves are generated, they extract momentum from the iceberg’s energy, resulting in an additional drag force affecting all iceberg motion. The magnitude of the drag is dependent on the spatial extent of the iceberg, relative velocity of the iceberg, and the local buoyancy frequency of the ocean. A more explicit formulation of the drag force upon icebergs due to internal wave generation is included in the Appendix. The magnitude of both the lift force due to rotational motion and the drag force due to internal ocean waves were analyzed and deemed relatively insignificant for large tabular icebergs and thus were excluded from this study. Quantitative comparison of these extra forces are included in Section 6.5.1.

6.4.2 Numerical Integration

Numerical integration of Eq. 6.1 gives the translational velocity which is used to update the future position of the iceberg. Similarly, solving Eq. 6.10 yields the instantaneous angular acceleration of the iceberg, and integration in time yields both the angular velocity and the physical angle of the modeled iceberg.

Explicit numerical integration techniques based upon Euler approximations have been used in previous iceberg studies; however, these approaches can lead to unstable solutions, particularly as the time step is increased [61,84]. For small icebergs (which have relatively small mass), numerical computation of Eq. 6.1 is straight forward; however, for large icebergs (which have very large mass), the dominant forces in Eq. 6.1 are the Coriolis and HPG forces (see Section 6.5.1), resulting in a high-order coupling between the northing and easting translational components. Therefore, significant perturbations in one direction directly affects the performance of the entire system, potentially resulting in an ill-conditioned system of coupled differential-algebraic equations.

While there are several ways to mitigate unstable numerical behavior caused by process noise, I have chosen a two-fold approach: 1) implement an appropriate (yet tractable) numerical solving technique to improve model accuracy and 2) introduce a regularization term to improve model robustness. For numerical computation, a variable order solver based upon the numerical

differentiation formulas taken from Shampine and Reichelt [85] is proposed. This functionality is incorporated into MATLAB's *ode15s* solver and has functional form of

$$\dot{\vec{x}} = g(\vec{x}) \quad (6.12)$$

where \vec{x} is the vector of parameters to estimate, $\dot{\vec{x}}$ is the time-derivative of \vec{x} , and $g(\cdot)$ generalizes to any non-linear operator. For this study, \vec{x} includes easting distance ($D_{i,E}$), easting velocity ($V_{i,E}$), northing distance ($D_{i,N}$), northing velocity ($V_{i,N}$), angle of rotational orientation (θ_i), and angular velocity ($V_{i,\theta}$) where

$$\vec{x} = [D_{i,E}, V_{i,E}, D_{i,N}, V_{i,N}, \theta_i, V_{i,\theta}]^T. \quad (6.13)$$

Numerical regularization is performed by augmenting Eq. 6.12 with an energy constraint to dampen energy in unstable modes. To minimize the energy in the system, it is desired that the composite instantaneous easting and northing forces in Eq. 6.1 be constrained such that they are both in geostrophic equilibrium, i.e., $\sum \vec{F}_E = 0$ and $\sum \vec{F}_N = 0$. This can be accomplished by augmenting Eq. 6.12 such that

$$\dot{\vec{x}} = g(\vec{x}) - \Gamma \cdot \frac{dJ}{d\vec{x}} \quad (6.14)$$

where Γ is a regularization constant and J is an objective function containing the energy constraint. For this study, $J = (\sum \vec{F}_E)^2 + (\sum \vec{F}_N)^2$. Note that small values of Γ result in minimal regularization, and increasing values of Γ result in the regularization constraint being more stringently imposed upon the instantaneous translational acceleration components, i.e., for large Γ , the iceberg is assumed to be traveling at steady-state and thus has an instantaneous acceleration of approximately zero. Appropriate values for Γ are explored in Section 6.5.1.

Because the equations of motion are a second-order system, regularization need only be performed in a single domain, i.e., position, velocity, or acceleration, in order to affect the propagation distance at each time step; therefore $dJ/d\vec{x}$ can be simplified to

$$\frac{dJ}{d\vec{x}} = [0, \frac{dJ}{dV_{i,E}}, 0, \frac{dJ}{dV_{i,N}}, 0, 0]^T. \quad (6.15)$$

I note that numerical instabilities primarily affect translational iceberg motion (not angular evolution); therefore, regularization in Eq. 6.15 is only applied to temper unstable translational modes, a topic discussed further in Section 6.5.1.

6.4.3 Data Assimilation

To predict iceberg motion, I can use the iceberg motion estimates directly; however, to mitigate model uncertainty, data assimilation techniques can be used to augment model predictions with empirical iceberg observations, resulting in more accurate motion estimates. Two methods are conventionally used to incorporate data into geophysical models: Kalman filtering [86] and variational analysis [87]. Each has inherent advantages and trade-offs. For instance, the first has an explicit covariance matrix, but model uncertainty is sometimes difficult to quantify. The latter is computationally less expensive but assumes zero modeling error. With the intent to use statistical properties of the assimilation technique as a metric to judge model performance, I choose to use the Kalman filter. With a discrete covariance matrix, model statistics can be computed at each iteration, resulting in a spatially and temporally varying description of model performance.

The Kalman filter is an iterative filter that consists of alternating measurement updates and prediction steps where the first step incorporates actual measurements and the second step uses statistical estimation techniques to predict the future state of the iceberg. Due to inherent nonlinearities in the estimation process (e.g., Eq. 6.2), an extended Kalman filter is used of form

$$\vec{x}_{k+1} = f(\vec{x}_k) + \vec{w}_k, \quad (6.16)$$

$$\vec{y}_k = \vec{x}_k + \vec{v}_k \quad (6.17)$$

where $f(\cdot)$ represents the non-linear iceberg propagation model, and \vec{x}_k denotes the state of the system at time k with modeling noise \vec{w}_k and measurement noise \vec{v}_k . The covariance of \vec{w}_k is defined as Q_k , and the covariance of \vec{v}_k is defined as R_k . Furthermore, I introduce the Jacobi matrix

$$A_k = \frac{\partial f(\vec{x}_k)}{\partial \vec{x}} \quad (6.18)$$

to linearize Eq. 6.16 about the current time step [88].

Due to seasonal radar backscatter characteristics, iceberg observations may be intermittently unavailable. As a result, I include an indicator function, I_k , that characterizes the availability of observation measurements in the Kalman filtering process. The indicator function is defined as $I_k \in [0, 1]$ where a value of one corresponds to an available measurement update at the k th iteration and zero corresponds to no available data. The state prediction and the measurement update equations are defined as

$$\vec{x}_{k+1|k} = f(\vec{x}_{k|k}), \quad (6.19)$$

$$\vec{x}_{k+1|k+1} = \vec{x}_{k+1|k} + I_{k+1}K_{k+1}(\vec{y}_{k+1} - \vec{x}_{k+1|k}) \quad (6.20)$$

where K is the Kalman gain [89]. The Kalman estimator covariance and the Kalman gain are calculated by

$$P_{k+1|k} = A_k P_{k|k} A_k^T + Q_k, \quad (6.21)$$

$$K_{k+1} = P_{k+1|k} (P_{k+1|k} + R_{k+1})^{-1}, \quad (6.22)$$

$$P_{k+1|k+1} = P_{k+1|k} - I_{k+1} K_{k+1} P_{k+1|k}. \quad (6.23)$$

While the MERS Antarctic iceberg database nominally contains daily iceberg positions, melt conditions and high winds can obscure iceberg radar returns, resulting in occasional gaps in daily reporting. Reporting gaps in the MERS Antarctic iceberg database follow two patterns. The first corresponds to the intermittent detection of icebergs in radar images such as during a large storm where the ability to detect icebergs using microwave scatterometry is randomly intermittent and temporally-uncorrelated [7, 8]. For this case, I model measurement arrival as a Bernoulli stochastic process. The second type of measurement availability corresponds to when an iceberg is not detected for an extended period of time. For example, due to seasonal melting conditions, the characteristic radar return of glacial ice in SeaWinds images is frequently reduced, making icebergs indistinguishable from surrounding sea water or sea ice for extended periods of time (e.g. a month) [7, 8]. I model this case as a deterministic sequence with a continuous dropout interval. The performance of the Kalman filter is analyzed under both conditions.

As per convention, there are two ways to analyze the performance of the Kalman filter: the matrix trace of P and the L-2 norm of P , denoted $Tr\{P\}$ and $\|P\|$, respectively [86, 89–91]. Both metrics are explored. Monte Carlo simulation is used to derive the average Kalman filter performance in Section 6.5.3.

6.5 Performance

To evaluate the performance of the iceberg motion model, simulation is first employed. Next the utility of the iceberg motion model is analyzed in case study of iceberg B09a which was named by the United States National Ice Center by their standard naming convention. Iceberg position, size, and orientation is compared using SeaWinds data products [8, 10].

6.5.1 Simulation

To simulate the iceberg model, one of the parameters I need is Γ . To select an appropriate value, first a range of gamma is investigated and then model performance is analyzed. A simulated iceberg with major axis of 45 km, minor axis length of 30 km, and keel depth of 270 m is simulated in the Weddell Sea with initial position at 62.0790°S and 53.0535°W . These parameters are similar to actual parameters for iceberg B09a. The iceberg simulation is initialized such that the major axis is oriented in the direction of the mean water flow. The motion model is propagated over 25 days with variable Γ . In this study, model performance was found to vary only with significant change in Γ ; therefore, logarithmic values of Γ are explored, specifically $\Gamma = [1e-3 \ 1e-2 \ 1e-1 \ 1 \ 1e1 \ 1e2]$. Sample iceberg tracks for these values are displayed in Fig. 6.1. Note that while the simulated iceberg tracks have similar large-scale movement profiles, various translational oscillations are observable. To highlight motion perturbations, an expanded view of iceberg observations is also included in Fig. 6.1.

I recognize that icebergs may have characteristic oscillatory motion due to external forcing, e.g., periodic tidal forces. While necessary for tracking intra-day iceberg motion, the cumulative effects of these oscillatory forces on iceberg motion integrate to zero as the temporal window is increased. Because these forces have not been included in the iceberg motion model, extreme oscillatory motion in the model is considered an artifact of numerical integration which I suppress.

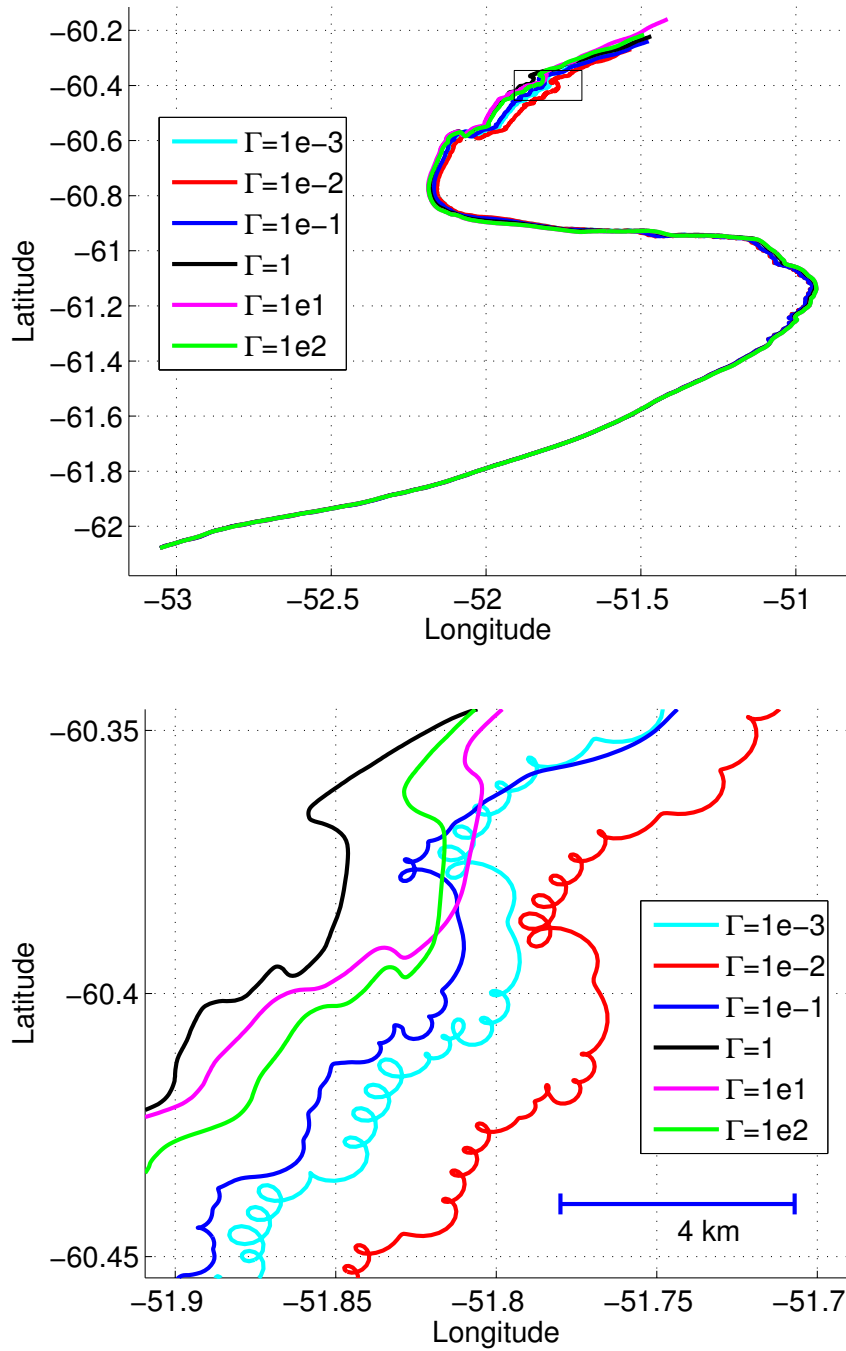


Figure 6.2: Simulated iceberg tracks in the Weddell Sea over a 100 day span where the position of the iceberg center is plotted with varying degrees of numerical regularization (Γ): Top) The full 100-day tracks. Bottom) A three-day section of the tracks outlined in (top) that highlights translational oscillations inherent to numerically integrating the equations of motion.

There are three methodologies for selecting an appropriate Γ : 1) a performance-based criterion, 2) a computationally efficient metric, and 3) a climatological standard. All three methodologies are investigated below and give insight into the inherent trade-offs with respect to different choices of Γ .

The first is performance-driven. From model observations, I note that models with $\Gamma < 1e-3$ frequently produce iceberg tracks with highly variable translational motion. Conversely, models with $\Gamma \geq 1e2$ produce iceberg tracks conforming to the steady-state solution. Therefore, I limit Γ to within $1e-3$ and $1e2$. Furthermore, note that $\Gamma \geq 1$ mitigates translational oscillations, see Fig. 6.1b. To maximize the instantaneous acceleration in the motion model, a small value of Γ is preferred. As a result, Γ is chosen to be unity to mitigate undesirable translational perturbations while minimizing the amount of regularization.

The second metric for selecting Γ is motivated by computational tractability. I have observed that computation time is related to the amount of regularization where an increase in Γ results in increased computation time. Thus, iceberg motion estimation is numerically more tractable for smaller Γ , supporting the decision to minimize Γ within the acceptable range.

The third criterion for selecting Γ is to choose a value consistent with climatological equilibrium. Formulation of the Coriolis and horizontal-pressure gradient forces assumes the ocean currents are in geostrophic balance [92]. Note that the energy constraint further enforces a geostrophic equilibrium constraint for all the forces in Eq. 6.1. [92] argues that the differential form of Eq. 6.1 (i.e., $\Gamma=0$), involves thinking of the ocean current as responding to the iceberg. Conversely, the steady-state form of Eq. 6.1 (i.e., $\Gamma \geq 1e2$), involves considering the iceberg motion as purely responsive to the ocean currents. A Γ between these extremes allows for a compromise of both philosophies. Due to the spatial extent of large tabular icebergs, an intermediate value of Γ is an intuitive choice to allow for the model to accurately describe the coupled effects of iceberg motion with ocean current propagation, reinforcing unity as our choice for Γ . For the remainder of this study, motion simulations are performed with $\Gamma = 1$.

I now consider the external forces included in the iceberg model (see Eq. 6.1). The external forces on the simulated iceberg with $\Gamma = 1$ in Fig. 6.1 are displayed in Fig. 6.2 where F_COR and F_HPG represent the Coriolis and horizontal-pressure gradient forces, respectfully. Note that the dominant forces are the Coriolis and horizontal-pressure gradient forces because they are propor-

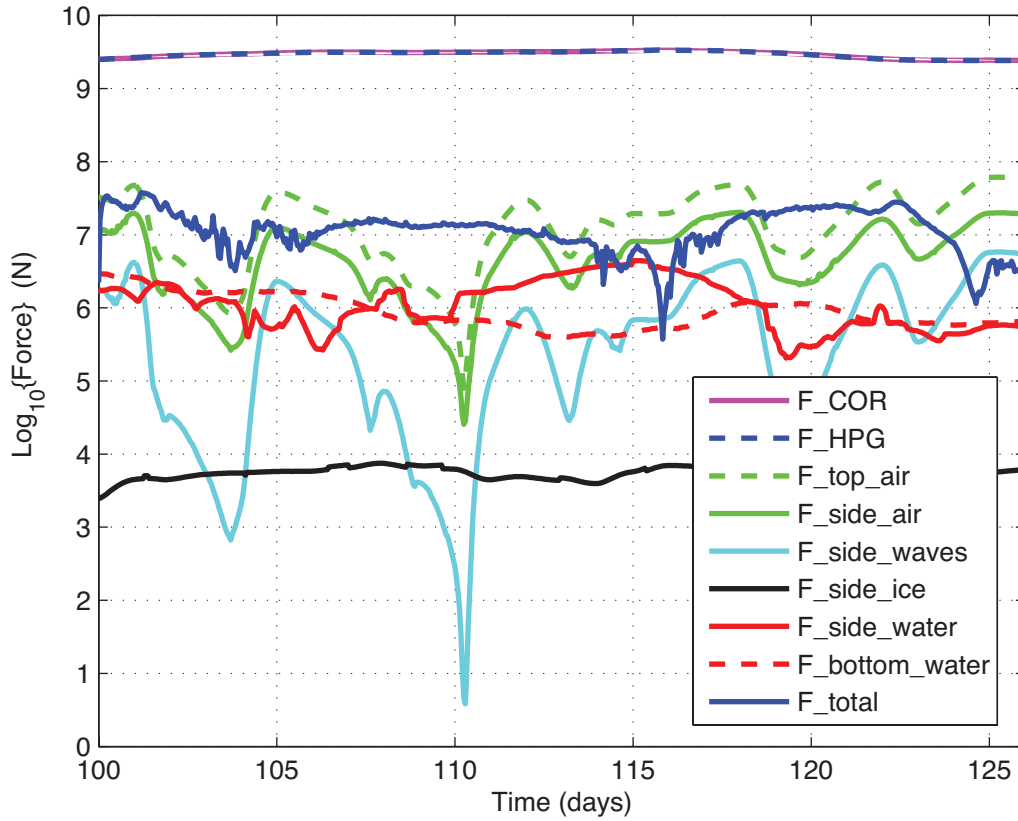


Figure 6.3: Forces included in the iceberg model in Fig. 6.1 for $\Gamma = 1$.

tional to the mass of the iceberg. In previous studies, these forces were secondary due to case studies that focused on only glacial ice fragments with small masses [58, 59, 61, 63, 64]. For very large icebergs, the situation changes. Aside from the two dominant forces, air flow along the iceberg’s top and side produces forces larger than the sheer forces due to water on the side and bottom on the iceberg, a consequence of the large spatial support of tabular icebergs in this dissertation. I note that the relative order of the forces presented in Fig. 6.2 are representative of the characteristic forces experienced by all large (≥ 5 km) tabular icebergs in the Weddell Sea.

Because the Coriolis and the HPG forces are the dominant forces in Eq. 6.1, the iceberg velocity follows the average velocity of the displaced water. For the simulated iceberg in Fig. 6.2, the iceberg velocity and the mean water flow velocity during the 25-day simulation are displayed in Fig. 6.3.

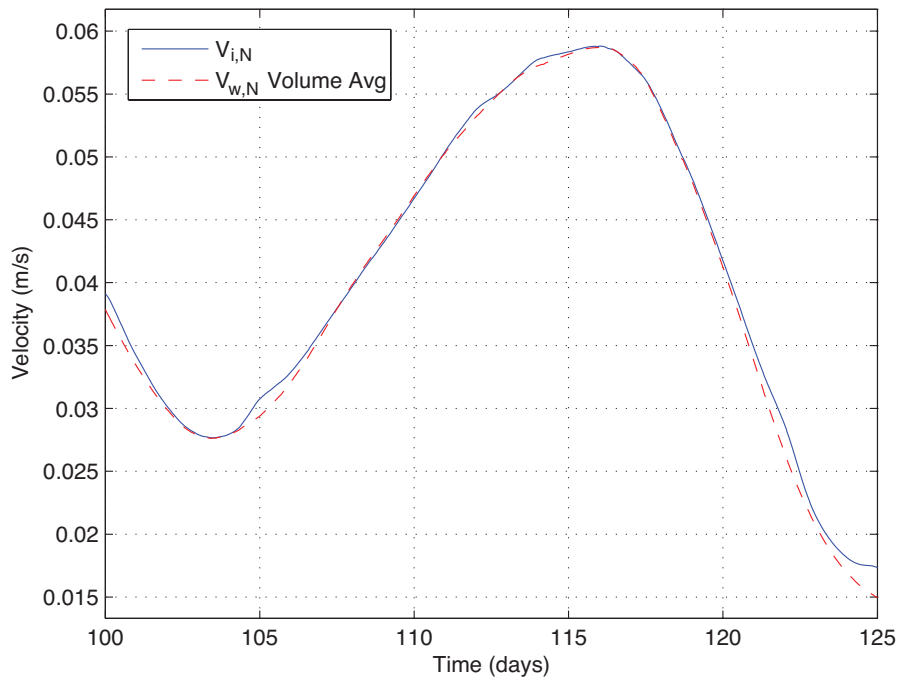
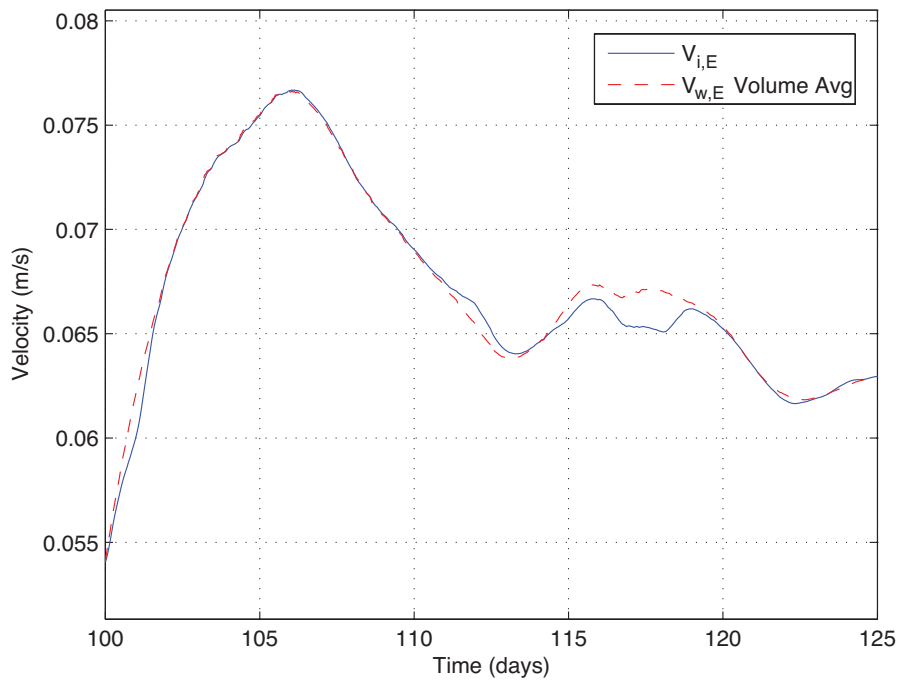


Figure 6.4: Simulated iceberg velocity and mean water velocity over the volume displaced by the iceberg in Fig. 6.1 for $\Gamma = 1$: Top) Easting velocities and (bottom) Northing velocities.

Because translational iceberg motion is dominated by the Coriolis and HPG forces, it is proposed that the remaining forces in Fig. 6.2 may be excluded from the iceberg motion model with negligible degradation of performance. To evaluate this proposal, it is necessary to analyze the influence the 6 other forces in Eq. 6.1 have on angular orientation. This is important because iceberg orientation is used to calculate the mean water velocity over the submerged iceberg profile, and the mean water velocity is used to calculate the HPG force. As a result, it is necessary to quantify the variability of the mean ocean current velocity over the iceberg's volume with respect to iceberg orientation angle.

To gain insight into the variability of the mean water velocity over the iceberg's volume, it is helpful to visualize ocean current variability over the iceberg's bottom surface. The initial water profile along the bottom surface for the iceberg in Fig. 6.2 is illustrated in Fig. 6.4. For comparison, the air profile along the top of the iceberg is also displayed in Fig. 6.4. Because of the large spatial extent of the iceberg, the bottom water velocity field contains spatially-diverse micro-eddies while the top wind profile is relatively homogeneous at this scale.

The mean water velocity over the iceberg's volume with respect to iceberg orientation angle is displayed in Fig. 6.5. The mean water velocity over the iceberg's bottom surface is also displayed in Fig. 6.5. For comparison, the mean air profile is displayed in Fig. 6.6. The iceberg orientation angle is defined such that 0° corresponds to the iceberg's major axis oriented eastward, and a positive-increasing angle corresponds to counter-clockwise motion. Note that the mean water velocity over the iceberg's displaced volume varies in magnitude by 13.1% and in direction by 1.4° . The mean water velocity over the iceberg's bottom surface is similar. The mean air velocity over the iceberg's top surface varies in magnitude by 0.25% over 0.03° . As a result, ocean and air current profiles are treated as heterogeneous and homogeneous climate fields, respectively, when calculating drag coefficients in Section 6.4.1. Also because the water velocity profile is correlated with the spatial orientation of the iceberg, the forces that affect iceberg orientation (all forces in Eq. 6.1 except the Coriolis and HPG forces) are maintained in this chapter, resulting in more accurate iceberg simulations.

I now analyze the magnitude of the extra forces introduced in Section 6.3: 1) the side "lift" force caused by rotational motion and 2) the additional drag force caused by the generation of internal ocean waves. To calculate the first, knowledge of iceberg rotation is necessary. In

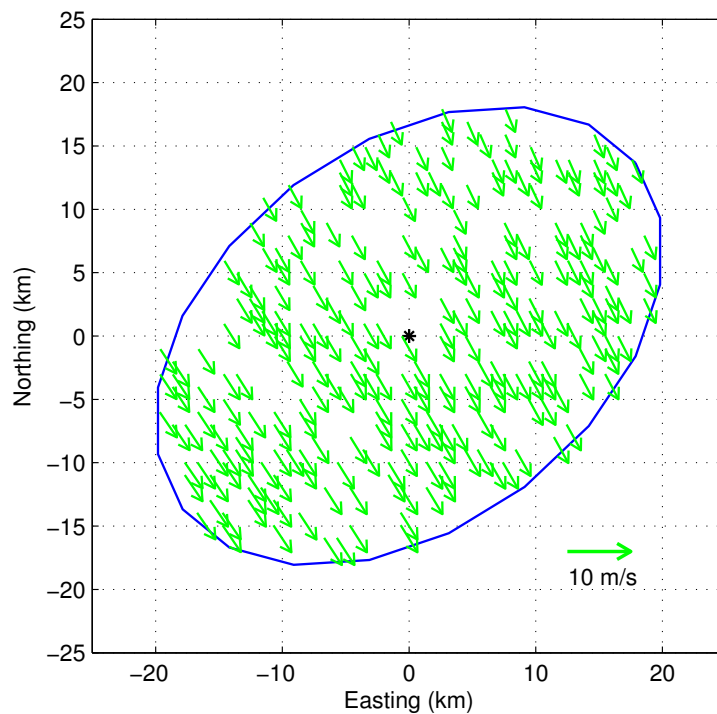
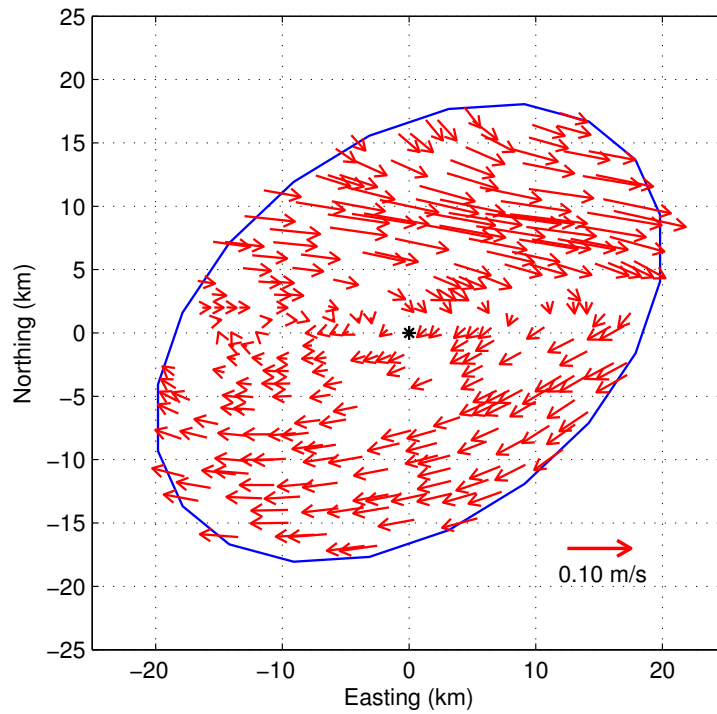


Figure 6.5: Initial flow profiles along the simulated iceberg's horizontal surfaces in the iceberg motion model: Top) water profile along the bottom and (bottom) wind profile along the top. Oceanographic mass-flow convention is used in these illustrations (as opposed to meteorological convention).

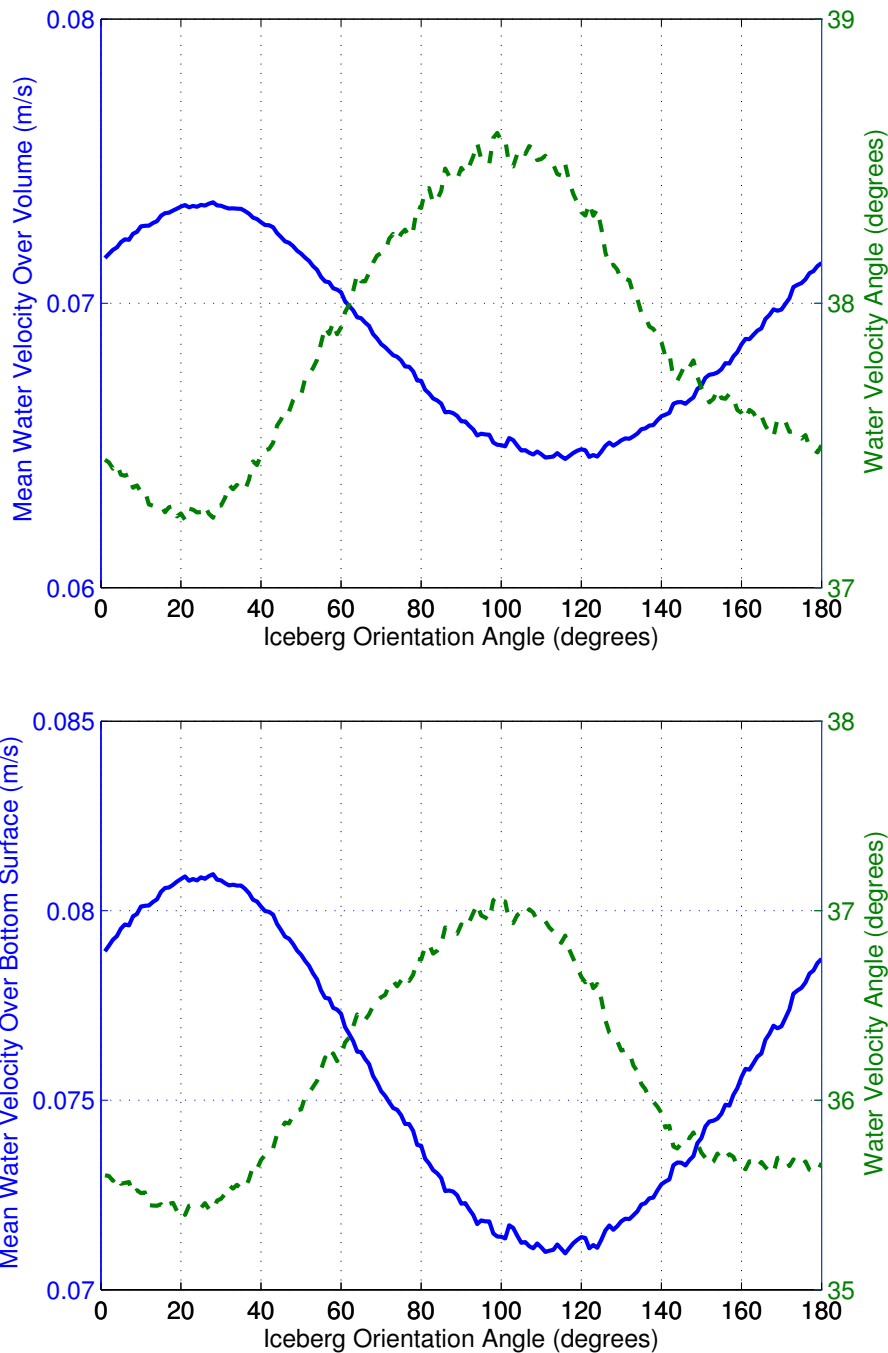


Figure 6.6: Average water velocity with respect to iceberg orientation angle. Velocities are depicted by magnitude (solid) and angle (dashed). Top) Mean water velocity over the displaced volume of the iceberg. Bottom) Mean water velocity over the bottom surface of the iceberg. Iceberg orientation angle is defined where 0° corresponds to the iceberg’s major axis oriented eastward, and a positive-increasing angle corresponds to counter-clockwise motion.

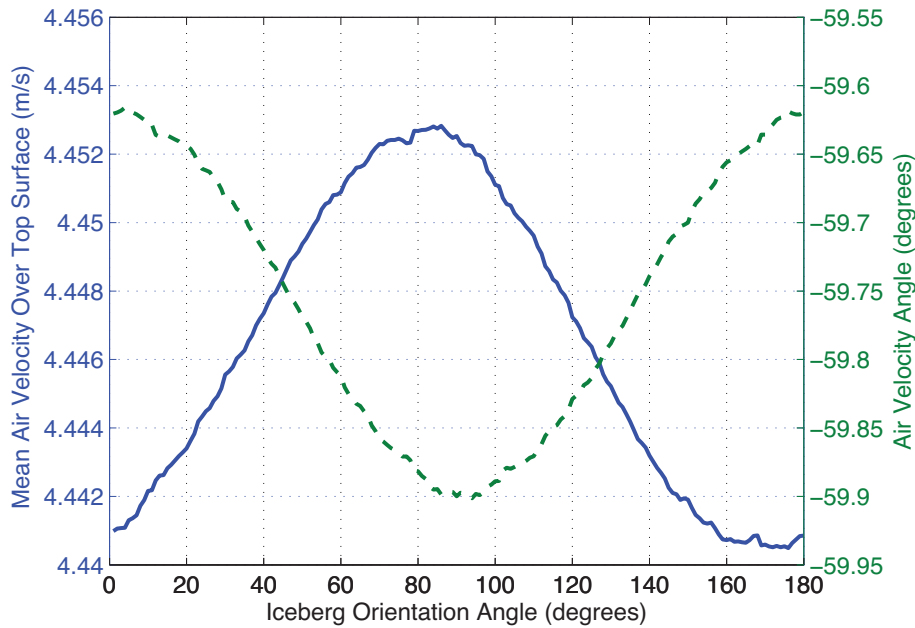


Figure 6.7: Average air velocity over the iceberg’s top surface with respect to iceberg orientation angle. Velocity is depicted in magnitude (solid) and angle (dashed). Iceberg orientation angle is defined where 0° corresponds to the iceberg’s major axis oriented eastward, and a positive-increasing angle corresponds to counter-clockwise motion.

the MERS Antarctic iceberg database, iceberg rotation rates rarely exceed 25° per day (see case study), with extreme rotation rates observed up to 45° per day [8, 93]. For the simulated iceberg in Fig. 6.2, using the extreme rotation rate produces an upper bound of $1e8$ N on the magnitude of the lift force that would be exerted on the simulated iceberg described in Fig. 6.2. However, I note that Eq. 6.11 assumes a homogeneous ocean current profile around the iceberg. Because complex ocean eddies over an iceberg’s bottom surface (e.g., Fig. 6.4a) are a dominant factor driving iceberg rotation, the net ocean circulation around an iceberg is potentially much less than values calculated using Eq. 6.11. As a result, the lift force is numerically insignificant compared to the Coriolis and HPG forces when calculating the translational motion for large tabular icebergs, thus the lift force is excluded from this study.

For the second extra force, the drag due to internal wave generation on the simulated iceberg in Fig. 6.2 is approximately $1e7$ Newtons (N). While comparable to the other forces in Eq. 6.1, dominant iceberg motion is translational movement; therefore, the extra drag force primarily extracts energy from the iceberg’s translational energy. Because translational motion is dominated by

the Coriolis and HPG forces ($1e9$ N), the amount of energy taken by the internal-wave drag force ($1e7$ N) is numerically insignificant. For large tabular icebergs, this extra drag force is related to the iceberg’s physical geometry (see Appendix) and thus will always be 1-2 orders of magnitude less than the Coriolis and HPG forces. Thus it is excluded from this study.

Note that under the same argument (i.e., numerical significance), the majority of the forces in Eq. 6.1 could also be excluded from this study; however, I have chosen to include all the forces in Eq. 6.1 to compare numerical results and relative importance with previous studies, specifically those that highlight small non-tabular icebergs.

6.5.2 Case Study

Next I apply the iceberg motion model to estimate iceberg parameters for a particular iceberg. For this analysis, an iceberg that characterizes dominant iceberg motion profiles is preferred. The availability of the external climate datasets limits our selection to icebergs between 2000-2004.

For this case study, I choose iceberg B09a because its track characterizes the movement profile of 90% of icebergs in the Southern Ocean [8]. Specifically, iceberg B09a calved off of the Ross glacial ice sheet and circumnavigated the Antarctic glacial continent westward until it arrived in the Weddell Sea where it was eventually ejected into the Scotia Sea along the “Iceberg Alley” corridor, making its way into the Antarctic Circumpolar current (ACC). The 2000-2003 segment of iceberg B09a’s track describes the iceberg’s journey as it circumnavigates part of the glacial continent, transverses the Weddell Sea, and enters the ACC. Iceberg B09a drifts outside of the standard tracking perimeter in the MERS database (above 52° S) at the beginning of 2003 [7]; this study focuses on icebergs in the main tracking region. The initial dimensions of iceberg B09a during the period of interest is 45×30 km. Iceberg B09a is an appealing case study because a portion of its track is in coastal water and the remainder is in the deep ocean, potentially allowing for a comparison of model performance with ocean depth. This is of interest because near-coastal waters potentially contain higher degrees of climatological uncertainty (Section 6.2.1). While this study emphasizes iceberg motion around the Antarctic glacial continent and in the Weddell Sea, additional motion studies throughout the Southern Ocean are contained in the companion study, [12].

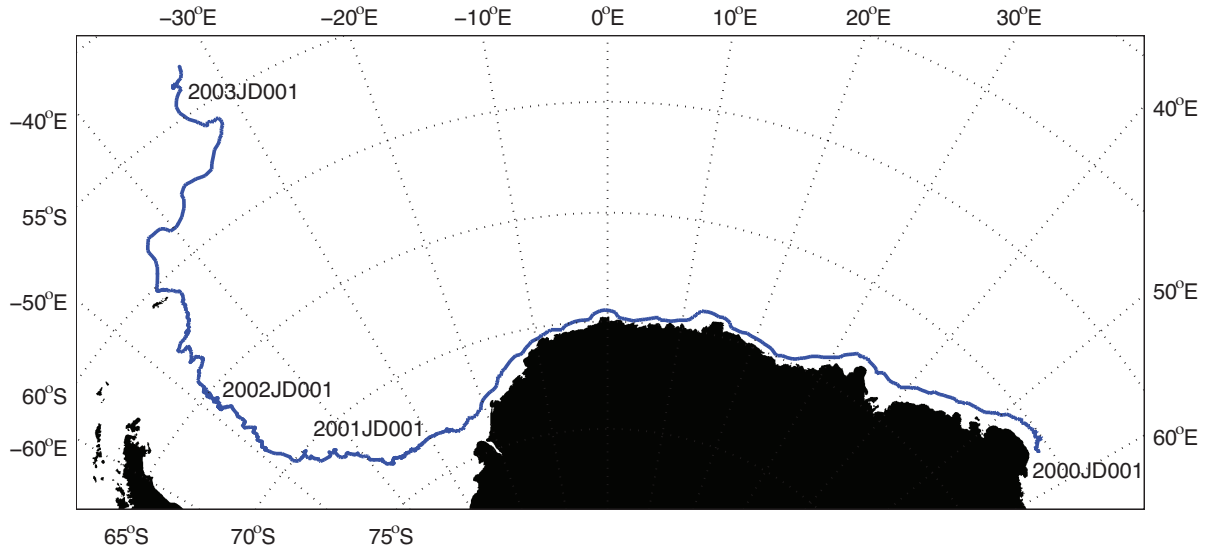


Figure 6.8: Positions of iceberg B09a from 2000 JD 001 to 2003 JD 25 as reported in the MERS Antarctic iceberg database.

The track of iceberg B09a from 2000 JD 001 to 2003 JD 25 is depicted in Fig. 6.7. Size estimates of iceberg B09a are calculated using the size estimation technique published in [10]. Estimates of the major axis and minor axis of iceberg B09a are displayed in Fig. 6.8. To highlight general movement trends, each dataset is filtered using a 101-pt Epanechnikov filter, overlaid on each image. Standard deviation between major-axis and minor-axis estimates and the non-parametric fit is 2.4 and 2.1 km, respectively. Estimates of the angle of rotation of iceberg B09a are displayed in Fig. 6.9. An 11-pt Epanechnikov filter is fitted to highlight net movement. Standard deviation between angle estimates and the non-parametric fit is 11.6° . More than 99% of the observed iceberg rotation rates are less than 25° per day, with the most extreme rotation rate being 33° per day. Keel depth is derived from the parent glacial ice sheet as referenced in [68] (255 m for the Ross ice sheet) and is assumed to be constant over the tracking period.

Due to uncertainties in the modeling process of iceberg B09a, the performance of the iceberg motion model is related to the length of the temporal window. Specifically, model performance is inversely related to the length of the temporal window. To quantify the performance of the iceberg motion model with respect to time, the iceberg model is initialized using observed daily positions of iceberg B09a and the iceberg model is projected up to 30 days into the future. Performance is measured with respect to the distance between the observed and simulated iceberg

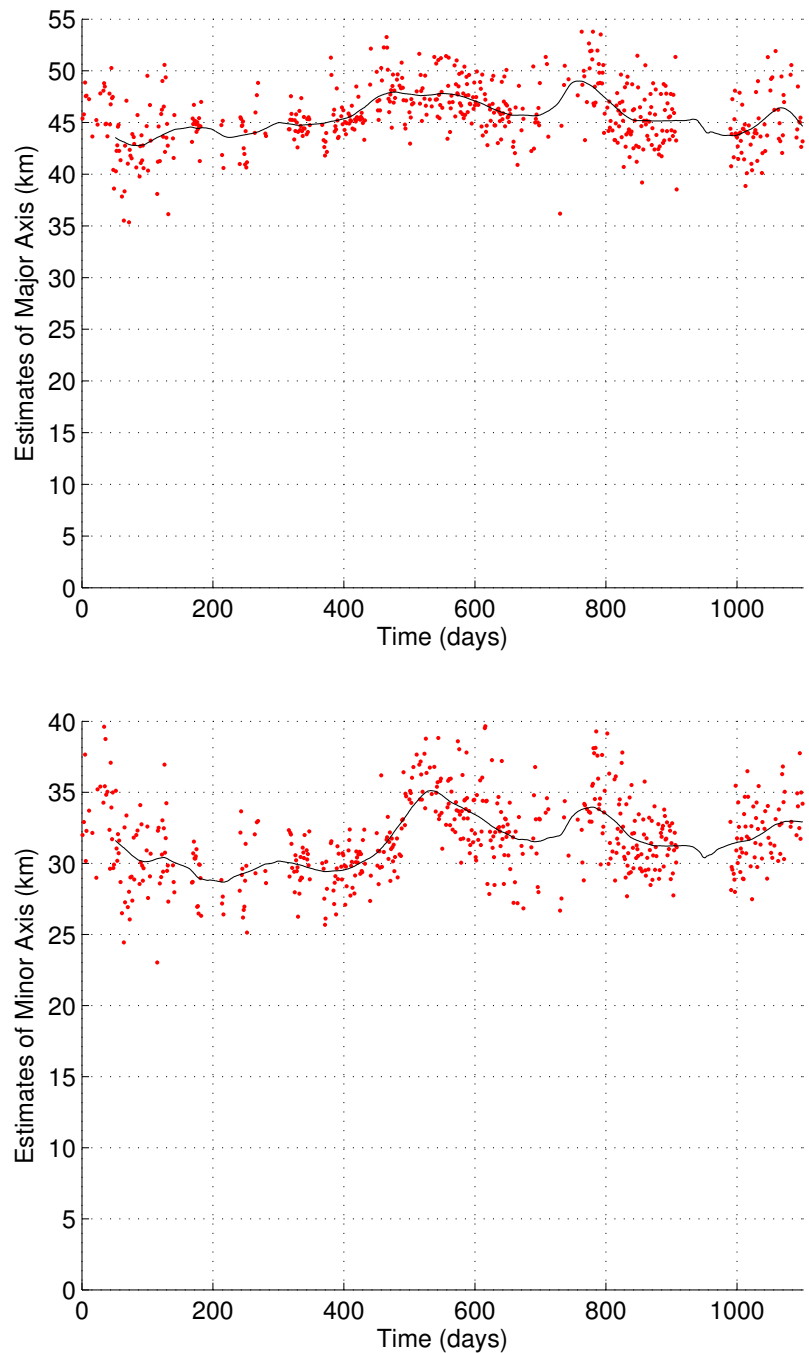


Figure 6.9: Characteristics of iceberg B09a in the Weddell Sea from 2000 JD 001 to 2003 JD 25: Top) Estimated major axis length. Bottom) Estimated minor axis length. Day 1 corresponds to 2000 JD 001. To highlight net iceberg movement, a trend curve is depicted using a 101-pt Epanechnikov filter.

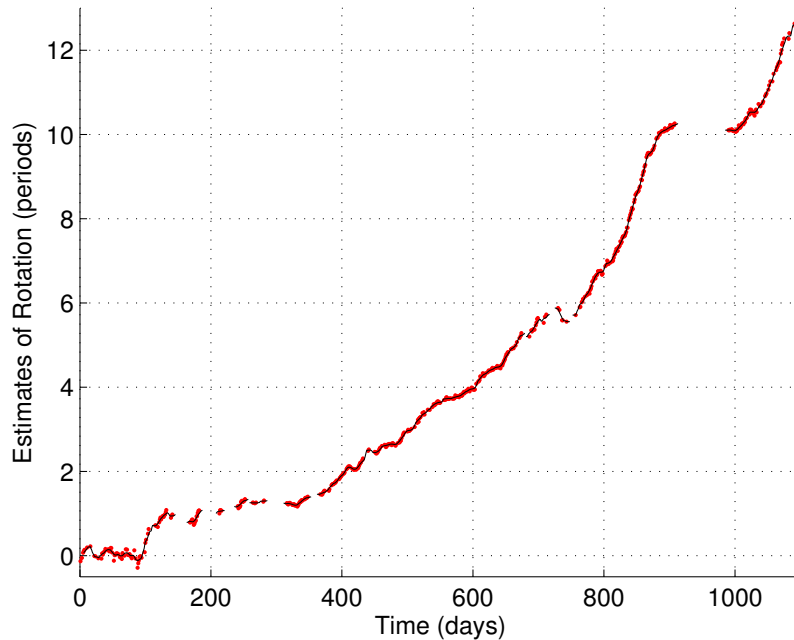


Figure 6.10: Estimated angle of rotational orientation of iceberg B09a from 2000 JD 001 to 2003 JD 25. To highlight net iceberg movement, a trend curve is depicted using an 11-pt Epanechnikov filter. Vertical axes have been scaled such that 360° correspond to one rotation period, and estimates have been unwrapped with respect to the initial day of study to show rotational evolution. An increasingly positive angle corresponds to counter-clockwise motion.

positions during the 30-day period. For example, the first performance run is where the motion model is initialized with iceberg parameters observed on 2000 JD 001 and the model is propagated to 2000 JD 031. The distance between the actual and simulated iceberg positions is computed for days 2-31. Distance is measured with respect to the centroid of each iceberg estimate.

This process is repeated for all observed positions of iceberg B09a from 2000 JD 002 to 2003 JD 25. Average model drift results are displayed in Fig. 6.10. Average differences in rotational orientation are also displayed in Fig. 6.10. Notice that the position drift between iceberg observations and simulated results is a linear trend over the 30-day window. Conversely, the angular drift between actual observations and simulated results is approximately linear for the first 4 days and then converges to approximately 65° . Note that the convergent behavior of the bottom figure in Fig. 6.10 between days 5 and 30 is not due to stabilization of iceberg rotation but is an artifact of angle wrapping of the iceberg model.

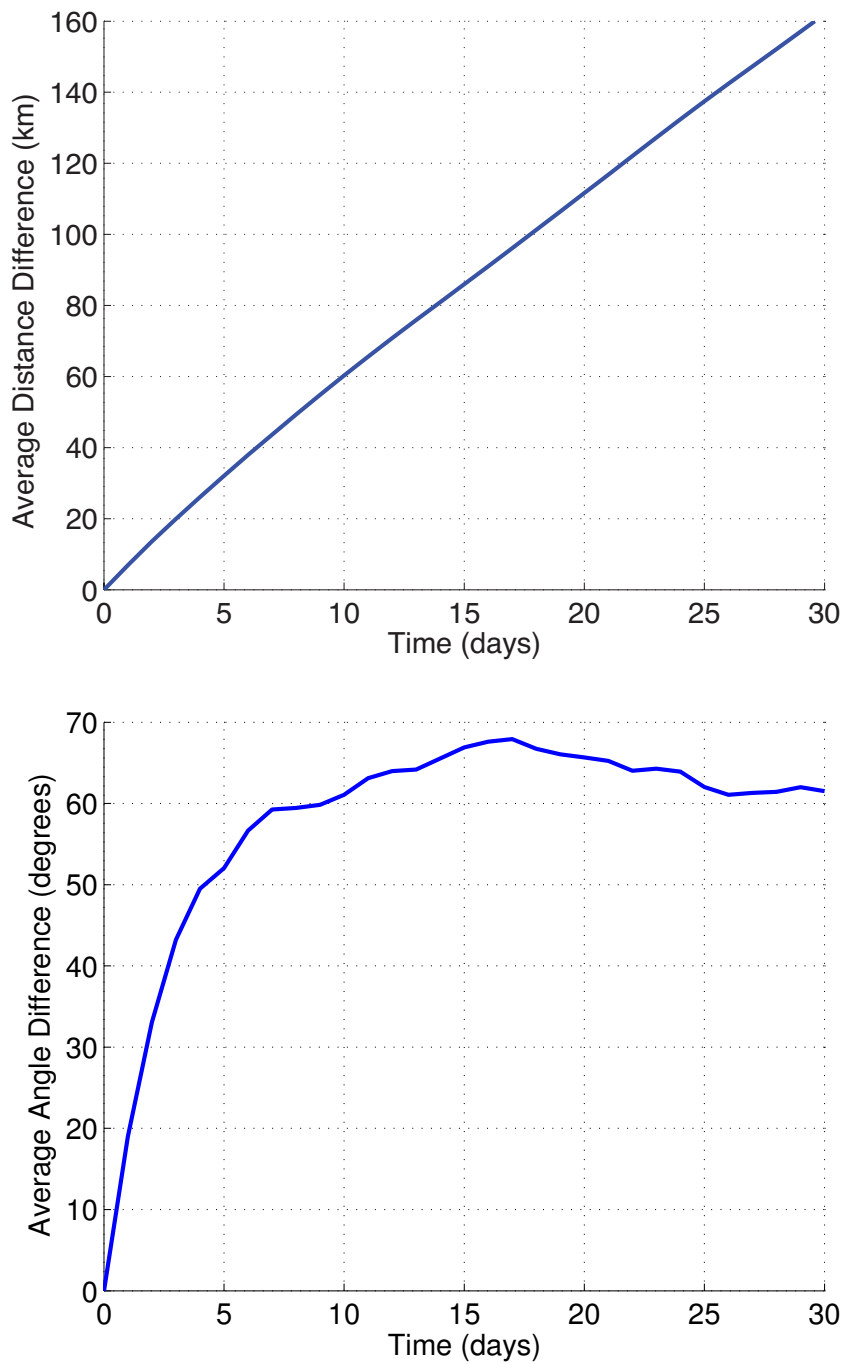


Figure 6.11: Performance analysis of the B09a iceberg model from 2000 JD 001 to 2003 JD 25. Top) Average difference between observed and simulated iceberg positions with respect to length of prediction. Iceberg position is defined with respect to the iceberg’s centroid. Bottom) Average difference between observed and simulated angle of rotational orientation with respect to length of prediction.

In addition to quantifying overall performance of the iceberg motion model, it is also advantageous to analyze model performance with respect to observable parameters, such as spatial location, ocean current speed, simulated iceberg speed, etc. The correlation between the performance of the iceberg motion model and several model parameters was tested, all producing translational and rotational drift profiles similar to values presented in Fig. 6.10. Simulated iceberg performance was not found to be correlated with OCCAM current velocities; however, simulated motion accuracy was found to be correlated with observed iceberg speed. A histogram of the observed iceberg speeds of iceberg B09a from 2000 JD 001 to 2003 JD 25 is displayed in Fig. 6.11. For comparison, a histogram of modeled iceberg speeds is also displayed in Fig. 6.11. Note that because the Coriolis and HPG forces are the dominant forces affecting translational motion of large tabular icebergs, observed iceberg speeds are an indirect Lagrangian indicator of underlying ocean current velocities, a theme discussed in [12].

To reduce sample estimation error, observed iceberg velocities are divided into 4 sample sets where each set has the same number of icebergs, and iceberg motion model performance is analyzed with respect to each quartile. The first set is defined as the iceberg model estimates where the observed iceberg speed for the given day is 0-0.03 m/s. The remaining sets are similarly partitioned with observed iceberg speeds of 0.03-0.05 m/s, 0.05-0.12 m/s, and 0.12-0.4 m/s, respectively. Spatial locations of where each set lies is illustrated in Fig. 6.12. Average translational drift between iceberg motion model estimates and observed iceberg positions is displayed in Fig. 6.13. Average rotational drift between iceberg motion model estimates and observed iceberg positions is also displayed in Fig. 6.13. Notice how average translational drift is related to observed iceberg velocity where slower observed speeds correspond to smaller average drift between observed iceberg and modeled iceberg positions.

6.5.3 Data Assimilation

To improve the performance of the iceberg motion model, data assimilation techniques are used to augment the iceberg motion model with actual iceberg measurements. As previously mentioned, I chose to use the extended-Kalman filter because of its explicit covariance matrix which was used to quantify model performance.

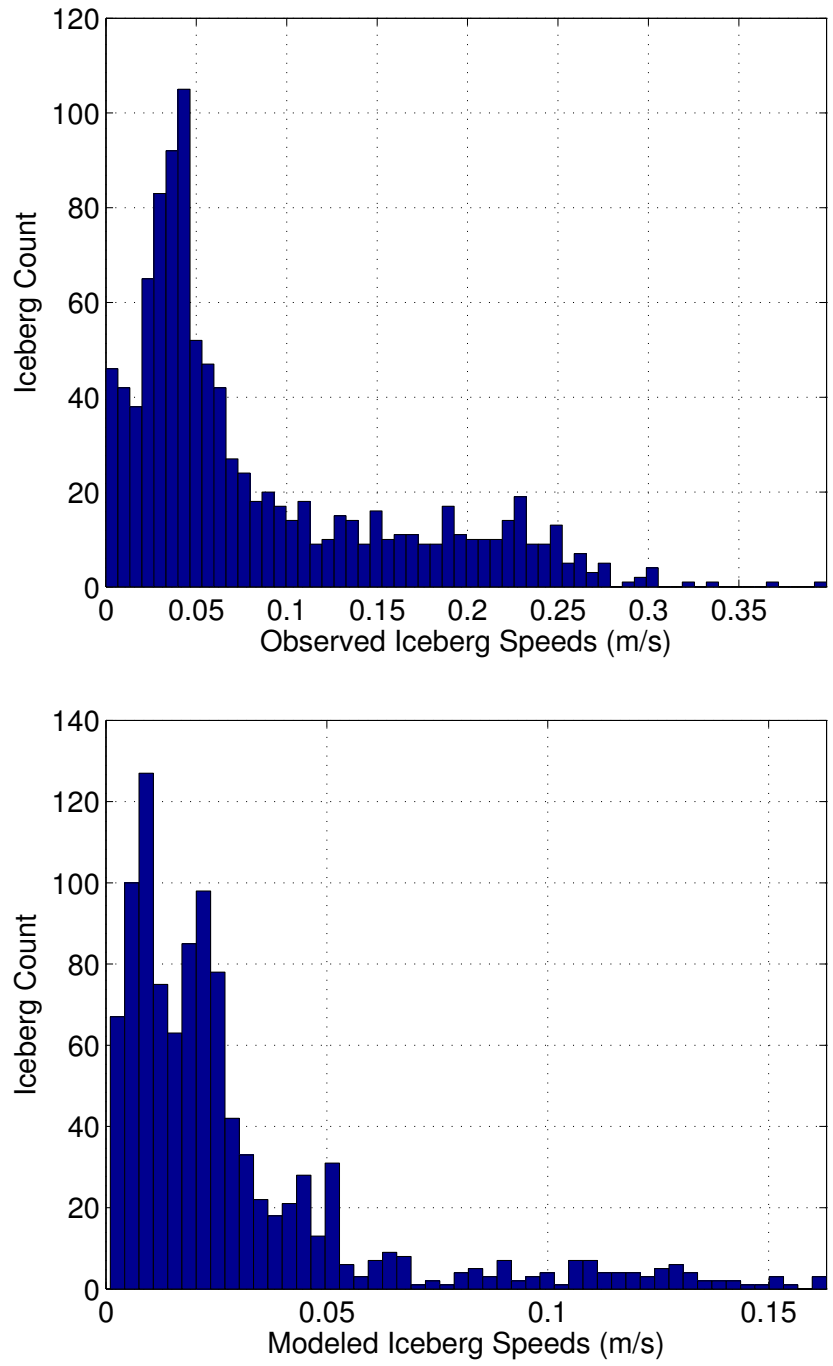


Figure 6.12: Histograms of the (top) observed and (bottom) simulated speeds of iceberg B09a from 2000 JD 001 to 2003 JD 25.

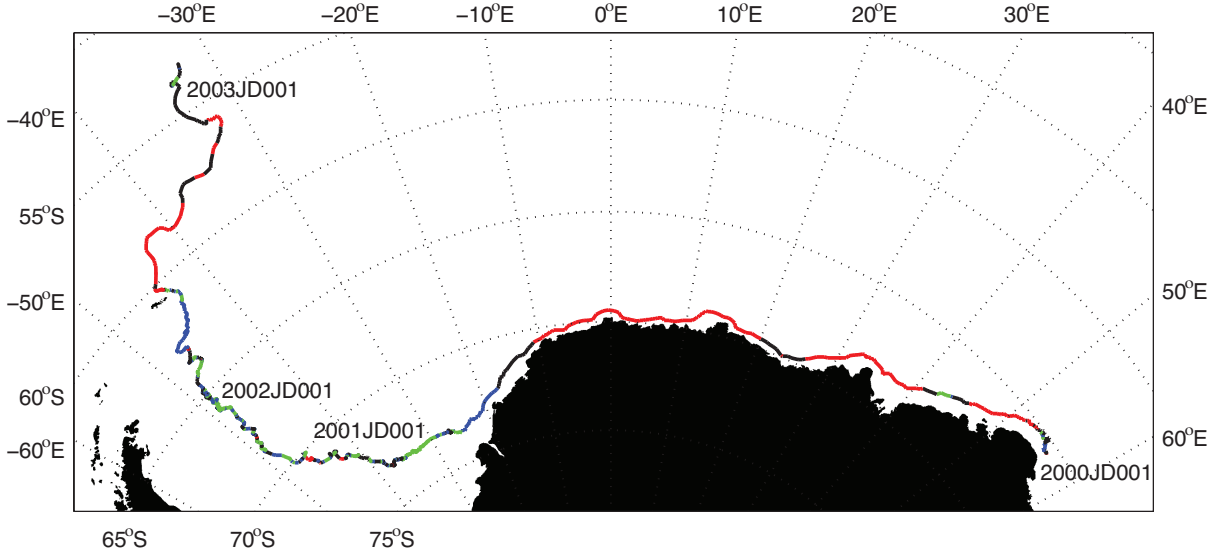


Figure 6.13: Track of the B09a iceberg model from 2000 JD 001 to 2003 JD 25 with velocity segments highlighted. Colors that highlight iceberg motion are defined in Fig. 6.13.

To apply the Kalman filter, it is necessary to derive explicit expressions for both model and observation uncertainty. Model performance is analyzed in Section 6.5.2. To populate the model covariance matrix, I chose the standard deviation (STD) of the translational motion of the model to be the mean drift distance between the iceberg motion model and observed iceberg positions as reported in Fig. 6.13 with respect to observed iceberg velocity. The covariance matrix P requires that the STD in both the easting and northing be explicitly stated. Because translational STD is directly related to observed iceberg speed, I define the translational STD in the easting direction, STD_dist_E , to be a weighted average of the total translational STD, STD_dist , where $STD_dist_E = STD_dist \cdot |V_{i,E}|/|V_i|$ where $|V_{i,E}|$ is the magnitude of the iceberg's eastward velocity and $|V_i|$ is the total iceberg's speed [88]. Similarly, $STD_dist_N = STD_dist \cdot |V_{i,N}|/|V_i|$. The STD of the angle, STD_ang , is set to the mean angular differences reported in Fig. 6.13, resulting in $Q = \text{diag}([STD_dist_E, STD_dist_N, STD_ang])^2$.

Actual iceberg observations have two sources of uncertainty: temporal and spatial. Daily temporal uncertainty is related to the time during a 24 hr period during which an iceberg measurement is recorded. Due to orbit geometry and swath width of the SeaWinds scatterometer, a single iceberg is frequently detected multiple times in a 24-hr period, especially at extreme lati-

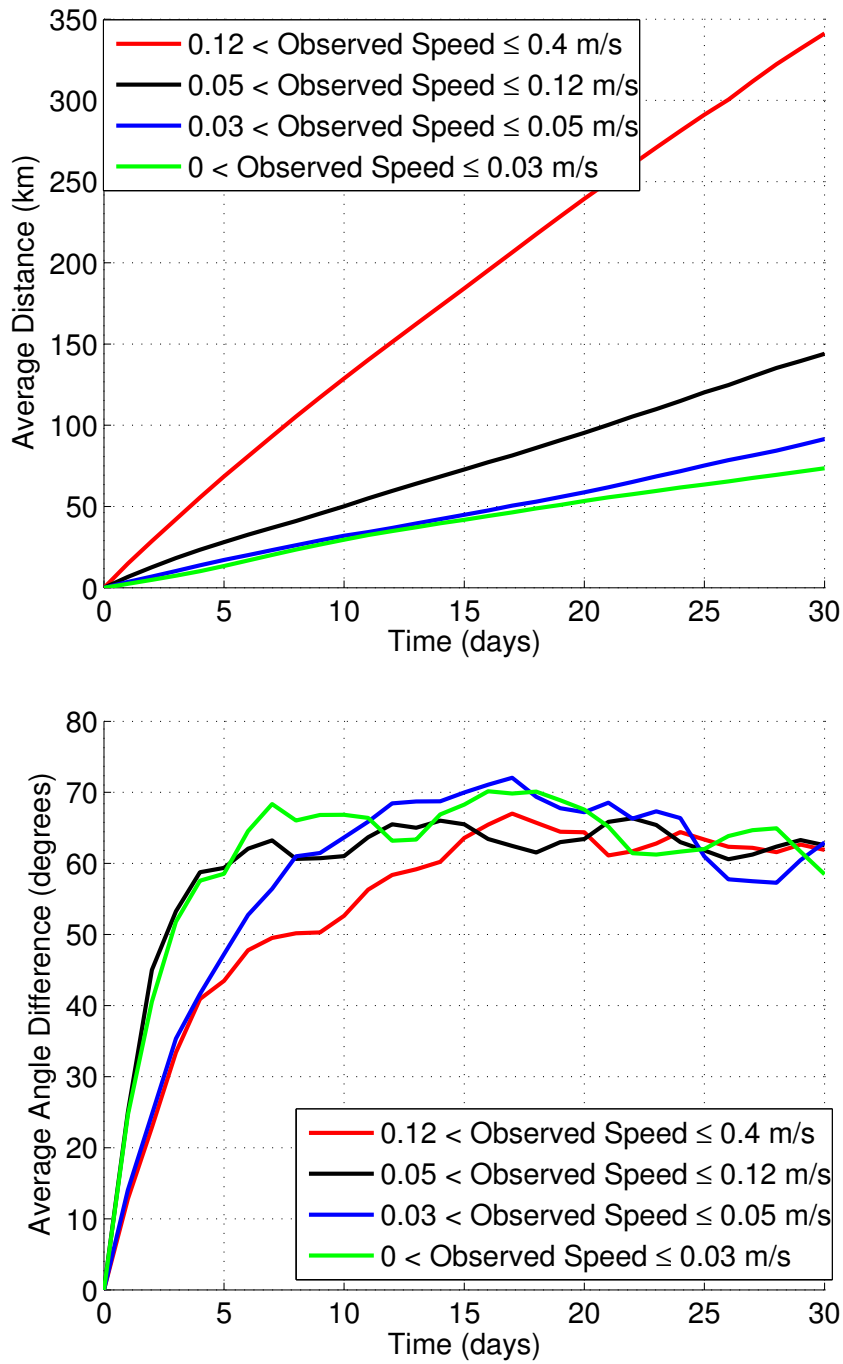


Figure 6.14: Performance analysis of the B09a iceberg model from 2000 JD 001 to 2003 JD 25. Performance is measured as the average distance between an iceberg’s observed position and predicted position, up to 30 days into the future. Distance is defined with respect to the iceberg’s centroid.

tudes [6,94]. When computing scatterometer images, all satellite swaths are included in the image formation process, resulting in an effective time of iceberg detection that varies in daily radar images [95]. Over the time span of the case study, iceberg B09a is detected an average of 4 times per day. Assuming each observation is uniformly distributed over a 24-hr time period, the expected STD of 4 such measurements is approximately 3.45 hours (12420 sec). The corresponding temporal observation uncertainty can be quantified as $R_{temporal} = \text{diag}(12420 \cdot [V_{iE}, V_{iN}, V_{iAng}])^2$.

The spatial deviation in SeaWinds measurements is related to the performance of the iceberg size estimation algorithm developed in [10]. For this study, I assume negligible uncertainty in estimating translational iceberg position [8]. However, as reported in Section 6.5.2 (Fig. 6.9), the STD of the angle estimates is 11.6° ; therefore, I set $R_{spatial} = \text{diag}([0, 0, 11.6])^2$. The statistical distributions of $R_{temporal}$ and $R_{spatial}$ are assumed to be independent and normally distributed; therefore, $R = R_{temporal} + R_{spatial}$.

Using the estimates of Q and R above, I now analyze the performance of the Kalman filter by observing the time-evolution of the matrix trace and norm of the covariance matrix, $Tr\{P\}$ and $\|P\|$. Kalman filter performance is also analyzed given intermittent iceberg observations where the frequency of measurement availability reflects the availability of iceberg observations in the MERS Antarctic iceberg database. As previously mentioned, measurement availability can be modeled in two ways: 1) as a Bernoulli random process with an associated probability of arrival and 2) as a deterministic data stream with a continuous dropout interval.

When the arrival of measurements is modeled as a Bernoulli random process, it is necessary to analyze the behavior of $Tr\{P\}$ and $\|P\|$ with respect to the probability of arrival, thus I sweep the probability of arrival from 100% to 30% in increments of 10%; arrival probabilities lower than 30% produce unstable behavior due to insufficient model wind-up time between update measurements and are excluded from this study. The P matrix corresponding to each arrival probability is denoted $P_{B,*}$ where $*$ is the probability of arrival, e.g., $P_{B,80}$ is the Kalman filter covariance matrix where measurement updates are modeled as a Bernoulli random process with an 80% arrival rate.

To compute the expected performance of $Tr\{P\}$ for each arrival rate, 25 instances are computed using Monte Carlo simulation and averaged. Results were smoothed using a 31-point median filter and are displayed in Fig. 6.14. For visual comparison, the square-root of $Tr\{P_{B,*}\}$ is also shown in Fig. 6.14. Similarly, $\|P_{B,*}\|$ is shown in Fig. 6.15, and the square-root of $\|P_{B,*}\|$

is displayed in Fig. 6.15. Notice that the trace and norm of P are similar in shape and magnitude because P is a diagonally-dominant matrix. Regions where the trace and norm are higher correspond to when the iceberg motion model diverges more from observed iceberg positions. Days 1-250 correspond to the rapid movement of iceberg B09a around the Antarctic glacial continent, days 250-1000 were when B09a transversed the Weddell Sea through Iceberg Alley, and days 1000+ were when B09a entered the ACC. The beginning of the spike in the trace around day 550 corresponds to when B09a traveled around Coronation Island (see Fig. 6.7).

While analyzing the trace of P gives us a sense of overall performance of the Kalman filter, analyzing sub-components of P gives added insight into the performance of the iceberg model. For instance, the first two rows and columns of P (denoted $P^{1,2}$) corresponds to the translational uncertainty of the Kalman estimate; similarly, the lower right-most element of P (denoted P^3) corresponds to the angular uncertainty. Analyzing the trace of each sub-matrix gives added insight into the Kalman filtering process. The square-root of $Tr\{P_{B,*}^{1,2}\}$ and $Tr\{P_{B,*}^3\}$ are displayed in Fig. 6.16. We note that the performance of $\|P_{B,*}^{1,2}\|$ is visually similar to the top figure in Fig. 6.16 and $\|P_{B,*}^3\|$ is mathematically identical to the bottom figure in Fig. 6.16; therefore, the norms of the sub-matrices are not shown. Spikes in the trace correspond to regions where the iceberg model diverges more from iceberg observations. I observe that the bottom figure in Fig. 6.14 and the top figure in Fig. 6.16 are essentially identical, emphasizing that total uncertainty in iceberg motion simulation is dominated by translational uncertainty. Also note that rotational uncertainty is largely independent of the translational uncertainty (and thus angular orientation is independent of iceberg speed), supporting earlier observations in Section 6.5.2.

For the second case, measurement updates are modeled as a deterministic data stream with a continuous dropout interval. To understand the behavior of $Tr\{P\}$ with respect to dropout size, I sweep the dropout interval using lengths of [1 2 4 8 16 32] days. To make each trial comparable, each dropout cycle is followed by a reacquisition period three times longer than the dropout interval, producing a duty cycle of 75%. The P corresponding to each dropout interval is denoted $P_{D,*}$ where $*$ is the dropout interval size. Multiple simulations were used to compute the expected performance of $Tr\{P\}$, and a 31-point median filter was used for smoothing. The time-evolution of $Tr\{P_{D,*}\}$ is displayed in Fig. 6.17. For ease of visualization, the square-root of $Tr\{P_{D,*}\}$ is also displayed in Fig. 6.17. Similarly, $\|P_{B,*}\|$ is shown in Fig. 6.18, and the square-root of $\|P_{B,*}\|$

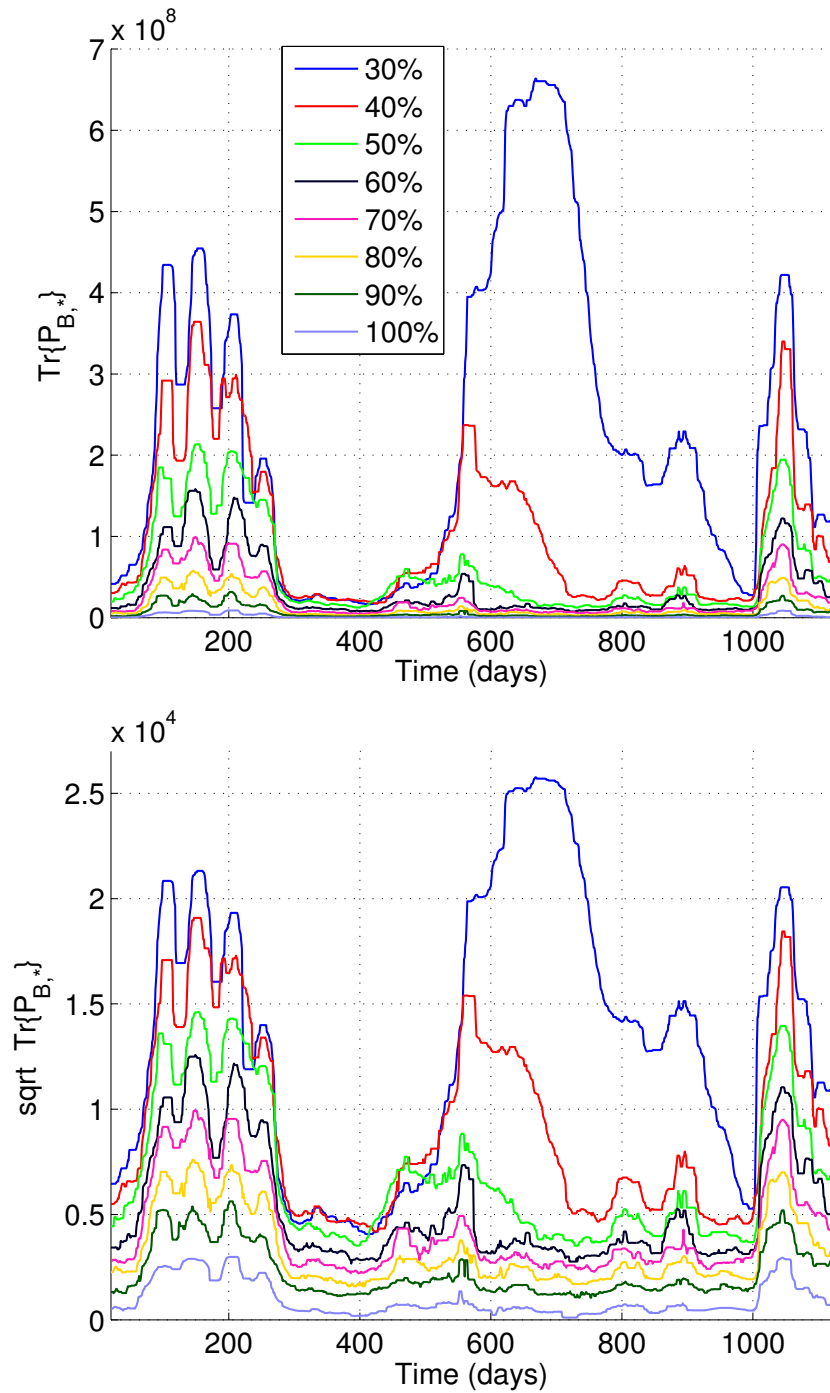


Figure 6.15: Time evolution of the trace of the Kalman filter covariance matrix, P , for iceberg B09a from 2000JD001 to 2003JD20. Measurement updates are modeled as a Bernoulli random process with arrival rates between 30% and 100%: Top) The trace of P . Bottom) square-root of the trace of P . The legend corresponds to both figures.

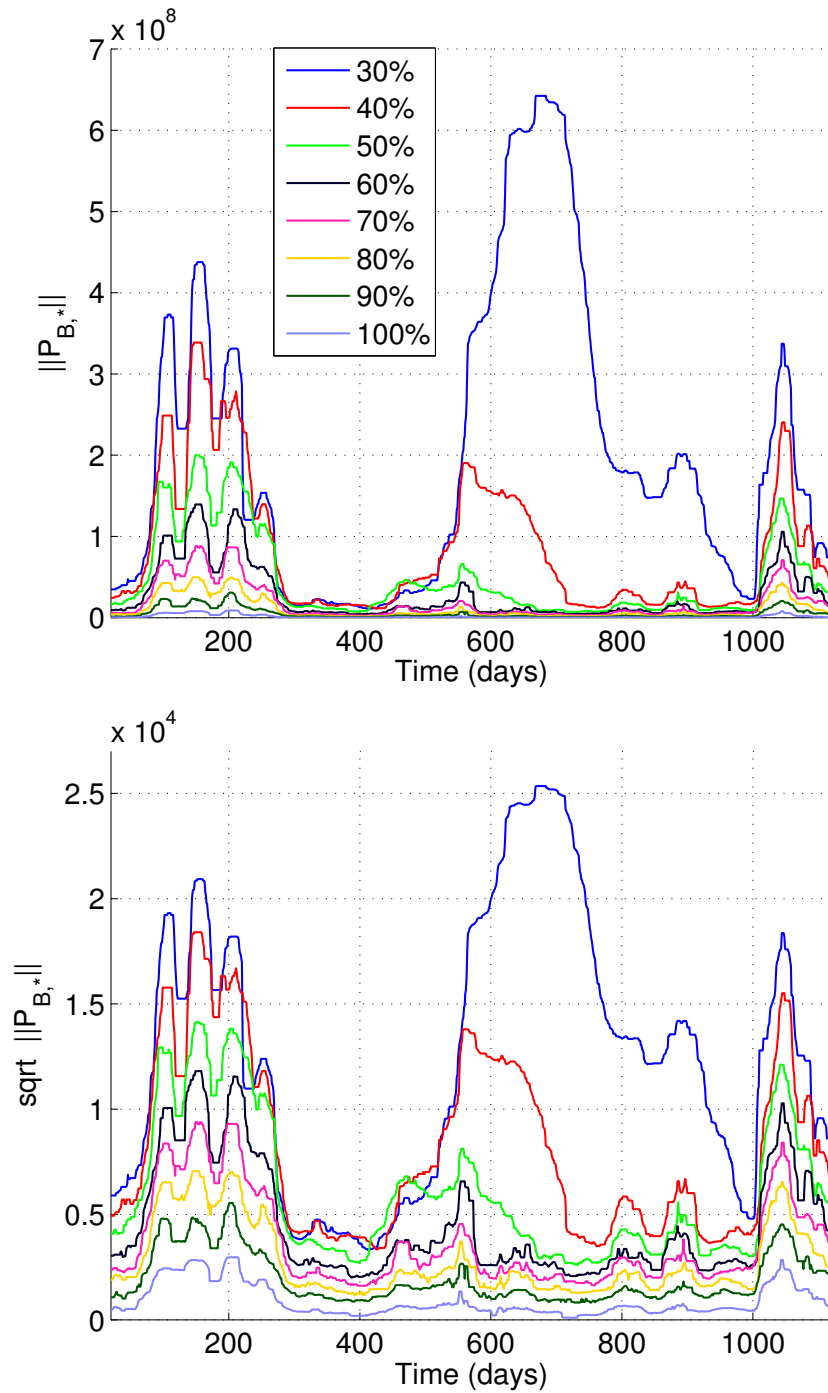


Figure 6.16: Time evolution of the norm of the Kalman filter covariance matrix, P , for iceberg B09a from 2000JD001 to 2003JD20. Measurement updates are modeled as a Bernoulli random process with arrival rates between 30% and 100%: Top) The norm of P . Bottom) the square-root of the norm of P . The legend corresponds to both figures.

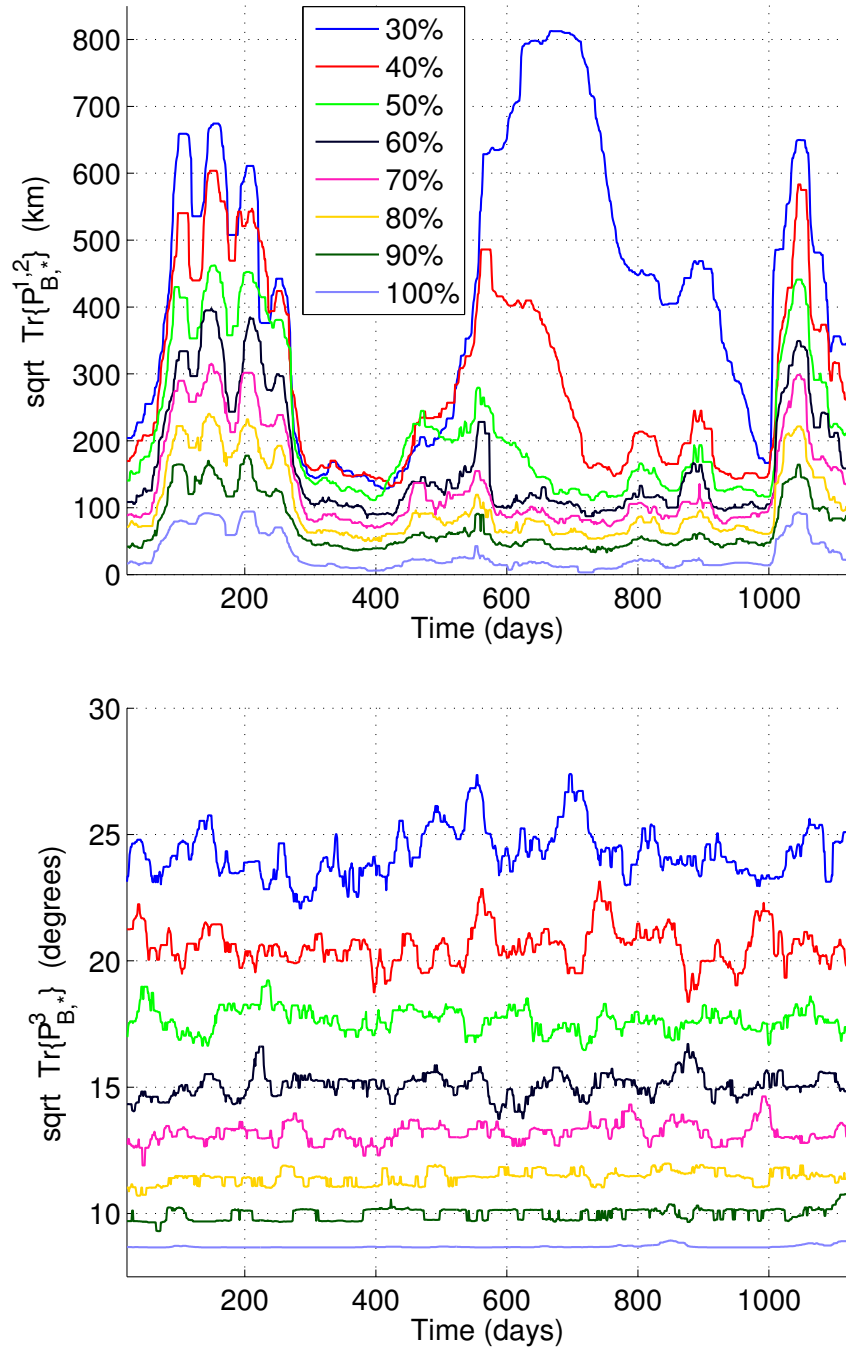


Figure 6.17: Time evolution of sub-components of the trace of the Kalman filter covariance matrix, P , for iceberg B09a from 2000JD001 to 2003JD20. Measurement updates are modeled as a Bernoulli random process with arrival rates between 30% and 100%: a) square-root of the trace of the first two rows and columns of P , and b) square-root of the lower-right-most element of P . The legend in (a) corresponds to both figures.

is displayed in Fig. 6.18. The time-evolution of sub-matrices $Tr\{P(1,2)_{D,*}\}$ and $Tr\{P(3)_{D,*}\}$ are displayed in Fig. 6.19. Note the similarities in overall behavior between the Bernoulli and deterministic cases.

6.6 Discussion

Conditions that contribute to iceberg motion uncertainty may be divided into three categories: 1) inaccurate source data, 2) completeness of the iceberg motion equations, and 3) numerical accuracy of solving the equations of motion. Uncertainty due to the source data can be further divided into spatial quantization errors and turbulence. Because translational iceberg motion is dominated by ocean currents (see Fig. 6.2), I focus the discussion on the OCCAM dataset.

The spatial quantization used in the OCCAM modeling process introduces uncertainty and artifacts into the iceberg motion model. In the OCCAM modeling process, the ocean current field is discretized using a grid size of $1/12^\circ$ in both latitude and longitude with a vertical size increasing with ocean depth, resulting in various voxel sizes. Each voxel is statically set as land or water [96]. As a result, characteristic land-water boundaries along the Antarctic coast, around islands, and bottom ocean topography are not well modeled, resulting in inconsistencies in both water speed and flow direction in OCCAM ocean current profiles. While these inconsistencies dissipate as the distance from the land-water boundary increases, icebergs frequently travel close to the Antarctic glacial continent and thus are affected by the transient ocean currents near the coast, increasing uncertainties in iceberg speed and direction [97].

Uncertainty in iceberg movement is also caused by turbulent ocean currents. Turbulent ocean currents large enough to affect tabular icebergs are frequently a result of water flow around large-scale geophysical obstructions or boundaries. For example, high-speed turbulent currents are observed in the Drake Passage due to the restriction and subsequent diffraction of the ACC as it passes between the Antarctic and South American continents. These observed high-speed currents form a periodic vortex stream (i.e., von Karman vortex street) with dramatic fluctuations in ocean current speed and direction. The characteristic vortex stream in the Drake Passage can be modeled as a time-periodic statistical distribution where the spatial frequency depends on characteristic geophysical parameters [98–100]. The ocean current profile at each time step in the OCCAM simulation represents only one instance of the underlying current distribution, and the

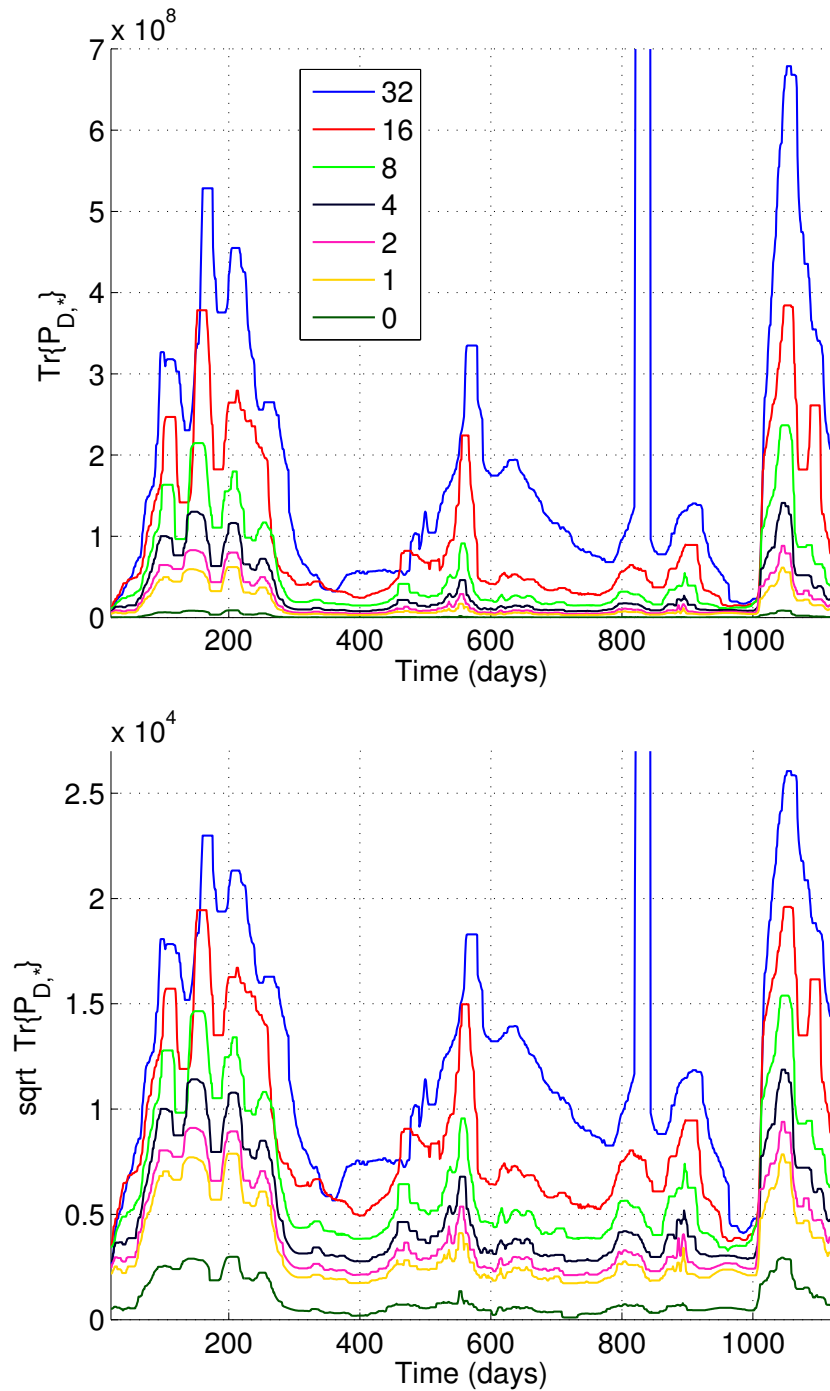


Figure 6.18: Time evolution of the trace of the Kalman filter covariance matrix, P , for iceberg B09a from 2000JD001 to 2003JD20. Measurement updates are modeled as a deterministic sequence with a continuous dropout interval where the size of the dropout interval is varied between one and 32 days: Top) the trace of P . Bottom) square-root of the trace of P . The legend corresponds to both figures. Vertical axes were scaled to be comparable with Figs. 6.14 and 6.16. The vertical spike in (top) around day 850 extends to approximately $1e12$.

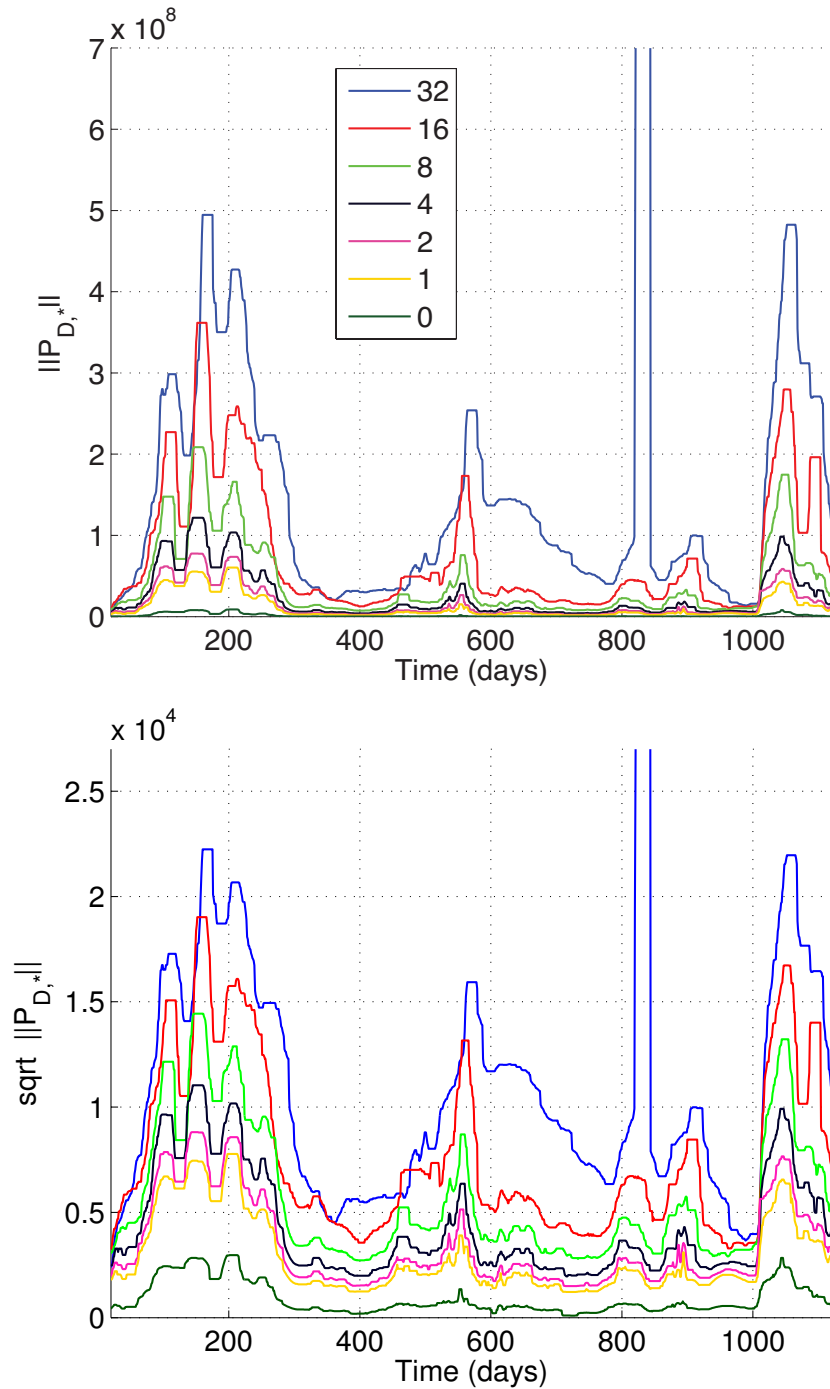


Figure 6.19: Time evolution of the norm of the Kalman filter covariance matrix, P , for iceberg B09a from 2000JD001 to 2003JD20. Measurement updates are modeled as a deterministic sequence with a continuous dropout interval where the size of the dropout interval is varied between one and 32 days: Top) the norm of P . Bottom) square-root of the norm of P . The legend corresponds to both figures. Vertical axes were scaled to be comparable with Figs. 6.14 and 6.16. The vertical spike in (top) around day 850 extends to approximately $1e12$.

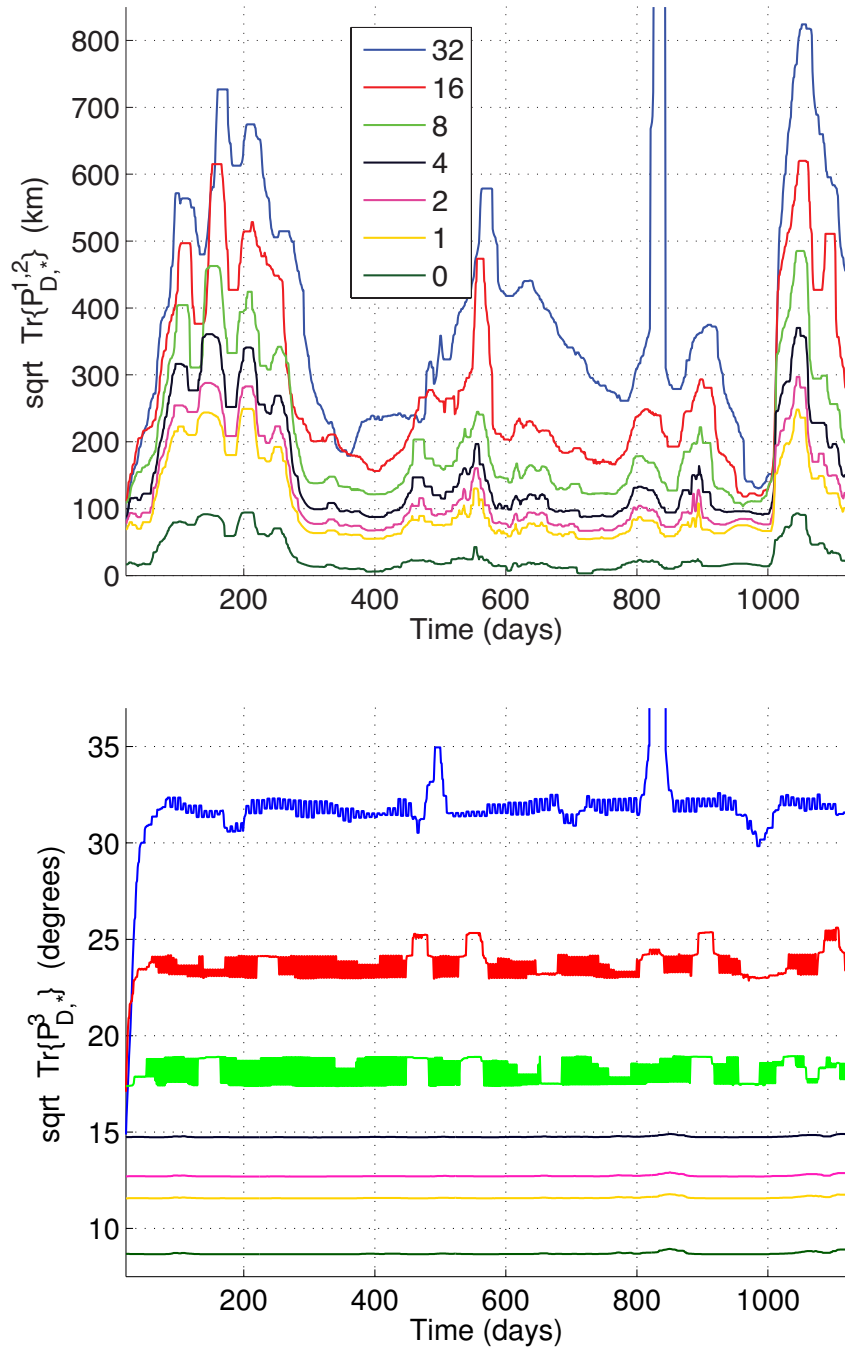


Figure 6.20: Time evolution of the trace and norm of the Kalman filter covariance matrix, P , for iceberg B09a from 2000JD001 to 2003JD20. Measurement updates are modeled as a deterministic sequence with a continuous dropout interval where the size of the dropout interval is varied between one and 32 days: Top) square-root of the trace of the first two rows and columns of P . Bottom) square-root of the lower-right-most element of P . The legend corresponds to both figures. Vertical axes were scaled to be comparable with Figs. 6.14 and 6.16. The vertical spike in (top) around day 850 extends to approximately $1e12$. The spike in (bottom) extends to approximately $1e5$.

average of instances over a month is reported in the OCCAM dataset [96]. As such, there is an inherent temporal window over which the OCCAM ocean measurements are accurate depending on how stationary the current distributions are over the monthly temporal window. In general, areas with low-speed currents have a more consistent distribution profile and thus have a larger temporal window over which the monthly-reported OCCAM values are accurate. Conversely, the distribution of ocean current speed and direction in regions containing high-speed currents are changing more rapidly and thus have a smaller temporal window over which OCCAM currents are accurate. For extreme ocean current speeds, the temporal window over which a single measurement accurately represents the cumulative ocean speed is much less than one month [101]. Thus areas with high-speed ocean currents are not characterized well in the OCCAM model dataset, a theme explored more in a companion study [12].

The second cause of uncertainty while estimating iceberg motion is due to the characteristic motion equations. There have been several studies to deterministically model the motion of icebergs (see Section 6.1) in which this study is included. While this study has briefly explored additional forces affecting tabular iceberg motion (see Section 6.4), this study is primarily focused on analytically solving for the characteristic forces conventionally used to describe iceberg motion. Due to incorporated analytical calculations that more accurately describe physical interactions between icebergs and underlying forcing fields, I expect the equations of motion in this chapter to have increased performance over previous iceberg models. However, compared to previous studies, I do recognize the limitation of the iceberg motion model to sufficiently characterize the force on a tabular iceberg due to sea ice. In the MERS Antarctic iceberg database, iceberg motion has been observed to be affected by extreme sea ice concentrations; however, the relationship between tabular icebergs and sea-ice characteristics has yet to be quantified, so an antiquated iceberg–sea-ice force profile was used in this study. As a result, the iceberg model in this chapter must be applied with care. Quantifying the effects sea-ice has on large tabular icebergs remains a topic of future research.

The third cause of iceberg motion uncertainty is due to numerical integration of the motion equations. As previously stated, a Runge-Kutta integration method is used to numerically solve the motion equations in a timely manner. For comparison, an explicit Euler finite-difference approximation of the differential-algebraic equations was also found to produce stable results for time

steps ≤ 0.01 days. However, when the Euler approximation is augmented with a regularization term similar to that discussed in Section 6.5.1, time steps as large as ≤ 0.1 days produce results similar to values obtained using Runge-Kutta. The fact that model performance is consistent with respect to Runge-Kutta and the less-precise Euler approximation suggests that dominant model uncertainties do not originate from numerical integration.

6.7 Conclusion

In summary, I developed an iceberg motion model for large tabular icebergs to estimate their translational and rotational evolution given external forcing fields. To characterize non-homogeneous forcing fields over the iceberg's exterior, I augmented the motion model with a three-dimensional construction to incorporate spatial dependence. Furthermore, the iceberg motion model is supplemented with a regularization term to dampen unstable translational motion.

The utility of the iceberg motion model is analyzed in simulation. The dominant forces affecting iceberg motion are the Coriolis and horizontal pressure-gradient forces. As a result, ocean currents are found to be the dominant force field driving iceberg motion, a theme explored more in a companion study [12]. The performance of the iceberg motion model is found to improve with the inclusion of a regularization term. Also, iceberg orientation is found to affect translational iceberg velocity. For example, the speed of an iceberg with a major-axis to minor-axis ratio of 3:2 was found to change up to 13% with respect to orientation angle.

The utility of the iceberg motion model is also analyzed in a case study of iceberg B09a, an iceberg that highlights the movement profile of 90% of tabular icebergs in the Southern Ocean. The performance of the iceberg motion model is found to be correlated with observed iceberg speeds where days with smaller observed iceberg motion corresponds to days that produce model estimates of improved performance.

Additionally, a Kalman filter is used to incorporate actual measurements into the estimation process of iceberg B09a, resulting in more accurate estimates of translational and rotational motion. The covariance matrix produced in the data assimilation process is used to quantify the performance of the iceberg motion model given intermittent iceberg observations. Fewer observations resulted in more uncertainty in the Kalman estimation process.

This study establishes the viability and utility of using a motion model to predict future positions of large tabular icebergs. Other applications of this study are to 1) analyze large-scale iceberg trends, 2) use the iceberg model in conjunction with observed iceberg positions to derive underlying forcing fields, and 3) to track observed icebergs backwards in time to determine an iceberg's parent glacial ice sheet such as back-tracking the glacial ice fragments detected off the coast of New Zealand in 2006 and 2009. The first two are analyzed in Chapter 7. The third is future work.

Chapter 7

Estimating Ocean Currents

7.1 Introduction

As part of the international cooperation during the fourth International Polar Year (IPY), recent studies have focused on expanding the knowledge of Earth's polar regions through the use of numerous on-site and remote sensing projects [5]. Many of these projects utilize estimates of polar ocean currents. On-site projects can directly measure local ocean parameters; however, remote polar studies frequently rely on estimates of ocean current characteristics derived using other means, such as numerical ocean simulations.

To simulate the ocean circulation within a computer model is a complex multiscale problem. It requires understanding of the physical principles of the ocean circulation, the mathematical formulation of these principles, and their numerical realization. Global ocean-simulation models are influenced by multiple uncertainties related to mathematical approximations and physical parametrizations. Modeling uncertainty is also affected by the forcing fields, initial conditions, and boundary conditions. Consequently, modeling ocean currents is an inherently uncertain task.

In this chapter, I analyze the fidelity of numerically-generated ocean currents using empirical observations of iceberg tracks in the Southern Ocean. The fidelity of numerically-generated ocean currents is analyzed using two methods. First, empirically observed iceberg positions are compared with simulated iceberg tracks generated using a previously-derived iceberg motion model. The iceberg motion model produces estimates of iceberg positions using external ocean current profiles [11]. Second, the iceberg motion model is inverted and augmented with empirical iceberg observations to produce iceberg-based estimates of ocean currents. Multiple iceberg-derived current estimates are combined using reconstruction techniques and compared with numerical ocean currents. The numerically-generated ocean current profiles used in this study are from the Ocean Circulation and Climate Advanced Modeling (OCCAM) project [65]. The iceberg

observations used in this study were tracked using the SeaWinds scatterometer and are cataloged in the Antarctic iceberg database developed by the Microwave Earth Remote Sensing (MERS) Laboratory at Brigham Young University [7].

This chapter is organized as follows: In Section 7.2, models used to estimate iceberg motion and reconstruct ocean currents are presented. The estimation algorithms used to produce simulated iceberg tracks and reconstruct ocean currents are developed in Section 7.3. In Section 7.4, OCCAM-based iceberg tracks are presented and compared with empirically-observed iceberg positions in the Southern Ocean. Iceberg-derived ocean currents are also presented and compared with OCCAM currents. Finally, Section 7.5 concludes.

7.2 Models

This section develops the models used to simulate iceberg motion and reconstruct ocean currents. First, the iceberg motion model is reviewed. Second, a physical iceberg model is developed. Last, the map projection and gridding scheme used to represent the stratified ocean currents is presented.

7.2.1 Iceberg Motion Model

The iceberg motion model developed in [11] is used to simulate iceberg positions given estimates of iceberg size and external forcing fields, such as ocean currents. The general form for the system of differential-algebraic equations that describe an iceberg's translational velocity, \vec{V}_i , with mass m is (repeated from Eq. 6.1 for convenience)

$$m \frac{d\vec{V}_i}{dt} = \vec{F}_w + \vec{F}_a + \vec{F}_s + \vec{F}_r + \vec{F}_c + \vec{F}_h \quad (7.1)$$

where \vec{F}_w is the force due to the surrounding water, \vec{F}_a is the force due to the atmosphere (i.e. near-surface winds), \vec{F}_s is the sea-ice drag, and \vec{F}_r is the wave radiation force. Forces induced as a result of the Earth's rotation are the Coriolis force, \vec{F}_c , and the horizontal-pressure gradient force, \vec{F}_h . All vector quantities are constrained to the two-dimensional plane that contains an iceberg's northing and easting velocity components.

As demonstrated in [11], the translational motion of an iceberg is numerically dominated (≥ 2 orders of magnitude) by the Coriolis and horizontal-pressure gradient forces. I also note that the instantaneous translational iceberg velocity at each time step is numerically insignificant (≤ 2 orders of magnitude) with respect to \vec{F}_c and \vec{F}_h ; therefore, Eq. 7.1 can be approximated by

$$0 = \vec{F}_c + \vec{F}_h \quad (7.2)$$

where

$$\vec{F}_c = -m \cdot f \cdot (\vec{k} \times \vec{V}_i), \quad (7.3)$$

$$\vec{F}_h = m \cdot f \cdot (\vec{k} \times \vec{V}_w) + m \frac{d\vec{V}_w}{dt}, \quad (7.4)$$

$$f = 2 \cdot 7.2921 \times 10^{-5} \cdot \sin(\phi), \quad (7.5)$$

and where \vec{k} is a unit vector perpendicular to the ocean's surface (pointing away from the Earth's center), ϕ is the latitude of interest, and \vec{V}_w is the mean water velocity over the iceberg's displaced volume. The volume displaced by an iceberg is also referred to as the spatial support of the iceberg [11]. I focus on large (> 5 km) tabular icebergs in this study.

The first term in Eq. 7.4 is numerically dominant for large tabular icebergs [11]. Consequently, Eqs. 7.2 - 7.5 can be further reduced to

$$\vec{V}_i = \vec{V}_w. \quad (7.6)$$

This relationship implies that, unlike smaller icebergs observed by Biggs et al [102], large tabular icebergs can be considered direct Lagrangian tracers of the average underlying ocean currents where the averaging is over the spatial support of the iceberg. Equation 7.6 coincides with empirical observations by Radikevich and Romanov [103].

The full iceberg motion model (Eq. 7.1) is used to simulate iceberg tracks given ocean current velocities in Section 7.3.1. The simplified iceberg motion model (Eq. 7.6) is used to estimate ocean currents given empirical observations of icebergs in Section 7.3.2.

7.2.2 Physical Iceberg Model

To simulate iceberg motion, I adopt the elliptical cylinder model from [11] for the shape of a large tabular iceberg. For this study, I simplify the elliptical cylinder iceberg model to a circular cylinder for two reasons. First, when simulating iceberg tracks, I am interested in the average simulated iceberg motion profile, independent of rotational orientation. Second, when deriving ocean currents, estimates of iceberg rotational orientation using techniques developed in [10] were not available.

Consequently, the radius of the cylinder is set to the average top-down radius of the observed iceberg as reported by the National Ice Center (NIC) [55]. The height of the cylinder is set to the average vertical height of the parent glacial ice sheet as documented in [68]. The height of the iceberg extending above the surrounding water or sea ice is adopted from [58] which assumes a ratio of draught to freeboard of 5:1 (16.7%).

7.2.3 Ocean Model

To estimate ocean currents, it is necessary to define the space spanned by the ocean currents used in the ocean current estimation process. To mitigate numerical bifurcations [58, 59, 63], I define the ocean current grid size to be smaller than the minimum iceberg size detectable using SeaWinds (5-6 km). This ensures multiple grid elements are always contained within the displaced volume of each iceberg.

For ease of implementation and product compatibility, I choose the horizontal spatial mapping of the ocean current model to be the standard map projection and grid spacing used for standard high-resolution SeaWinds image data products [7]. The mapping projection of the ocean current model corresponds to a polar-stereographic map, centered on the South Pole and extending to approximately 52°S. Surface gridding is defined on a Cartesian grid with spacing of 2.225×2.225 km. Vertical discretization corresponds to the waterline and the ocean current stratification as defined in the OCCAM current dataset [96].

7.3 Estimation Algorithms

In this section, I outline two estimation algorithms using empirical observations of icebergs. First, the methodology used to simulate iceberg positions given ocean current profiles is developed. Second, I explore the converse problem, i.e., I derive a methodology to estimate ocean currents given knowledge of iceberg positions.

7.3.1 Iceberg Tracks Simulation

In this study, the period of the iceberg motion simulation is long (up to 5 years) with respect to observed iceberg ablation [7, 10]; therefore, iceberg size is not constant. Consequently, physical iceberg size is varied on a daily basis using NIC size estimates that are spatially interpolated [55].

To augment the iceberg motion simulation with a spatially-dependent iceberg size model, I first identify spatial regions that contain characteristic iceberg movement trends. Using the Antarctic iceberg database, large tabular icebergs are found to follow three characteristic movement profiles: 1) icebergs move westward along the coast of the glacial continent in the Antarctic Coastal Current until 2) icebergs leave the coastal region and move northward until 3) icebergs merge with the Antarctic Circumpolar Current (ACC) around 63°S and move predominantly eastward. The approximate regions defined by each segment are illustrated in Fig. 7.0. Virtually all icebergs observed using SeaWinds consecutively follow these three segments of characteristic iceberg motion except for iceberg fragments that break off from icebergs already following this cycle as well as icebergs in the Weddell Sea near the Antarctic Peninsula where icebergs travel northward along the coast, thereby combining the first two movement profiles.

Iceberg sizes are spatially interpolated using NIC size estimates in each of the regions defined in Fig. 7.0. Specifically, iceberg size is linearly interpolated with respect to longitude along the Antarctic coast. In this study, I define the coastal zone to be up to 200 km away from the Antarctic glacial continent. When the iceberg moves into Region 2, iceberg size is interpolated using NIC sizes with respect to latitude, and last, iceberg size is interpolated with respect to longitude in Region 3. Because the accuracy of NIC size estimates depends upon the skill and proficiency of each analyst (analysts rotate approximately every two years), I impose a strictly decreasing constraint upon the evolving iceberg size in the iceberg motion simulation.

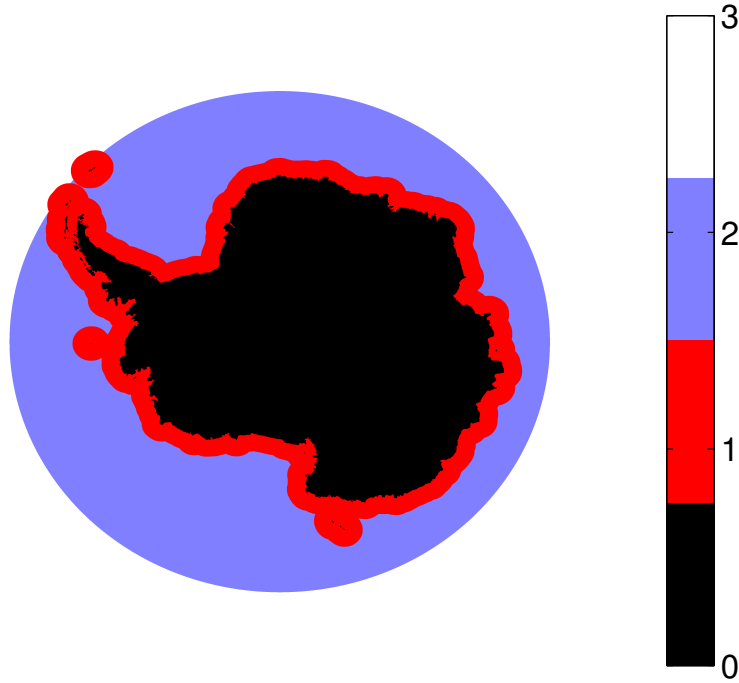


Figure 7.1: Regions of characteristic iceberg movement in the Southern Ocean. Region 0 corresponds to the Antarctic glacial continent; this study does not analyze glacial ice movement in this region. Region 1 corresponds to the Antarctic coast (out to 200 km) around the glacial continent where icebergs predominantly travel westward. Region 2 is defined as the space between the coast and 63°S where icebergs primarily travel northward. Region 3 is north of 63°S where icebergs predominantly drift eastward in the ACC.

7.3.2 Ocean Currents

Here, I develop an algorithm to estimate ocean currents using iceberg positions. As derived in Eq. 7.6, the velocity of large tabular icebergs is proportionally related to the ocean currents driving the iceberg motion. Thus observed iceberg velocities can be used to estimate the velocity of ocean currents driving iceberg motion. Iceberg positions are obtained from the Antarctic iceberg database, and iceberg velocities are calculated using iceberg positions.

To describe the ocean current estimation process, I define an indicator function $I(j, t, n) \in [0, 1]$ that references iceberg j at time t in the Antarctic iceberg database where n is a spatial index that references the grid cells in the ocean current model. The estimation methodology is implemented by superimposing the physical iceberg model developed in Section 7.2.2 over the

ocean current grid defined in Section 7.2.3. Voxels whose midpoints lie within the physical iceberg model are assigned an indicator value of unity. A value of zero is assigned to voxels that lie outside the iceberg model. Mathematically, the ocean current estimation process can be expressed as

$$\vec{V}_w(j,t,n) = \vec{V}_i(j,t) \cdot I(j,t,n) \quad (7.7)$$

where the velocity of ocean currents corresponding to voxels with an indicator value of zero remains undefined.

Because ocean currents in multiple voxels are estimated per iceberg position, the ocean current estimation process is an underdetermined system. Therefore, it is necessary to include a constraint in order to uniquely (and efficiently) estimate ocean currents. To produce a first-order approximation of ocean currents, I assume ocean currents are spatially homogeneous over the iceberg's displaced volume. Note that utilizing this constraint has an inherent smoothing effect on the ocean current estimates; consequently, iceberg-derived ocean currents in this study are appropriate only for large-scale current studies.

For example, suppose I estimate the ocean currents driving a tabular iceberg of diameter 25 km eastward at 0.5 m/s. The corresponding physical iceberg model is superimposed over the ocean current grid such as in Fig. 7.1. Cells whose midpoints lie within the physical iceberg model are given an indicator value of unity; the midpoints of these cells are highlighted in Fig. 7.1. Using the inverted iceberg motion model, the eastward ocean current velocity of ocean currents corresponding to the highlighted voxels is set to the observed eastward iceberg velocity, i.e., 0.5 m/s. Similarly, estimated northward ocean current velocities for each highlighted cell are initialized to zero because observed iceberg motion in this example is strictly eastward.

To improve the resolution of ocean current estimates, reconstruction techniques can be used to combine multiple current estimates into a single, averaged estimate of ocean current velocity. To obtain multiple estimates per voxel, I augment Eq. 7.7 with a temporal window where all iceberg observations within the window are used in the reconstruction process. Due to numerical stability and computational efficiency, I choose a conventional weighted-averaging reconstruction

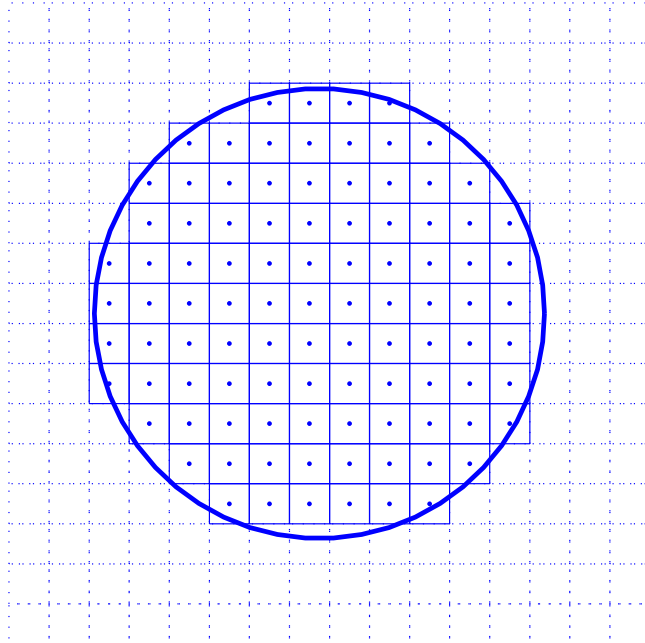


Figure 7.2: Top-down illustration of the physical iceberg shape model superimposed over the ocean current grid. The midpoints of cells that lie within the iceberg shape model are highlighted.

algorithm [24], represented as

$$\vec{V}_w(n) = \frac{\sum_{j,t} \vec{V}_i(j,t) \cdot I(j,t,n)}{\sum_{j,t} I(j,t,n)} \quad (7.8)$$

where t defines the temporal window. Ocean currents corresponding to voxels with an indicator value of zero remain undefined.

Appropriate lengths for the temporal window in the ocean current estimation process depend on the variability of the ocean currents. If the temporal window is small with respect to the underlying ocean current distribution, iceberg-derived ocean currents reflect the instantaneous ocean currents. Conversely, if the temporal window is long with respect to the underlying ocean current distribution, iceberg-derived ocean currents better fit climatological ocean currents. In this chapter, multiple temporal windows are explored and analyzed in Section 7.4.2. Uniquely quan-

tifying the length of the temporal window for regions in the Southern Ocean remains a topic of future research.

7.4 Performance

Using the algorithms developed in Section 7.3, there are two ways to analyze the fidelity of OCCAM currents. First, OCCAM-driven iceberg tracks are compared with empirically-observed iceberg positions. Second, OCCAM currents are compared directly with iceberg-based ocean currents. OCCAM currents overlap with iceberg observations in the Antarctic iceberg database from 2000-2004. Over this period, there are approximately 80 icebergs in the Antarctic iceberg database whose sizes are documented that are also used in this section.

7.4.1 Iceberg Tracks

OCCAM-driven iceberg tracks are generated using the iceberg motion model developed in Section 7.3.1. Using the iceberg motion model, a single iceberg track is simulated for each of the 80 icebergs from 2000-2004. Each simulation is initialized with the initial position and size of each of the 80 icebergs. Specifically, simulated iceberg positions are set to the first position of each iceberg as reported in the Antarctic iceberg database, top-down iceberg sizes are set to the initial NIC size, and vertical heights are set to the vertical height of the associated parent glacial ice sheet. Each iceberg simulation is propagated from the first date of detection until the end of 2004 or until the iceberg's diameter reduces in size < 5 km, whichever occurs first. The empirically-observed tracks of the 80 icebergs detected between 2000-2004 are displayed in Fig. 7.2. OCCAM-driven iceberg tracks simulated using the initial positions and sizes of the 80 icebergs are displayed in Fig. 7.3.

Notice that the OCCAM-driven iceberg tracks in Fig. 7.3 are similar to the empirically-observed iceberg tracks in Fig. 7.2. However, there are some regions where the iceberg motion model does not produce expected results. For example, one simulated iceberg track in the Ross Sea (Fig. 7.3) did not travel far enough north for the size model to realistically mitigate iceberg size; consequently, this iceberg track may not reflect realistic iceberg motion. Also, simulated iceberg tracks suggest slower westward ocean currents in coastal regions that correspond to the South Atlantic and South Indian Oceans. While the iceberg motion model does not handle all

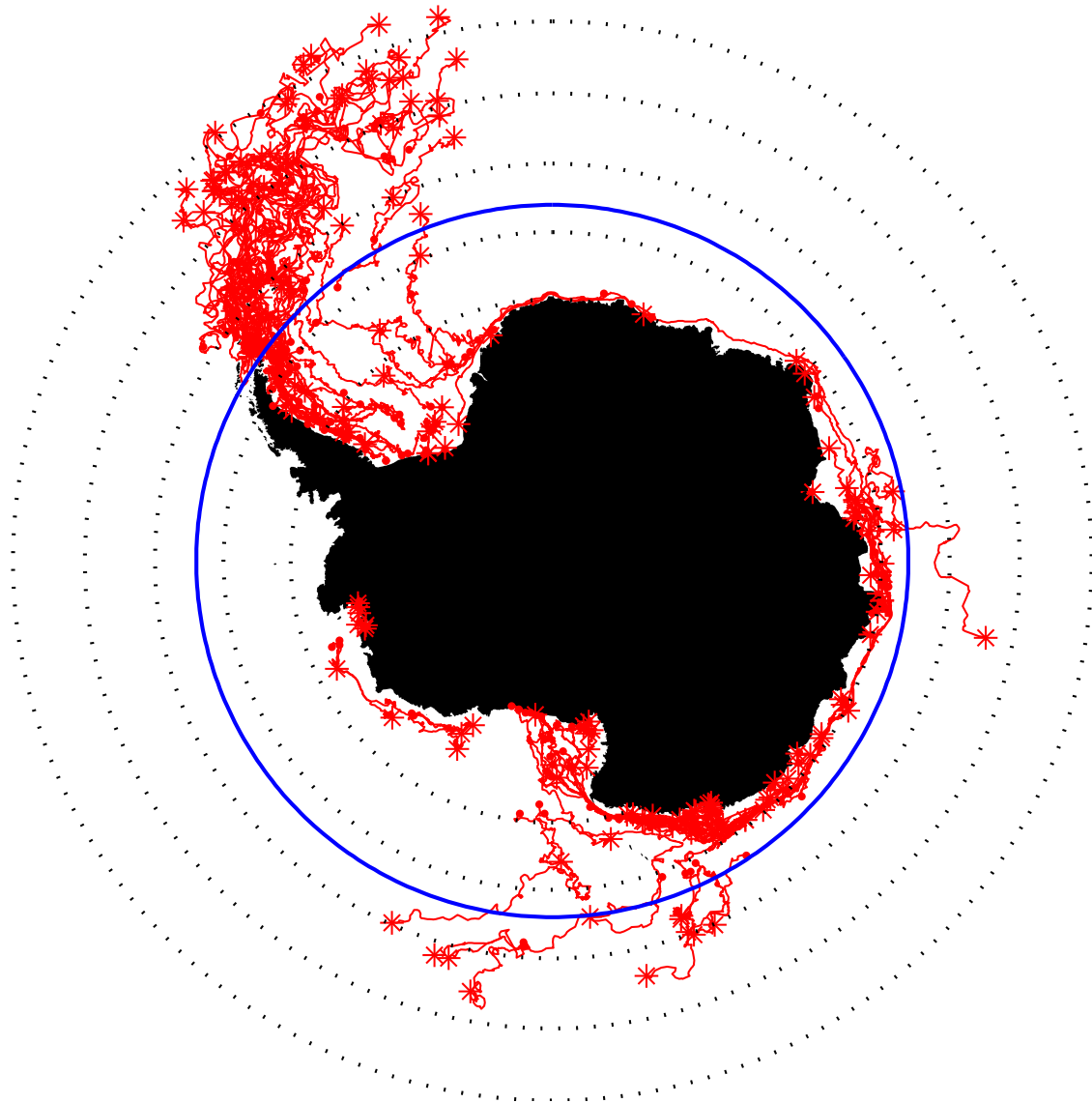


Figure 7.3: Observed tracks of approximately 80 tabular icebergs from 2000-2004. Initial and final positions are highlighted with a dot and star, respectively. Dashed rings correspond to lines of latitude from 50-70°S in increments of 5°. The solid ring corresponds to 63°S.

cases, the iceberg motion model performs well overall with more than 98% of simulated iceberg tracks coinciding with empirical iceberg positions.

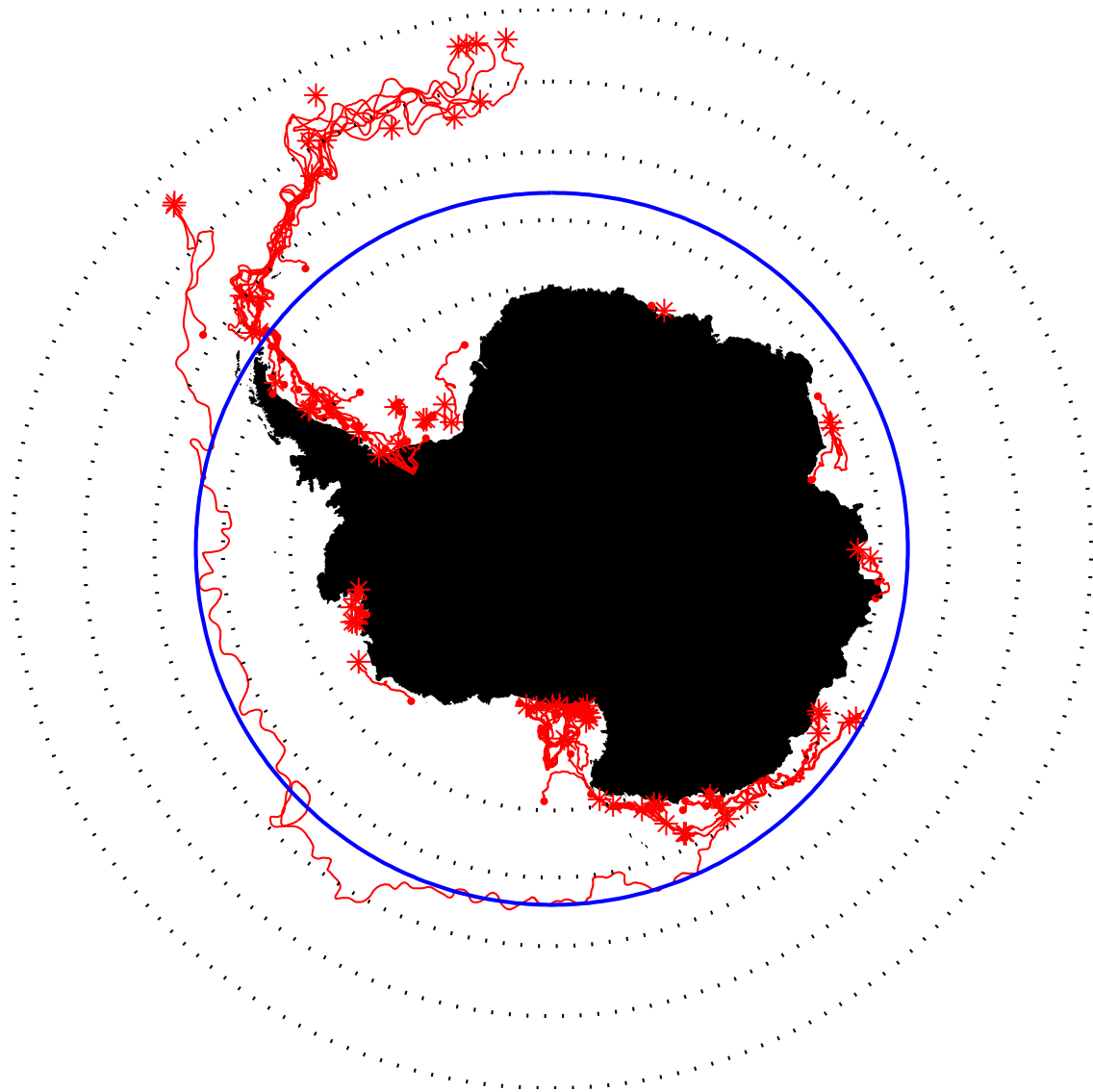


Figure 7.4: Simulated OCCAM-driven tracks of approximately 80 tabular icebergs initialized using the icebergs in Fig. 7.2. Initial and final positions are highlighted with a dot and star, respectively. Dashed rings correspond to lines of latitude from 50-70°S in increments of 5°. The solid ring corresponds to 63°S.

Table 7.1: RMS differences between iceberg-based surface currents and OCCAM surface currents from Figs. 7.6 and 7.7. Regions are defined in Fig. 7.0.

	Velocity Direction	All Regions	Region 1	Region 2	Region 3
RMS Difference (cm/s)	Easting	9.29	8.30	6.00	11.90
	Northing	8.38	4.99	6.45	12.85

7.4.2 Ocean Currents

In this section, iceberg-based ocean currents are derived using the ocean current estimation algorithm developed in Section 7.3.2. These iceberg-based currents are compared with OCCAM currents.

Due to the variable length of the temporal window in Eq. 7.8, iceberg-based ocean currents can be derived in multiple ways. For illustrative purposes, I derive ocean currents estimated using all icebergs detected using SeaWinds from 1999-2009 whose physical sizes are documented by the NIC (approximately 170 icebergs). For simplicity, I display a slice of the iceberg-derived ocean currents that corresponds to the surface layer. Easting and northing iceberg-based ocean current velocities are shown in Figs. 7.4 and 7.5, respectively.

Next, I compare iceberg-based ocean currents with OCCAM currents using two approaches: First, OCCAM currents are compared with iceberg-based ocean currents derived using a maximum-length temporal window. Second, OCCAM current are compared with iceberg-based ocean currents estimated using a minimum-length temporal window.

First, iceberg-based ocean currents are derived using Eq. 7.8 where the temporal window is set to the maximum overlap between the Antarctic iceberg database and the OCCAM dataset, i.e., five years. These climatological iceberg-based currents are compared with OCCAM currents averaged over the same 5-year window. Differences between the eastward and northward surface velocities (i.e., iceberg-based currents minus OCCAM currents) are shown in Figs. 7.6 and 7.7, respectively. The root-mean-squared (RMS) difference between the iceberg-derived surface currents and OCCAM surface currents are included in Table 7.0. For reference, the average iceberg-derived and OCCAM ocean current velocities in each region are included in Table 7.1.

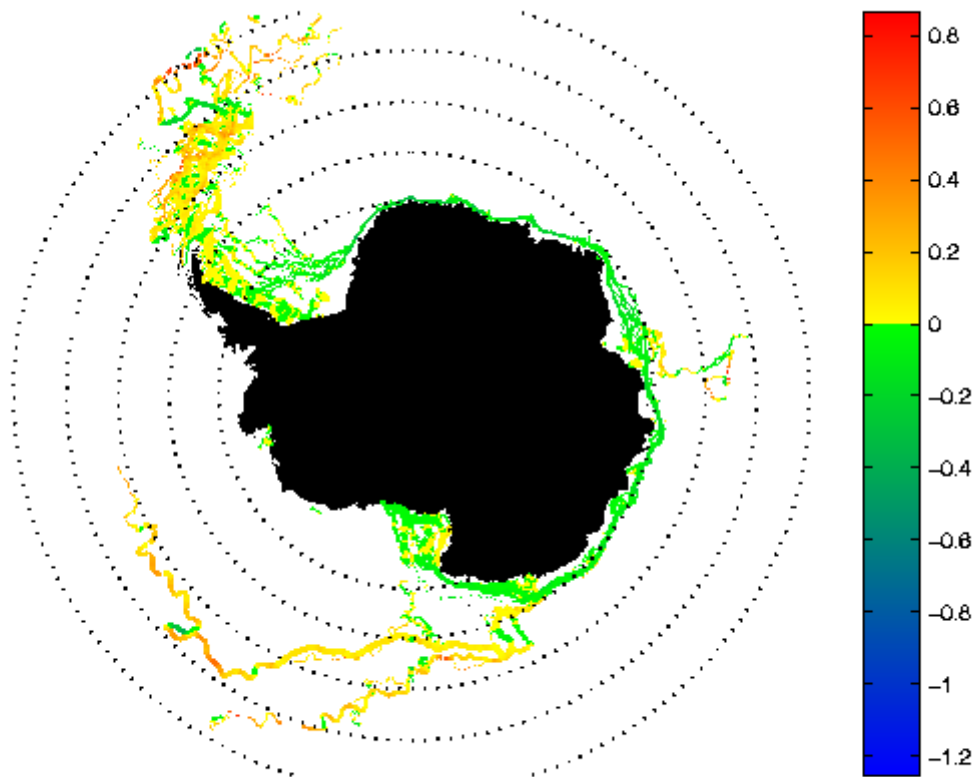


Figure 7.5: Eastward velocity (in m/s) of iceberg-based surface currents estimated using iceberg observations from 1999-2009. Dashed rings correspond to lines of latitude from 50-70°S in increments of 5°.

Table 7.2: Average iceberg-based and OCCAM surface current velocities for each region. Regions are defined in Fig. 7.0.

Surface Current Velocity (cm/s)	Velocity Direction	All Regions	Region 1	Region 2	Region 3
Iceberg-derived	Easting	0.88	-3.45	-1.20	8.10
	Northing	2.79	1.35	3.50	4.65
OCCAM	Easting	2.09	0.24	0.10	6.26
	Northing	0.75	0.30	0.30	1.74

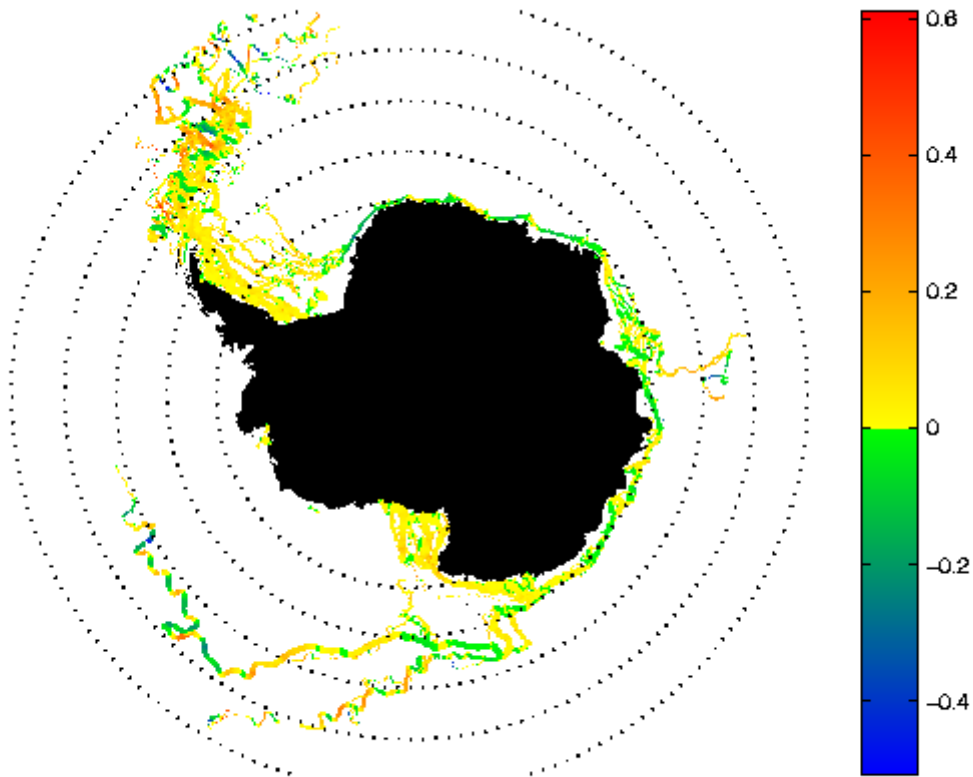


Figure 7.6: Northward velocity (in m/s) of iceberg-based surface currents estimated using iceberg observations from 1999-2009. Dashed rings correspond to lines of latitude from 50-70°S in increments of 5°.

From Figs. 7.6 and 7.7, spatially-consistent differences between the iceberg-based ocean currents and OCCAM currents are observed around the Antarctic coast. Iceberg-based currents elsewhere generally coincide with the numerical OCCAM ocean currents. These observations coincide with RMS differences in Table 7.0 for Regions 1 and 2. The higher RMS differences in Region 3 are a result of the iceberg-derived currents and OCCAM currents not matching in the ACC. Due to the turbulent behavior of currents in the ACC; this is expected [11, 98–100].

For the second case, iceberg-based ocean currents are derived using a temporal window length set to the temporal resolution of the Antarctic iceberg database, 24 hours. Iceberg-based ocean currents are estimated for each daily iceberg position in the Antarctic iceberg database from 2000-2004 and compared with daily OCCAM currents using an RMS difference approach. To pro-

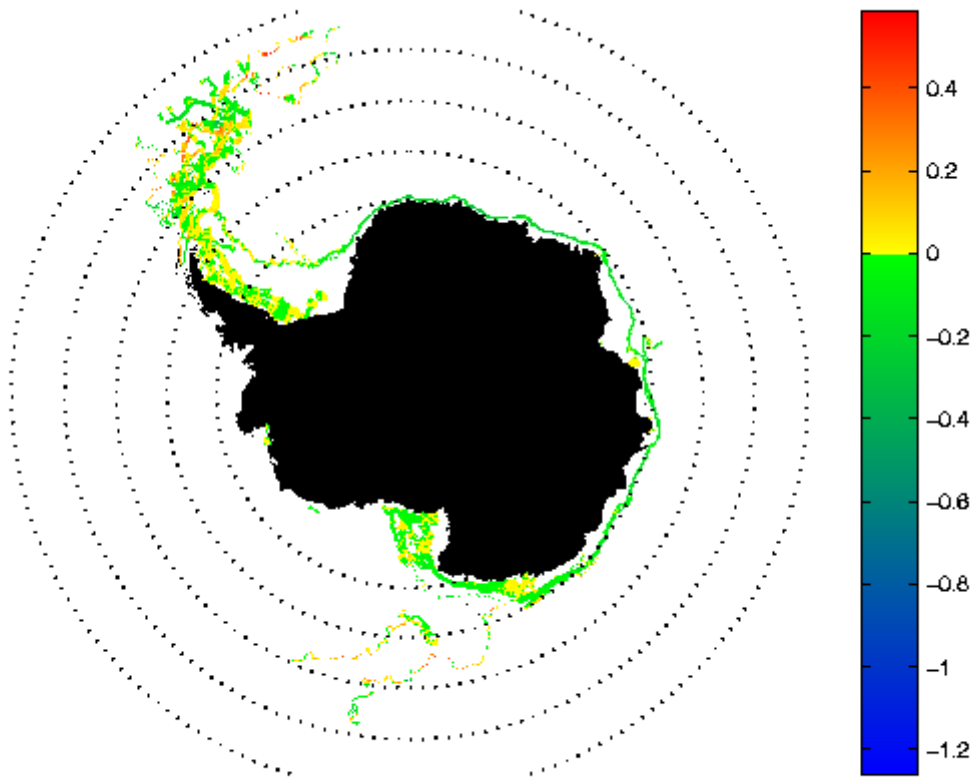


Figure 7.7: Difference in eastward velocities (in m/s) between iceberg-derived surface currents and OCCAM surface currents. Iceberg-derived currents were estimated using iceberg observations from 2000-2004. OCCAM currents were averaged over the same temporal window. Dashed rings correspond to lines of latitude from 50-70°S in increments of 5°.

duce daily OCCAM currents, monthly-reported OCCAM currents are treated as mid-month values and linearly interpolated. Easting and northing RMS surface current differences are spatially computed over the standard polar-stereographic map and displayed in Figs. 7.8 and 7.9, respectively. The average RMS errors between the daily iceberg-based ocean currents and the daily OCCAM currents are included in Table 7.2.

Note that RMS values in Table 7.2 are similar to values in Table 7.0 for each region. In Fig. 7.8, increased eastward errors are observed in the regions that correspond to the Antarctic Coastal Current and the ACC. In Fig. 7.9, elevated northward errors are observed in the western Weddell Sea, western Ross Sea, and ACC.

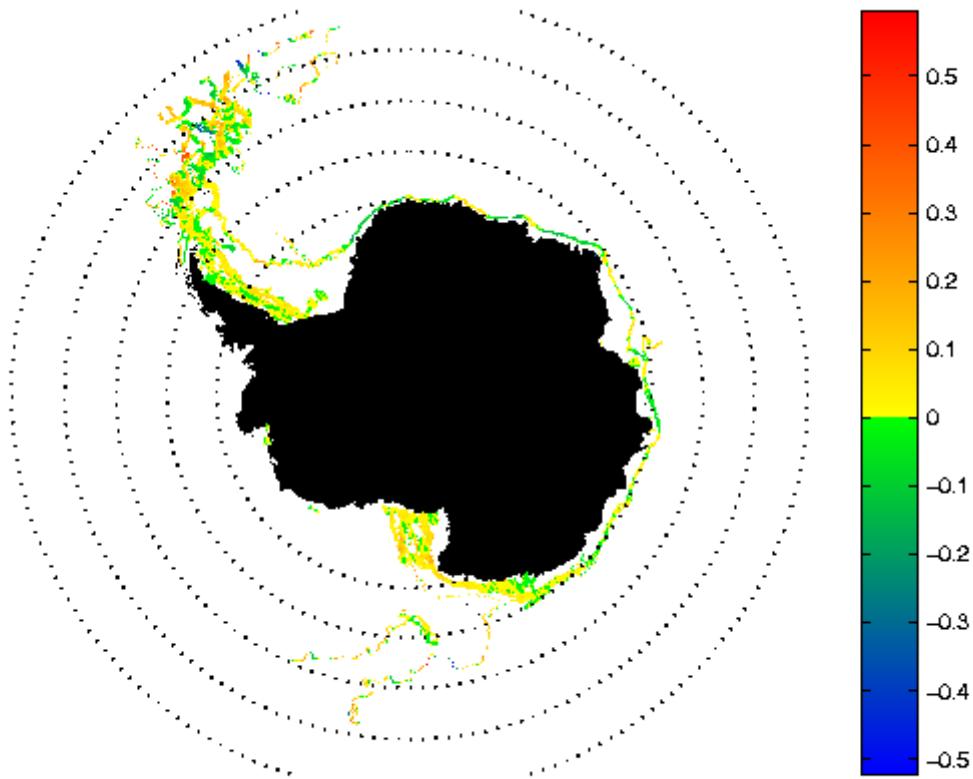


Figure 7.8: Difference in northward velocities (in m/s) between iceberg-derived surface currents and OCCAM surface currents. Iceberg-derived currents were estimated using iceberg observations from 2000-2004. OCCAM currents were averaged over the same temporal window. Dashed rings correspond to lines of latitude from 50-70°S in increments of 5°.

Table 7.3: RMS errors between iceberg-based surface currents and OCCAM surface currents from 2000-2004. Iceberg-based ocean currents are estimated using a window of 24 hours. Monthly-reported OCCAM currents were interpolated to produce daily estimates. Regions are defined in Fig. 7.0.

	Velocity Direction	Entire Ocean	Region 1	Region 2	Region 3
RMS Error (cm/s)	Easting	10.87	9.26	6.83	13.99
	Northing	10.38	5.76	6.98	15.62

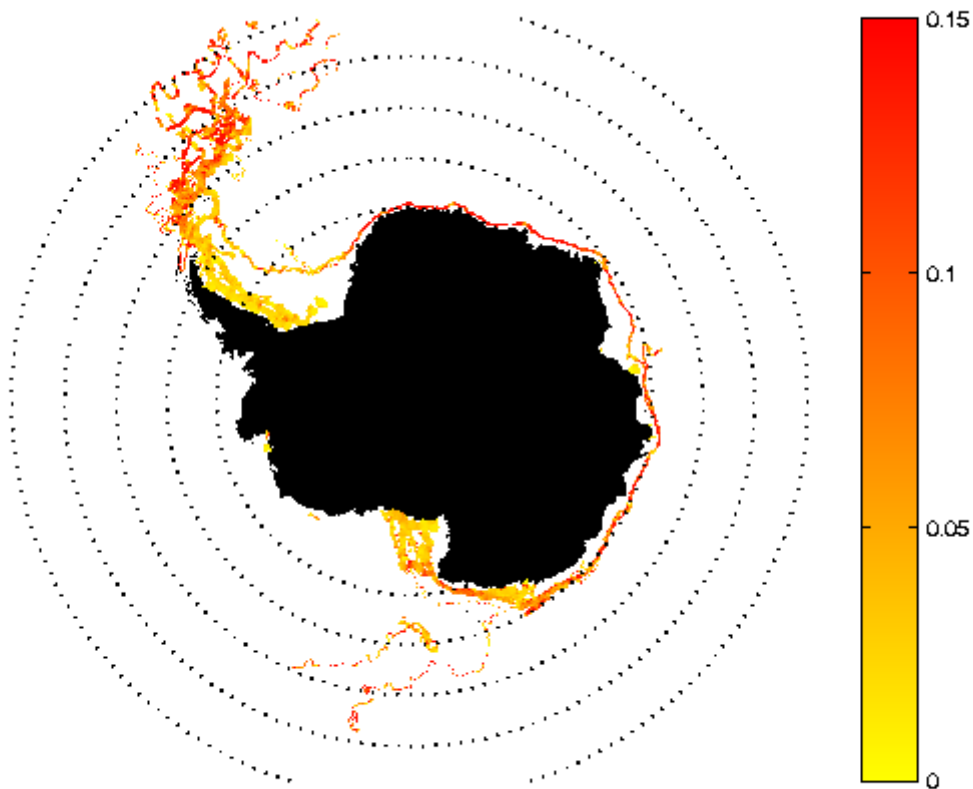


Figure 7.9: Eastward RMS errors (in m/s) between iceberg-based surface currents and OCCAM surface currents. Iceberg-based currents were estimated with a temporal window of 24 hours using all iceberg observations from 2000-2004. Dashed rings correspond to lines of latitude from 50-70°S in increments of 5°.

RMS errors are also calculated between the daily iceberg-based ocean currents and OCCAM currents averaged over time. Two types of OCCAM averages are explored: 1) OCCAM currents are averaged for each Julian day for years 2000-2004, denoted JD1 through JD365 OCCAM averages, and 2) all OCCAM currents are averaged from 2000-2004, referred to as the 5-YR OCCAM average. The RMS methodology used to produce Table 7.2 is repeated where daily iceberg-based currents are compared with both the JD OCCAM averages and the 5-YR OCCAM average. Results for both cases are presented in Table 7.3.

Note that nearly all RMS differences in Table 7.3 are marginally improved over the RMS differences in Table 7.2. This observation implies that, on average, daily iceberg-based ocean cur-

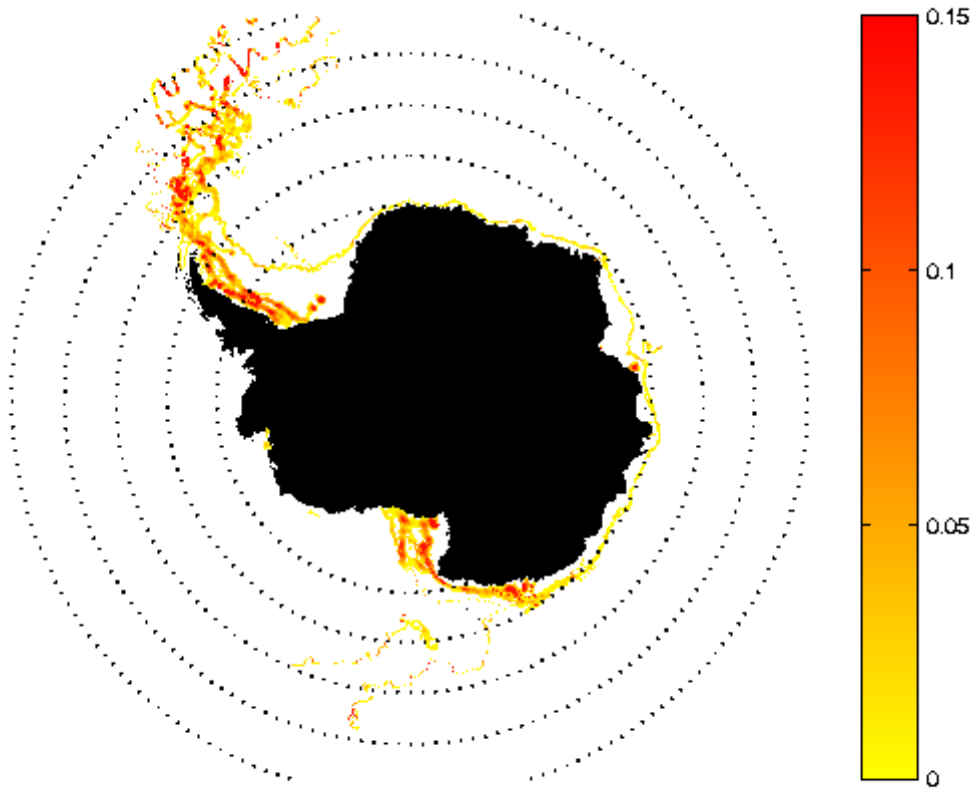


Figure 7.10: Northward RMS errors (in m/s) between iceberg-based surface currents and OCCAM surface currents. Iceberg-based currents were estimated with a temporal window of 24 hours using all iceberg observations from 2000-2004. Dashed rings correspond to lines of latitude from 50-70°S in increments of 5°.

Table 7.4: RMS errors between iceberg-based surface currents and OCCAM surface currents from 2000-2004. Iceberg-based currents are estimated using a window of 24 hours. OCCAM currents are averaged as noted below, see text for details. Regions are defined in Fig. 7.0.

		RMS Difference (cm/s) per Geographic Region			
OCCAM Dataset	Velocity Direction	Entire Ocean	Region 1	Region 2	Region 3
JD Averages	Easting	10.60	9.31	6.82	13.32
	Northing	9.68	5.64	6.96	14.33
5-YR Average	Easting	10.65	9.40	6.84	13.33
	Northing	9.78	5.72	7.01	14.46

rents are more similar to climatological (i.e., year-averaged) OCCAM currents than daily OCCAM currents.

7.5 Conclusion

In summary, I developed two methods to analyze the fidelity of numerically-generated ocean currents from the OCCAM project. The first method utilizes an iceberg motion simulation, and the second relies on ocean currents derived from empirical observations of iceberg motion. The iceberg motion model from [11] is simplified and augmented with an iceberg melting model using NIC size estimates. The iceberg motion model is inverted, producing an algorithm that estimates ocean currents given observations of icebergs. Furthermore, multiple ocean current estimates within a temporal window are combined using a weighted-average reconstruction algorithm.

The utility of the first approach is analyzed using OCCAM currents to drive simulations for over 80 icebergs. OCCAM-based iceberg tracks were found to coincide with observed iceberg positions in the Weddell and Ross Seas. Results also suggest that the Antarctic Circumpolar Current is more accurately modeled than the Antarctic Coastal Current.

The utility of the second approach is analyzed by comparing OCCAM currents with iceberg-based ocean currents. As observed in [11], OCCAM currents were found to coincide more with iceberg-derived ocean currents in regions where icebergs are observed with slower drift speeds. Also, iceberg-based ocean currents were found to coincide better with OCCAM currents averaged over multiple years than with daily OCCAM current profiles. Consequently, averaged OCCAM values are recommended for use in iceberg motion simulations. Utilizing averaged OCCAM current profiles also reduces memory requirements, making related studies more computationally efficient.

This study demonstrates the utility of using observations of icebergs to 1) analyze the fidelity of numerical ocean currents and 2) estimate ocean currents driving iceberg motion. Ocean currents developed in this chapter can be used directly in oceanic studies. Additionally, through the use of data assimilation techniques, iceberg-based ocean currents can be used to augment numerical ocean simulations, thereby improving the accuracy of ocean current estimates throughout the Southern Ocean.

Chapter 8

Conclusion

8.1 Summary of Contributions

In this dissertation, I have presented multiple iceberg studies using the SeaWinds scatterometer. Here, I briefly review the major contributions of these studies and highlight principle results.

First, I formalized a methodology for detecting icebergs using microwave scatterometer images. To maximize both backscatter contrast and temporal resolution in SeaWinds images, daily horizontal-polarization SIR images were used in the iceberg detection process. Using the iceberg detection methodology, I cataloged iceberg positions into the MERS Antarctic iceberg database. Characteristic motion trends of icebergs in the MERS database were analyzed, and 90% of icebergs were found to travel westward along the Antarctic coast, accumulate in the Weddell Sea, and travel northward along “Iceberg Alley” until merging with the Antarctic Circumpolar Current. Iceberg positions were validated using collocated high-resolution satellite imagery and by navigating the 2005, 2008, and 2009 NSF cruise ships in real-time to physically intercept several large tabular icebergs in the Weddell and Scotia Seas.

To supplement iceberg position reports, I developed two estimation algorithms to estimate an iceberg’s major-axis length, minor-axis length, and angle of rotational orientation. The first algorithm was an image-based approach and the second was a measurement-based approach that used raw SeaWinds measurements. Maximum-likelihood objective functions that relate backscatter to model-based simulated backscatter for each case were also developed, and regularization terms were derived to increase numerical stability.

The utility of both iceberg size estimation algorithms were analyzed in simulation and case study. While both approaches were found to be viable, image-based estimates marginally out-perform measurement-based values. Over a year, approximately 70% of the daily iceberg size

estimates converged to accurate values, compared to previous methods that produced only 7% over the same period.

To estimate translational and rotational iceberg evolution, I developed an iceberg motion model for large tabular icebergs. The iceberg motion model was augmented with a three-dimensional construction to characterize non-homogeneous forcing fields over the iceberg's exterior. Drag coefficients were also analytically calculated to accurately model the friction and pressure drag over the iceberg's exterior. The iceberg motion model was also supplemented with a regularization term to dampen unstable translational motion.

Dominant forces affecting iceberg motion were found to be the Coriolis and horizontal pressure-gradient forces. As a result, ocean currents are the dominant forcing field driving iceberg motion. Iceberg orientation was found to affect translational iceberg speed up to 13%. Iceberg motion model performance was found to be correlated with observed iceberg drift speeds.

A Kalman filter was used to incorporate actual measurements into the iceberg motion model. The covariance matrix produced in the data assimilation process was used to quantify the performance of the iceberg motion model given intermittent iceberg observations. Fewer observations resulted in more uncertainty in the Kalman estimation process.

Inverting the iceberg motion model, I developed an algorithm to reconstruct ocean currents given observations of iceberg position and motion. Both the ocean current reconstruction algorithm and the iceberg motion model were used to analyze the fidelity of ocean currents from the OCCAM project.

OCCAM-based iceberg tracks were found to coincide with observed iceberg positions in the western Weddell Sea, the western Ross Sea, and in the Antarctic Circumpolar Current. OCCAM currents were found to underestimate westward ocean current speeds around the coast of the Antarctic glacial continent. OCCAM currents were also found to underestimate northward currents in the Weddell and Ross Seas. Additionally, differences between reconstructed ocean currents and OCCAM currents were found to be smaller when OCCAM currents were averaged over multiple years.

Even though SeaWinds was never designed to track icebergs, this dissertation demonstrates that SeaWinds is an excellent platform from which to detect, track, and estimate parameters of

large tabular icebergs. These iceberg parameters can in turn be used to derive related geophysical parameters (e.g., ocean current velocities).

8.2 Future Work

Future work following this dissertation includes applying the research presented in this dissertation to currently active scatterometers (e.g., OceanSat-2, HY-2, and ASCAT). Several other potential research areas are listed below.

As previously mentioned, an iceberg detection methodology was developed in Chapter 3 using h-pol backscatter measurements. One future study is to augment iceberg detection with v-pol measurements. Using both types of measurements would likely make the iceberg detection algorithm more robust to low backscatter contrast conditions such as iceberg surface melting and high speed winds around the iceberg. Also, iceberg detection could be improved if augmented with estimates of future iceberg positions produced from the iceberg motion model developed in Chapter 6. Depending on the region, forecasts of iceberg motion could accurately predict an iceberg's position several days into the future.

Another area of future research is optimizing the iceberg size estimation algorithms developed in Chapter 5. One of the limitations of the iceberg size estimation algorithms (especially the measurement-based approach) is computational expense. Utilizing advanced optimization algorithms such as simulated annealing or random sample consensus (RANSAC) could reduce computation time as well as improve the accuracy of iceberg size estimates.

The iceberg size estimation algorithm could be utilized on the entire MERS Antarctic iceberg database to derive a combined spatial-temporal iceberg melting model. In addition to producing size estimates, the iceberg size estimation algorithm also produces estimates of iceberg backscatter. Backscatter values from the entire MERS database could be compiled to create an iceberg backscatter model.

To improve forecasts of iceberg movement, the iceberg motion model outlined in Chapter 6 could be augmented with an iceberg–sea-ice interaction model. Sea ice has been reported to have dramatic effects on the movement of large tabular icebergs, such as halting iceberg motion as well as changing an iceberg's drift directions [8, 97].

Previous large-scale studies of iceberg motion incorporated a statistical model of iceberg calving rates and locations [58, 59, 63]. To produce a comparable study, the large-scale iceberg simulation in Chapter 7 could be augmented with a statistical iceberg seed model. Such a statistical iceberg prior that details the spatial and temporal variability of icebergs in the Southern Ocean could be produced using the MERS Antarctic iceberg database.

To improve the accuracy of both the iceberg motion model and the ocean current reconstruction algorithm, image-based size estimates of all icebergs in the MERS Antarctic iceberg database could be used.

The accuracy of the ocean current reconstruction algorithm could be improved by utilizing more advanced reconstruction techniques. Such techniques may include a non-uniform weighting in the current weighted-averaging algorithm to produce estimates biased in time. Weighting could be useful for NRT estimation of ocean currents. Another proposal would be to adapt the SIR algorithm to reconstruct stratified ocean currents.

To increase the spatial and temporal diversity in the ocean current reconstruction process, ocean currents can be reconstructed using Lagrangian and Eulerian ocean buoys in addition to observations of iceberg size and motion.

Optimizing the length of the temporal window used in the ocean current reconstruction process would also increase the accuracy of estimated ocean currents. Because window length depends on characteristics of the true underlying ocean currents, this information is usually unavailable; however, studies from the fourth IPY might be used to derive appropriate window lengths in some case study regions with the intention of quantifying window lengths with an observable parameter, such as observed iceberg speed [11].

By augmenting the iceberg motion model with more accurate ocean currents, the motion model could be used to backtrack icebergs in the Southern Ocean to their parent glacial ice sheet. For example, backtracking the glacial ice fragments detected off the coast of New Zealand in 2006 and 2009. By backtracking icebergs to their parent glacial ice sheet, their initial keel depth will be known; consequently, these icebergs could be included in the ocean current reconstruction process.

Bibliography

- [1] K. Smith, Jr., “Free-drifting icebergs in the Southern Ocean: an overview,” *Deep-Sea Research II*, vol. 58, pp. 1277–1284, June 2011. 1, 29, 33, 45
- [2] G. Stephenson, Jr., J. Sprintall, S. Gille, M. Vernet, J. Helly, and R. Kaufmann, “Subsurface melting of a free-floating Antarctic iceberg,” *Deep-Sea Research II*, vol. 58, pp. 1336–1345, June 2011. 1
- [3] A. Jenkins, “The impact of melting ice on ocean waters,” *Journal of Physical Oceanography*, vol. 29, no. 9, pp. 2370–2381, 1999. 1
- [4] IIP, “From sea, to air, to space: Nearly 100 years of IIP iceberg tracking technology and beyond,” <http://www.navcen.uscg.gov/>, update 2012. 2
- [5] IPY, “IPY Project Database,” <http://www.ipy.org/>, update 2012. 4, 121
- [6] M. Spencer and D. Long, “Improved resolution backscatter measurements with the SeaWinds pencil-beam scatterometer,” *IEEE Transactions on Geoscience and Remote Sensing*, vol. 38, no. 1, pp. 89–104, 2000. 7, 109
- [7] Microwave Earth Remote Sensing Laboratory, “Scatterometer Climate Record Pathfinder,” <http://www.scp.byu.edu/>, update 2012. 7, 8, 14, 18, 27, 29, 31, 64, 73, 74, 79, 90, 100, 122, 124, 125
- [8] K. Stuart and D. Long, “Tracking large tabular icebergs using the SeaWinds Ku-band microwave scatterometer,” *Deep Sea Research II*, vol. 58, no. 11-12, pp. 1285–1300, 2011. 7, 8, 29, 45, 79, 90, 91, 99, 100, 109, 142
- [9] J. Ballantyne, “Using space borne microwave sensors to track large antarctic icebergs,” Master’s thesis, Brigham Young University, 2002. 7
- [10] K. Stuart and D. Long, “Iceberg size and orientation estimation using SeaWinds,” *Cold Regions Science and Technology*, vol. 69, no. 1, pp. 39–51, 2011. 8, 77, 79, 80, 91, 101, 109, 124, 125
- [11] K. Stuart, D. Long, and J. Vanderhoff, “Trajectory modeling of large tabular icebergs,” *Cold Regions Science and Technology*, in review. 8, 121, 122, 123, 124, 134, 139, 143
- [12] K. Stuart and D. Long, “Ocean current analysis using Antarctic icebergs,” *Cold Regions Science and Technology*, in review. 8, 9, 78, 100, 105, 118, 119

- [13] M. Vernet, K. Smith Jr., A. Cefarelli, J. Helly, R. Kaufmann, H. Lin, D. Long, A. Murray, B. Robison, H. Ruhl, T. Shaw, A. Sherman, J. Sprintall, G. Stephenson Jr., K. Stuart, and B. Twining, “Islands of ice: Influence of free-drifting Antarctic icebergs on pelagic marine ecosystems,” in *Oceanography*, 2012, vol. 25, no. 3, pp. 16–17. 8
- [14] M. Owen, K. Stuart, and D. Long, “Ultra-high-resolution near-coastal wind retrieval for QuikSCAT.” *Proceedings of SPIE Vol. 6680*, Aug 2007, pp. 26–27. 8
- [15] K. Stuart and D. Long, “Antarctic iceberg and sea ice melting patterns,” vol. 5. *Proceedings of the International Geoscience and Remote Sensing Symposium*, Boston, MA, 2008, pp. 192–195. 8
- [16] —, “Iceberg size and orientation estimation using SeaWinds.” *Proceedings of the International Geoscience and Remote Sensing Symposium*, Honolulu, HI, 2010, pp. 2394–2397. 8
- [17] D. Long and M. Spencer, “Radar backscatter measurement accuracy for a spaceborne pencil-beam wind scatterometer with transmit modulation,” *IEEE Transactions on Geoscience and Remote Sensing*, vol. 35, no. 1, Jan 1997. 10
- [18] M. Spencer, C. Wu, and D. Long, “Tradeoffs in the design of a spaceborne scanning pencil beam scatterometer: application to SeaWinds,” *IEEE Transactions on Geoscience and Remote Sensing*, vol. 35, no. 1, pp. 115–126, Jan 1997. 10, 13
- [19] D. Early and D. Long, “Image reconstruction and enhanced resolution imaging from irregular samples,” *IEEE Transactions on Geoscience and Remote Sensing*, vol. 39, no. 2, pp. 291–302, 2001. 10, 11, 14, 28
- [20] M. Spencer and D. Long, “Improved resolution backscatter measurements with the SeaWinds pencil-beam scatterometer,” *IEEE Transactions on Geoscience and Remote Sensing*, vol. 38, no. 1, pp. 89–104, 2000. 10, 11, 13, 14, 51
- [21] S. Dunbar, B. Weiss, B. Stiles, J. Huddleston, P. Callahan, G. Shirliffe, K. Perry, and C. Hsu, *QuikSCAT Science Data Product User’s Manual. Version 3.0*, JPL, Sept 2006, ftp://podaac.jpl.nasa.gov/ocean_wind/quikscat/L2B/doc/QSUG_v3.pdf. 11, 12, 13
- [22] I. Ashcraft and D. Long, “The spatial response function of SeaWinds backscatter measurements,” W. L. Barnes, Ed. *Proceedings of SPIE Vol. 5151 Earth Observing Systems VIII*, Aug 2003, pp. 609–618. 11, 13
- [23] B. Williams, M. Owens, and D. Long, “The Ultra High Resolution QuikSCAT Product.” *Proceedings of the IEEE Radar Conference*, Pasadena, CA, 2009, pp. 1–6. 13
- [24] D. Long, P. Hardin, and P. Whiting, “Resolution enhancement of spaceborne scatterometer data,” *IEEE Transactions on Geoscience and Remote Sensing*, vol. 31, no. 3, pp. 700–715, May 1993. 13, 27, 128
- [25] F. Ulaby, R. Moore, and A. Fung, *Microwave Remote Sensing*. Addison-Wesley, 1981, vol. 1. 18, 21, 155

- [26] S. Haykin, E. Lewis, R. Raney, and J. Rossiter, *Remote Sensing of Sea Ice and Icebergs*. John Wiley & Sons, Inc., 1994. 18, 21, 156
- [27] D. Long, R. Collyer, R. Reed, and D. Arnold, "Dependence of the normalized radar cross section of water waves on Bragg wavelength-wind speed sensitivity," *IEEE Transactions on Geoscience and Remote Sensing*, vol. 34, no. 3, May 1996. 18, 20
- [28] F. Naderi, M. Freilich, and D. Long, "Spaceborne radar measurement of wind velocity over the ocean - an overview of the NSCAT scatterometer system," vol. 79, no. 6, Jun 1991. 18, 20
- [29] N. Sharma and E. D'Sa, "Assessment and analysis of QuikSCAT vector wind products for the Gulf of Mexico: a long-term and hurricane analysis," *Sensors*, vol. 8, no. 3, pp. 1927–1949, Mar 2008. 20
- [30] R. Massom, *Satellite Remote Sensing of Polar Regions*. Lewis Publishers, 1991. 20
- [31] H. Zwally, J. Comiso, C. Parkinson, D. Cavalieri, and P. Gloersen, "Variability of Antarctic sea ice 1979-1998," *Journal of Geophysical Research*, vol. 107, no. C5, 2002. 20
- [32] M. Drinkwater, D. Long, and A. Bingham, "Greenland snow accumulation estimates from satellite radar scatterometer data," *Journal of Geophysical Research*, vol. 106, no. D24, pp. 33 935–33 950, Dec 2001. 20
- [33] R. Forester, D. Long, K. Jezek, S. Drobot, and M. Anderson, "The onset of Arctic sea-ice snowmelt as detected with passive- and active-microwave remote sensing," *Annals of Glaciology*, vol. 33, 2001. 20
- [34] L. Kunz and D. Long, "Melt detection in Antarctic ice-sheets using spaceborne scatterometers and radiometers," *IEEE Transactions on Geoscience and Remote Sensing*, 2004. 20
- [35] T. Scambos, C. Hulbe, M. Fahnestock, and J. Bohlander, "The link between climate warming and break-up of ice shelves in the Antarctic peninsula," *Journal Glaciology*, vol. 46, pp. 516–530, 2000. 20
- [36] T. Scambos, O. Sergienko, A. Sargent, D. MacAyeal, and J. Fastook, "ICESat profiles of tabular iceberg margins and iceberg breakup at low latitudes," *Geophysical Research Letters*, vol. 32, no. L23S09, 2005. 20, 31, 73
- [37] R. Bindshadler and E. Rignot, "'Crack' in the polar night," *EOS, Transactions, American Geophysical Union*, vol. 82, pp. 497–505, 2001. 26
- [38] M. Kristensen, "Iceberg calving and deterioration in Antarctica," *Progress Physical Geography*, vol. 7, pp. 313–328, 1983. 26, 73
- [39] J. Ballantyne, "A multidecadal study of the number of Antarctic icebergs using scatterometer data," Brigham Young University online report: (<http://www.scp.byu.edu/data/iceberg/IcebergReport.pdf>), Tech. Rep., 2002. 26, 27

- [40] M. Lazzara, K. Jezek, T. Scambos, D. MacAyeal, and C. van der Veen, “On the recent calving of icebergs from the Ross ice shelf,” *Polar Geography*, vol. 23, pp. 201–212, 1999. 26
- [41] D. Macayeal, M. Okal, J. Thom, K. Brunt, Y. Kim, and A. Bliss, “Tabular iceberg collisions within the coastal regime,” *Journal of Glaciology*, vol. 54, no. 185, 2008. 27
- [42] J. Tournadre, K. Whitmer, and F. Girard-Arduin, “Iceberg detection in open water by altimeter waveform analysis,” *Journal of Geophysical Research*, vol. 113, no. C08040, 2008. 27, 33
- [43] M. Schodlok, H. Hellmer, G. Rohardt, and E. Fahrbach, “Weddell Sea iceberg drift: five years of observations,” *Journal of Geophysical Research*, vol. 111, 2006. 27, 45
- [44] NIC, “National Ice Center,” <http://www.natice.noaa.gov/>, update 2010. 30
- [45] B. Guily, “The drift of icebergs under wind action,” *Journal of Geophysical Research*, vol. 93, no. C4, pp. 3608–3612, Apr 1988. 30, 45
- [46] H. Stephen and D. Long, “Study of iceberg B10A using scatterometer data,” vol. 3. Proceedings of the International Geoscience and Remote Sensing Symposium, Honolulu, HI, 2000, pp. 1340–1342. 31, 48
- [47] H. Anderson and D. Long, “Sea ice mapping method for SeaWinds,” *IEEE Transactions on Geoscience and Remote Sensing*, vol. 43, no. 3, pp. 647–657, 2005. 38
- [48] Q. Remund and D. Long, “Sea ice mapping using ku band scatterometer data,” *Journal of Geophysical Research*, vol. 104, no. C5, pp. 11 515–11 527, 1999. 38
- [49] J. Haarpaintner, R. Tonboe, D. Long, and M. van Woert, “Automatic detection and validity of the sea-ice edge: an application of enhanced-resolution QuikScat/SeaWinds data,” *IEEE Transactions on Geoscience and Remote Sensing*, vol. 42, no. 7, pp. 1433–1443, 2004. 38
- [50] K. Stuart and D. Long, “Tracking large tabular icebergs using the SeaWinds Ku-band microwave scatterometer,” *Deep Sea Research II*, vol. 58, pp. 1285–1300, June 2011. 47, 73, 74, 75
- [51] G. Troglio, J. Benediktsson, G. Moser, and S. Serpico, “Crater detection based on marked point processes.” Proceedings of the International Geoscience and Remote Sensing Symposium, Honolulu, HI, 2010, pp. 1378–1381. 48
- [52] G. Crocker, “Size distributions of bergy bits and growlers calved from deteriorating icebergs,” *Cold Regions Science and Technology*, vol. 22, no. 1, pp. 113–119, Nov 1993. 48, 49
- [53] S. Savage, G. Crocker, M. Sayed, and T. Carrieres, “Size distributions of small ice pieces calved from icebergs,” *Cold Regions Science and Technology*, vol. 31, no. 2, pp. 163–172, July 2000. 48, 49

- [54] G. Bigg, M. Wadley, D. Stevens, and J. Johnson, “Modelling the dynamics and thermodynamics of icebergs,” *Cold Regions Science and Technology*, vol. 26, no. 2, pp. 113–135, Oct 1997. 48, 49
- [55] National Ice Center, “Southern Hemisphere Iceberg,” <http://www.natice.noaa.gov/>, update 2012. 55, 65, 124, 125
- [56] O. Sergienko, T. Scambos, D. MacAyeal, and J. Fastook, “Tabular icebergs in the Southern Atlantic: melt pond geometry, and margin evolution,” *EOS, Transactions American Geophysical Union*, vol. 85, no. 47, pp. C22A–07, 2004. 73
- [57] S. Smith, “Hindcasting iceberg drift using current profiles and wind,” *Cold Regions Science and Technology*, vol. 22, pp. 33–45, 1993. 76, 84
- [58] G. Bigg, M. Wadley, D. Stevens, and J. Johnson, “Modelling the dynamics and thermodynamics of icebergs,” *Cold Regions Science and Technology*, vol. 26, no. 2, pp. 113–135, Oct 1997. 76, 77, 78, 79, 82, 84, 94, 124, 143
- [59] R. Gladstone and G. Bigg, “Iceberg trajectory modeling and meltwater injection in the Southern Ocean,” *Journal of Geophysical Research*, vol. 106, no. C9, pp. 19 903–19 915, 2001. 76, 77, 84, 85, 94, 124, 143
- [60] C. Lichey and H. Hellmer, “Modeling giant-iceberg drift under the influence of sea ice in the Weddell Sea,” *Antarctica, Journal of Glaciology*, vol. 47, no. 158, pp. 452–460, 2001. 76, 77, 84, 85
- [61] I. Kubat and M. Sayed, “An Operational Model of Iceberg Drift,” *International Journal of Offshore and Polar Engineering*, vol. 15, no. 2, pp. 125–131, 2005. 76, 84, 87, 94
- [62] H. Keys and D. Fowler, “Sources and movement of icebergs in the south-west Ross Sea,” *Ann. Glaciol.*, 1989. 77
- [63] J. Jongma, E. Driesschaert, T. Fichefet, H. Goosse, and H. Renssen, “The effect of dynamic-thermodynamic icebergs on the southern ocean climate in a three-dimensional model,” *Ocean Modelling*, vol. 26, pp. 104–113, 2009. 77, 81, 85, 94, 124, 143
- [64] K. Eik, “Iceberg drift modelling and validation of applied metocean hindcast data,” *Cold Regions Science and Technology*, vol. 57, pp. 67–90, 2009. 77, 78, 83, 84, 94
- [65] National Oceanography Centre, “Ocean Circulation and Climate Advanced Modelling Project,” <http://www.noc.soton.ac.uk/JRD/OCCAM/>, update 2012. 78, 80, 121
- [66] National Snow and Ice Data Center, “Sea Ice Concentrations from Nimbus-7 SMMR and DMSP SSM/I-SSMIS Passive Microwave Data,” <http://nsidc.org/>, update 2012. 79
- [67] —, “Polar Pathfinder Daily 25 km EASE-Grid Sea Ice Motion Vectors,” <http://nsidc.org/>, update 2012. 79

- [68] J. Dowdeswell and J. Bamber, “Keel depths of modern Antarctic icebergs and implications for sea-floor scouring in the geological record,” *Marine Geology*, vol. 243, pp. 120–131, 2007. 79, 101, 124
- [69] W. Weeks and M. Mellor, “Some elements of iceberg technology.” Proceedings of the First Conference on Iceberg Utilization for Freshwater Production, 1978. 79
- [70] S. Savage, G. Crocker, M. Sayed, and T. Carrieres, “Size distributions of small ice pieces calved from icebergs,” *Cold Regions Science and Technology*, vol. 31, pp. 163–172, 2000. 80, 86
- [71] B. Munson, D. Yound, and T. Okiishi, *Fundamentals of Fluid Mechanics*, 6th ed. John Wiley & Sons, Inc, 2009. 83, 84
- [72] M. Akiba, S. Morooka, K. Shirakawa, and K. Chuman, “Experimental Study on Improvement of Inlet Orifice in BWR Core,” *Journal of Nuclear Science and Technology*, vol. 38, no. 9, pp. 793–798, 2001. 83
- [73] M. Wang and P. Catalano, “Prediction of high reynolds number flow over a circular cylinder using LES with wall modeling,” Center for Turbulence Research, Tech. Rep., 2001. 83
- [74] W. Khan, J. Culham, and M. Yovanovich, “Fluid Flow Around and Heat Transfer from Elliptical Cylinders: Analytical Approach,” *Journal of Thermophysics and Heat Transfer*, vol. 19, no. 2, 2005. 83
- [75] T. Scambos, personal communication, 2012. 83
- [76] E. Hunke and D. Comeau, “Sea ice and iceberg dynamic interaction,” *Journal of Geophysical Research*, vol. 116, 2011. 84
- [77] M. Crepon and M. Houssais, “The Drift of Icebergs Under Wind Action,” *Journal of Geophysical Research*, vol. 93, no. C4, pp. 3608–3612, 1988. 86
- [78] R. Dewey, D. Richmind, and C. Garrett, “Stratified Tidal Flow over a Bump,” *Journal of Physical Oceanography*, vol. 35, no. 1911-1927, 2005. 87, 158
- [79] T. Bell, “Topographically generated internal waves in the open ocean,” *Journal of Geophysical Research*, vol. 80, no. 320-327, 1975. 87, 158
- [80] S. Kelly, J. Nash, and E. Kunze, “Internal-tide energy over topography,” *Journal of Geophysical Research*, vol. 115, no. C06014, 2010. 87, 158, 159
- [81] H. Wells and S. Vosper, “The accuracy of linear theory for predicting mountain-wave drag: Implications for parametrization schemes,” *Q. J. R. Meteorological Society*, vol. 136, pp. 429–441, 2010. 87, 158, 159
- [82] K. Lamb, “Nonlinear interaction among internal wave beams generated by tidal flow over supercritical topography,” *Geophysical Research Letters*, vol. 31, no. L09313, p. 4, 2004. 87, 158, 159

- [83] J. Vanderhoff, “A numerical and observational investigation of short and long internal wave interactions,” Ph.D. dissertation, University of California San Diego, 2007. 87, 158
- [84] E. Hairer and G. Wanner, *Solving Ordinary Differential Equations II: Stiff and Differential-Algebraic Problems*, 2nd ed. Springer-Verlag Berlin Heidelberg, 1996. 87
- [85] L. Shampine and M. Reichelt, “The MATLAB ODE Suite,” *SIAM Journal on Scientific Computing*, vol. 18, pp. 1–22, 1997. 88
- [86] M. Hayes, *Statistical Digital Signal Processing and Modeling*. John Wiley & Sons, Inc., 1996. 89, 91
- [87] T. Warner, *Numerical Weather and Climate Prediction*. Cambridge University Press, 2011. 89
- [88] T. Moon and W. Stirling, *Mathematical Methods and Algorithms*. Prentice Hall, 2000. 89, 107
- [89] S. Kluge, K. Reif, and M. Brokate, “Stochastic Stability of the Extended Kalman Filter With Intermittent Observations,” *IEEE Transactions on Automatic Control*, vol. 55, no. 2, 2010. 90, 91
- [90] K. Reif, S. Gunther, E. Yaz, and R. Unbehauen, “Stochastic Stability of the Discrete-Time Extended Kalman Filter,” *IEEE Transactions on Automatic Control*, vol. 44, no. 4, 1999. 91
- [91] M. C. N. van de Wouw, W. Heemels, and H. Nijmeijer, “Stabilization of Networked Control Systems with Large Delays and Packet Dropouts.” Proceedings of the American Control Conference, Seattle, WA, June 11-13, 2008, pp. 4991–4996. 91
- [92] H. Gaskill and J. Rochester, “A new technique for iceberg drift prediction,” *Cold Regions Science and Technology*, vol. 8, no. 3, pp. 223–234, 1984. 93
- [93] Microwave Earth Remote Sensing Laboratory, “Scatterometer Climate Record Pathfinder,” <http://www.scp.byu.edu/>, update 2012. 99
- [94] I. Ashcraft and D. Long, “The spatial response function of SeaWinds backscatter measurements,” W. L. Barnes, Ed. Proceedings of SPIE Vol. 5151 Earth Observing Systems VIII, Aug 2003, pp. 609–618. 109
- [95] D. Early and D. Long, “Image reconstruction and enhanced resolution imaging from irregular samples,” *IEEE Transactions on Geoscience and Remote Sensing*, vol. 39, no. 2, pp. 291–302, 2001. 109
- [96] A. Coward and B. de Cuevas, *The OCCAM 66 Level Model: physics, initial conditions and external forcing*, National Oceanography Centre, Southampton, <http://www.noc.soton.ac.uk/JRD/OCCAM/OCCAM-p25k66-run202.pdf>, 2005. 114, 118, 124

- [97] M. Abrahamowicz, “A thermodynamic and dynamic lagrangian model for icebergs: A data-model intercomparison for the Southern Ocean,” Master’s thesis, McGill University, 2007. 114, 142
- [98] C. Tansley and D. Marshall, “Flow past a cylinder on a β plane, with application to Gulf Stream separation and the Antarctic Circumpolar Current,” *Journal of Physical Oceanography*, vol. 31, pp. 3274–3283, 2001. 114, 134
- [99] J. Nycander, K. Doos, and A. Coward, “Chaotic and regular trajectories in the Antarctic Circumpolar Current,” *Tellus A*, vol. 54, pp. 99–106, 2002. 114, 134
- [100] M. Meredith, P. Woodward, T. Chereskin, D. Marshall, L. Allison, G. Bigg, K. Donohue, K. Heywood, C. Hughes, A. Hibbert, A. McC. Hogg, H. Johnson, L. Jullion, B. King, H. Leach, Y. Lenn, M. Morales Maqueda, D. Munday, A. Naveira Garabato, C. Provost, J. Sallee, and J. Sprintall, “Sustained monitoring of the Southern Ocean at Drake Passage: Past achievements and future priorities,” *Reviews of Geophysics*, vol. 49, no. RG4005, 2011, doi:10.1029/2010RG000348. 114, 134
- [101] D. Luce and T. Rossby, “On the size and distribution of rings and coherent vortices in the Sargasso Sea,” *Journal of Geophysical Research*, vol. 113, no. C05011, 2008. 118
- [102] G. Bigg, M. Wadley, D. Stevens, and J. Johnson, “Prediction of iceberg trajectories for the North Atlantic and Arctic Oceans,” *Geophysical Research Letters*, vol. 23, no. 24, pp. 3587–3590, 1996. 123
- [103] V. Radikevich and Y. Romanov, “Using observations of iceberg drift for determining currents in the Pacific sector of the Southern Ocean,” *Oceanology*, vol. 35, no. 1, pp. 130–139, 1995. 123
- [104] F. Ulaby, *Fundamentals of Applied Electromagnetics*. Pearson Prentice Hall, 2004. 155
- [105] D. Draper and D. Long, “Evaluating the effect of rain on SeaWinds scatterometer measurements,” *Journal of Geophysical Research*, vol. 109, no. C02005, 2004, doi:10.1029/2002JC001741. 155
- [106] D. Long, R. Collyer, R. Reed, and D. Arnold, “Dependence of the normalized radar cross section of water waves on bragg wavelength-wind speed sensitivity,” *IEEE Transactions on Geoscience and Remote Sensing*, vol. 34, no. 3, pp. 656–666, May 1996. 155
- [107] G. Timco and W. Weeks, “A review of the engineering properties of sea ice,” *Cold Regions Science and Technology*, vol. 60, no. 2, pp. 107–129, 2010. 156
- [108] N. Fofonoff and R. Milland Jr., “Algorithms for computation of fundamental properties of seawater,” in *UNESCO technical papers in marine science*, ser. 44, 1983. 158

Appendix A

Map of the Southern Ocean

Because this dissertation emphasizes standard SeaWinds image products, it is helpful to review the polar stereographic map projection used to represent SeaWinds backscatter images of the Southern Ocean. A map of the Antarctica and the Southern Ocean is included in Fig. A.0. Geographic regions referred to in the dissertation are also labeled. Quadrants are used in NIC nomenclature to designate new icebergs.

Because the map is centered on the South Pole, all outward directions from the center of Fig. A.0 correspond to north, and inward vectors correspond to south. Similarly, clockwise motion corresponds to eastward movement, and counter-clockwise to westward.

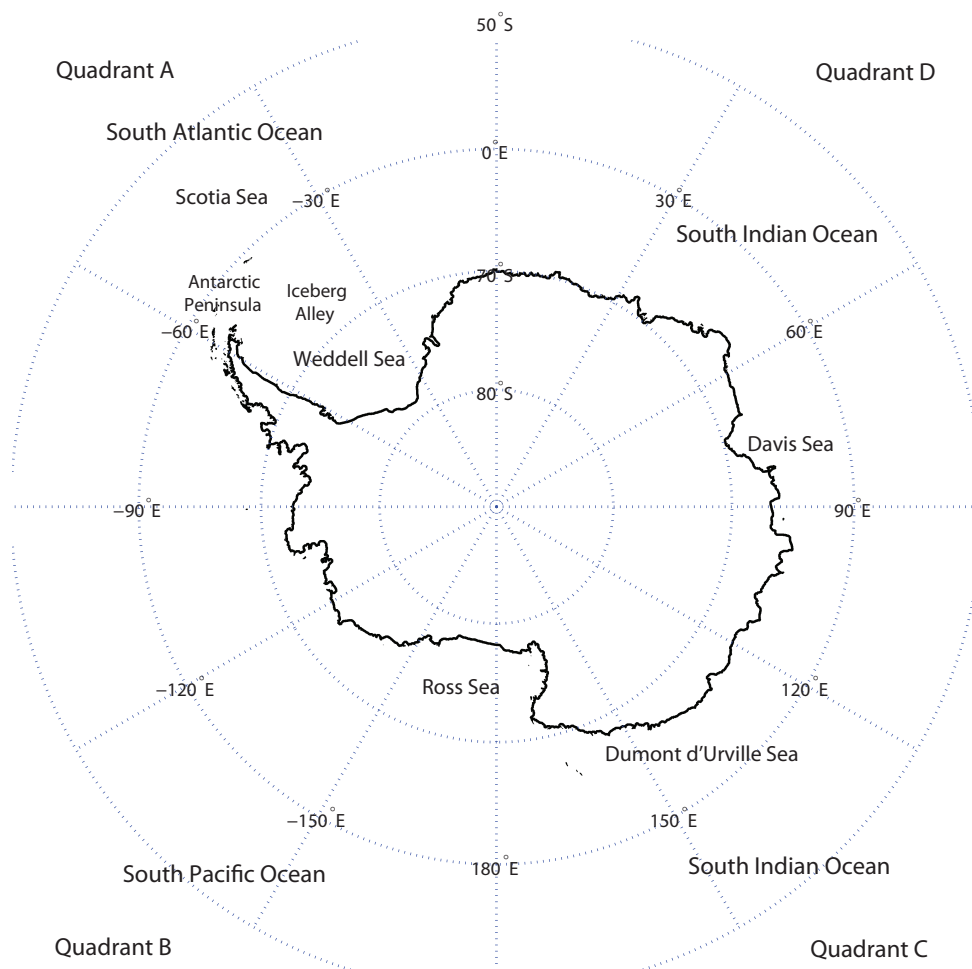


Figure A.1: Polar stereographic map of Antarctica and the Southern Ocean.

Appendix B

A Review of Microwave Scattering from Antarctic Targets

To better interpret SeaWinds backscatter images, a brief explanation of the dominant characteristics contributing to radar backscatter is helpful. First, surface and volume scattering is reviewed. Second, the microwave scattering properties from common scatterers in the Southern Ocean are presented.

B.1 Surface and Volume Scattering

The backscatter measurements collected by SeaWinds are the result of a combination of surface scatter and volume scatter. Surface scatter is the portion of energy reflected at the air-surface boundary. Volume scatter is the portion of energy transmitted into the Earth, potentially reflecting off internal particles.

The dominant electromagnetic factor that influences surface and volume scatter is the change in permittivity at the air-surface boundary. Permittivity relates to a material's ability to transmit an electric field. Permittivity is a complex value where the real part indicates the ability to store energy within a medium and the imaginary component relates to the dissipation of energy within the medium. If the relative difference in the real part of the permittivity is small between the air and target, a large fraction of the incident energy is transmitted into the Earth. The greater the difference in the real part of the permittivity at the air-surface boundary, the more the object's surface acts like a perfect electric conductor and thus the more energy reflected away from the boundary.

If the imaginary component of the permittivity is small, the energy transmitted into the target propagates to a characteristic penetration depth. The penetration depth is the characteristic depth electromagnetic waves penetrate into a structure. This energy reflects off internal particles and contributes to volume scattering. If a large imaginary component of the permittivity exists, the energy transmitted into the target is absorbed, therefore there is not a significant volume scattering component.

Dominant physical properties that influence surface and volume scatter include surface roughness, particle size, and particle density of the target. Surface roughness determines the directionality of the energy reflected at the air-surface boundary. An incident wave reflecting off a relatively flat surface results in a reflected wave with a high directivity. Surface roughness on the order of the operating wavelength causes overall signal dispersion, enabling some incident energy to be reflected in all directions. The greater the random surface roughness, the more energy is reflected in all directions.

Particle size and density of the target affect the intensity of the associated volume scatter. Particle sizes equal to or greater than the operating wavelength reflect radar pulses. Targets com-

posed of particles smaller than microwaves produce significantly smaller volume scatter and are only detectable in very large quantities. Similarly, particle density is also correlated with volume scatter intensity. For instance, if more particles exist within a radar footprint, more energy will be reflected by a single radar pulse.

In summary, backscatter measurements collected by SeaWinds are a combination of surface scatter and volume scatter. Surface scatter and volume scatter intensity is affected by differences in the real part of the permittivity at the air-target boundary. A large permittivity difference results in greater surface scatter and less volume scatter. Surface scatter directionality is determined by target-surface roughness. Volume scatter intensity is also affected by penetration depth, particle size and particle density of the target [25].

B.2 Antarctic Scatterers

In order to better understand the enhanced resolution data products used in this dissertation, a review of the most common Antarctic scatterers is helpful. In the Southern Ocean, dominant microwave scatterers are sea water, sea ice, and glacial ice. Backscatter profiles for each of these scatterers have been compiled and factors contributing to each characteristic profile are highlighted below.

Dominant factors affecting surface and volume scatter of sea water, sea ice, and glacial ice are outlined below. Seasonal changes that define annual trends in backscatter measurements are also discussed.

B.2.1 Sea Water

To analyze surface and volume scattering components of sea water, knowledge of the electromagnetic and physical properties of sea water is necessary. Sea water has a high relative permittivity compared to that of air and is considered a good conductor [104]. Therefore a dominant portion of incident energy is reflected back into the air, resulting in a large surface scattering component and a small volume scattering component.

The directivity of the reflected wave at the surface is governed by the geometry of the incident wave and the surface roughness of the sea water. Because SeaWinds transmits at an oblique angle with respect to the ocean's surface, the reflected pulse is generally directed away from the scatterometer, resulting in low σ° measurements. Other surface characteristics affecting directionality of the reflected wave include the presence of rain or wind. If strong rain is present, sea water surface features are randomly roughened, generally increasing the surface scattering back to the antenna [105]. Surface scattering is also related to the presence of near-surface winds. Near-surface winds induce capillary waves on the ocean's surface. These surface perturbations roughen the ocean's surface and may result in higher backscatter [106].

Volume scattering is related to the amount of energy transmitted into sea water, the characteristic penetration depth of sea water, and the subsequent reflections off internal particles. Because of the relatively large real component of the permittivity of sea water, only a small fraction of the incident energy is actually transmitted into sea water. Because conductivity and penetration depth are inversely related, sea water's high conductivity results in minimal sea-water penetration and thus negligible volume scattering. Therefore, the dominant element contributing to sea-water backscatter is surface scattering.

The average backscatter return from sea water from 1999 to 2009 is displayed in Fig. 3.4. Notice an overall seasonal trend. Sea water backscatter is generally higher during the austral winter, peaking around Julian day 225. This trend is due to increased surface perturbations during the austral winter.

B.2.2 Sea Ice

To analyze the surface and volume scattering components of sea ice, knowledge of the physical and electromagnetic properties of sea ice is necessary. Compared to the permittivity between air and sea water, the permittivity difference between air and sea ice is smaller. Consequently, less energy is reflected at the air-surface boundary and a significant portion of energy may be transmitted into the sea ice. As a result, both surface scattering and volume scattering contribute to the overall backscatter signature of sea ice.

The factor that most affects the surface scattering of sea ice is surface roughness. If the sea ice has rough surface features (\geq the size of the operating wavelength), more incident energy is scattered in all directions. For example, pancake ice is formed in turbulent oceanic conditions, resulting in rough-edged fragments of sea ice. Due to these rough surface characteristics, associated surface scatter is dispersed in all directions, resulting in higher backscatter signatures from pancake ice. Conversely, grease ice is formed in calm conditions and is characterized with a smooth, uniform growth pattern. As a result, incident waves reflected from grease ice have a higher directivity away from an oblique incident wave, resulting in a lower backscatter profile [26, 107].

Factors that influence the volume scattering of sea ice include sea ice height, penetration depth, particle size, particle density, and the presence of surface moisture. Sea-ice height is related to the age of the sea ice. For example, multi-year sea ice is taller in height than first-year sea ice. As a result, multi-year sea ice has the potential for greater penetration depth and thus increased volume scattering. Once energy is transmitted into sea ice, it reflects off internal particles. Unfortunately, sea ice particles are usually smaller than wavelengths at Ku-band; therefore, volume scatter from sea ice is small.

The intensity of volume scatter from sea ice is also dependent on the presence of surface moisture. If surface moisture is present, microwave penetration is negligible, volume scattering is minimized, and the dominant scattering component is surface scattering. Note that even though the presence of surface moisture on sea ice results in a lower backscatter return, there is usually significant enough surface scattering from rough surface features to distinguish between sea ice and sea water.

On a large scale, the intensity of backscatter measurements collected by SeaWinds is a function of sea ice concentration. For example, backscatter from an area with a 90% sea ice concentration will produce a stronger backscatter signature than an area with a 50% sea ice concentration.

The average backscatter return from sea ice from 1999 to 2009 is displayed in Fig. 3.4. On average, the backscatter profile from sea ice is greater than sea water and smaller than glacial ice. Also notice an overall seasonal sea-ice backscatter trend. Sea ice backscatter is generally higher during the austral summer, peaking around Julian day 50. This trend is due to differences in overall sea ice area in the Southern Ocean, see Fig. 3.5. Most of the 19 million square kilometers of sea ice around Antarctica during the austral winter is first-year sea ice, and the majority of the 3 million square kilometers of sea ice that survives the austral ablation is multi-year fast ice. Therefore,

the relatively-high backscatter detected during the austral summer, JD1-100, corresponds to multi-year sea ice. The low-backscatter profile of the period from JD100-150 corresponds to fast ice and newly-grown first-year sea ice. Backscatter from JD150-300 predominantly characterizes the 19 million square kilometers of first-year sea ice. The period JD300-350 characterizes the onset of the austral ablation and corresponds with overall first-year sea ice thinning and recession.

B.2.3 Glacial Ice

To analyze the surface and volume scattering components of glacial ice, knowledge of the electromagnetic and physical properties of glacial ice is necessary. Glacial ice has the same relative permittivity of sea ice. As a result, a small fraction of incident energy is reflected at the air-surface boundary, resulting in minimal surface scattering. The majority of the incident microwave energy is transmitted into the interior of the glacial ice medium, contributing to volume scattering.

The factor that most affects surface scattering of glacial ice is surface roughness. Significant surface roughness (\geq the size of the operating wavelength) usually exists on the surface of glacial ice. As a result, a small portion of energy from the incident wave is reflected back toward the SeaWinds scatterometer.

Factors that most influence the volume scatter from glacial ice are glacial ice penetration depth, particle size, particle density, and the presence of surface moisture. Once energy is transmitted into sea ice, it readily reflects off internal particles. Because multiple years of snow accumulation are necessary to create glacial ice, ice particles are compressed together, generally resulting in a dense structure of large ice particles. The size of these crystals are commonly large enough to reflect microwave energy. As a result, glacial ice particles readily reflect microwaves.

Due to a large penetration depth, large particle size, and dense structure, glacial ice usually has large associated volume scattering. In reality, the contribution of volume scatter is so large that it is the dominant scattering component contributing to overall backscatter. This is the reason icebergs tend to be bright compared to sea water and sea ice such as in Fig. 3.1.

One case where volume scattering is reduced is when significant moisture is present on the surface of glacial ice. When surface moisture is present, the high permittivity of the surface water increases the conductivity of the surface glacial ice, minimizing penetration depth and reducing overall volume scatter. During the austral ablation, glacial ice frequently contains large pools of surface water. Under these conditions, the volume scatter from glacial ice is minimized and the radar intensity resembles that of ocean water.

The average backscatter return from glacial ice below 55°S from 1999 to 2009 is displayed in Fig. 3.4. Note that the backscatter from glacial ice remains relatively constant throughout the year. Also notice h-pol backscatter measurements have a slightly higher return than v-pol, a property used to optimize the iceberg detection process.

Appendix C

Drag on an Iceberg due to Internal Ocean Waves

Internal waves are generated by the flow of ocean currents over the lower portion of an iceberg in the same manner waves are generated by flow over bottom sea topography and stationary ocean ridges [78–83]. These waves extract momentum from the flow of an iceberg, resulting in an associated drag force on the iceberg. The magnitude of the drag is dependent on the iceberg scale, translational velocity, and local stratification of the ocean (i.e., ocean buoyancy frequency). If the frequency of the waves generated by the iceberg is less than the local buoyancy frequency, internal waves are generated [78, 79]. In the case of flow of water under an iceberg, the frequency of waves generated (ω) is related to the scale of the iceberg and the relative velocity of the water flow under it. For sinusoidal trains of topography, $\omega = 2\pi|V_i - V_w|/\lambda$ where λ is the wavelength of topography in the direction of flow. For sinusoidal topography, the internal waves generated have the same wavelengths as the topography; however, for isolated topography, multiple waves at different wavelengths are generated. The wavelengths of the generated waves are defined by the range of wavelengths necessary to spatially define the mountain-like shape of the bottom topography. The wider the mountain, the longer the wavelengths of the generated internal waves [82].

The buoyancy frequency of the ocean is found by calculating the depth-dependent density of the ocean, a characteristic profile found by using available salinity and temperature profiles reported in the OCCAM dataset and can be approximated by

$$\begin{aligned}\rho_T &= 1000 \cdot \left(1 - \frac{(T + 288.9414)(T - 3.9863)^2}{508929.2(T + 68.12963)} \right), \\ A &= 0.824493 - 4.0899 \times 10^{-3} \cdot T \\ &\quad + 7.6438 \times 10^{-5} \cdot T^2 \\ &\quad - 8.2467 \times 10^{-7} \cdot T^3 \\ &\quad + 5.3675 \times 10^{-9} \cdot T^4, \\ B &= -5.724 \times 10^{-3} + 1.0227 \times 10^{-4} \cdot T \\ &\quad - 1.6546 \times 10^{-6} \cdot T^2, \\ C &= 4.8314 \times 10^{-4}, \\ \rho &= \rho_T + A \cdot S + B \cdot S^{3/2} + C \cdot S^2\end{aligned}\tag{C.1}$$

where ρ is the estimated potential density of the ocean with respect to salinity S (PSU) and temperature T (°C) [108]. The buoyancy frequency of the ocean, N , is found by using the dynamic

density profile from Eq. C.1 in

$$N = \sqrt{-\frac{\partial \rho}{\partial z} \cdot \frac{g}{\rho_o}} \quad (\text{C.2})$$

where $\rho_o = 1027.85 \text{ kg/m}^3$, g is the acceleration constant due to gravity, and z is vertical ocean depth. To represent the cumulative buoyancy frequency of the ocean near the generation region, N is vertically averaged over the lower portion of the iceberg's keel, producing the average oscillating frequency of the ocean over the iceberg's volume, N_{avg} , where internal waves may be expected. Upper ocean layers are mixed layers (i.e., not stably-stratified in density) and thus do not support internal waves [80].

The frequency of waves generated by an iceberg depends on iceberg geometry. To obtain a first-order approximation, I treat the submerged portion of the tabular iceberg as a Gaussian-shaped bump attached to a horizontal platform. The wavelengths comprising the Gaussian profile can be approximated as $\lambda = 0.83 \cdot b$ where b is the half-width (i.e., average radius) of the iceberg's top-down profile [81]. As a result, the estimated drag due to internal wave generation, F_{IW} , is

$$F_{IW} = \rho_o |V_i| H^2 N_{avg} L \quad (\text{C.3})$$

where H is the keel depth of the iceberg and L is the length of the iceberg perpendicular to the iceberg's translational motion.

For the simulated iceberg in Section 6.5.1, salinity and temperature profiles result in an iceberg buoyancy frequency of approximately 5 cycles per hour. This restorative oscillation combined with an iceberg velocity of 0.1 m/s (from Fig. 6.3) produces a drag force on the order of $1e7 \text{ N}$. Although nonlinearities were not accounted for, it is expected that higher-order approximations of iceberg geometry would not change the order of the magnitude of the result very much [81, 82].